Comment l'organisation physique des agrégats nano-particulaires fer – matière organique contrôle-t-elle leur réactivité ?

Anthony Beauvois

UNIVERSITÉ DE RENNES 1

THESE DE DOCTORAT DE

L'UNIVERSITE DE RENNES 1

ECOLE DOCTORALE N° 600
Ecole doctorale Ecologie, Géosciences, Agronomie et Alimentation
Spécialité : Sciences de la Terre et de l'Environnement

Par
Anthony BEAUVOIS

Comment l'organisation physique des agrégats nano-particulaires fer – matière organique contrôle-t-elle leur réactivité ?

Thèse présentée et soutenue à Gif-sur-Yvette, le 07 octobre 2020
Unité de recherche : Géosciences Rennes

Rapporteurs avant soutenance :

Bruno LANSON, Directeur de recherche, ISTerre, Université Grenoble Alpes

Laurent MICHOT, Directeur de recherche, PHENIX, Sorbonne université

Composition du Jury :

Cécile QUANTIN, Professeure, Géosciences Paris-Sud, Université Paris-Saclay, **Présidente du Jury**

Bruno LANSON, Directeur de recherche, ISTerre, Université Grenoble Alpes

Laurent MICHOT, Directeur de recherche, PHENIX, Sorbonne université

Olivier DIAT, Directeur de recherche, ICSM, CEA Marcoule

Co-directeurs de thèse
Mélanie DAVRANCHE, Professeure, Géosciences Rennes, Université de Rennes 1

Delphine VANTELON, Responsable de ligne, synchrotron SOLEIL

Jacques JESTIN, Directeur de recherche, LLB, CEA Saclay

Remerciements

Une belle aventure de trois années s'achève avec ce manuscrit ! Trois années qui furent enrichissantes tant sur le plan scientifique qu'humain. Je tiens donc à remercier les personnes qui ont permis, de près ou de loin, à l'accomplissement de ce travail de thèse.

Ce travail de thèse est le fruit d'une étroite collaboration entre trois laboratoires dont je remercie les directeurs pour leur accueil : Olivier Dauteuil (Géosciences Rennes), Jean Daillant (synchrotron SOLEIL) et Eric Eliot (Laboratoire Léon Brillouin). Je remercie également les différents financeurs de cette thèse : la région Bretagne, le synchrotron SOLEIL, le LLB (projet 'ORPHREA') et l'Institut National des Sciences de l'Univers *via* « l'initiative structurante EC2CO-BIOHEFECT » (projet 'ISAAP').

En tout premier lieu, j'adresse mes plus profonds et sincères remerciements aux trois personnes sans qui ce projet ne pourrait pas avoir eu lieu : *mes directrices et directeur de thèse*. Je vais m'astreindre à faire des choix pour écrire en quelques lignes ce que je pourrais écrire sur plusieurs pages…

Merci **Delphine**, pour tout ! D'abord, merci de m'avoir fait confiance pour ce projet. Merci pour ton aide et ta disponibilité : tu as toujours su trouver du temps pour discuter des données, de l'écriture, des présentations, de mes doutes,… et ce même quand tu n'en avais pas (bon, je reconnais qu'en débarquant dans ton bureau avec mon ordinateur sous le bras, je ne te laissais pas forcément le choix…). Merci pour toutes les manips et tous les plans B qui allaient avec (et les plans C, D, etc) : même quand 'ça ne marche pas', on trouve quelque chose à faire, on ne perd pas les photons, et finalement on obtient des résultats !

Merci **Mélanie**, pour tout ! Merci d'avoir fait confiance à Delphine et, par conséquent, de m'avoir fait confiance, et ce tout au long de la thèse. Merci pour tous les échanges que nous avons pu avoir : entre toutes tes réunions et tous tes cours, tu as toujours pris le temps de répondre à mes questions, à mes sollicitations de discussion, à mes doutes. Merci d'avoir partagé avec moi les manips et je pense en particulier aux séances cryo-MET pendant lesquelles il fallait se vêtir chaudement (mais 'le jeu en valait la chandelle').

Merci **Jacques**, pour tout ! Merci pour ta confiance, les discussions que nous avons pu avoir, en particulier sur la diffusion. Merci pour les manips au MLZ qui m'ont permis de mieux te connaître.

Finalement, **merci à vous trois** ! Votre investissement, vos savoirs/compétences complémentaires et vos qualités humaines confèrent toute sa force à la collaboration Géosciences Rennes/SOLEIL/LLB. Cela forme un tout cohérent, enrichissant et agréable qui m'a permis de vivre ma thèse dans les meilleures conditions tout en apprenant énormément de choses. Pour cela, je ne vous remercierai jamais assez !

Je tiens également à remercier les membres de mon jury. Merci à **Bruno Lanson** et **Laurent Michot** d'avoir rapporté le manuscrit et pour la discussion enrichissante qui s'en est suivie. Merci à **Cécile Quantin** et **Olivier Diat** pour toutes les discussions et tous les conseils qu'ils m'ont prodigué au cours des comités de suivi de thèse et en tant qu'examinatrice et examinateur.

Mes prochains remerciements s'adressent à la 'team LUCIA'.

Merci **Camille** pour ta gentillesse, nos discussions (vélo entre autres) et le temps que tu as consacré aux manips cryo-STXM (depuis la préparation jusqu'au traitement des données en passant par les manips à ALBA). Merci de nous avoir fait profiter d'une petite soirée dehors après une période où nous été enfermé.es… C'est un réel plaisir de travailler/discuter avec toi ! Merci **Gildas** (bon, je te place encore avec LUCIA), mon 'copain à SOLEIL', pour les discussions scientifiques (et pas que), pour tes conseils, pour les cafés de l'aprem', pour la Goldschmidt :-). Merci **Benedikt** pour ton aide dans les manips de mirco-fluidique. Merci **Nicolas**, **Pierre**, **Damien** pour tous les moments et toutes les explications sur la ligne. Bref, merci à tous pour la bonne humeur qui règne sur la ligne et qui mène à des moments agréables !

Les remerciements suivants sont pour toute l'équipe Nano-BioGéochimie (NBG).

Martine, pour ta disponibilité, ta gentillesse, les discussions (diverses et variées), ton professionnalisme, ta rigueur scientifique, ton implication, je te remercie sincèrement. J'ai apprécié de travailler avec toi ! Merci **Elaheh (Elie)**, ma 'copine à Géosciences', pour m'avoir expliqué le fonctionnement des labos, pour m'avoir aiguillé dans les protocoles d'expérimentation, pour tous les moments que nous avons partagé (finalement, on voit souvent les choses du même œil ;-)) : nos repas du midi, nos sorties… Merci également à **Charlotte**, qui a permis, par son implication, aux manips d'adsorption d'être menées à terme. Merci **Aline**, **Anne-Catherine**, **Rémi**, **Mathieu**, **Julien**, **Patrice** pour votre aide et les échanges (scientifiques ou non) que nous avons pu avoir au cours de ces 3 années.

Je remercie également **tous les membres du LLB** (que je ne citerai pas, par peur d'en oublier). Pendant mes passages, assez peu fréquents il faut bien le reconnaître, vous m'avez toujours très bien accueilli. Merci **Olivier** (du LIONS) pour l'aide que tu as pu m'apportée lors de mes premières manips en solo sur le XEUSS.

Les remerciements qui suivent s'adressent à toutes les personnes avec qui j'ai travaillé au cours de ma thèse.

Merci **Hervé** pour tout le temps que tu m'as consacré en micro-fluidique (confection de wafers, puces, expérimentations,…). Merci pour tous les cafés et petits déjeuners que nous avons partagé en amont de nos réunions de travail ! Merci **Aurélien** et **Denis** pour votre investissement et votre expertise dans les observations cryo-MET.

Merci **Valérie** pour ton accueil sans faille sur ROCK, ta gentillesse et tes explications pour la MCR-ALS (nous nous souviendrons en particulier du sapin de Noël). Merci **Thomas** d'avoir passé mes suspensions sur SWING et d'avoir pris le temps de regarder les données avec moi ! Merci **Karine** et **Stéphanie** pour l'aide que vous avez pu me prodiguer au laboratoire de chimie et votre disponibilité. Thank you **Andrea** for cryo-TXM images and your tenacity in these laborious experiments. Thank you **Marie-Sousai** and **Baohu** for SANS measurements!

Je tenais également à remercier les personnes avec qui j'ai enseigné au cours de ma thèse.

Merci **Anne (L)** pour m'avoir demandé comme 'moniteur' dans l'UE 303. Merci **Anne (B)**, **Guilia**, **Katell** pour tous vos conseils/aides/réponses à mes questions dans la préparation de TD. Enseigner avec vous fut une expérience riche et agréable ! Merci à tous les autres **moniteurs** (étudiants ou pas) avec qui j'ai eu le plaisir d'encadrer des TP.

Merci **Amélie**, pour ma première expérience de recherche, pour m'avoir fait découvrir (et surtout aimé) le synchrotron et pour avoir toujours gardé un œil sur moi !

Je remercie également tous les « jeunes chercheurs » que j'ai croisés durant ces trois années (thésard.es, post-docs,…). Je pense aux rennaises et rennais : **Alice**, **Aurélie**, **Zélie**, **Edwige**, **Sen**, **Florent**, **Mara**, **Phoom**, **Corentin**, **Christophe**, **Chloé**, **Caroline** (et toutes celles et ceux que j'aurai oublié par mégarde…). Je pense également à vous, qui êtes /étiez à SOLEIL : **Daniela**, **Baptiste**, **Corentin**, **Julie**, **Manon**. Merci à toutes et tous pour votre gentillesse, votre aide ou encore nos discussions variées !

Les prochains remerciements sont pour les amis-copains.

Quand je dis copains, je pense amis. Merci **Armand**, tout simplement d'être MON AMI, depuis quelques années maintenant, sur qui je peux toujours compter ! Merci **Mélissa**, une amie fidèle ! Merci à vous tous, que j'ai rencontré pendant le magistère et avec qui j'ai partagé de bons moments : **Nathy**, **Nico**, **Marie**, **Blaise** (les séances piscine), **Meije**, **Gab**, **Ju**, **JB**, **Lucie** (je garderai en mémoire un certain craquage à SOLEIL),… Vous avez été des soutiens sans faille dans cette aventure ! Merci aux copains de prépa, que je vois peu mais que je n'oublie pas : **Anna**, **Brice**, **Léa**, **Sabrina**, **Marie-Alix**, **Nathan**, **Alice**, **Clémentine**.

Merci à toutes les personnes que j'aurai pu oublier par mégarde (et toutes mes excuses !)

Les derniers remerciements, et non des moindre, s'adressent bien entendu à la famille !

Merci à **Nathalie**, **Philippe** et **Paul**, pour vos encouragements, et tout le reste !

Enfin, je termine cette longue liste par mes **parents**, évidemment ! Vous avez toujours été derrière moi, vous m'avez toujours poussé (mais jamais forcé), encouragé, soutenu, même quand mes choix d'orientation vous ont surpris (auriez-vous pu croire que je ferai une thèse il y a 4 ans en arrière ?). Merci à mes 'p'tites' **sœurs**, **Jade** et **Tatane** d'un soutien à toute épreuve. Trois mots, simples, résument tout ce que je pourrai dire : ***je vous aime***.

Et, merci **Emilie**, d'être à mes côtés au quotidien, de me supporter (surtout en période de rédaction…), de partager tant de choses avec moi, d'avoir coordonné l'après-soutenance, (d'avoir insisté pour avoir un p'tit chat) ! Merci d'être là, tout simplement.

Sommaire

Chapitre I. Introduction

I.1. Les agrégats fer-matière organique (Fe-MO)

I.1.1. Importance des agrégats Fe-MO dans les systèmes environnementaux

Les oxyhydroxydes de fer(III) sont ubiquistes dans les systèmes environnementaux. Ils présentent des structures cristallographiques (ferrihydrite, goethite, hématite, magnétite,…), des tailles (de l'ordre du micromètre au nanomètre) et des morphologies variées (Guo et Barnard, 2013; Rabajczyk et Namieśnik, 2014). La matière organique (MO) naturelle est, elle aussi, très présente dans l'environnement. Sa composition, extrêmement variable, dépend du milieu duquel elle est issue et dans lequel elle a été transformée (Thurman, 1985; Leenheer et Croué, 2003). Sa taille varie de la particule à la molécule en solution. En réponse au changement climatique, l'abondance de matière organique dissoute tend à croître comme l'ont par exemple montré Evans et al. (2005). Dans les systèmes environnementaux riches en MO, le Fe(III) s'associe à la matière organique pour former des hétéro-agrégats biphasiques fer-matière organique (Fe-MO). Ces objets ont été observés dans des systèmes naturels aussi différents que les zones humides, notamment les zones humides ripariennes (Guénet et al., 2016; Lotfi-Kalahroodi et al., 2019; Ratié et al., 2019), les tourbières (Pokrovsky et al., 2005; ThomasArrigo et al., 2014) ou les permafrosts (Pokrovsky et al., 2011; Hirst et al., 2017). Ces agrégats Fe-MO sont des vecteurs majeurs des éléments traces dans l'environnement (Pédrot et al., 2008; Pokrovsky et al., 2011; Stolpe et al., 2013). La compréhension de la dynamique et du devenir des agrégats Fe-MO dans les systèmes naturels est donc cruciale. Un des paramètres important du contrôle de cette dynamique est notamment l'organisation structurale des phases de Fe et de la matière organique.

I.1.2. Organisation structurale des agrégats Fe-MO

Longtemps, la structure et l'organisation des agrégats Fe-MO a été représentée par des oxyhydroxydes de Fe mal cristallisés enchevêtrés dans une matrice de MO (Figure I-1).

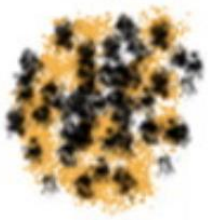

Figure I-1 – Représentation simplifiée longtemps utilisée pour schématiser les agrégats Fe-MO (Poggenburg et al., 2016).

Les techniques de caractérisation fines telles que la spectroscopie d'absorption des rayons X (XAS), la diffusion des rayons X et des neutrons à petits angles (SAXS et SANS) ou encore la microscopie électronique en transmission (MET) haute résolution ont permis de considérablement améliorer la description de leur organisation structurale. De nombreuses études XAS ont démontré la formation de liaisons entre les phases de Fe et la MO, impliquant majoritairement les groupements carboxyliques de la MO. A partir d'agrégats synthétisés au laboratoire, il a été montré que les phases de Fe s'organisent en monomères, oligomères et nanoparticules de type ferrihydrite (Nps-Fh), tous liés à la MO (e.g. Vilgé-Ritter et al., 1999; Karlsson et Persson, 2010; Mikutta, 2011; Mikutta et Kretzschmar, 2011; Chen et al., 2014; ThomasArrigo et al., 2018). La proportion de chacune des espèces de Fe dépend du rapport Fe/carbone organique (CO). Pour de faibles rapports Fe/CO, le Fe est principalement sous forme d'oligomères complexés à la MO. Pour un rapport molaire Fe/CO = 0.003, Karlsson et Persson (2012) ont montré que le Fe se trouvait principalement sous forme de complexes Fe-MO monomériques. Pour un rapport Fe/CO = 0.004, Mikutta et Kretzschmar (2011) ont mis en évidence une proportion importante de trimères de Fe(III) liés à la MO. Ces résultats permettent d'expliquer de manière détaillée, les mécanismes impliqués dans l'inhibition de la croissance et la cristallinité des phases de Fe par la MO (Pédrot et al., 2011). Pour de forts rapports Fe/CO ($\geq$ 0.8), le Fe forme principalement des hydroxydes de taille nanométrique liés à la MO (Mikutta et al., 2008; ThomasArrigo et al., 2018). Pour des valeurs intermédiaires de Fe/CO, les oligomères de Fe(III) et les Nps-Fh se forment simultanément (Vantelon et al., 2019, Annexe 1) et coexistent (Chen et al., 2014;

Guénet et al., 2017). Il est à noter que les agrégats Fe-MO prélevés sur le terrain présentent une organisation similaire d'oligomères de Fe(III) et de Nps-Fh (Karlsson et al., 2008; Guénet et al., 2016; Herzog et al., 2020). Cependant, certaines études ont également montré la présence de nano-lépidocrocite dans des zones humides ou des tourbières (ThomasArrigo et al., 2014; Guénet et al., 2016). Cette différence peut s'expliquer par des cinétiques de formation des agrégats Fe-MO plus lentes dans l'environnement qu'au laboratoire, favorisant ainsi la formation de lépidocrocite.

Plus récemment, Guénet et al. (2017), à partir d'une démarche expérimentale combinant XAS, SAXS, SANS et MET, ont précisé la structure des agrégats Fe-MO et notamment l'organisation des différentes formes du Fe et de la MO entre elles. Cette approche a permis de mettre en évidence une organisation fractale du Fe. Des billes primaires de Fe (rayon ~ 0.8 nm) s'assemblent en agrégats primaires (rayon ~ 4 nm), correspondant aux Nps-Fh observées en XAS. Ces derniers sont soit isolés ou auto-assemblés en un agrégat secondaire (rayon > 100 nm). La MO, quant à elle, est décrite comme une sphère compacte (rayon ~ 90 nm) liée à l'agrégat secondaire de Fe et sous forme de (macro)molécules isolées liées aux Nps-Fh et aux oligomères de Fe. Gentile et al. (2018) ont montré que la MO formait également un assemblage fractal.

Un schéma bilan, adapté de différentes études, résume la complexité de l'organisation structurale des agrégats Fe-MO (Figure I-2).

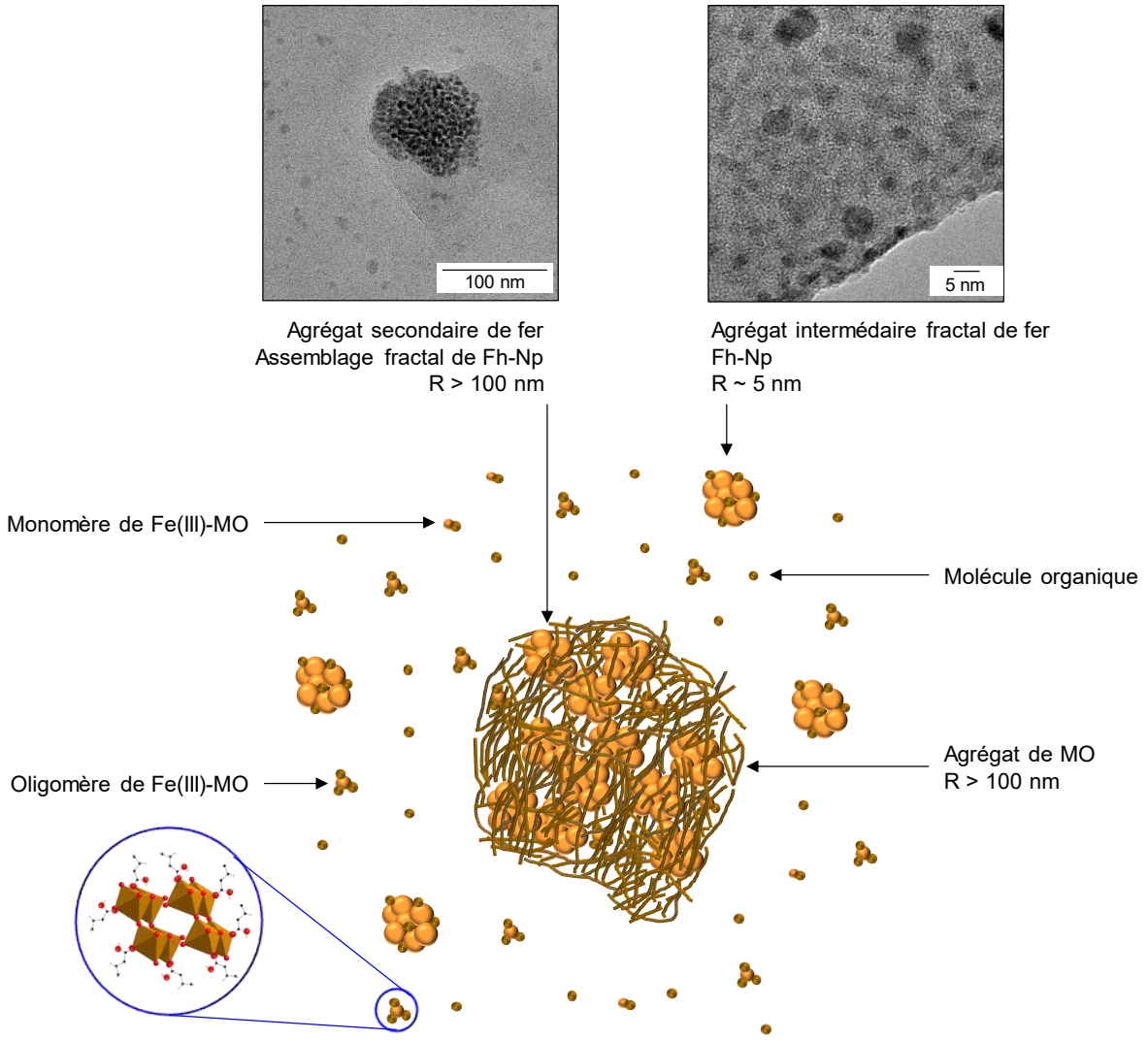

Figure I-2 – Observation en microscopie électronique à transmission et représentation schématique de l'organisation complexe des hétéroagrégats fer-matière organique (schéma adapté de Guénet et al. (2017); Gentile et al. (2018); Vantelon et al. (2019); Davranche et al. (2020)).

Cependant, cette organisation structurale complexe varie en fonction des conditions physico-chimiques, comme le pH, la force ionique, la concentration des composants ou encore le type de MO (Pullin et Cabaniss, 2003; Baalousha et al., 2008; Siéliéchi et al., 2008; van Schaik et al., 2008).

I.2. Interaction entre les cations majeurs et les composants des agrégats Fe-MO.

La présence de cations majeurs peut également être un facteur déterminant pour la structure des agrégats Fe-MO. En effet, ils peuvent présenter une affinité pour l'une ou

l'autre des composantes des agrégats, voire même pour les deux. Il convient donc de faire un état des lieux des connaissances de l'interaction entre les cations majeurs et la MO, le Fe ou les agrégats Fe-MO dans leur ensemble. Compte-tenu de leurs grandes concentrations dans les systèmes naturels, le choix s'est porté sur le calcium (Ca) et l'aluminium (Al).

I.2.1. Le calcium

Le Ca est un cation majeur donc naturellement présent en grande quantité dans l'environnement. Plusieurs études se sont intéressées à l'interaction entre le Ca et la MO. Des simulations de dynamique moléculaire ont montré la formation de complexes de sphère interne entre le Ca et les groupements carboxyliques de la MO (Kalinichev et Kirkpatrick, 2007; Iskrenova-Tchoukova et al., 2010). En présence de Ca, la MO forme un réseau supramoléculaire, comme cela a pu être observé avec des acides humiques par exemple (Baalousha et al., 2006). Ces résultats s'expliquent par la diminution de la charge globalement négative de la MO due à l'adsorption du Ca^{2+} (Baalousha et al., 2006; Iskrenova-Tchoukova et al., 2010). Cabaniss (2011) a d'ailleurs montré que le Ca a plus d'affinité pour les macromolécules à forte charge négative que pour les petites molécules dont la charge négative est plus faible.

Compte-tenu de ces interactions Ca-MO, la question de la compétition avec d'autres cations se pose. Cabaniss (2009) a modélisé la complexation de plusieurs cations, présents simultanément, par la MO naturelle. Son étude a montré que le Ca possède une faible force de liaison avec la MO en comparaison d'autres cations tels que le Cu(II), l'Al(III), le Pb(II), le Zn(II) ou le Ni(II). Ceci est en accord avec les résultats de Milne et al. (2003) qui ont montré une faible complexation du Ca par la MO par rapport aux cations métalliques. En revanche, le Ca et le Cd(II) ont une affinité comparable pour la MO (Cabaniss, 2009) et il existe une compétition entre ces deux cations pour leur liaison aux acides fulviques (Cao et al., 2006). De même, malgré la plus grande affinité du Cu(II) pour la MO (Cabaniss, 2009), Iglesias et al. (2003) ont montré qu'à fortes concentrations, le Ca pouvait être un compétiteur du Cu,

mettant ainsi en lumière l'importance de la concentration en cations dans les phénomènes de complexation.

Puisque le Ca peut se complexer à la MO et, qu'à forte concentration, il peut être un compétiteur efficace des métaux, des études se sont intéressées à l'influence du Ca sur des associations Fe-MO. La formation de complexes ternaires Fe-MO-Ca a été mise en évidence dans plusieurs études (Weng et al., 2005; Davis et Edwards, 2017; Adhikari et al., 2019). En particulier, Davis et Edwards (2017) ont montré que pour de fortes concentrations en Ca, sa complexation avec la MO permet à l'hydrolyse du Fe de se poursuivre. Adhikari et al. (2019) ont également montré que la réactivité des associations Fe-MO était modifiée en présence de Ca. En effet, le Ca favorise la formation de rouille verte plutôt que de magnétite et sidérite lors de la réduction des associations Fe-MO. De même, la vitesse de bioréduction du Fe dans les agrégats Fe-MO est plus faible en présence de Ca (Adhikari et al., 2019). Des études ont également proposé la formation de complexes ternaires Fe-Ca-MO à pH 6.25 (Sowers et al., 2018a; Sowers et al., 2018b). Cependant, selon Weng et al. (2005) et Ali et Dzombak (1996), le Ca interagit très peu avec le Fe à pH = 6.5, l'adsorption de Ca à la surface de goethite étant quasiment nulle. De même, Senn et al. (2015) ont démontré que lors de la formation d'oxyhydroxydes de Fe en présence de Ca à pH = 7, le Ca reste sous forme de cations hydratés et ne forme pas de liaison covalente avec le Fe.

I.2.2. L'aluminium

L'Al est également un élément très présent dans les systèmes naturels. La capacité de l'Al à former des flocs avec les matières en suspension (MES) et les colloïdes a été largement étudiée (e.g. Packham, 1965; Letterman et al., 1982; Goldberg, 1987; Dentel, 1988; Van Benschoten et Edzwald, 1990; Duan et Gregory, 2003). Les différentes études ont démontré que les capacités de floculation dépendent des conditions physico-chimiques comme, par exemple, le pH (Goldberg, 1987) ou la température (Van Benschoten et Edzwald, 1990). Dans des conditions proches de celles rencontrées dans les systèmes naturels (pH neutre), ces différentes études ont permis de discriminer plusieurs mécanismes

de floculation en fonction de la concentration en Al. Ainsi, pour de faibles concentrations, l'Al est majoritairement présent sous forme ionique. Ces espèces peuvent s'adsorber à la surface des MES, chargées négativement, provoquant leur déstabilisation colloïdale. A plus faibles concentrations en Al, l'adsorption à la surface des MES s'accentue, impliquant un renversement de la charge de surface qui devient globalement positive. Les MES retrouvent alors leur état colloïdal (Letterman et al., 1982). A des fortes concentrations, l'Al précipite en hydroxydes qui forment des flocs avec les colloïdes qui sédimentent (Duan et Gregory, 2003). En particulier, les hydroxydes d'Al peuvent coaguler la matière organique (e.g. Lu et al., 1999; Masion et al., 2000; Wang et al., 2002; Yu et al., 2010; Jin et al., 2018).

L'Al forme également des complexes forts avec la MO (Tipping et al., 1995; Cabaniss, 2009; Ferro-Vázquez et al., 2014). Quand il est présent, l'Al entre en compétition avec des métaux tels que Pb(II), Cd(II), Cu(II), Zn(II) ou encore les terres rares dans les interactions avec la MO (Pinheiro et al., 2000; Tipping, 2005; Marsac et al., 2012). En modélisant la complexion des métaux par la MO, Cabaniss (2011) a montré que l'Al a une grande affinité pour les sites phénoliques. Cependant, Pinheiro et al. (2000) ont mis en évidence l'effet compétiteur de l'Al vis-à-vis de la formation de liaisons entre les sites carboxyliques de la MO, le Pb(II) et le Cd(II). Cette compétition existe également avec les terres rares (Marsac et al., 2012). Ces deux études mettent en évidence la liaison entre l'Al et les sites carboxyliques de la MO pour des pH < 9. Dans ces conditions, une majorité des sites phénoliques est protonnée au contraire des groupements carboxyliques. Ces derniers, chargés négativement et plus abondants, sont donc plus disponibles que les sites phénoliques. Des mesures d'absorption des rayons X au seuil K de l'Al ont permis de montrés que la MO limite la polymérisation et la cristallisation des oxyhydroxydes d'Al (Hay et Myneni, 2008; Hu et al., 2008; Xu et al., 2010; Hagvall et al., 2015). En présence de MO, l'Al est donc essentiellement sous forme d'oligomères et d'hydroxydes amorphes dont la proportion augmente avec le rapport Al/CO. Plus particulièrement, Hagvall et al. (2015) ont mis en évidence la formation de complexes mononucléaires Al-MO dans lesquels l'Al est lié aux groupements carboxyliques de la MO.

L'Al est également connu pour interagir avec les oxyhydroxydes de fer. L'Al s'insère dans les structures cristallographiques de la lépidocrocite, de la goehtite ou encore de la ferrihydrite. Le taux de substitution du Fe par l'Al dépend du type d'oxyhydroxydes de Fe. Kim et al. (2015) ont montré que pour des rapports molaires Al/Fe = 0.1 les rapports molaires Al/Fe varient entre 0.3 et 0.4, respectivement, pour la lépidocrocite, la goethite ou la ferrihydrite, (Hazemann et al., 1991; Hansel et al., 2011; Cismasu et al., 2012; Adra et al., 2013). L'Al peut également s'adsorber à la surface de la ferrihydrite (Hansel et al., 2011). Ces interactions entre l'Al et les oxyhydroxydes de Fe contrôlent leur réactivité. La capacité d'adsorption des oxyhydroxydes de fer substitués à l'Al augmente par rapport aux oxyhydroxydes de Fe purs, notamment pour le Cr (Ni et al., 2016), les sulfates (Namayandeh et Kabengi, 2019) ou les phosphates (Harvey et Rhue, 2008). Ces résultats sont expliqués par les défauts de structures des oxyhydroxydes de fer inhérents à la présence d'Al. De plus, Ekstrom et al. (2010) ont observé une vitesse de bioréduction du Fe(III) plus lente pour des hydroxydes de Fe-Al que pour les hydroxydes de Fe. Ce résultat est attribué au fait que l'Al inhibe le transfert d'électrons lors de la réduction (Masue-Slowey et al., 2011).

Dans les systèmes naturels, des agrégats Fe-Al-OM porteurs d'éléments traces ont été mis en évidence (Pokrovsky et al., 2005). Malgré la plus grande affinité du Fe que de l'Al pour la MO, l'Al interagit avec la MO dans les systèmes triphasiques Fe-MO-Al (Nierop et al., 2002).

I.3. Réactivité des hétéro-agrégats

La taille nanométrique des oxyhydroxydes de Fe leur confère une grande surface spécifique et donc une importante capacité à adsorber les métaux et métalloïdes (Hofmann et al., 2004; Hua et al., 2012; Wang et Shadman, 2013; Hiemstra et al., 2019). La MO a, elle aussi, de nombreux sites réactifs et une grande affinité pour les métaux et les métalloïdes (Milne et al., 2003; Cabaniss, 2009; Cabaniss, 2011).

Certaines études ont montré que la réactivité des hétéro-agrégats organo-minéraux vis-à-vis des métaux répond à une règle d'additivité. La capacité d'adsorption totale d'un

hétéro-agrégat est décrite comme la somme de la capacité d'adsorption intrinsèque de chacun de ses composants. C'est le cas pour l'adsorption de Co(II) sur des minéraux naturels en présence d'acide humique (Léonardite) (Zachara et al., 1994) ou d'Eu(III) sur l'illite en présence de MO (Bruggeman et al., 2010). Cependant, beaucoup d'études ont démontré que cette règle ne permettait pas de reproduire la réactivité des agrégats organo-minéraux. C'est le cas pour l'adsorption par l'hématite, de Cd(II) en présence d'acides humiques (Vermeer et al., 1999) ou de Cu(II) en présence d'acides fulviques ou humiques (Christl et Kretzschmar, 2001; Saito et al., 2005) ou encore de Cu(II) et Pb(II) ou Tb(III) sur des argiles en présence d'acides fulviques ou humiques (Heidmann et al., 2005; Lippold et Lippmann-Pipke, 2009). La raison principale des écarts entre le modèle d'additivité et les observations expérimentales est la non prise en compte des interactions entre les différentes composantes des hétéro-agrégats. Ceci a été confirmé par Guénet et al. (2017) qui ont montré une augmentation des capacités d'adsorption des agrégats Fe-OM avec l'augmentation du rapport Fe/CO. Ce résultat s'explique par les modifications structurales survenant avec l'augmentation du rapport Fe/CO qui induisent une meilleure disponibilité des sites d'adsorption du Fe. Ceci met ainsi en évidence l'étroite relation entre l'organisation structurale des hétéro-agrégats et leur réactivité.

I.4. Techniques de caractérisation : de l'échelle macroscopique à l'échelle atomique

Etant donnée l'organisation multi-échelle complexe des hétéro-agrégats Fe-MO, la détermination des mécanismes mis en jeu dans leur formation nécessite l'utilisation de plusieurs techniques expérimentales. Ainsi, la spectroscopie d'absorption des rayons X (XAS) permet de sonder l'échelle atomique. La diffusion des rayons X à petits angles (SAXS) et la microscopie électronique à transmission (MET) décrit l'échelle nanométrique. L'échelle microscopique peut être étudiée avec la diffusion de neutrons à petits angles (SANS) et la cryo-MET. Finalement, les agrégats Fe-MO peuvent être observés de manière globale à l'échelle sub-micrométrique *via* l'imagerie par cryo-microscopie des rayons X à transmission

(cryo-TXM). Cette approche multi-échelle de la caractérisation structurale des agrégats Fe-MO est schématisée à la Figure I-3. Le Tableau I-1 décrit succinctement les différentes techniques.

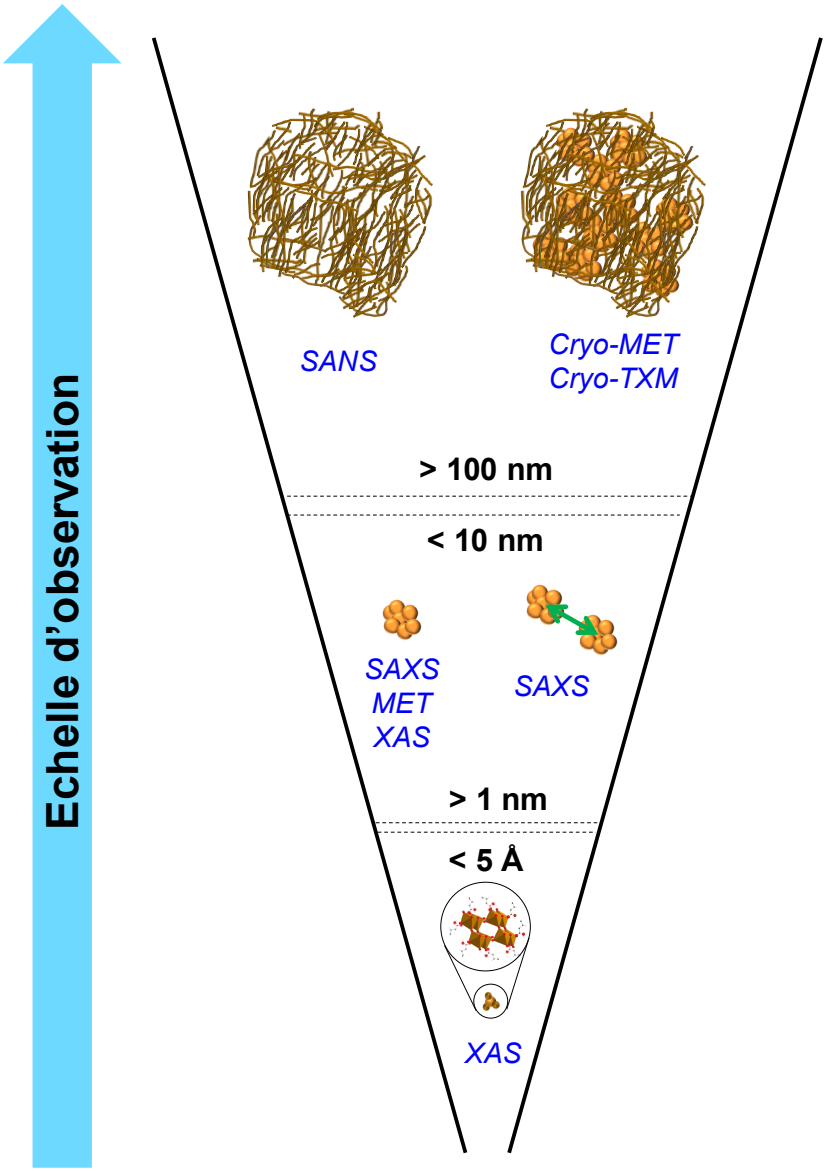

Figure I-3 – Vue d'ensemble de la caractérisation multi-échelle des agrégats Fe-MO *via* une approche multi-techinques. SANS : diffusion de neutrons à petits angles ; TXM : microscopie des rayons X à transmission ; MET : microscopie électronique à transmission ; SAXS : diffusion des rayons X à petits angles et XAS : spectroscopie d'absorption des rayons X.

Tableau I-1 – Aperçu des techniques d'analyse utilisées pour l'analyse de l'organisation multi-échelle des agrégats Fe-MO.

Technique	Description
XAS*	**Etudier la spéciation du Fe (seuil K du Fe) et la spéciation et l'interaction du Ca (seuil K du Ca) et de l'Al (seuil K de l'Al) avec les agrégats Fe-MO** La spectroscopie d'absorption des rayons X permet de sonder l'environnement local autour de l'atome absorbeur. La partie XANES du spectre donne des informations sur l'état d'oxydation de l'atome absorbeur et plus généralement sur son environnement électronique ainsi que des informations qualitatives sur sa structure cristallographique et sa géométrie. La partie EXAFS du spectre donne des informations sur la nature, le nombre et la distance des voisins de l'atome absorbeur. *Les solutions sont lyophilisées. La poudre obtenue est mélangée avec de la cellulose sous forme de pastille pour les mesures au seuil K du Fe (en transmission) et du Ca (en fluorescence). La poudre est écrasée sur feuille d'indium pour les mesures au seuil K de l'Al (en fluorescence).*
SAXS⁑	**Etude de l'organisation des nanoparticules de Fe** La diffusion des rayons X aux petits angles permet de ne sonder que les phases de Fe des agrégats Fe-MO. En effet, l'intensité diffusée ne dépend que de la densité électronique de l'objet diffusant, qui est bien plus importante pour le Fe que pour la MO. Cette technique nous permet d'extraire la taille des nanoparticules ainsi que leur organisation. *Les solutions sont introduites dans des capillaires en borosilicates de 1.5 mm de diamètre*
SANS⁑⁑	**Etude de l'organisation de la MO** La diffusion de neutrons aux petits angles permet de ne sonder que la MO lorsque les échantillons sont synthétisés dans D_2O. Les neutrons n'étant pas chargés, ils interagissent avec le noyau d'un élément. Pour un même élément, l'interaction neutron-noyau dépend donc de sa constitution isotopique. Ainsi, en changeant le solvant en faisant varier le rapport H_2O/D_2O, il est possible de masquer la contribution du Fe au signal de diffusion : c'est la variation de contraste. Cette technique donne donc des informations sur la taille et l'organisation de la MO. *Les solutions sont introduites dans des cuves en quartz de 2 mm d'épaisseur.*

*XAS : spectroscopie d'absorption des rayons X. ⁑SAXS : diffusion des rayons X à petits angles. ⁑⁑SANS : diffusion de neutrons à petits angles.

Tableau 1 (suite) – Aperçu des techniques d'analyse utilisées pour l'analyse de l'organisation multi-échelle des agrégats Fe-MO

Technique	Description
	Observation des nanoparticules de Fe et des agrégats
(Cryo)-MET*	Les nanoparticules de Fe sont beaucoup plus denses que la MO. Couplée à des analyses EDX, la microscopie électronique à transmission permet d'observer les nanoparticules de Fe, de déterminer leur tailles et leur morphologie. Dans le cas de la cryo-MET, la vitrification des échantillons permet de s'affranchir d'éventuelles modifications structurales dues au séchage. De plus, le fait que les agrégats soient figés dans une matrice de glace sur la grille permet de défocaliser très légèrement la caméra pour mieux faire la distinction entre le carbone de la grille et celui de la MO. *Pour le MET classique, une goutte d'échantillon diluée avec une solution à la même force ionique est déposée sur une grille de cuivre recouverte de carbone et laissée sécher à l'air libre. Pour le cryo-MET, une goutte de solution déposée sur une grille de cuivre recouverte de carbone est vitrifiée par plonge rapide dans de l'éthane liquide*
	Observation des agrégats dans leur ensemble
Cryo-TXM⁂	Les images de microscopie des rayons X à transmission ont été enregistrées à 520 eV, dans la « fenêtre de l'eau ». Dans ces conditions, le contraste entre l'eau et les constituants des agrégats est maximisé ce qui permet de pouvoir les observer. Tout comme la cryo-MET, la vitrification permet de s'affranchir d'éventuels artéfacts liés au séchage des agrégats. *Une goutte de solution déposée sur une grille de cuivre recouverte de carbone est vitrifiée par plonge rapide dans de l'éthane liquide*

*MET : microscopie électronique à transmission. ⁂TXM : microscopie des rayons X à transmission.

I.4. Objectifs de la thèse

Considérant l'ubiquité des hétéro-agrégats Fe-MO dans les systèmes naturels et leur capacité à transporter les polluants, il est essentiel de comprendre comment leur organisation structurale influe sur leur réactivité. Si l'organisation structurale des hétéro-agrégats Fe-MO et leur réactivité ont été étudiées dans plusieurs travaux, peu d'études se sont intéressées à la description complète de leur structure en présence d'ions majeurs et à leur impact sur leur réactivité. Le choix des ions s'est porté sur le Ca et l'Al étant donné leur forte concentration dans les systèmes naturels. De plus, le Ca et l'Al ont la capacité de coaguler et floculer la MO. L'Al a, quant à lui, également la capacité d'interagir avec les différentes phases du Fe. L'impact de leur présence et de leur concentration sur les hétéro-agrégats Fe-MO pourraient donc être majeure et remettre en cause les connaissances que nous avons de leur réactivité.

L'objectif de ce travail de thèse a donc été de comprendre comment le Ca ou l'Al modifiaient l'organisation structurale d'agrégats Fe-MO et les conséquences sur leur capacité d'adsorption. Pour répondre à cette problématique, deux volets ont été abordés :

- **Comprendre l'impact du Ca et de l'Al sur l'organisation multi-échelle des hétéro-agrégats Fe-MO.**

Pour mener à bien cet objectif, des agrégats Fe-MO ont été synthétisés au laboratoire par oxydation-hydrolyse de Fe(II) en présence de MO, Ca ou Al. Différents rapports Fe/CO et Ca-Al/Fe ont été utilisés. L'impact de Ca ou Al sur l'organisation multi-échelle des hétéro-agrégats Fe-MO (Figure I-2) a ensuite été finement décrite *via* une approche multi-technique. Cette démarche combine des mesures XAS, SANS et SAXS ainsi que de l'imagerie MET et STXM. Les mécanismes mis en jeu dans les modifications structurales ont été mis en évidence.

- **L’influence du Ca sur les capacités d’adsorption des associations Fe-MO vis-à-vis de l’arsenic.**

L’objectif de cette partie a été de comprendre l’impact du Ca sur la réactivité des agrégats Fe-MO à la lumière des modifications structurales et des mécanismes mis en jeux. Pour ce faire, j’ai réalisé des expériences d’adsorption d’arsenic (As) sur les agrégats dont l’organisation multi-échelle a été finement étudiée. Le choix du métalloïde s’est porté sur l’As car il possède une meilleure affinité pour le Fe que pour la MO et les mécanismes d’adsorption de l’As sur le Fe sont bien documentés (Ona-Nguema et al., 2005). Ce choix a été fait pour une première approche, dans le but de mieux discriminer les mécanismes mis en jeu, en s’intéressant uniquement aux phases ferriques.

Enfin, une partie conclusion clôt ce manuscrit. Elle reprend les principaux résultats et les place dans un contexte environnemental. Cette dernière partie propose également des perspectives au regard de ce travail de thèse.

Chapitre II. Impact des cations majeurs sur l'organisation structurale des nano-agrégats fer-matière organique

II.1. Impact du calcium sur l'organisation structurale des agrégats fer-matière organique

Cette partie correspond à un article publié dans la revue Environmental Science: Nano *: How does calcium drive the structural organization of iron-organic matter aggregates? A multiscale investigation, Anthony Beauvois, Delphine Vantelon, Jacques Jestin, Camille Rivard, Martine Bouhnik-Le Coz, Aurélien Dupont, Valérie Briois, Thomas Bizien, Andrea Sorrentino, Baohu Wu, Marie-Sousai Appavou, Elaheh Lotfi-Kalahroodi, Anne-Catherine Pierson-Wickmann, Mélanie Davranche, DOI : 10.1039/D0EN00412J*

Résumé

Les agrégats hétérogènes fer-matière organique (Fe-MO) jouent un rôle majeur dans la mobilité des polluants. Leur organisation physique et structurale dépend des conditions physico-chimiques qui prévalent dans les systèmes naturels. Le calcium (Ca), présent en quantité importante dans l'environnement et ayant une grande affinité pour la MO pourrait être un paramètre majeur influant sur la structure des agrégats Fe-MO. Des agrégats modèles Fe-OM-Ca ont été synthétisés à différents rapports Fe/carbone organique (CO) et Ca/Fe en utilisant un acide humique, représentatif de la MO naturelle. L'impact du Ca sur les agrégats Fe-OM a été étudié en combinant la spectroscopie d'absorption des rayons X, de la diffusion des rayons X et des neutrons aux petits angles ainsi que des techniques d'imagerie. Les phases de fer sont constituées d'oligomères de Fe(III), de nanoparticules de Fe(III) et de ferrihydrite (Fh) de taille nanométrique, tous liés à la MO ou enchevêtrés dans un agrégat de MO. Les nanoparticules de fer présentent une organisation fractale constituée de billes primaires agrégées en agrégats primaires de Fe (Fe-PA). Ces derniers sont eux-mêmes enchevêtrés dans des agrégats de MO. Pour un rapport Ca/CO < 0,026, les agrégats primaires de Fe sont organisés en un troisième niveau, appelé agrégat secondaire de Fe. Pour Ca/OC ≥ 0,026, la MO forme un réseau micrométrique dans lequel le Ca est lié sous forme de dimère aux sites carboxyliques de la MO. Dans ces conditions, les Fe-PA sont

distribués dans le réseau de MO, distants les uns des autres. Toutes ces transitions structurales sont pilotées par le Ca, qui écrante partiellement les interactions entre le Fe et la MO. La formation d'un tel réseau micrométrique devrait avoir un impact sur la réactivité de surface des phases Fe ainsi que sur la mobilité du Fe, de la MO et des éléments associés, notamment dans la porosité du sol où ils sont produits dans des conditions naturelles.

Abstract

Iron-organic matter (Fe-OM) aggregates are a key factor in the control of pollutant mobility. Their physical and structural organization depends on the prevailing physicochemical conditions during their formation and on their variations. Among these conditions, calcium (Ca) could be a major parameter given its high concentrations in the environment and its affinity for OM. Mimetic environmental Fe-OM-Ca associations were synthesized at various Fe/organic carbon (OC) and Ca/Fe molar ratios using Leonardite humic acid as OM model. The impact of Ca on Fe-OM aggregates was studied by a combination of X-ray absorption spectroscopy, small angle X-ray and neutron scattering and imaging techniques (TEM, cryo-TEM and cryo-TXM). Iron phases are constituted of Fe(III)-oligomers, Fe(III)-nanoparticles and ferrihydrite (Fh), all bound or embedded by OM. Iron phases exhibit a fractal organization with Fe-primary beads aggregated as Fe-primary aggregates (Fe-PA) which themselves are embedded in an OM aggregates. For Ca/OC (mol/mol) < 0.026, Fe-PA aggregate in a third level as a Fe-secondary aggregate. For Ca/OC ≥ 0.026, OM forms a large Ca-branched network in which Ca is bound as a dimer to OM carboxylic sites. In such conditions, Fe-PA are distributed in the OM network, distant from each other. All these structural transitions are driven by Ca which partially screens the Fe-OM interactions. The formation of such micrometric network should impact both the surface reactivity of the Fe phases as well as the mobility of Fe, OM and associated elements, notably in the soil porosity where they are produced under natural conditions.

II.1.1. Introduction

Environmental nanoparticles are ubiquitous in natural systems (Wigginton et al., 2007). Among them, natural iron-organic matter (Fe-OM) aggregates are of major importance due to their high amounts in natural systems such as in wetlands (Guénet et al., 2016; Lotfi-Kalahroodi et al., 2019; Ratié et al., 2019), peatlands (Pokrovsky et al., 2005; ThomasArrigo et al., 2014) or permafrosts (Pokrovsky et Schott, 2002; Hirst et al., 2017). They are mainly produced in soils via anthropogenic forcing and geochemical and physical processes such as alteration and erosion, oxidation-reduction variations occurrence subsequent to soil water-saturation/desaturation alternation. The production of these aggregates has tended to strongly increase in recent decades due to global warming which result in an increase in rainfall frequency, volume and intensity as well as permafrost thawing. Due to their nanometric size and their high specific surface area, they are known to be a key factor in the mobility of metals and metalloids in environmental systems (Wigginton et al., 2007; Pédrot et al., 2008; Stolpe et al., 2013; ThomasArrigo et al., 2014; Guénet et al., 2016). Their ability to adsorb metal(loid)s depends on the size, morphology and structural arrangement between the Fe and OM phases (Ritter et al., 2006; Mikutta et Kretzschmar, 2011). Several studies have investigated the structural organization of Fe phases formed during Fe(II) oxidation-hydrolysis or Fe(III) hydrolysis in the presence of OM (Karlsson et Persson, 2010; Mikutta, 2011; Pédrot et al., 2011; Chen et al., 2014; Guénet et al., 2017; Vantelon et al., 2019). Irrespective of the process of formation, the Fe speciation depends on the Fe/organic carbon (OC) ratio. For very low Fe/OC ratios, the dominant Fe species are Fe(III) oligomers bound to OM (Mikutta et Kretzschmar, 2011; Karlsson et Persson, 2012) while for high Fe/OC ratio, nanoparticulate Fe embedded in an OM matrix are formed (Mikutta et al., 2008; ThomasArrigo et al., 2018). For intermediate Fe/OC ratios, Fe-OM aggregates contain two distinct Fe phases: Fe(III) oligomers bound to OM and nano-sized ferrihydrite (Fh) embedded in an OM matrix (Karlsson et al., 2008; Chen et al., 2014; Vantelon et al., 2019). According to Chen et al. (2014), a decrease in Fe(III) oligomers occurs to the benefit of Fh with an

increasing Fe/OC ratio. Guénet et al. (2017) demonstrated that the Fe part is organized according to a fractal network composed of Fe primary beads (radius ≈ 0.8 nm) that associate to form Fe primary aggregates (radius ≈ 5 nm) that are themselves associated as Fe secondary aggregates (radius > 100 nm). They described the OM part as a compact aggregate (radius ≈ 90 nm) bound to Fe secondary aggregates as well as isolated molecules bound to Fe primary aggregates. The size of Fe-OM aggregates increases with the increasing Fe/OC ratio.

These species were also observed in organic soil as Fe monomers and Fe oxyhydroxides bound to OM (Karlsson et al., 2008) and in boreal rivers as nano-Fh and Fe-OM complexes (Herzog et al., 2020). ThomasArrigo et al. (2014) reported the presence of lepidocrocite (Lp) and Fh in a peatland soil. Guénet et al. (2016) studied a riparian wetland soil and provided evidence of the presence of nano-Lp embedded in an OM matrix, as well as small Fe clusters (i.e. oligomers) and Fe monomers bound to OM.

In the absence of OM, Fe(II) oxidation-hydrolysis leads to the formation of micrometric-sized aggregates of nano-Lp (Schwertmann et Cornell, 2000; Pédrot et al., 2011) whereas with humic acid (HA), Fe oxyhydroxides of nanometric size are formed (Pédrot et al., 2011; Guénet et al., 2016; Vantelon et al., 2019). Therefore, organic matter controls the behavior of Fe in organic environments and the physical, chemical and morphological organization of Fe-OM aggregates is influenced by the prevailing physico-chemical conditions such as pH, ionic strength or other major cations (Pullin et Cabaniss, 2003; Baalousha et al., 2008; van Schaik et al., 2008). In natural waters, calcium (Ca) is a major ion with a concentration ranging from 1.0×10^{-2} to 1.0×10^{-4} mol L^{-1} (Iglesias et al., 2003). Several studies have investigated the impact of Ca on the structural organization of natural OM. Calcium acts as a coagulating agent for OM by forming cationic bridges between molecules, preferentially involving carboxylic groups (Ouatmane et al., 1999; Kalinichev et Kirkpatrick, 2007; Christl, 2012) but also via phenolic groups with increasing pH values (Adusei-Gyamfi et al., 2019). Kalinichev and Kirkpatrick, (2007) reported the formation of OM supramolecular structures with Ca. Calcium has also been shown to increase the adsorption of fulvic acids (FA) on goethite

(Weng et al., 2005) leading to the formation of goethite-Ca-FA ternary associations, and to aggregate OM with clay minerals (Kloster et Avena, 2015). Adhikari et al. (2019) provided evidence that the hydrolysis of Fe(III) with OM and Ca leads to the formation of Fh-OM-Ca precipitates in which OM acts as a bridge between Fh and Ca. Davis and Edwards (2017) demonstrated that Ca^{2+} complexation by OM enhances Fe(III) hydrolysis resulting in better polymerization of Fe with Ca. However, there are lacks of information on the overall structural organization of Fe-OM-Ca associations.

The aim of this study is therefore to provide a complete characterization of the impact of Ca on the composition and structural organization of Fe-OM aggregates. For this purpose, we synthesized Fe-OM-Ca associations with various Fe/OC and Ca/Fe ratios. Calcium interactions with Fe-OM and Fe speciation were investigated by X-ray absorption spectroscopy (XAS) at the Ca and Fe K-edge. The arrangement of nanoparticulate Fe and OM was probed combining small-angle X-rays scattering (SAXS), small-angle neutrons scattering (SANS) and very small-angle neutrons scattering (VSANS). The overall size of the aggregates was investigated by cryo-transmission X-ray microscopy (cryo-TXM) and cryo-transmission electron microscopy (cryo-TEM).

II.1.2. Experimental method

II.1.2.1. Sampling and chemical analyses

II.1.2.1.a. Laboratory syntheses

All aqueous solutions were prepared with ultrapure water (Milli-Q-Integral®, Millipore). Samples (Figure II.1-1) were synthesized at three Fe/OC molar ratios (i.e. 0.02, 0.05 and 0.08) and at four Ca/Fe molar ratios (i.e. 0, 0.1, 0.5 and 1) following the procedure described by Guénet et al. (2017). Samples were labelled Fe*xx*-Ca*yy*, where Fe*xx* and Ca*yy* represent the Fe/OC and the Ca/Fe ratios, respectively. The OM used was Leonardite Humic Acid (HA) (International Humic Substances Society) with the elemental composition C = 63.81%, O = 31.27%, H = 3.70% and N = 1.23% (as a mass fraction). A 1.79×10^{-2} mol L^{-1} iron(II) stock

solution was prepared with $FeCl_2.4H_2O$ (Sigma Aldrich). From this solution, three Fe(II)-Ca(II) stock solutions were prepared at [Ca] = 2.50×10^{-3} mol L^{-1}, 1.25×10^{-2} mol L^{-1} and 2.50×10^{-2} mol L^{-1} with $CaCl_2.2H_2O$ (Sigma Aldrich). Aggregates (Fe-OM-Ca) were synthesized using a titration of a HA suspension at [OC] = 1.00×10^{-1} mol L^{-1} with the Fe(II)-Ca(II) solution at 0.05 mL min^{-1} in 5×10^{-3} mol L^{-1} of NaCl using an automated titrator (Titrino 794, Metrohm). The pH was kept constant at 6.5 with a 0.1 mol L^{-1} NaOH solution using a second titrator (Titrino 794, Metrohm) at a set pH mode. The accuracy of the pH measurement was ± 0.04 pH units. A fraction of each sample was subjected to filtration at 0.2 µm (cellulose acetate membrane filter, Sartorius) and ultrafiltration at 30 kDa (Vivaspin VS2022, Sartorius). Each 0.2 µm filter was rinsed before use with ultrapure water and each 30 kDa ultrafiltration cell was rinsed 10 times with NaOH 0.1 mol L^{-1} and two times with ultrapure water. Two samples were also prepared using the same protocol but without Fe at Ca concentrations of 1.00×10^{-4} and 5.00×10^{-3} mol L^{-1}.

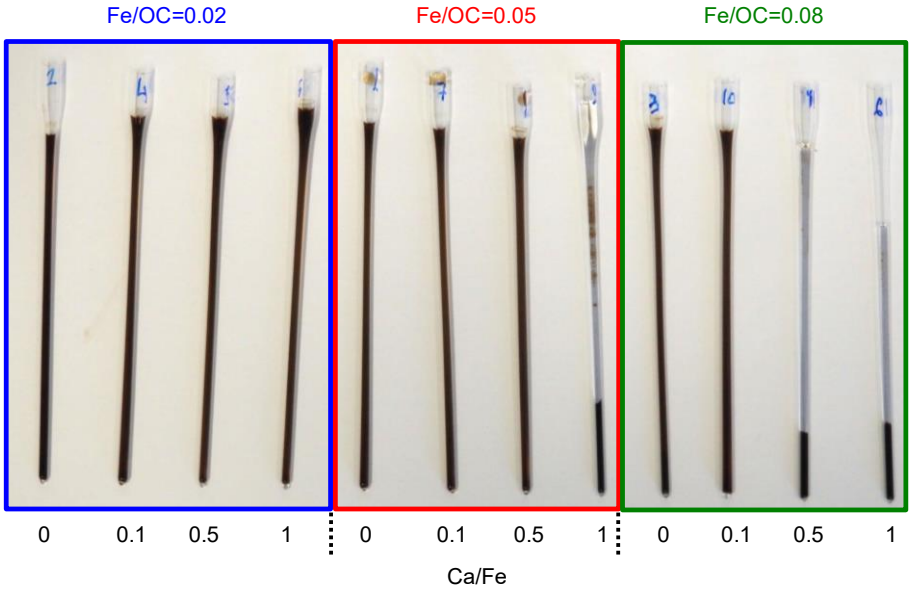

Figure II.1-1– Samples after they stayed vertically into capillaries for SAXS measurements.

II.1.2.1.b. Chemical analyses

Organic carbon concentrations were determined using an organic carbon analyser (Shimadzu TOC-V CSH). The accuracy of the OC measurement was determined to be ±5% using a standard solution of potassium hydrogen phthalate (Sigma Aldrich). The Fe and Ca

concentrations were measured by ICP-MS using an Agilent Technologies 7700x instrument at the University of Rennes 1. To eliminate OM, samples were pre-digested with 14.6 mol L^{-1} HNO_3 and suprapure® 30% H_2O_2 at 90°C and evaporated. The final concentrations of Fe, Ca, and OC are reported in Table II.1-1 for the filtrates and ultrafiltrates and in Table II.1-2 for the bulk.

Table II.1-1 – OC, Ca and Fe concentration (mmol L^{-1}) in the filtrate obtained after filtration at 0.2 µm and ultrafiltration 30 kDa for every sample. <LOD: below the limit of detection (LOD). The uncertainties were calculated from the triplicate.

Sample	OC	Fe	Ca
	< 0.2 µm		
Fe0.02-Ca0.0	51.6 ± 0.7	1.07 ± 0.03	0.10 ± 0.01
Fe0.02-Ca0.1	49.7 ± 1.1	1.03 ± 0.01	0.20 ± 0.01
Fe0.02-Ca0.5	45.6 ± 0.5	0.91 ± 0.01	0.52 ± 0.02
Fe0.02-Ca1.0	39.7 ± 0.2	0.94 ± 0.04	0.98 ± 0.03
Fe0.05-Ca0.0	48.1 ± 2.4	2.05 ± 0.55	0.08 ± 0.02
Fe0.05-Ca0.1	38.7 ± 0.1	2.33 ± 0.07	0.29 ± 0.01
Fe0.05-Ca0.5	17.3 ± 1.1	0.96 ± 0.04	0.76 ± 0.02
Fe0.05-Ca1.0	1.9 ± 0.3	<LOD	1.66 ± 0.01
Fe0.08-Ca0.0	41.1 ± 0.4	3.06 ± 0.07	0.08 ± 0.01
Fe0.08-Ca0.1	19.7 ± 2.9	1.61 ± 0.29	0.24 ± 0.03
Fe0.08-Ca0.5	2.0 ± 0.2	<LOD	1.19 ± 0.05
Fe0.08-Ca1.0	1.1 ± 0.1	<LOD	3.28 ± 0.08
	< 30 kDa		
Fe0.02-Ca0.0	4.6 ± 0.6	0.01 ± 0.01	0.01 ± 0.01
Fe0.02-Ca0.1	4.1 ± 0.4	0.01 ± 0.01	0.01 ± 0.01
Fe0.02-Ca0.5	3.2 ± 0.4	0.01 ± 0.01	0.04 ± 0.01
Fe0.02-Ca1.0	2.5 ± 0.2	<LOD	0.24 ± 0.01
Fe0.05-Ca0.0	3.3 ± 0.4	0.01 ± 0.01	<LOD
Fe0.05-Ca0.1	2.7 ± 0.2	0.01 ± 0.01	0.03 ± 0.01
Fe0.05-Ca0.5	1.9 ± 0.1	<LOD	0.38 ± 0.01
Fe0.05-Ca1.0	1.6 ± 0.1	<LOD	1.63 ± 0.05
Fe0.08-Ca0.0	2.4 ± 0.3	<LOD	0.01 ± 0.01
Fe0.08-Ca0.1	2.3 ± 0.3	<LOD	0.05 ± 0.01
Fe0.08-Ca0.5	2.2 ± 0.4	<LOD	1.19 ± 0.02
Fe0.08-Ca1.0	0.9 ± 0.1	<LOD	3.22 ± 0.06

Table II.1-2 – Fe, Ca and OC concentrations. *Theoretical values, n.d.: not determined. Exp: experimental. Theo: theoretical. The uncertainties were calculated from the triplicate.

Sample name	Fe (mmol L^{-1})	Ca (mmol L^{-1})	OC (mmol L^{-1})	Ca/Fe (mol/mol)		Fe/OC (mol/mol)		Ca/OC (mol/mol)
				Exp	Theo	Exp	Theo	Exp
Fe0.00-Ca_4	0*	0.10*	58.0*	-	-	n.d.	0.00	0.002
Fe0.00-Ca_200	0*	5.00*	58.0*	-	-	n.d.	0.00	0.091
Fe0.02-Ca0.0	1.21 ± 0.05	0.10 ± 0.01	56.3 ± 0.9	0.10	0.10	0.02	0.02	0.002
Fe0.02-Ca0.1	1.07 ± 0.09	0.22 ± 0.02	54.3 ± 1.0	0.09	0.10	0.02	0.02	0.004
Fe0.02-Ca0.5	1.20 ± 0.08	0.65 ± 0.04	57.7 ± 1.7	0.10	0.10	0.02	0.02	0.011
Fe0.02-Ca1.0	1.30 ± 0.03	1.28 ± 0.04	55.8 ± 0.2	0.11	0.10	0.02	0.02	0.023
Fe0.05-Ca0.0	2.98 ± 0.22	0.10 ± 0.01	55.5 ± 0.9	0.25	0.25	0.05	0.05	0.002
Fe0.05-Ca0.1	3.23 ± 0.08	0.40 ± 0.01	55.5 ± 0.1	0.27	0.25	0.06	0.05	0.007
Fe0.05-Ca0.5	2.80 ± 0.13	1.45 ± 0.06	55.5 ± 0.9	0.24	0.25	0.05	0.05	0.026
Fe0.05-Ca1.0	2.70 ± 0.12	2.80 ± 0.09	51.9 ± 2.8	0.24	0.25	0.05	0.05	0.054
Fe0.08-Ca0.0	4.75 ± 0.12	0.10 ± 0.01	61.6 ± 1.0	0.36	0.40	0.08	0.08	0.002
Fe0.08-Ca0.1	5.00 ± 0.07	0.60 ± 0.01	60.8 ± 0.3	0.38	0.40	0.08	0.08	0.010
Fe0.08-Ca0.5	4.79 ± 0.10	2.38 ± 0.07	55.2 ± 1.9	0.40	0.40	0.09	0.08	0.043
Fe0.08-Ca1.0	4.95 ± 0.06	4.73 ± 0.01	51.8 ± 1.1	0.44	0.40	0.10	0.08	0.091

II.1.2.2. Structural characterizations

II.1.2.2.a. XAS data acquisition and analysis

A fraction of each sample was freeze dried (Freeze dryer Alpha 1-2 LD plus, Christ). The obtained powder was pressed into a 6 mm pellet mixed with cellulose (Merck). X-ray absorption spectroscopy (XAS) at the Ca K-edge was performed on the LUCIA (Flank et al., 2006; Vantelon et al., 2016) beamline at the SOLEIL synchrotron (Saint-Aubin, France). The fixed exit double-crystal monochromator was equipped with Si(111) crystals. Spectra were recorded in fluorescence mode using a 60 mm² mono-element silicon drift diode detector (Bruker). The energy was calibrated using the calcite reference for which the first inflection point was set to 4045 eV.

The Fe K-edge spectra were recorded on the ROCK (Briois et al., 2016) beamline at the SOLEIL synchrotron. A Si(111) channel-cut was used as the monochromator. Spectra were recorded in transmission mode using three ionization chambers (Ohyo Koken) filled with N_2. The energy was calibrated using a Fe foil located between the 2nd and the 3rd ionization chambers and measured simultaneously with the samples. Calibration was done by setting the maximum of the first derivate of the Fe foil to 7112 eV. The references used for further data analysis were Fh and Lp synthesized following the procedure described in Schwertmann and Cornell (2000).

All XAS data were processed using the Athena software (Ravel et Newville, 2005) including the Autbk algorithm (Rbkb = 1, k-weight = 3). Normalized Ca spectra were obtained by fitting the pre-edge region with a linear function and the post-edge region with a quadratic polynomial function. The Fourier transforms of the k^3-weighted extended X-ray absorption fine structure (EXAFS) spectra were calculated over a range of 2-10.5 Å^{-1} using a Hanning apodization window (window parameter = 1). Back Fourier filters were extracted over the R-range of 1.3-3.1 Å, using the same apozidation window shape. The EXAFS fittings were performed in the 1.3–3.6 Å distance range with the Artemis (Ravel et Newville, 2005) interface to IFEFFIT using least-squares refinements. The paths used to fit the Ca K-edge

EXAFS were calculated from Ca-acetate (Klop et al., 1984) and Ca-2-furancarboxylate (Paluchowska et al., 1996) using the FEFF6 algorithm included in the Artemis interface (Rehr et al., 1992; Newville, 2001). Normalized Fe spectra were obtained by fitting the pre-edge region with a linear function and the post-edge region with a quadratic polynomial function. The Fourier transforms of the k^3-weighted EXAFS spectra were calculated over a range of 2-12.5 $Å^{-1}$ using a Hanning apodization window (window parameter = 1). Back Fourier filters were extracted over the R-range of 1.15-4.1 Å, using the same apodization window shape. The EXAFS data were analysed by linear combination fitting (LCF) available in the Athena software on the range 3-12.5 $Å^{-1}$; all component weights were forced to be positive. The references used were Fh, Lp and three pure components extracted from the *in situ* synthesis of Fe-OM aggregates by Vantelon et al. (2019), i.e. Fe(II), Fe(III)-oligomers and Fe(III)-Np that correspond to Fe(III) nano-oxyhydroxides, all bound or embedded in a HA matrix. The best LCF fit was determined for the minimum *n*-components for which the R-factor was better than 10% of the fit with *n+1* components. As without any constraint the total LCF weight for each sample was between 0.95 and 1.05, it was arbitrarily fixed to 1 to facilitate comparisons between each sample.

II.1.2.2.b. SAXS data acquisition and analysis

Small angle X-ray scattering (SAXS) measurements were performed on the SWING beamline at the SOLEIL synchrotron. Two sample-to-detector distances (1 and 6 m) were used with a wavelength of 1.03 Å. This setup allowed access to a momentum transfer q range of 2.0×10^{-3}-0.7 $Å^{-1}$. Measurements were also performed on the XEUSS 2.0 spectrometer from Xenocs (CEA-LIONS/LLB, Saclay, France). Two sample-to-detector distances (33 and 249 cm) were used with a wavelength of 1.54 Å (Cu X-ray source). This setup allowed access to a momentum transfer range of 4.5×10^{-3}-0.5 $Å^{-1}$. Measurements were performed on the suspensions except for the three settled samples (Figure II.1-1) for which the experiments were carried out on the precipitate. All scattering curves were rescaled as a function of the apparent concentration in the high q range.

The cluster fractal model described in Guénet et al. (2017) was used to analyse the SAXS curves. For centrosymmetric nanoparticles dispersed in a continuous solvent, here water, the scattered intensity is described by the following equation (eq. II.1-1):

$$I(q)=\varphi.V.\Delta\rho^2.P(q).S(q) \qquad \text{(eq. II.1-1)}$$

where φ is the volume fraction, V is the volume of the scattered entities, $\Delta\rho^2$ is the contrast term, P(q) is the form factor and S(q) is the structure factor. The model was established considering that the samples are composed of Fe spherical poly-dispersed primary beads (Fe-PB). Part of these PB is organized as Fe primary aggregates (Fe-PA) described by a form factor according to a finite number of PB and a fractal dimension. These Fe-PA self-assembled as a third aggregation level, i.e. the Fe secondary aggregates (Fe-SA).

II.1.2.2.c. SANS and VSANS acquisition and analysis

The neutron scattering length density (SLD) of H_2O is SLD_{H_2O} = -0.56×10^{10} cm^{-2} while SLD_{D_2O} = 6.4×10^{10} cm^{-2}. Considering SLD_{OM} = 1.18×10^{10} cm^{-2} and SLD_{Fe} = 6.05×10^{10} cm^{-2} (Guénet et al., 2017), Fe-Ca-OM aggregates were synthesized in D_2O to match the Fe contribution to the neutron scattering and to only characterize the OM part. We completed the SANS investigation with a second intermediate contrast at 50/50% H_2O/D_2O to see whether we can identify a local contribution of the OM scattering signal. Small-angle neutron scattering (SANS) experiments were performed on the PA20 beamline (LLB, Saclay, France). Three sample-to-detector distances (2, 8 and 18 m) were used with a wavelength of 6 Å. This setup allowed access to a momentum transfer range of 2.1×10^{-3}-0.3Å^{-1}. SANS measurements were also performed on KWS-2 diffractometers (Radulescu et al., 2015) operated by the Jülich Centre for Neutron Science (JCNS) at the Heinz Maier-Leibnitz Zentrum (MLZ) in Garching, Germany. Using a sample-to-detector distance of 1.1 m and 7.6 m with a wavelength of 7 Å (Δλ/λ = 10%) and a sample-to-detector distance of 19.5 m with a wavelength of 10 Å (Δλ/λ = 10%): the q-range 1.9×10^{-3}-4.5×10^{-1} Å^{-1} was covered. Very small-angle neutron scattering (VSANS) experiments were carried out with KWS-3 diffractometers (Pipich et Fu, 2015) operated by the JCNS at the MLZ. Using a neutron wavelength of 12.8 Å

with Δλ/λ = 17% and a sample to detector distance of 0.51 m, 1.25 m and 9.2 m, a q-range from approximately 2.1×10^{-4}-5.0×10^{-2} $Å^{-1}$ was covered. Like for SAXS, SANS measurements were performed on suspensions except for the three settled samples (Figure II.1-1) for which experiments were carried out on the precipitate. All scattering curves were rescaled to the apparent concentration in the high q range. Data were corrected and calibrated using the Pasinet and QtiKWS softwares.

SANS curves were fitted using the SasView software with the following Guinier-Porod equation (Hammouda, 2010) (eq. II-2):

$$I(q) = \begin{cases} \frac{G}{q^s} \exp\left(\frac{-q^2 R_g^2}{3-s}\right) & \text{for } q < q_{cut-off} \\ \frac{D}{q^\alpha} & \text{for } q > q_{cut-off} \end{cases} \qquad \text{(eq. II.1-2)}$$

where G and D are scaling factors for the Guinier and Porod domains respectively, R_g is the gyration radius that corresponds to a typical size of the system, s is a parameter illustrating the nonspherical form of the object (s = 0 for a sphere, s = 1 for rods and s = 2 for lamellae) and α is the slope of the curve related to the fractal dimension (D_f) of the object. The $q_{cut-off}$ defines the limit between the Guinier and the Porod regime.

II.1.2.2.d. Imaging

For the TEM measurements, 5 µL of the samples were dropped on a copper grid with a lacy carbon coated film (Agar scientific, AGS166-3) and then dried at room temperature. Transmission electron microscopy images were recorded using a JEOLL 100CXII instrument at 100 kV (THEMIS Analytical Facility, University of Rennes 1) equipped with an X-ray energy dispersive spectroscopy (XEDS) detector (Kevex detector with an ultrathin window). For the cryo-TEM measurements, samples were vitrified using a Leica EM GP immersion under controlled humidity and temperature (Dubochet et McDowall, 1981). Samples were deposited on glow-discharged electron microscope grids followed by blotting and vitrification by rapid freezing in liquid ethane (-184°C). Grids were transferred to a single-axis cryo-holder (model 626, Gatan) and were observed using a 200 kV electron microscope (Tecnai G2 T20 Sphera, FEI) equipped with a 4k × 4k CCD camera (model USC 4000, Gatan). Micrographs

were acquired under low electron doses using the camera in binning mode 1 and at a nominal magnification of 50,000x. For the cryo-TXM measurements, samples were frozen using a Leica EM GP immersion freezer. The environmental chamber was kept at 20°C with 80% humidity. Four µL of the sample were dropped on a hydrophilized (air plasma treated using Henniker HPT-100 plasma treatment) carbon coated copper grid (Quantifoil R2/2 type grid). The grid was blotted with n°1 Whatman filter paper prior to freezing and then automatically plunged into liquid ethane. The samples were stored in liquid nitrogen until further use. The cryo-TXM images were recorded at the full field transmission soft X-ray microscope installed at the MISTRAL beamline (Sorrentino et al., 2015) of the ALBA synchrotron. A capillary condenser lens after the monochromator exit slit focuses the radiation to the sample. After the sample, a Fresnel zone plate with outermost zone width of 25 nm was used as objective lens to record a magnified image on a direct illumination CCD detector (Pixis XO by Princeton Instruments with 1024 × 1024 pixels and 13 µm pixel size). The spatial resolution of the system is limited by the objective lens and was estimated to be 23 nm half pitch at 520 eV using a Siemens star pattern with 30 nm smallest features (Otón et al., 2015). The magnification used for the transmission image was × 1300, corresponding to an effective pixel size of 10 nm. Twenty images with an exposure time of 3 seconds each were acquired and then averaged. The average transmitted intensity I and the corresponding Flat Field I_0 (i.e. the incident intensity on the sample) were used to obtain the transmission T, related to the linear absorption coefficient of the sample by the Beer-Lambert law. The energy was set to 520 eV to maximize the contrast between water and carbon, calcium and iron rich regions of the imaged suspension.

II.1.3. Results and discussion

II.1.3.1. Iron speciation within aggregates

Fe speciation within the aggregates was studied by XAS at Fe K-edge. The XANES spectrum of Fe(II) exhibits a white line at 7127.5 eV while the white line of Fe(III) species

occurs at 7132.5 eV and their shape are similar and representative of Fe(III) in an octahedral symmetry (Wilke et al., 2001) (Figure II.1-3). The weak pre-edge at 7115 eV is relevant for octahedral species (Voegelin et al., 2010). The intensity of the shoulder at 7148.5 eV is high for Np, Fh, Lp and samples as compared to the oligomer, suggesting a higher polymerisation.

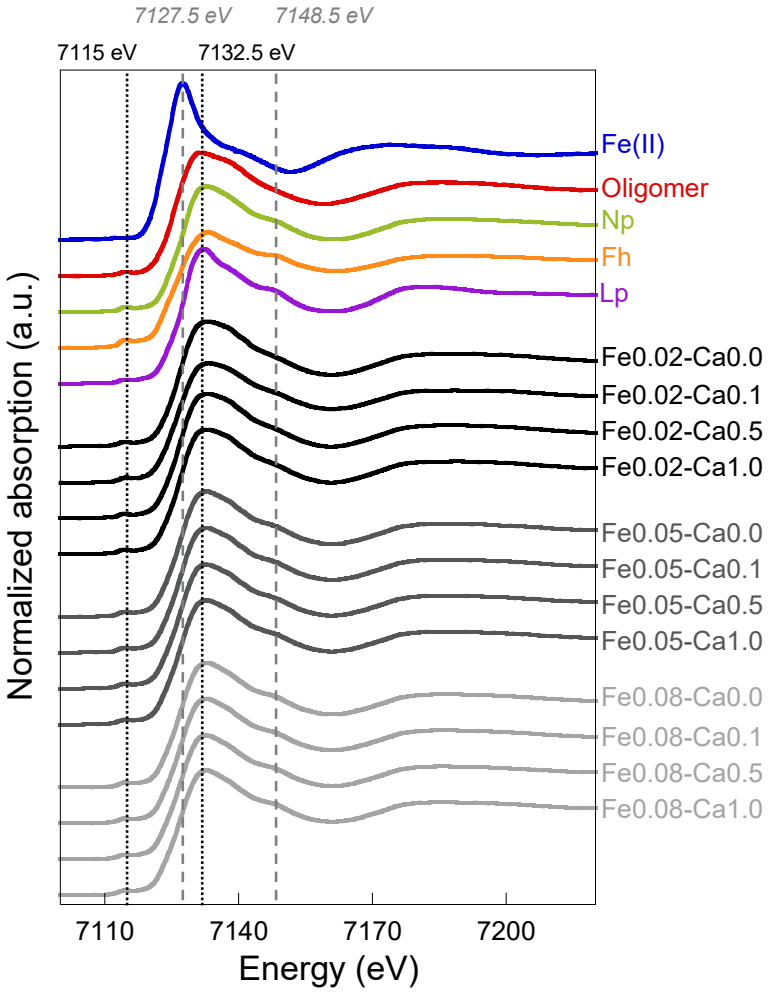

Figure II.1-2 – Fe K-edge XANES spectra of Fe-OM-Ca aggregates and Fe references used to perform linear combination fitting.

All EXAFS spectra exhibit a maximum of amplitude at 6.3 $Å^{-1}$ (Figure II.1-3). Fe(II) and Fe(III)-oligomer spectra exhibit a damping shape that is close to monotonous. The oscillations of the Fe(II) spectra are shifted to low photoelectron wavevector, k, values as compared to Fe(III) species. Iron(III)-Np and Fh exhibit a shoulder at 5.1 $Å^{-1}$ and an oscillation at 7.5 $Å^{-1}$ that are more intense for Fh than Fe(III)-Np (Figure II.1-3a). The Lp

spectrum is well-structured with a shoulder at 4.7 $Å^{-1}$, a strong oscillation at 7.2 $Å^{-1}$ and a smaller one at 7.9 $Å^{-1}$. For the Fe-OM-Ca aggregates, the oscillations occurred at the same k values as the Fe(III) references evidencing the presence of Fe(III). More precisely, two different behaviours can be observed depending on the Fe/OC ratio. Spectra for Fe/OC = 0.02 exhibit a monotonous shape except at 7.5 $Å^{-1}$ where a shoulder occurs (Figure II.1-3b). Samples formed at Fe/OC = 0.05 and Fe/OC = 0.08 exhibit more structured EXAFS spectra with an additional shoulder at 5.1 $Å^{-1}$ and a pronounced shoulder at 7.4 $Å^{-1}$ (Figure II.1-3c and d).

Guénet et al. (2016) demonstrated that nano-Lp coexist with small Fe-clusters bound to OM in riparian wetland soils. Similar results were demonstrated by ThomasArrigo et al. (2014) who provided evidence of Fh and Lp occurrence in OM-rich environmental systems. Moreover, Vantelon et al. (2019) demonstrated that within Fe(III)-OM aggregates for Fe/OC = 0.08, Fe(III)-oligomers and Fe(III)-Np occurred together. Linear combination fittings were performed on the EXAFS spectra of the Fe-OM-Ca aggregates using the signal of Fe(II), Fe(III)-oligomers, Fe(III)-Np, Fh and Lp. Only Fe(III)-oligomers and Fe(III)-Np EXAFS signals were necessary to reproduce by LCF the experimental data for Fe/OC = 0.02 whereas for the highest Fe/OC ratio, Fe(III)-oligomers, Fe(III)-Np and Fh EXAFS signals were needed. If they exist, Fe(II) and Lp amount were below the detection limit (Figure II.1-3 and Table II.1-3). Several studies similarly demonstrated that with fulvic or humic acids, Fe(II) oxidation-hydrolysis did not produce Lp (Pédrot et al., 2011; Chen et Thompson, 2018; Vantelon et al., 2019). This discrepancy regarding the occurrence of Lp could be explained by the variability in the physico-chemical conditions prevailing during aggregate formation.

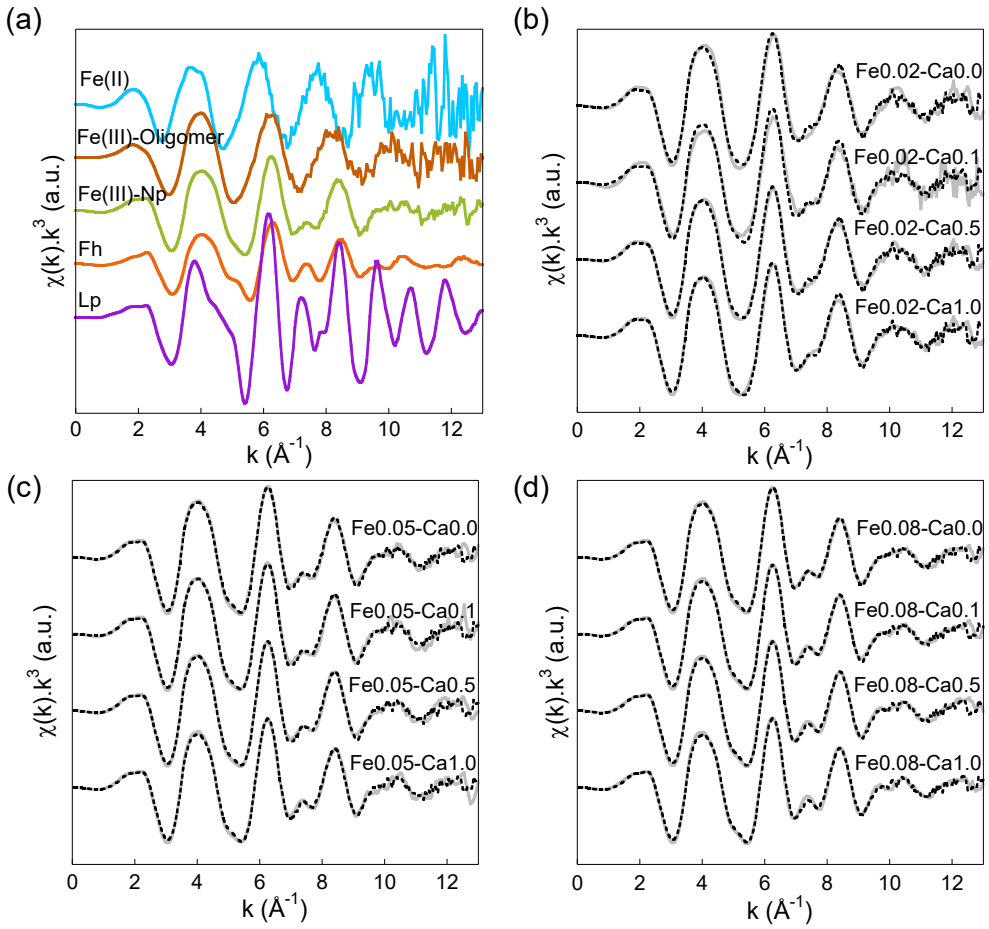

Figure II.1-3 – Iron K-edge EXAFS spectra of (a) references used for LCF and samples at (b) Fe/OC = 0.02, (c) Fe/OC = 0.05 and (d) Fe/OC = 0.08. Solid lines are experimental data and dotted lines are the LCF results.

Table II.1-3 – Fitting parameters obtained for the best LCF for samples with Fe/OC = 0.02, 0.05 and 0.08. The error on each components weight is estimated at ±10%.

Sample	Oligomer	Nanoparticle	Ferrihydrite	R-factor (×10^{-3})
Fe0.02-Ca0.0	0.31	0.69	0	29.0
Fe0.02-Ca0.1	0.20	0.80	0	66.7
Fe0.02-Ca0.5	0.30	0.70	0	18.0
Fe0.02-Ca1.0	0.26	0.74	0	17.4
Fe0.05-Ca0.0	0.18	0.59	0.23	9.94
Fe0.05-Ca0.1	0.20	0.58	0.22	16.6
Fe0.05-Ca0.5	0.20	0.54	0.26	11.3
Fe0.05-Ca1.0	0.17	0.52	0.31	13.4
Fe0.08-Ca0.0	0.15	0.55	0.30	6.99
Fe0.08-Ca0.1	0.14	0.52	0.34	6.59
Fe0.08-Ca0.5	0.13	0.53	0.34	8.42
Fe0.08-Ca1.0	0.12	0.54	0.34	9.37

For Fe/OC = 0.02, and Ca/Fe = 0.0 and 0.1, the EXAFS signal features at 5.1 and 7.4 $Å^{-1}$ are not perfectly reproduced by LCF. For Fe/OC = 0.08, Fe(III)-oligomers are described as tetramers bound to OM (Vantelon et al., 2019). However, Vilgé-Ritter et al. (1999) and Mikutta and Kretzschmar (2011) described Fe(III)-oligomers as trimers for Fe/OC = 0.02 and 0.004 respectively. For Fe/OC = 0.02, Fe(III) monomers bound to OM were also reported by Karlsson and Persson (2012). The tiny discrepancy observed between the data and LCF can therefore be explained by the difference in the Fe/OC ratio for the references used for fitting. The Fe(III)-Np signal may also be slightly different than the one used for the fit due to a particle size effect. In any case, for Fe/OC = 0.02, Fe occurs at around 30% as Fe(III)-oligomers and 70% as Fe(III)-Np irrespective of the Ca/Fe ratio (Figure II.1-4). For Fe/OC = 0.05 and 0.08, Fe is organized as Fe(III)-oligomers, Fe(III)-Np and Fh. With increasing Fe/OC and Ca/Fe, Fe(III)-Np remains constant (around 55%) whereas Fe(III)-oligomers amount decrease in favour of Fh until reaching a steady state at 13% Fe(III)-oligomers, 34% Fh and 53% Fe(III)-Np for Fe/OC = 0.08 and Ca/Fe ≥ 0.1. These results are in agreement with Chen et al. (2014). By co-precipitating Fe(III) with OM at Fe/OC = 0.44, they provided evidence that 72 % of Fe was organized as Fh and 28% as so-called “insoluble Fe(III)-OM” species (described by van Schaik et al. (2008) as Fe trimers bound to OM).

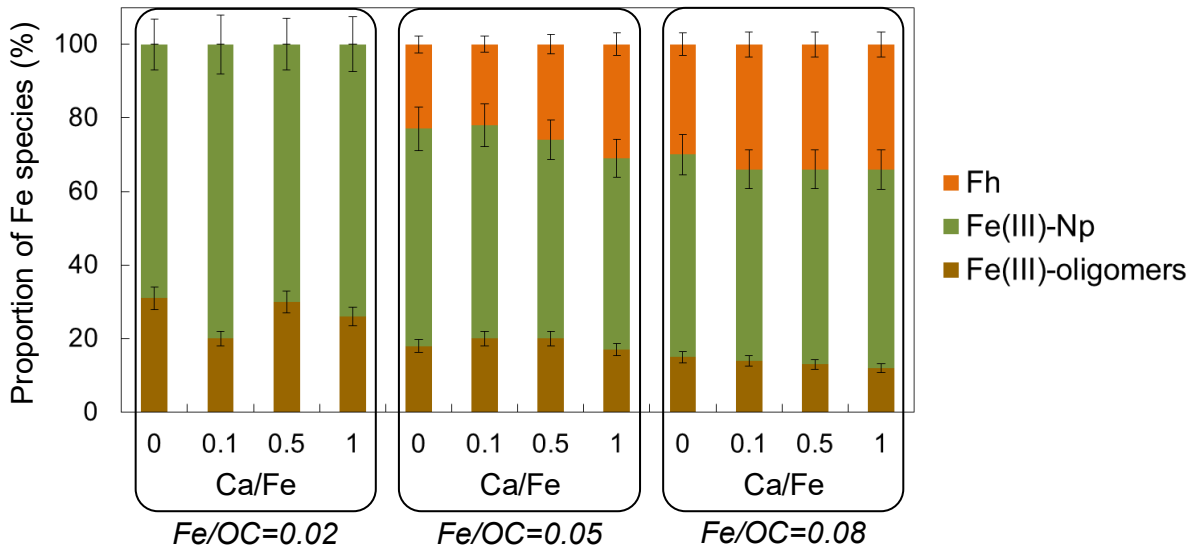

Figure II.1-4 – Proportion of Fe(III)-oligomers (brown), Fe(III)-Np (green) and Fh (orange) determined by LCF of the EXAFS data shown in Figure II.1-3.

II.1.3.2. Structural organization of Fe particles in the aggregates

SAXS measurements are used to investigate the Fe part of Fe-OM-Ca aggregates (Figure II.1-5). The X-ray contrast only depends on the electronic density of the element, which is significantly larger for Fe as compared to OM (the OM part is thus invisible in the scattering signal). The high q part of the scattering curve corresponds to the form factor of Fe primary beads (Fe-PB) that can be modelled with a spherical form factor with a radius equal to 0.8 nm. These Fe-PB are consistent with the coherent scattering domains of Fh described by Michel et al. (2007). All curves exhibit a shoulder between 10^{-2} and 10^{-1} $Å^{-1}$ indicating a characteristic size of Fe, corresponding to Fe primary aggregates (Fe-PA) made of Fe-PB. This shoulder shifts to the lowest q with the increasing Ca/Fe ratio, indicating that the size of the Fe-PA increases. Two different behaviors of the inflexion shape can be observed depending on the Fe/OC ratio. For Fe/OC = 0.02, the inflexion is lower without Ca than with Ca. By contrast, the increasing Ca/Fe ratio leads to the attenuation of the inflexion for Fe/OC = 0.05 and 0.08. At low q, the increase in intensity indicates the aggregation of Fe-PA as larger objects, i.e. Fe secondary aggregates (Fe-SA) for which the size cannot be determined given the limited q range. At intermediate q, the form factor of Fe-PA was extracted to determine their radius (Figure II.1-6, Table II.1-4 and Figure II.1-7) which increases with the increasing Fe/OC ratio as demonstrated by Guénet et al. (2017). Furthermore, the Fe-PA size also increases with the increasing Ca/Fe ratio while their morphology remains constant as highlighted by the Fe-PA fractal dimension which is ~2.4 irrespective of the Fe/OC or Ca/Fe ratio (Table II.1-4).

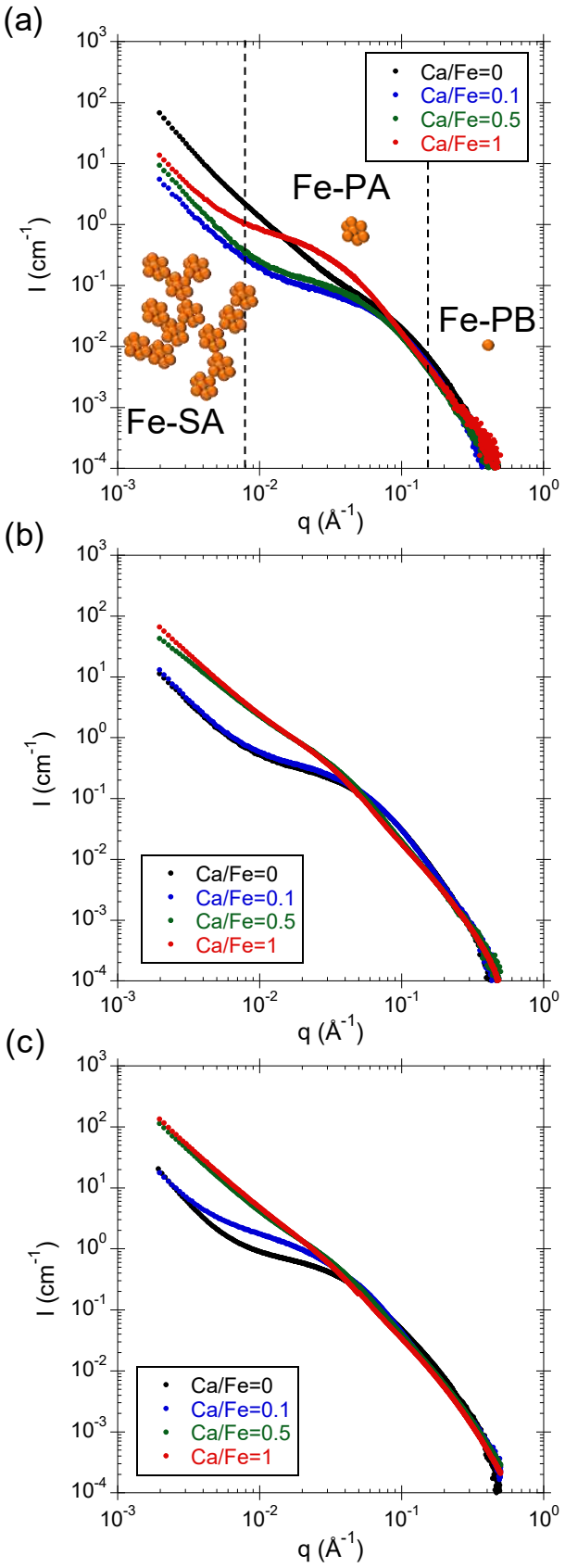

Figure II.1-5 – SAXS curves for samples with (a) Fe/OC = 0.02, (b) Fe/OC = 0.05 and (c) Fe/OC = 0.08. In (a) Fe-PB, Fe-PA and Fe-SA are represented in their corresponding scattering domain.

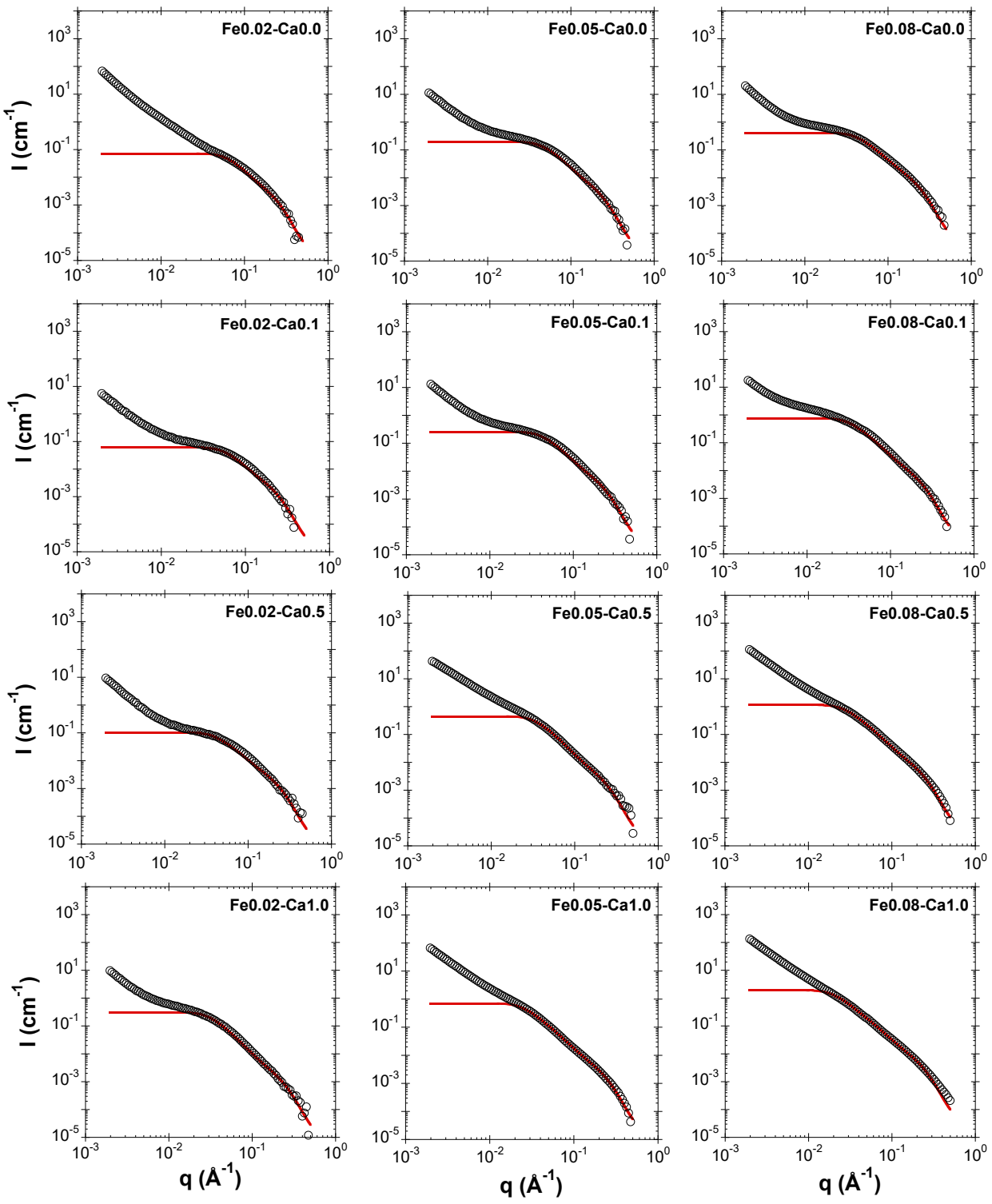

Figure II.1-6 – SAXS curves (black empty circles) and the modelled Fe-PA form factor (red line) for all samples.

Table II.1-4 – Fitting parameters used to simulate the form factor of the intermediate aggregates. Fixed parameters were the radius of the primary bead R_0=0.8 nm, the log normal distribution σ=0.3 and the contrast $\Delta\rho^2=2.37\times10^{21}$ cm^{-4}. The errors on the parameters were 15%. (*) represent the parameters adjusted for fitting the curves and (**) represent the parameter calculated from parameter denoted (*)

Sample	φ_0 ($\times10^{-4}$)*	N_{PA}*	R_{PA} (nm)**	D_{fPA}*
Fe0.02-Ca0.0	7.00	6	1.6	2.5
Fe0.02-Ca0.1	5.50	6.5	1.8	2.3
Fe0.02-Ca0.5	5.00	12	2.6	2.1
Fe0.02-Ca1.0	4.00	45	3.5	2.6
Fe0.05-Ca0.0	9.50	12	2.3	2.4
Fe0.05-Ca0.1	10.0	15	2.5	2.4
Fe0.05-Ca0.5	7.50	32	3.1	2.6
Fe0.05-Ca1.0	7.50	55	4.2	2.4
Fe0.08-Ca0.0	20.0	12	2.5	2.2
Fe0.08-Ca0.1	15.0	30	3.3	2.4
Fe0.08-Ca0.5	15.0	45	3.9	2.4
Fe0.08-Ca1.0	14.0	80	5.4	2.3

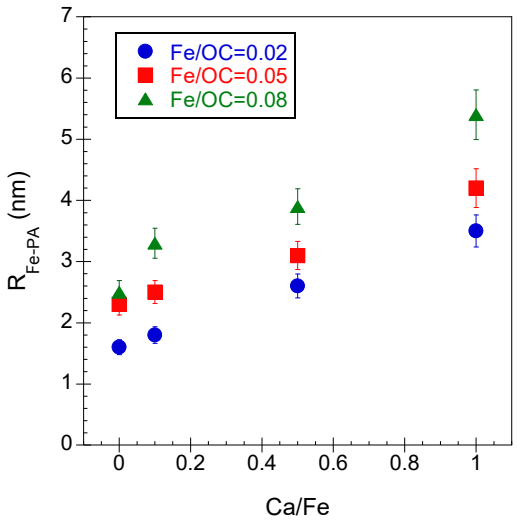

Figure II.1-7 – Variations in the radius of the Fe primary aggregates relative to Ca/Fe for Fe/OC = 0.02 (blue circles), 0.05 (red squares) and 0.08 (green triangles).

Dividing the total scattered intensity by the calculated Fe-PA form factor, we extracted an apparent structure factor -S_T- (Figure II.1-8a) that describes the Fe-SA. In our experimental q range, no plateau was observed at low q values, the Fe-SA size could thus not be calculated. However, the increase of the $S_T(q)$ intensity as a power law in the range 8×10^{-2}-1×10^{-3} $Å^{-1}$ is relevant to the Fe-SA contribution. The shoulder observed between

3×10^{-1} and 7×10^{-2} Å^{-1} in $S_T(q)$ indicates interactions between the Fe-PA inside the Fe-SA. Modelling this peak with a Percus-Yevick function (Robertus et al., 1989) allows calculating the center-to-center distance d_0 between Fe-PA within the Fe-SA (Figure II.1-8b and Table II.1-5).

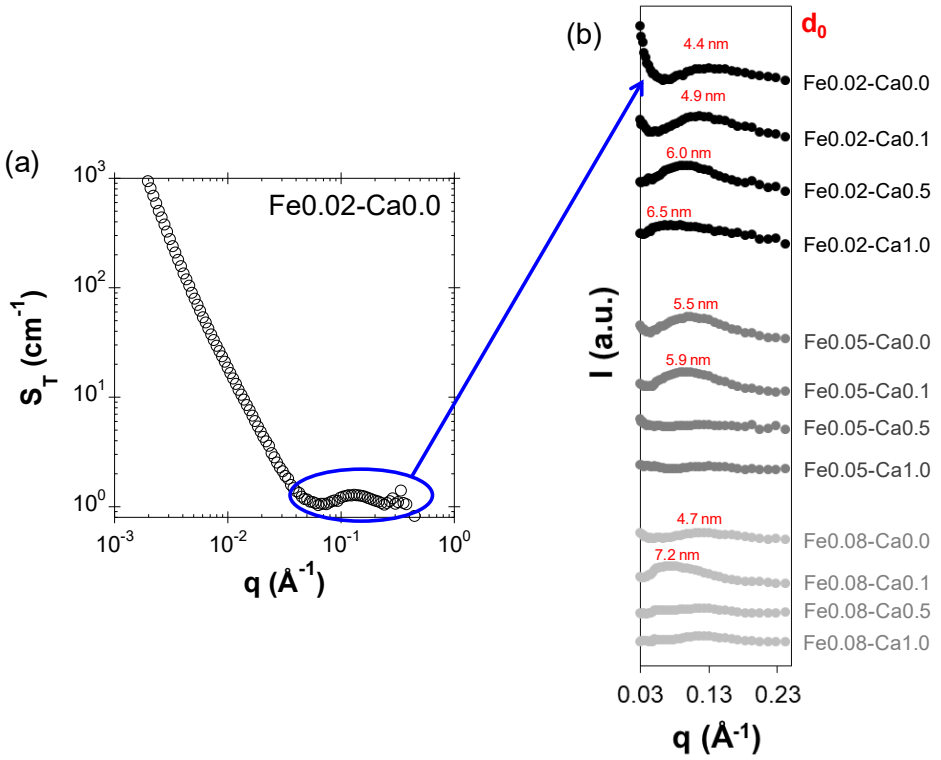

Figure II.1-8 – (a) Apparent total structure factor $S_T(q)$ for Fe0.02-Ca0.0 and (b) evolution of the peak representing the interaction between PA.

Table II.1-5 – Values of the centre-to-centre distance d_0 between Fe-PA. A '-' is reported when the correlation peak of Fe-PA did not occur, indicating an increase in the distance between Fe-PA.

d0 (nm)		Ca/Fe 0.0	0.1	0.5	1.0
Fe/OC	0.02	4.4	4.9	6.0	6.5
	0.05	5.5	5.9	-	-
	0.08	4.7	7.2	-	-

For samples exhibiting the lowest Ca contents, d_0 increases with increasing Fe/OC and Ca/Fe ratios as a response to the increase in Fe-PA size since the d_0 values range from $2\times R_{PA}$ to $2.8\times R_{PA}$. However, the key result is observed for the four samples exhibiting the highest Ca contents for which no peak occurred, suggesting a loss of correlation between

Fe-PA in response to a longer distance between Fe-PA and/or a larger d_0 dispersity. As a result, the presence of Ca leads to a long range correlation between the Fe-primary aggregates.

At Fe/OC = 0.05, TEM observations showed black spherical entities (Figure II.1-9). The XEDS analysis revealed the presence of Fe indicating that these black dots are Fe particles, as previously observed for synthetic and natural samples (Neubauer et al., 2013; Guénet et al., 2017; Lotfi-Kalahroodi et al., 2019). Their compact spherical and nanometric size (between 2 and 6 nm) is consistent with Fe-PA identified by SAXS. Moreover, their size increases with the increasing Ca/Fe ratio from ~ 2 nm for Fe0.05-Ca0.0 and Fe0.05-Ca0.1 (Figure II.1-9a and b) to ~ 5.5 nm for Fe0.05-Ca1.0 (Figure II.1-9d), confirming the SAXS results.

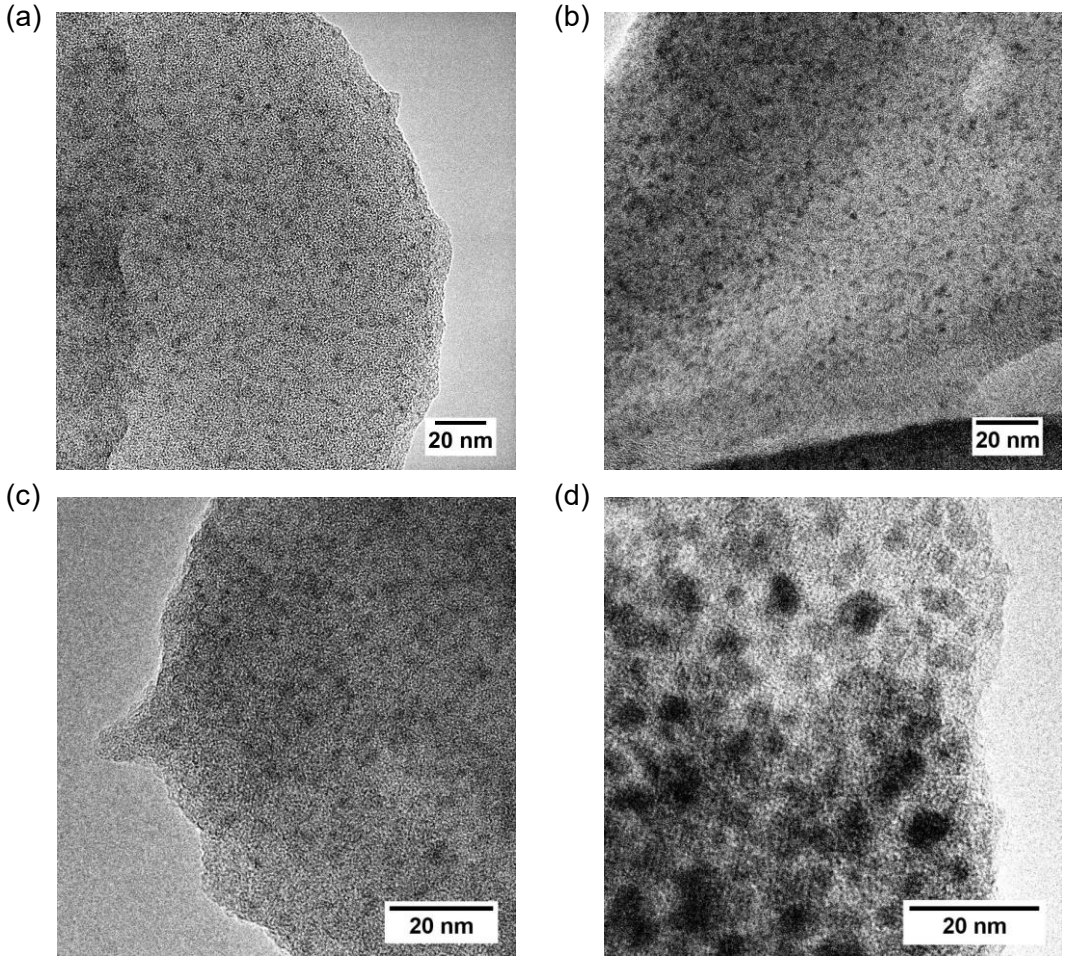

Figure II.1-9 – Transmission electron microscopy images of the aggregates for Fe/OC = 0.05 and (a) Ca/Fe 0, (b) Ca/Fe 0.1, (c) Ca/Fe 0.5 and (d) Ca/Fe 1. The grey scales are arbitrary.

II.1.3.3. Structural arrangement of OM in the aggregates

SANS measurements with a 100 % D_2O contrast allowed to match the iron scattering contribution to the signal and to access the OM part of the aggregates. For SANS curves with 100 % D_2O contrast (Figure II.1-10a,b,c), the inflexion observed for $q < 10^{-3}$ $Å^{-1}$ suggests a typical size for the OM aggregates. This inflexion shifts to the lower q when increasing Ca/Fe ratio suggesting an increase of the OM size. However, these curves exhibit the same slope in the q domain between 10^{-3} and 10^{-1} $Å^{-1}$ irrespective to the Fe/OC or the Ca/Fe ratio, suggesting no local scattering contribution from OM phases. To enforce this observation, SANS curves with 50/50% H_2O/D_2O contrast were measured (Figure II.1-10d,e,f). At this specific contrast, both the contribution of OM and the Fe is visible. For $q > 10^{-2}$ $Å^{-1}$, this contrast can also be used to test if another OM organization (e.g. smaller molecules than the OM aggregates) could contribute to the signal. In the q domain between 10^{-3} and 10^{-2} $Å^{-1}$, no differences were observed between samples as all the curves exhibit the same slope. In the q domain between 10^{-2} and 10^{-1} $Å^{-1}$, an inflexion occurs for samples with the highest Ca/Fe ratios, suggesting a variation in the local organization. In this range, the SANS and SAXS curves can be superimposed showing an identical signal provided mainly by Fe-PA (Figure II.1-11). This result confirms that no local modification of OM occurs as its local scattering contribution is the same irrespective of the Fe/OC and Ca/Fe ratios.

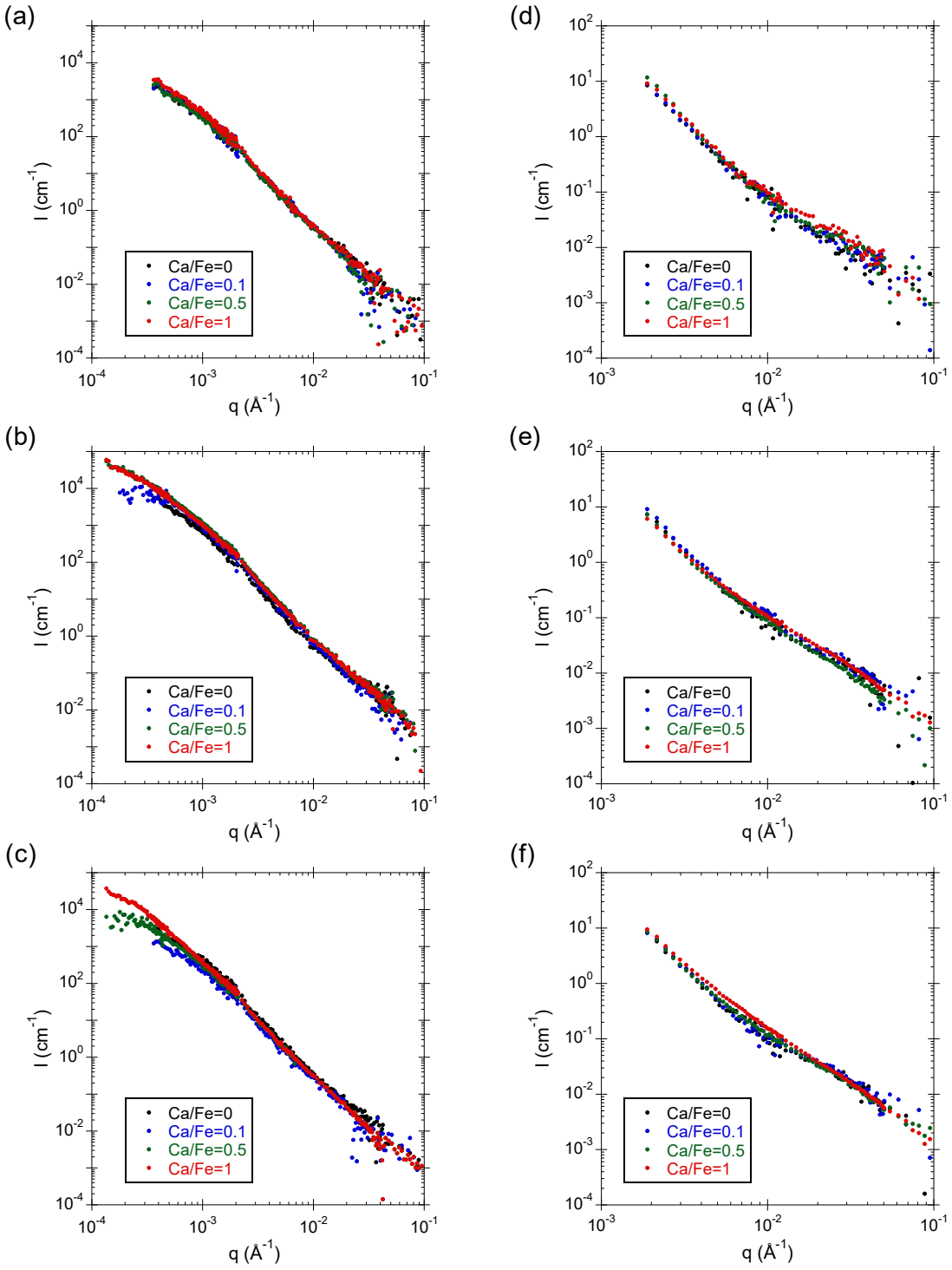

Figure II.1-10 – SANS curves with 100% D_2O contrast for samples with a Fe/OC ratio of (a) 0.02, (b) 0.05and (c) 0.08, and with contrast at 50/50% H_2O/D_2O for samples with a Fe/OC ratio of (d) 0.02, (e) 0.05 and (f) 0.08.

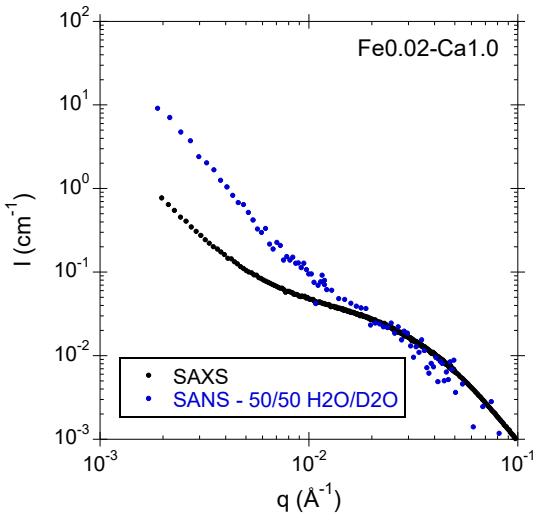

Figure II.1-11 – SAXS curve (black) compared to SANS curve with contrast at 50/50 H_2O/D_2O (blue).

All 100% D_2O contrast curves were fitted with the Guinier-Porod equation (eq. II.1-2) (Figure II.1-12). The parameters used are reported in Table II.1-6. The radius of OM, R_{OM}, was calculated from the radius of gyration R_g (determined by the fit of the SANS curves) with the following equation:

$$R_{OM} = R_g \times \sqrt{\frac{5}{3}}$$

Table II.1-6 – Fitting parameters used in SasView software with the Guinier-Porod equation. Fitted parameters are denoted (*), fixed parameters are denoted (**).

Sample	Scale*	R_g (nm)*	R_{OM} (nm)	α**
Fe0.02-Ca0.0	3210	303	394	2.7
Fe0.02-Ca0.1	3291	288	374	2.9
Fe0.02-Ca0.5	4560	364	473	2.7
Fe0.02-Ca1.0	5510	336	437	2.9
Fe0.05-Ca0.0	8659	336	437	2.9
Fe0.05-Ca0.1	8600**	300**	390	3.0
Fe0.05-Ca0.5	52303	619	805	2.8
Fe0.05-Ca1.0	56927	668	868	2.8
Fe0.08-Ca0.0	4125	310	403	2.8
Fe0.08-Ca0.1	1685	270	351	2.8
Fe0.08-Ca0.5	5817	388	504	2.8
Fe0.08-Ca1.0	39273	706	918	2.9

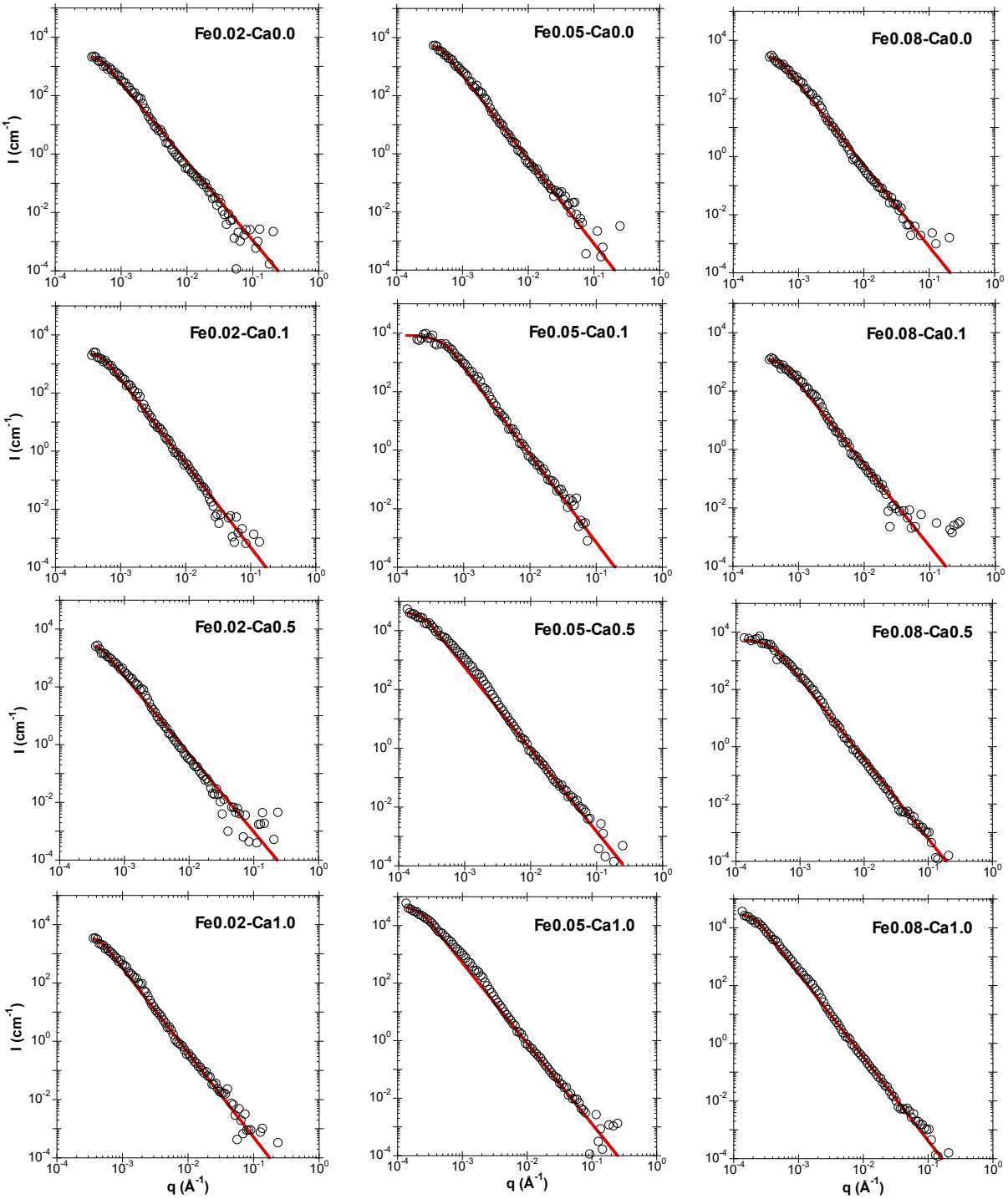

Figure II.1-12 – SANS curves with contrast at 100% D_2O (black empty circles) and the Guinier-Porod modelling (red line) for all samples.

All curves exhibit a fractal dimension, D_f around 2.8, consistent with previous observations on synthetic samples (Guénet et al., 2017) and natural samples (Jarvie et King, 2007; King et Jarvie, 2012). However, several studies reported a D_f value for OM between 2 and 2.5 (Osterberg et Mortensen, 1992; Osterberg et Mortensen, 1994; Diallo et al., 2005). Osterberg and Mortensen (1992) and Guénet et al. (2017), applied a Guinier model on natural and synthetic aggregates at Fe/OC = 0 or 0.01, respectively to obtain a gyration radius for OM from 30 nm (Osterberg et Mortensen, 1992) to approximately 100 nm (Guénet et al., 2017). The Guinier plateau tends to disappear with the increasing Fe/OC ratio in Guénet et al. (2017) and Osterberg and Mortensen (1992). However, Diallo et al. (2005) did not observe the same trend for natural aggregates. In our work, VSANS was used to reach lower q, to provide better evidence of a Guinier plateau and to calculate the typical OM size (Figure II.1-13 and Table II.1-6). The results showed an increase in OM size with the increasing Ca/Fe ratios without any local reorganization of the OM phase.

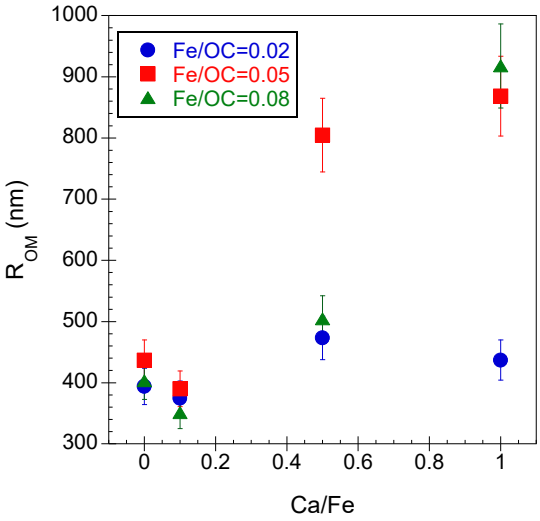

Figure II.1-13 – Evolution of the OM radius relative to Ca/Fe ratio.

II.1.3.4. Calcium interaction with the aggregates

Calcium interactions with the components of the Fe-OM aggregates were characterized by collecting XAS spectra at Ca K-edge. XANES spectra exhibit a pre-edge at 4041 eV which is assigned to the 1s→3d transition (Fulton et al., 2003; Martin-Diaconescu et al., 2015) with electric dipole character when the 3d orbitals are hybridized with p orbitals and

electric-quadrupole one (Figure II.1-13). The 1s→3d electric dipole transition is forbidden for centrosymmetric complexes, then pre-edge structure gains only weak intensity from electric quadrupole transition. In calcite, Ca is surrounded by six O in an octahedral geometry (Graf, 1961) so that the intensity of its pre-edge is relatively weak. The white line at 4045 eV represents the 1s→4p transition and the resonance at 4072 eV corresponds to a $KL_{II,III}$ multielectronic excitation (Fulton et al., 2003). Thus, according to Martin-Diaconescu et al.(2015), in our samples the lack of structure in the XANES spectra and the high intensity of the pre-edge indicate that more than six O are surrounding Ca in the first coordination shell.

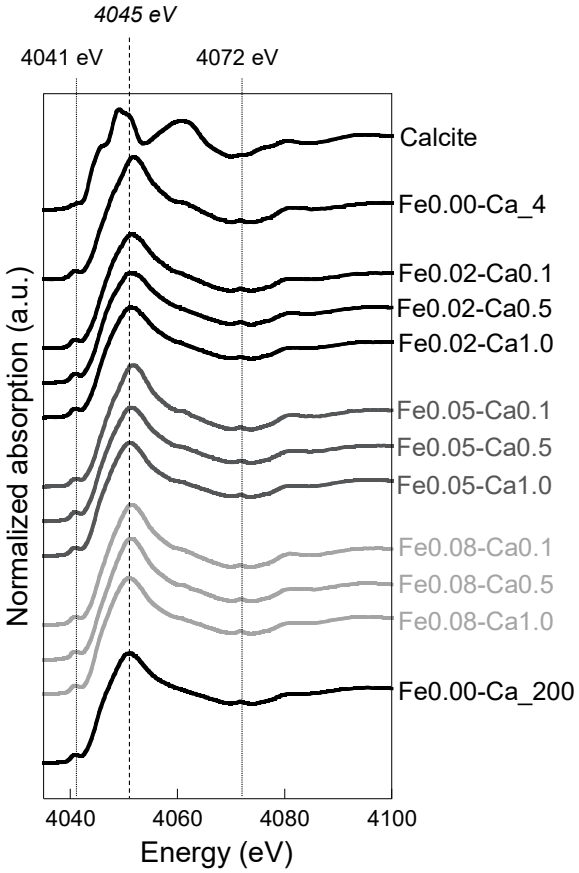

Figure II.1-14 – Ca K-edge XANES spectra for sample.

Magnitude of EXAFS Fourier transform exhibits a first intense peak at 1.8 Å corresponding to the contribution of oxygens neighbours in the first coordination shell (Figure II.1-15). A shoulder is visible for the highest Ca content at 2.1 Å. A second weak oscillation is

observable at 2.8 Å and a third more intense peak occurs at 3.3 Å, not corrected from phase shift.

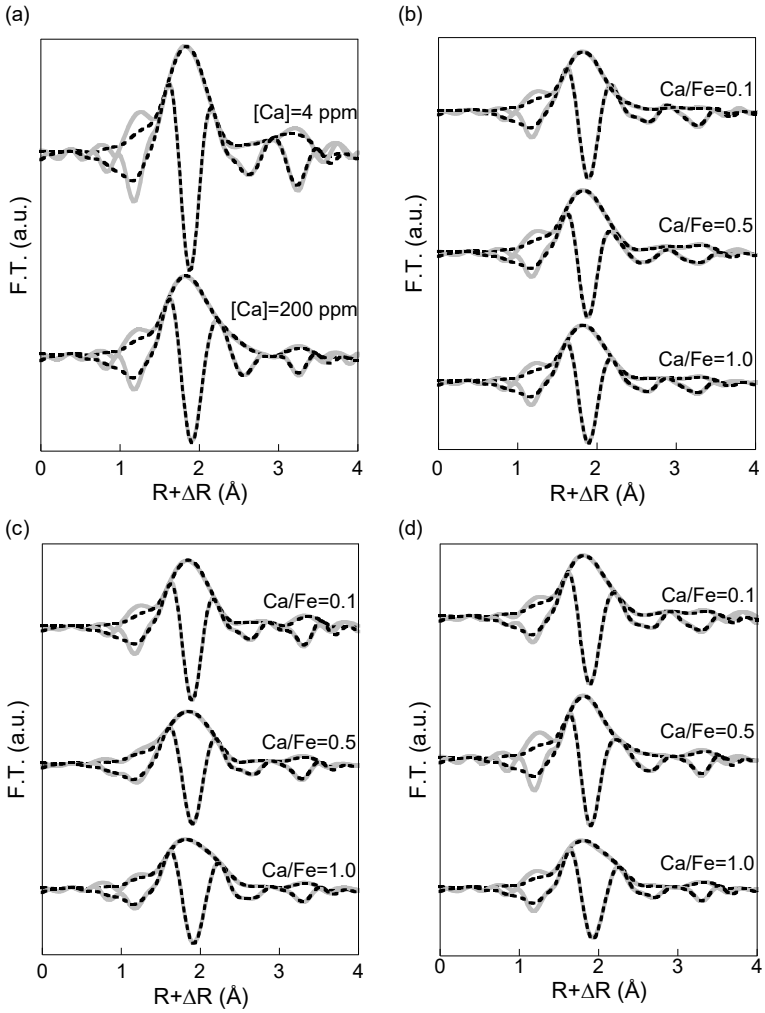

Figure II.1-15 – Magnitude and imaginary part of the Fourier transform if the Ca K-edge EXAFS spectra for sample (a) without Fe, (b) Fe/OC = 0.02, (c) Fe/OC = 0.05 and (d) Fe/OC = 0.08. The grey solid lines are the experimental data and the black dotted lines are the fit results

EXAFS spectra (Figure II.1-16) exhibit a maximum of amplitude at 4.5 $Å^{-1}$. A signal shift can be observed at the low k value for the highest Ca concentration. Two weak shoulders are also observed at 4 and 6 $Å^{-1}$.

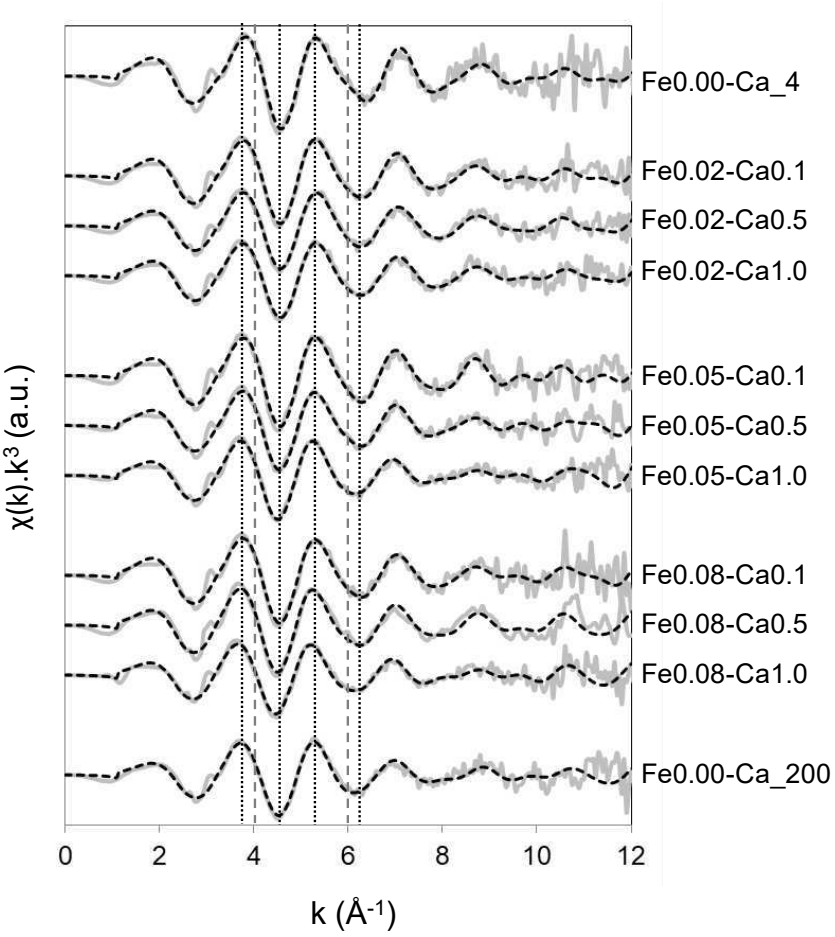

Figure II.1-16 – Calcium K-edge EXAFS of Fe-OM-Ca aggregates. Grey solid lines are the experimental data and the black dotted lines are the fit results.

Before fitting the EXAFS signal of the samples, it was necessary to determine the amplitude reduction factor S_0^2 and the energy shift parameter ΔE. For this purpose, the calcite signal was fitted (Figure II.1-17). First, the coordination number (N) and the interatomic distance (R) of each path were fixed in agreement with the crystallographic data from Graf (1961) to determine S_0^2, ΔE and the Debye-Weller factors σ^2 of each path. In a second time, the fit quality was improved by adjusting the R of each path. Iterations were completed by adjusting R, σ^2 of each path as well as S_0^2 and ΔE. The presented results in Table II.1-7 are the one obtained for the best fit with S_0^2=1.00 and ΔE=4.92 eV.

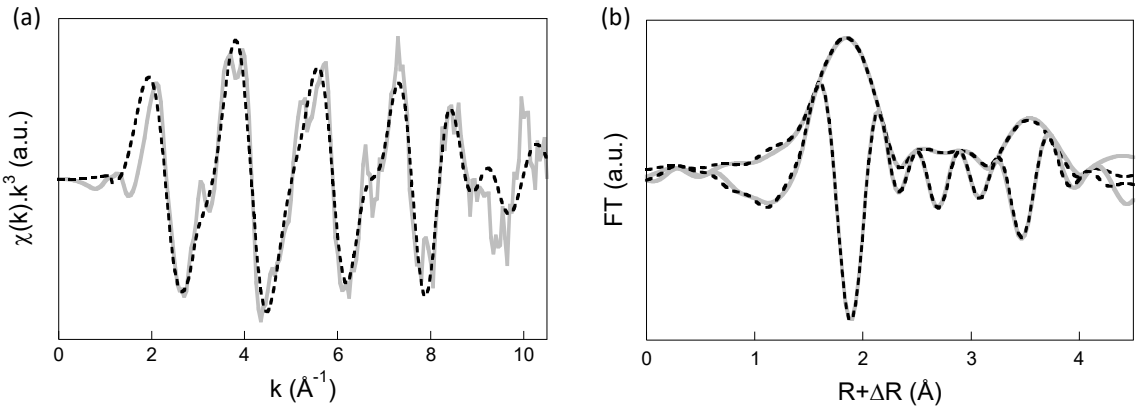

Figure II.1-17 – (a) EXAFS signal and (b) Fourier transforms of calcite material. Solid lines are experimental data and dotted lines are the fit results.

Table II.1-7 – EXAFS fit results for calcite. Fixed parameters are reported with a "*".

Path	Parameter	Value
Ca-O1	N	6.0*
	R	2.37
	σ²	0.010
Ca-C1	N	6.0*
	R	3.25
	σ²	0.011
Ca-O2	N	6.0*
	R	3.57
	σ²	0.017
MS Ca-O-C	N	12*
	R	3.38
	σ²	0.003
Ca-Ca	N	6.0*
	R	4.03
	σ²	0.015

The EXAFS spectra were fitted with the following procedure. The first step was to fit the data with six O at 2.39 Å to reproduce the intense peak at 1.8 Å (Figure II.1-18a). However, the fit did not well reproduce this peak so that a second Ca-O was added in the first Ca coordination shell (Figure II.1-18b). With 3.1 O at 2.30 Å and 3.7 O at 2.46 Å, the first intense

peak at 1.8 Å was well reproduced. The peak at 3.3 Å was then fitted by adding Ca as second neighbour (Figure II.1-18c). With 0.9 Ca at 3.82 Å, we were able to fit the peak at 3.3 Å and the oscillations that occur in the imaginary part of the FT. This fit was not good enough between 2.2 and 3.1 Å. Adding 0.5 C at 3.07 Å, the oscillation in the imaginary part of the FT at 2.5 Å was better fitted (Figure II.1-18d). Finally, with the addition of 2 C at 3.61 Å, the EXAFS FT (magnitude and imaginary part) was well-fitted between 2.5 and 3.1 Å (Figure II.1-18e).

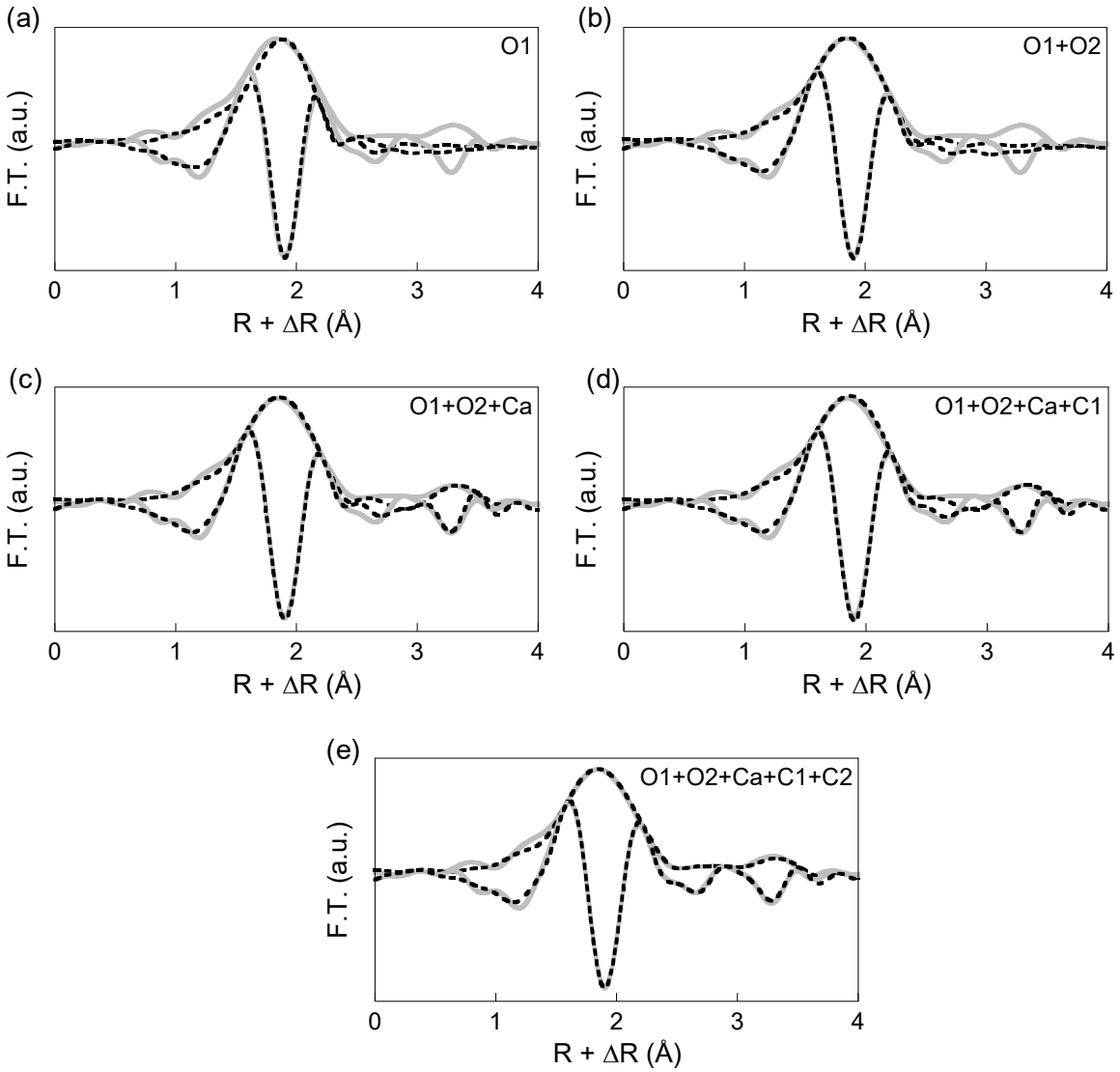

Figure II.1-18 – Magnitude and imaginary part of the Ca K-edge EXAFS spectra Fourier transform shell by shell fitting for sample Fe0.05-Ca0.5. Experimental data are reported in grey solid line and the fit results are reported in black dotted line.

Finally, the spectra were first fitted using two Ca-O distances (Ca-O1 at 2.31 Å and Ca-O2 at 2.48 Å) for the first coordination shell of Ca that was used to reconstruct the first Fourier transform peak. The second peak was fitted with two different C as second neighbors (Ca-C1 at 3.10 Å and Ca-C2 at 3.60 Å). A contribution of Ca as third nearest neighbors at 3.85 Å was then used to fit the third peak, providing evidence of the formation of Ca dimers. The complete fit results are reported in Table II.1-8.

The O number in the first coordination shell remains constant at 6.5 ± 0.6 for all the samples. This result is consistent with XANES data and is representative of a Ca coordination number higher than six for an organic Ca complex (Martin-Diaconescu et al., 2015) or hydrated soluble Ca (Fulton et al., 2003). In the second coordination shell, the C number also remains constant around 2.8 ± 0.3. Carbon in the second coordination shell is characteristic of the formation of Ca-OM inner sphere complexes. The Ca number was also constant around 0.8 ± 0.1 demonstrating the formation of dimers. The Ca-Ca distance at 3.85 Å corresponds to Ca dimers bound by two O. To summarize, Ca forms dimers bound to OM as an inner sphere complex. Performing OC sorption experiments on Fh with Ca, Sowers et al. (2018) suggested the formation of Fe-Ca-OC ternary complexes in which Fe was bound to Ca via an O. The presence of the Ca-OC inner complex occurrence is consistent with Ca binding to OM via carboxylic group as previously observed by Kalinichev and Kirkpatrick (2007) and Iskrenova-Tchoukova et al. (2010). In their studies, binding with phenolic groups was also suggested. However, for our experimental pH at 6.5, phenolic groups remain protonated and weakly available for binding (Adusei-Gyamfi et al., 2019). Moreover, during reduction, Adhikari et al. (2019) reported a higher release and degradation of phenolic OC as compared to carboxylic OC. Here, Ca binding to carboxylic groups is therefore the more expected process and no Fe neighbor could be added in the fit of the second coordination shell of the Ca EXAFS.

Table II.1-8 – Ca K-edge EXAFS fit results.

Sample	R-factor	Ca-O1		Ca-O2		Ca-C1		Ca-C2		Ca-Ca	
		N	*R(Å)*	*N*	*R(Å)*	*N*	*R(Å)*	*N*	*R(Å)*	*N*	*R(Å)*
OM-[Ca]=4 ppm	0.0089	3.6	2.31	3.0	2.46	0.4	3.10	3.7	3.61	1.1	3.82
Fe0.02-Ca0.1	0.0033	3.4	2.31	3.2	2.47	0.5	3.09	2.7	3.59	0.9	3.83
Fe0.02-Ca0.5	0.0028	3.4	2.31	2.7	2.48	0.6	3.07	2.2	3.59	0.6	3.84
Fe0.02-Ca1.0	0.0029	3.1	2.31	2.8	2.47	0.6	3.09	2.0	3.58	0.6	3.82
Fe0.05-Ca0.1	0.0037	3.6	2.32	3.1	2.47	0.7	3.08	2.4	3.57	1.1	3.85
Fe0.05-Ca0.5	0.0035	2.9	2.30	3.3	2.46	0.6	3.09	2.0	3.61	0.8	3.84
Fe0.05-Ca1.0	0.0012	3.1	2.32	3.6	2.49	1.1	3.08	1.8	3.62	0.7	3.85
Fe0.08-Ca0.1	0.0024	3.6	2.31	3.3	2.48	0.6	3.10	2.6	3.60	0.8	3.85
Fe0.08-Ca0.5	0.0100	3.8	2.33	3.1	2.51	1.0	3.12	1.9	3.63	0.8	3.85
Fe0.08-Ca1.0	0.0038	3.0	2.33	3.2	2.51	0.7	3.14	1.3	3.66	0.6	3.86
OM-[Ca]=200 ppm	0.0026	3.0	2.32	3.0	2.49	1.4	3.07	1.3	3.60	0.5	3.81

The amplitude reduction factor S_0^2 and theenergy shift parameter ΔE were respectively set to 1.00 and 4.95 eV by fitting the signal of calcite over the range of 1.3-4 Å (the calcite fit is reported in Figure II.1-17 and the corresponding fitting parameters are reported in Table II.1-7). *N* is the coordination number and *R* is the interatomic distance (Å). The Debye-Weller factors σ^2 were fixed to 0.004 Å² to compare the evolution of each coordination number. The error on N and R are usually estimated to be ± 10% and ± 1%, respectively.

II.1.3.5. Overall organization of Fe-OM-Ca aggregates

The overall organization of Fe-OM-Ca associations was observed by cryo-TEM (Figure II.1-19a,b and c) and cryo-TXM imaging (Figure II.1-19d). The cryo-TEM observation of Fe0.08-Ca0.1 (Figure II.1-19a) exhibits dispersed black spherical entities consistent with Fe-PA described from SAXS and observed by TEM (Figure II.1-9). The yellow arrows highlight dots showing higher Fe-PA density locally. They are embedded in a less intense background of ~100 nm which could be assigned to an OM aggregates. This aggregate was subjected to electron beam irradiation. During irradiation, some bubbles were formed (red arrows on Figure II.1-19b) which indicates damaged organic compounds. Consequently, the ~100 nm aggregate highlighted by yellow arrows was assigned to Fe-SA in an OM aggregate as described by Guénet et al. (2017). By contrast, for higher concentrations of Ca, cryo-TEM observation of Fe0.08-Ca0.5 displays dispersed black dots embedded in a dark background (Figure II.1-19c). These observations indicate Fe-PA embedded in an OM matrix and therefore correspond to an OM network trapping Fe-PA. The cryo-TXM observation of the same sample (Figure II.1-19d) revealed darker features at the centre and on the right of the image, indicating the presence of OM, Ca and Fe that confirms the micrometric network formation. These results clearly provide evidence for the significant impact of Ca on Fe-OM structural organization, varying from aggregates to a micrometric network.

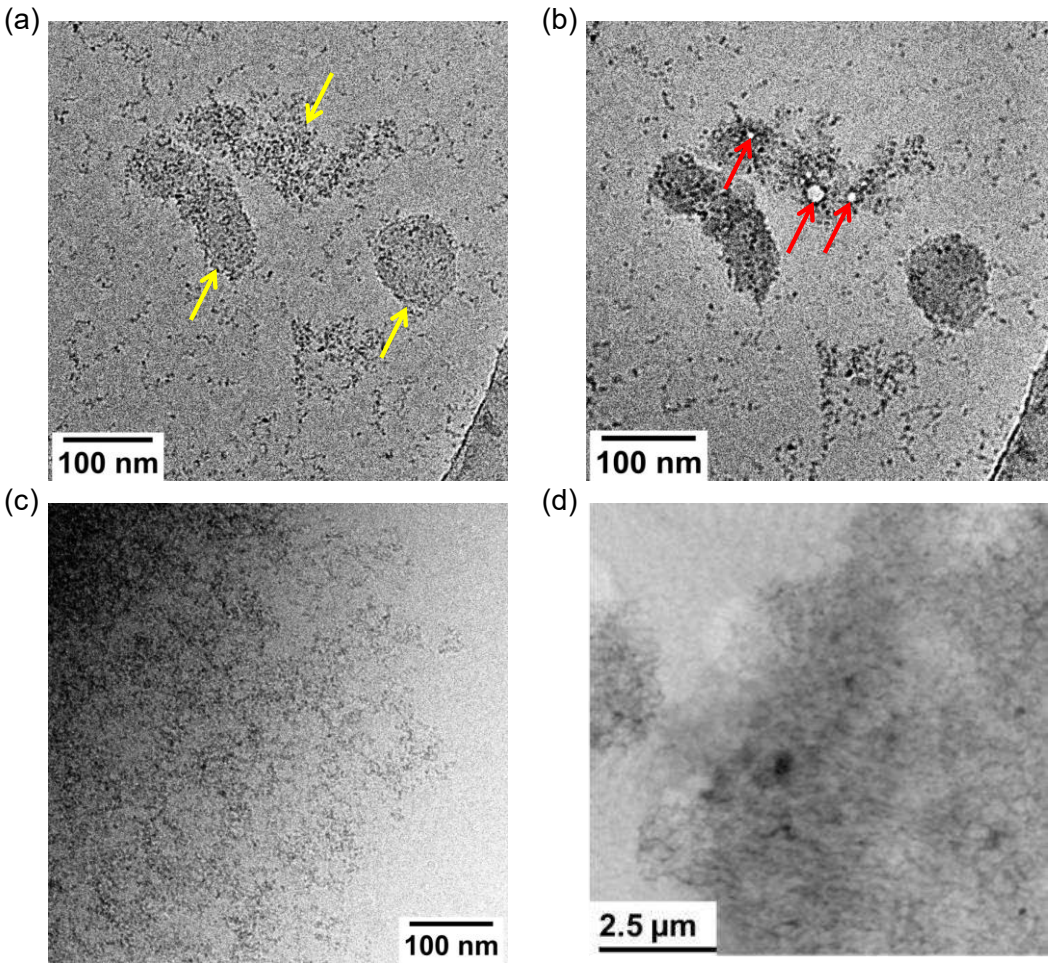

Figure II.1-19 – Cryo-TEM imaging of (a) Fe0.08-Ca0.1, (b) Fe0.08-Ca0.1 after electron beam irradiation, (c) Fe0.08-Ca0.5 and (d) cryo-TXM imaging of Fe0.08-Ca0.5. The dense part at the bottom right in (a) and (b) corresponds to the thin carbon film on the grid. The 2 µm white circles and a grey background in the top left of (d) correspond to the holes and the carbon film on of the grid, respectively.

The formation of a micrometric network was also confirmed with filtration and ultrafiltration experiments (Table II.1-9). For Fe0.08-Ca0.1 the presence of OM, Fe and Ca in the > 0.2 µm and 0.2 µm-30 kDa fractions demonstrated the existence of aggregates with a size < 200 nm. For Fe0.08-Ca0.5, 96 % of the OC and 100 % of the Fe is in the > 0.2µm fraction while SAXS measurements and TEM observations provided evidence of the existence of Fe-PA with a size ≈ 5 nm. These results encouraged the formation of an OM micrometric network trapping Fe-PA.

Table II.1-9 – OC, Ca and Fe concentration (mmol L^{-1}) for Fe0.08-Ca0.1 and Fe0.08-Ca0.5. <LOD: below the limit of detection (LOD).

Fractions	Fe0.08-Ca0.1			Fe0.08-Ca0.5		
	OC	Ca	Fe	OC	Ca	Fe
>0.2 µm	36.5 ± 3.2	0.35 ± 0.02	3.4 ± 0.3	54.9 ± 2.1	1.2 ± 0.1	4.77 ± 0.1
0.2 µm-30 kDa	17.4 ± 3.2	0.17 ± 0.03	1.6 ± 0.3	<LOD	<LOD	<LOD
<30 kDa	2.3 ±0.3	0.05 ± 0.01	<LOD	2.2 ± 0.4	1.2 ± 0.1	<LOD

II.1.4. Fe-OM-Ca associations: from aggregates to a micrometric network

It was demonstrated that calcium controls the structural organization of the Fe-OM-Ca association through its binding to OM via carboxylic groups (COOH). It is thus appropriate to present the results depending on Ca/OC molar ratio since SANS measurements highlight a significant increase of the OM size from Ca/OC ≥ 0.026 (Figure II.1-20). This observation is in accordance with cryo-TEM and cryo-TXM images which provide evidence of the OM micrometric network formation from Ca/OC ≥ 0.026.

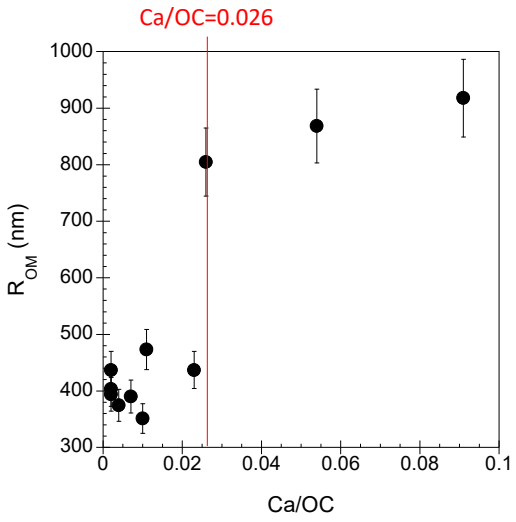

Figure II.1-20 – Evolution of the OM radius relative to Ca/OC ratio.

Fe-OM-Ca associations therefore exhibit two distinct organizations depending on the Ca/OC ratio. For Ca/OC < 0.026, Fe-OM-Ca associations are organized as aggregates. Iron exhibits a fractal organization in which Fe-PB (radius ≈ 0.8 nm) formed Fe-PA (radius ≈ 5 nm) that is either isolated or embedded in an OM aggregate (radius ~ 100 nm) resulting in the formation of Fe-SA (radius > 100 nm), as already described (Guénet et al., 2017) (Figure II.1-21, left). For Ca/OC ≥ 0.026, the organization of the Fe-OM-Ca association is drastically different. All OM is branched out by Ca and forms a micrometric network in which all Fe-PB and Fe-PA are embedded (Figure II.1-21, right). The presence of Ca also results in an increase in Fe-PA size from 2 nm to 5 nm. Therefore, while Ca did not directly interact with Fe, Ca atoms screen interactions between Fe and OM thereby allowing for the growth of Fe-PA. Calcium drives the organizational mechanism of OM which in turn controls the size and the distribution of Fe-PA in the OM aggregate or in the OM network. Thus, calcium drives the structural transition in this system. These significant modifications of the structural organizations modify the size of the global aggregates and their colloidal stability (Figure II.1-1). For Ca/OC < 0.026, Fe-OM-Ca associations are composed of aggregates which stay in suspension and can be transported with the water flow. For Ca/OC ≥ 0.026, the formation of a micrometric network results in the settlement of Fe-OM-Ca associations and their immobilization by gravitational settling and/or trapping the soil porous media (Kretzschmar et Schäfer, 2005).

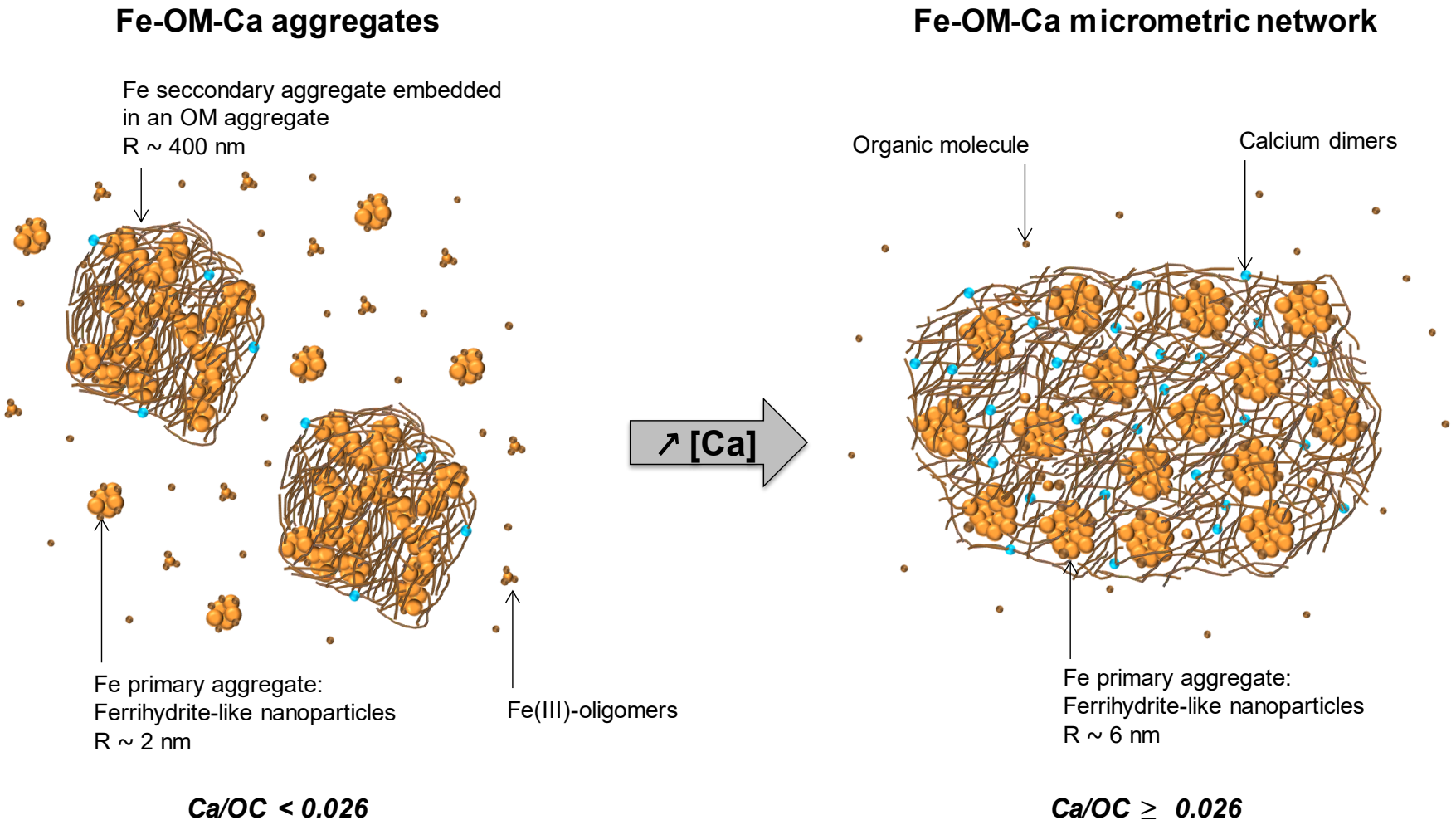

Figure II.1-21 – Schematic representation of the structural organization of the Fe-OM-Ca associations depending on the Ca/OC ratio.

In environmental waters, OM is known to control Fe phases by inhibiting their growth and crystallinity. Organic matter also enables the formation of complexes formed with a Fe oligomer and its carboxylic functional group (Karlsson et Persson, 2010; Pédrot et al., 2011; Guénet et al., 2017; Vantelon et al., 2019). Given that Leonardite HA is composed of 7.46×10^{-3} mol of COOH per gram of C (Ritchie et Perdue, 2003), an apparent COOH concentration can be calculated for our samples (Table II.1-10).

Table II.1-10 – Concentration of the carboxylic groups (COOH) (mol L^{-1}) and COOH/Ca ratios for Fe0.08-Ca0.1 and Fe0.08-Ca0.5.

Fractions	**Fe0.08-Ca0.1**		**Fe0.08-Ca0.5**	
	COOH (mol L^{-1})	**COOH/Ca**	**COOH (mol L^{-1})**	**COOH/Ca**
> 0.2 µm	3.22×10^{-3}	9.2	4.92×10^{-3}	4.2
0.2 µm-30 kDa	1.56×10^{-3}	8.7	-	-

In Fe-OM-Ca associations, Ca is bound to OM via COOH with a COOH/Ca = 3. For Fe0.08-Ca0.1, the COOH/Ca ratio within aggregates is close to 9 and therefore some carboxylic groups remain available for the Fe phases. For Fe0.08-Ca0.5, COOH/Ca = 4.2 in the OM micrometric network. As a consequence, carboxylic groups are less available for binding the Fe species. In the OM network, Fe phases are not as covered by the organic molecule and their adsorption capacity should therefore be higher. Furthermore, for the highest Ca amounts, the Fe(III)-oligomer content decreases in favour of Fh, increasing the sorption capacities of the Fe aggregates. Conversely, the size of the nanoparticular Fe phases is allowed to increase and nanoparticles larger than 20 nm exhibit lower adsorption capacities (Auffan et al., 2008). The Fe-OM-Ca adsorption capacities could therefore be lower with increasing Ca amounts and the subsequent continuous network formation. The formation of a continuous network leads to two antagonist effects with regard to the Fe-OM-Ca adsorption capacities, which need to be investigated in further studies. In addition, the presence of Ca should impact the Fe-OM aggregates reactivity regards bioreduction processes. Pédrot et al. (2011) demonstrated that the bioreduction of Fe(III)-OM colloids was significantly faster than that of nano-Lp. They suggested that OM acts as an electron shuttle during the reduction process. Adhikari et al. (2019) reported a decrease of the Fh-OM co-

precipitates bioreduction rate in the presence of Ca. The partial screening of the interactions between Fe and OM evidenced in our study could explain this result: the OM, bound to Ca, could not act as electron shuttle anymore.

II.1.5. Conclusion

We demonstrated the impact of Ca on the structural organization of Fe-OM aggregates. The structural organization of Fe-OM-Ca associations is controlled by the occurrence of Ca through its binding to OM carboxylic groups. Fe-OM-Ca associations can have two distinct organizations depending on the Ca/OC ratio. For low Ca concentrations, Fe-OM-Ca associations are organized as aggregates in which Fe exhibits three aggregation levels: (i) isolated Fe primary beads bound to organic molecules, that can be aggregated as (ii) Fe primary aggregates which can themselves form (iii) Fe secondary aggregates embedded in an OM aggregate (Figure II.1-21). A structural transition occurs with the increasing Ca/OC ratio until an OM micrometric network is formed. This structural transition is driven by Ca which mainly interacts with OM COOH sites. Calcium acts as a bridge between the organic molecules and allows the formation of a large OM network. As organic molecules are preferentially connected to each other by Ca bridges, they are less available for binding Fe which is less covered by OM, allowing for the growth of ferrihydrite-like nanoparticular structures as indicated by their size increase. The impact of Ca on the overall structural organization is of major importance regarding:

- the permafrost thawing which is increasing in response to climate change, Pokrovsky et al. (2011) reported increasing amounts of Ca in surface waters;
- the importance of Ca in the control of the availability of the Fh-like Np binding sites;
- the capacity of Ca to prevent the ability of OM to act as an electron shuttle in bioreduction processes;
- the Ca ability to control the mobility of Fe-OM aggregates and associated elements through the formation of a micrometric network.

II.2. Impact de l'aluminium sur l'organisation structurale des agrégats fer-matière organique

Dans la première partie, j'ai montré que la présence du Ca lors de la formation des agrégats de Fe-MO a un impact important sur leur stabilité colloïdale en solution. Dans ce système, le Ca n'interagit qu'avec la MO : aucune des techniques fines de caractérisation utilisées n'a permis de mettre en évidence une quelconque interaction avec le Fe. Et pourtant, sa présence induit des modifications de sa spéciation et donc de sa réactivité. En interagissant avec la MO, le Ca diminue les quantités de Fe complexé, le taux de recouvrement des nanoparticules de Fe diminue produisant un accroissement de la taille des nanoparticules mais aussi de leur nombre. Dans les systèmes environnementaux, le Ca n'est, cependant, pas le seul cation majeur et un certain nombre d'entre eux peut interagir non seulement avec la MO naturelle, mais aussi avec les différentes phases du Fe. C'est le cas de Al qui selon sa spéciation peut se complexer à la MO (Lippold et al., 2005; Tipping, 2005). Il est également connu pour interagir avec les oxyhydroxydes de fer(III) puisqu'il peut s'insérer dans leur structure, comme c'est le cas pour la ferrihydrite ou bien s'adsorber à sa surface (Hansel et al., 2011; Cismasu et al., 2012; Adra et al., 2013). A la différence du Ca, l'Al est donc susceptible d'interagir avec l'un ou l'autre ou même les deux composants et son impact sur l'organisation structurale des agrégats Fe-OM devrait être différent de celui du Ca. J'ai donc choisi, dans une deuxième partie de ce travail, d'étudier l'impact de l'Al sur l'organisation des phases de Fe et des matières organiques dans les agrégats diphasiques Fe-MO.

Cette partie correspond à un article qui sera soumis prochainement dans la revue Environmental Science: Nano *: Inside the mechanisms by which aluminum impacts the iron-organic matter structural organization, Anthony Beauvois, Delphine Vantelon, Jacques Jestin, Valérie Briois, Erwan Paineau, Thomas Bizien, Mélanie Davranche.*

Résumé

L'organisation structurelle des agrégats naturels hétérogènes et multiphasiques dépend des conditions physico-chimiques qui prévalent dans l'environnement. Parmi ces conditions, la présence d'ions majeurs peut être un paramètre crucial à prendre en compte. Dans cette étude, nous avons choisi d'étudier l'impact de l'aluminium sur les agrégats de fer-matière organique pour deux raisons : 1) Al peut interagir avec la MO et 2) il peut s'incorporer dans les oxyhydroxydes de Fe ou s'adsorber à leur surface. Nous avons synthétisé des agrégats modèles Fe-MO-Al à différentes [Fe] et [Al] pour teneur en MO constante. Pour de faibles concentrations en Fe et Al, les agrégats Fe-OM-Al forment une suspension colloïdale. Au sein des agrégats, le Fe est présent sous forme d'oligomères de Fe(III) ainsi que de nanoparticules de type ferrhydrite (Np-Fh). Quant à l'Al, il se trouve sous forme de monomères, d'oligomères et d'hydroxydes amorphes polymérisés, tous liés à la MO. Nous avons pu observer que les phases de Fe et d'Al interagissent l'une avec l'autre. Pour de fortes teneurs en Fe at Al, les oligomères de Fe(III) et les monomères/oligomères d'Al polymérisent ce qui conduit à l'augmentation la taille et de la quantité des Np-Fh et des hydroxydes d'Al amorphes, toujours liés à la MO. Les agrégats Fe-OM-Al ainsi formés perdent leur stabilité colloïdale puisqu'ils décantent. L'impact de l'Al sur la structure des agrégats de Fe-OM pourrait également avoir un impact sur le devenir des polluants dans l'environnement. La formation d'hydroxydes amorphes d'Al et l'augmentation de la proportion de Np-Fh, qui possèdent une capacité de sorption supérieure à celle des oligomères de Fe(III), entraînent une augmentation de la disponibilité des sites réactifs de surface et, par conséquent, une augmentation de la capacité d'adsorption des agrégats de Fe-OM.

Abstract

Structural organization of heterogeneous and multiphasique natural aggregates depends on the physicochemical conditions prevailing in the environment. Among such conditions, major ions might be of major importance. In this study we chosen to investigate the impact of aluminum onto iron-organic matter aggregates for two reasons, 1) Al can interact with OM and 2) can be incorporate in Fe-oxyhydroxides or adsorbed at their surface. Mimetic environmental Fe-OM-Al aggregates were synthesized at various [Fe] and [Al] with a constant OM concentration. At low [Al+Fe], Fe-OM-Al aggregates exhibit a colloidal behavior. Within the aggregates, Fe is as Fe(III)-oligomers and ferrhydrite-like nanoparticles (Fh-like Np) and Al as monomers, oligomers and polymerized As amorphous hydroxides, all bound to OM. Aluminum and Fe phases interacted with each other. At high [Fe+Al], Fe(III)-oligomers and Al monomers/oligomers polymerized which increase the size and quantity of Fh-like Np and amorphous Al hydroxides resulting in a large settling aggregates. The Al impact on the Fe-OM aggregates structure could also impact the fate of pollutants. The occurence of Al amorphous hydroxides and the increase of Fh-like Nps, which were demonstrated to exhibit higher sorption capacity than Fe(III)-oligomers, lead to the expansion of surface reactive sites availability and subsequently to the increase of Fe-OM aggregates sorption capacity.

II.2.1. Introduction

It is now widely recognized that heterogeneous colloids and nano-aggregates control the biogeochemical cycle of many organic and inorganic contaminants (Wigginton et al., 2007). Among them, iron-organic matter (Fe-OM) aggregates were intensively studied in the last decade (Pokrovsky et Schott, 2002; Pédrot et al., 2008; Pédrot et al., 2011; Stolpe et al., 2013; ThomasArrigo et al., 2014; Guénet et al., 2017; Beauvois et al., 2020b). The majority of these studies were focused on the structure and notably the physical interactions in between Fe phases and OM macromolecules or colloids. Recently, Beauvois et al., (2020b) demonstrated that the structure of the overall Fe-OM aggregate is strongly influenced by the presence of calcium (Ca). Calcium drives a structural transition from a Fe-OM colloidal aggregate to a Ca-branched micrometric network. By acting as a Fe competitor, the presence of Ca decreases the recovery of Fe phases by OM and indirectly involves the formation of ferrihydrite-like nanoparticles (Fh-like Np) rather than Fe(III)-oligomers. However, in environmental systems, Ca is not the only one major ion. Among them, aluminum (Al) is also of particular interest regarding its high concentration (Klöppel et al., 1997; Dia et al., 2000; Pokrovsky et al., 2005; Tipping, 2005; Ščančar et Milačič, 2006) and the control that it might exert on the Fe-OM aggregates structure. Aluminum is known indeed to have high affinity for natural OM (Lippold et al., 2005; Tipping, 2005; Marsac et al., 2012; Adusei-Gyamfi et al., 2019). Several studies demonstrated that the interaction between Al and OM impacts the Al speciation (Hu et al., 2008; Hay et Myneni, 2010; Xu et al., 2010; Hagvall et al., 2015). Organic matter limits the crystallinity of Al-hydroxides, and even prevent the Al monomers polymerization for high OM/Al ratios (Hay et Myneni, 2010; Hagvall et al., 2015). Moreover, Hagvall et al. (2015) provided evidence of the formation of mononuclear Al chelate with OM via its carboxylic sites. Aluminum is also known to strongly interact with Fe since Al can be incorporated in the Fe (hydr)oxides structure such as in lepidocrocite for Al/Fe molar ratio up to 0.1 (Kim et al., 2015) and goethite (Hazemann et al., 1991) or ferrihydrite (Hansel et al., 2011; Cismasu et al., 2012; Adra et al., 2013) for Al/Fe molar ratio

up to 0.3-0.4. Aluminum occurrence could therefore strongly control the Fe-OM aggregates structure and behavior by forming natural mixed Fe-Al-OM aggregates (Pokrovsky et al., 2005). Nierop et al. (2002) observed that, even though Fe binds the OM much strongly than the Al, the latter is still bound to OM. Even more, they reported that at low (Fe+Al)/organic carbon ratios, Al controlled the precipitation since it corresponded, in their study, to conditions in which Al concentration was higher than the one of Fe(III).

In such context, the aim of the present study is to investigate the control that Al could exert on the Fe-OM nano-aggregates structure. For this purpose, Fe-Al-OM aggregates were synthesized at various Fe/OC and Al/Fe molar ratios as well as Al substituted Fh and Al-OM associations, which were deeply characterized to be used as references. Aluminum interactions with Fe phases and OM were probed by X-ray absorption near edge structure (XANES) at the Al K-edge. To achieve the overview on the Al impact on Fe structural organization, Fe speciation within the Fe-Al-OM aggregates was studied performing Fe K-edge extended X-ray absorption fine structure (EXAFS). The arrangement of Fh-like nanoparticles within the aggregates was investigated carrying out small-angle X-ray scattering (SAXS) experiments.

II.2.2. Experimental method

II.2.2.1. Sample syntheses and elemental composition

II.2.2.1.a. Synthesis of Fe-OM-Al aggregates

Samples (Figure II.2-1) were synthesized at 3 Fe/OC molar ratios (i.e. 0.02, 0.05 and 0.08) and at 4 Al/Fe molar ratios (i.e. 0, 0.1, 0.5 and 1) following the procedure described by Guénet et al. (2017). Samples were labelled Fe*yy*-Al*xx*, where Fe*yy* and Al*xx* represented the Fe/OC and the Al/Fe ratios, respectively. Leonardite humic acid (LHA) (International Humic Substances Society) with the elemental composition C = 63.81%, O = 31.27%, H = 3.70% and N = 1.23% (as a mass fraction) was used as an OM model. A 1.8×10^{-2} mol L^{-1} Fe^{2+} stock solution was prepared with $FeCl_2.4H_2O$ (Sigma Aldrich). From this solution, 3 Fe^{2+}-

Al^{3+} stock solutions were prepared at [Al] = 1.8×10^{-3} mol L^{-1}, 8.9×10^{-3} mol L^{-1} and 1.8×10^{-2} mol L^{-1} with $AlCl_3$ (Sigma Aldrich). Aggregates (Fe-OM-Al) were synthesized by the titration of a LHA suspension at [OC] = 1.00×10^{-1} mol L^{-1} with a Fe^{2+}-Al^{3+} solution at 0.05 mL min^{-1} in 5×10^{-3} mol L^{-1} of NaCl using an automated titrator (Titrino 794, Metrohm). The pH was kept constant at 6.5 with a 0.1 mol L^{-1} NaOH solution using a second titrator (Titrino 794, Metrohm) at a set pH mode. The accuracy of the pH measurement was ± 0.04 pH units.

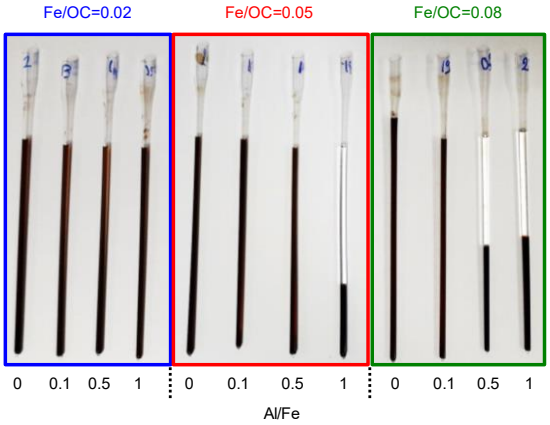

Figure II.2-1 – Fe-OM-Al aggregates after they stayed vertically into capillaries for SAXS measurements.

II.2.2.1.b. Synthesis of references

Ferrihydrite (Fh) and amorphous Al hydroxide (am-Al-hydrox) were synthesized from an Fe^{3+} and Al^{3+} stock solution by dissolving $Fe(NO_3)_3.9H_2O$ and $Al(NO_3)_3.9H_2O$ (Sigma Aldrich), respectively. Al-substituted ferrihydrite (Al-Fh) samples were synthesized from Fe^{3+}-Al^{3+} stock solutions prepared by dissolving $Fe(NO_3)_3.9H_2O$ and $Al(NO_3)_3.9H_2O$ to obtain Al/Fe molar ratios of 0.01, 0.05, 0.1, 0.2, 0.3 and 0.4. Samples were labelled Al-Fh*xx* were *xx* represents the Al/Fe ratio. Pure Fh, am-Al-hydrox and Al-Fh were synthesized following the procedure described by Schwertmann et Cornell (2000). They were prepared by setting rapidly the pH at 7 (to ensure a monophasic formation) with a 1 mol L^{-1} KOH solution using a Mettler Toledo SevenEasy TM pH-meter, under continuous stirring (at 250 rpm). After 24h, to ensure the pH is stable, the suspensions were centrifuged at 8872 g and washed 3 times with Milli-Q water. The precipitates were dried and shredded at room temperature.

The Al-OM aggregates were synthesized by dissolving $AlCl_3$ powder in a LHA suspension at pH = 6.5 with [OC] = 5.8×10^{-2} mol L^{-1} to reach Al/OC molar ratios of 0.0003, 0.002 and 0.086. For Al/OC = 0.0003, the Al concentration of 2.00×10^{-5} mol L^{-1} was calculated with the visual Minteq software to avoid Al precipitation The ratios Al/OC = 0.002 and 0.086 were chosen as they corresponded to the Al/OC ratios within Fe0.02-Al1.0 and Fe0.08-Al1.0, respectively. The samples were labelled Al-OM0.0003, Al-OM0.002 and Al-OM0.086 for Al/OC = 0.0003, 0.002 and 0.086, respectively. The suspensions were stirred for 24h to ensure a stable pH = 6.5. The expected concentrations and molar ratios of all the samples and references are summarized in Table II.2-1.

Table II.2-1 – Initial concentrations and molar ratios of all synthesized samples

	Sample name	Concentrations (mmol L^{-1})			Ratios (mol/mol)		
		OC	Fe	Al	Fe/OC	Al/Fe	Al/OC
Fe-OM-Al aggregates	Fe0.02-Al0.0	60.5	1.30	-	0.02	0.0	0.000
	Fe0.02-Al0.1	60.5	1.30	0.13	0.02	0.1	0.002
	Fe0.02-Al0.5	60.5	1.30	0.65	0.02	0.5	0.011
	Fe0.02-Al1.0	60.5	1.30	1.30	0.02	1.0	0.021
	Fe0.05-Al0.0	60.5	3.18	-	0.05	0.0	0.000
	Fe0.05-Al0.1	60.5	3.18	0.32	0.05	0.1	0.005
	Fe0.05-Al0.5	60.5	3.18	1.59	0.05	0.5	0.027
	Fe0.05-Al1.0	60.5	3.18	3.19	0.05	1.0	0.054
	Fe0.08-Al0.0	60.5	4.49	-	0.08	0.0	0.000
	Fe0.08-Al0.1	60.5	4.49	0.45	0.08	0.1	0.005
	Fe0.08-Al0.5	60.5	4.49	2.25	0.08	0.5	0.043
	Fe0.08-Al1.0	60.5	4.49	4.50	0.08	1.0	0.086
References	Fh	-	200	-	-	-	-
	am-Al-hydrox	-	-	200	-	-	-
	Al-Fh0.01	-	196	2	-	0.01	-
	Al-Fh0.08	-	189	9	-	0.05	-
	Al-Fh0.1	-	181	18	-	0.1	-
	Al-Fh0.2	-	167	33	-	0.2	-
	Al-Fh0.3	-	155	46	-	0.3	-
	Al-Fh0.4	-	144	58	-	0.4	-
	Al-OM0.0003	57.8	-	0.02	-	-	0.0003
	Al-OM0.002	57.6	-	0.12	-	-	0.002
	Al-OM0.086	58.0	-	4.88	-	-	0.086

II.2.2.1.c. Chemical composition of the Al substituted Fh

Aluminum content in Al-Fh samples was measured collecting the X-ray fluorescence (XRF) signal of the samples on the LUCIA beamline (Flank et al., 2006; Vantelon et al., 2016) at the SOLEIL synchrotron (Saint-Aubin, France). For this purpose the monochromator of the beamline was equipped with KTP crystals. The energy was set to 1800 eV and the XRF spectra collection time was set to 1 minute. Detection was performed with a 60 mm² mono-element silicon drift diode detector (Bruker). The Al-Fh powders were crushed on an indium foil and fixed on a copper plate for measurements. The area of the Al Kα emission peak (occurring at 1486 eV) is proportional to the [Al]. They were thus fitted using the KaleidaGraph software with the Levanberg-Marquardt algorithm.

II.2.2.2. Structural characterization

II.2.2.2.a. XRD measurements

The X-ray measurements (XRD) experiments on Al-Fh and am-Al-hydrox were performed on the MORPHEUS platform (Laboratoire de Physique des Solides, Université Paris-Sud, Orsay) on a rotating anode generator (Rigaku HU3R, Japan) with molybdenum radiation (λ_{Mo} Kα = 0.711 Å) delivered by a multilayer W/Si mirror optics (Xenocs FOX 2D Mo 25-INF). The samples were held in borosilicate capillary tubes (0.7 mm, WJMGlas/Müller GmbH, DE) and then placed in an evacuated chamber (primary vacuum), allowing a high signal over background ratio, beneficial for measuring weak XRD signals. Two-dimensional XRD diagrams were recorded by an X-ray-sensitive plate detector (MAR345, pixel size = 150 µm) placed after the exit window of the chamber with a sample-to-detector distance of 310 mm. The curves of scattered intensity I as a function of the scattering vector modulus Q ($Q=4\pi/\lambda_{Mo}.\sin(\theta_{Mo})$ with 2θ the scattering angle) were obtained from the azimuthal angular integration of the scattering patterns using homemade software. A gibbsite XRD pattern was measured for reference in reflection mode with a D2-phaser diffractometer (Bruker) with a Cu X-ray source (λ_{Cu} Kα = 1.54 Å) using the Bragg-Brentano geometry. The gibbsite powder was flattened on the sample-holder to present a smooth surface. The pattern was recorded over

the range 10-75° by step of 0.02° with 1s counting time. To compare all the XRD patterns, the Q range was converted into a θ_{Cu} scattered angle.

II.2.2.2.b. XAS data acquisition and analysis

The Fe K-edge X-ray absorption spectroscopy (XAS) experiments for Al-Fh samples were carried out on the LUCIA beamline (Flank et al., 2006; Vantelon et al., 2016) at the SOLEIL synchrotron. The powders were pressed into a 6 mm pellet mixed with cellulose (Merck) prior XAS measurements. The X-ray absorption near edge structure (XANES) spectra were collected by steps of 2 eV below the edge, 0.1 eV in the edge region and of 1 eV behind the edge, with a counting time of 3 s per point using a monochromator equipped with a pair of Si(311) crystals. The extended X-ray absorption fine structure (EXAFS) spectra were collected by steps of 2 eV below the edge, 0.2 eV in the edge region and increasing from 1 to 4 eV behind the edge, with a counting time of 5 s per point using a monochromator equipped with a pair of Si(111) crystal. In both cases, the data were collected at room temperature, under primary vacuum (10^{-2} mbar), in transmission using a Si diode detector. For Fe-OM-Al aggregates, the samples were freeze dried (Freeze dryer Alpha 1-2 LD plus, Christ) prior being pressed into 6 mm pellet mixed with cellulose. The Fe-OM-Al aggregates XAS measurements at the Fe K-edge were performed on the ROCK beamline (Briois et al., 2016) at the SOLEIL synchrotron using a Si(111) channel-cut monochromator. The spectra were recorded at room temperature in transmission using ionization chambers (Ohyo Koken) filled with N_2. A Fe foil located between the 2nd and the 3rd ionization chamber was measured along with the samples to calibrate the energy. For all XAS at Fe K-edge experiments, the energy was calibrated by setting the maximum of the first XAS spectrum derivate of a Fe foil to 7112 eV. For Al K-edge XANES measurements, the powders of Al-Fh and Fe-OM-Al aggregates were crushed on an indium foil and fixed on a copper plate. The spectra were recorded on the LUCIA beamline (Flank et al., 2006; Vantelon et al., 2016) at the SOLEIL synchrotron using a KTP(011) double-crystal monochromator. The energy was calibrated by setting the first inflexion point of the Al K-edge of an aluminum foil at 1559 eV. Spectra were

collected by steps of 2 eV below the edge, 0.2 eV in the edge region and 1 eV behind the edge, with a counting time of 15 to 30 s per point depending on Al content. The measurements were performed at room temperature under primary vacuum (10^{-2} mbar) in fluorescence mode using a 60 mm² mono-element silicon drift diode detector (Bruker) and corrected for the detector dead time.

All XAS data processing were performed with the Athena software including the Autbk algorithm (Rbkb = 1, k-weight = 3) (Ravel et Newville, 2005). The Fe spectra were normalized by fitting the pre-edge region with a linear function and the post-edge region with a quadratic polynomial function. The Fourier transforms of the k^3-weighted EXAFS spectra were calculated over a range of 2-11 $Å^{-1}$ for data from LUCIA and 2-12.5 $Å^{-1}$ for data from ROCK using a Hanning apodization window (window parameter = 1). The EXAFS data were analyzed by linear combination fitting (LCF) available in the Athena software on the range 3-12.5 $Å^{-1}$; all component weights were forced to be positive. The references used were Fh, Lp and three pure components extracted from the *in situ* synthesis of Fe-OM aggregates by Vantelon et al. (2019), i.e. Fe(II), Fe(III)-oligomers (a combinations of oligomers of different size, including monomers) and Fh-like nanoparticles (Fh-Nps). The best LCF fit was determined for the minimum *n*-components for which the R-factor was better than 10% of the fit with *n+1* components. As without any constraint the total LCF weight for each sample was between 0.95 and 1.05, it was arbitrarily fixed to 1 to facilitate comparisons between each sample. The EXAFS data were also simulated over the 1.15-4.1 Å range using the Artemis interface (Ravel et Newville, 2005) to IFEFFIT with least-squares refinements. The theoretical paths used for fitting were calculated from a goethite structure (Hazemann et al., 1991) with the FEFF6 algorithm (Rehr et al., 1992; Newville, 2001) from the Artemis software.

The Al data were corrected for self-absorption based on the theoretical chemical formula of the mineral phases contained in the samples and by applying the procedure provided in the Athena software. For better clarity of the plots, data were slightly smoothed using the iterative smoothing procedure of the Athena software, setting the number of

iterations to 1. A synthetic gibbsite was used as a reference for Al K-edge experiments processing.

II.2.2.2.c. SAXS measurements

Small angle X-ray scattering (SAXS) were recorded on the SWING beamline at the SOLEIL synchrotron. Two sample-to-detector distances (1 and 6 m) were used with a wavelength of 1.03 Å to reach a q range of 2.0×10^{-3}-0.7 $Å^{-1}$. The measurements were carried out on the suspension or in the precipitate for the settled samples (Figure II.2-1).

The SAXS curves were analyzed using a cluster fractal model (Guénet et al., 2017; Beauvois et al., 2020b). According to this model, the scattered intensity I(q) of centrosymmetric nanoparticles dispersed in a continuous solvent is described by eq II.2-1:

$$I(q)=\varphi.V.\Delta\rho^2.P(q).S(q) \quad \text{(eq. II.2-1)}$$

where φ is the volume fraction, V is the volume of the scattered entities, $\Delta\rho^2$ is the contrast term, P(q) and S(q) are the form and the structure factor, respectively. The model was built with the hypothesis that the particulate Fe is organized as spherical poly-dispersed primary beads (Fe-PB) aggregated into a Fe primary aggregate (Fe-PA). The Fe-PA are described by a form factor according to a finite number of Fe-PB and a fractal dimension and can be aggregated as a Fe secondary aggregate (Fe-SA).

II.2.3. Results

II.2.3.1. Chemical composition of Al substituted Fh

The XRF spectra obtained for Al-Fh samples were plotted in Figure II.2-2. With the hypothesis that Al-Fh0.01 contained 1% of Al and knowing its XRF peak area, this sample was used as a reference to calculate the theoretical XRF peak areas for the others Al-Fh samples (Table II.2-2). The deviation between the experimental and theoretical peaks areas allowed calculating the experimental Al/Fe ratio. Taking into account experimental errors, the Al/Fe ratio within Al-Fh samples was found to be identical to the experimental ratio.

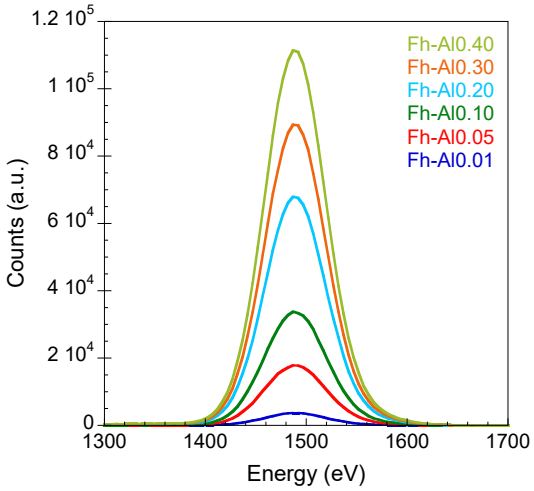

Figure II.2-2 – XRF spectra of the Al Kα line for the Fh-Al samples.

Table II.2-2 – Initial and experimental Al/Fe ratio. The latter being calculated according to the deviation between the experimental and theoretical Al Kα XRF peak area.

Sample	Initial Al/Fe	Experimental peak area	Theoretical peak area	Experimental Al/Fe
Al-Fh0.01	0.01	288	288	0.01
Al-Fh0.05	0.05	1395	1439	0.05
Al-Fh0.10	0.10	2643	2796	0.09
Al-Fh0.20	0.20	5306	5139	0.21
Al-Fh0.30	0.30	6979	7154	0.29
Al-Fh0.40	0.40	8688	8922	0.39

II.2.3.2. Structural characterisation of Al substituted ferrihydrites

The XRD pattern of am-Al-hydrox exhibited broad peaks centered at 18.2, 20.4, 36.5, 37.6 64.7°2θ and a larger one occurring between 43 and 52°2θ (Figure II.2-3). All the peaks position were in agreement with peaks position of gibbsite XRD pattern. However, the peaks of am-Al-hydrox were less resolved than for gibbsite: the protocol of Schwertmann and Cornell (2000) applied to aluminum therefore led to the formation of amorphous pseudo-gibbsite. The XRD patterns of Fh exhibited two broad peaks centered at 34°2θ and 61°2θ that are relevant of 2-lines Fh (Ekstrom et al., 2010; Hansel et al., 2011; Cismasu et al., 2012; Adra et al., 2013; Wang et al., 2013) as expected with the protocol of Schwertmann and Cornell (2000). The d spacing values of these characteristic peaks and the corresponding diffraction grille (hkl) were 0.250 nm (110) and 0.151 nm (115) (Wang et al.,

2013). Ferrihydrite is known to be able to incorporate Al until Al/Fe = 0.3-0.4 molar ratio (Hansel et al., 2011; Cismasu et al., 2012; Adra et al., 2013). As a consequence, the XRD patterns of Al-Fh samples displayed the two same broad peaks as the Fh. For Al/Fe ≥ 0.2, the first peak was lightly shifted, from 34°2θ to 33.2°2θ, revealing changes in the unit cell due to the incorporation of Al into the structure. None of the peaks displayed by the am-Al-hydrox XRD pattern was visible for the Al-Fh suggesting that no additional phase than Al-Fh was formed. These results are in agreement with Cismasu et al. (2012) and Adra et al. (2013).

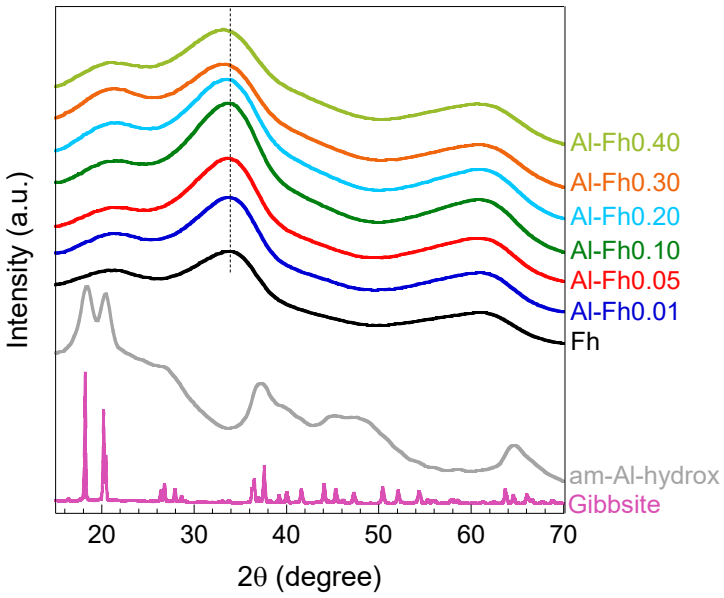

Figure II.2-3 – XRD patterns of am-Al-hydrox and the Al-substituted ferrihydrites, collected with a Mo (λ = 0.711 Å) rotating anode generator.

II.2.3.3. Modification of Fh structure with Al substitution

The XANES spectra at the Fe K-edge were typical of Fh and Al-substituted Fh (Hofmann et al., 2013) (Figure II.2-4a). The shape and the related intensity of the edge position at 7127 eV as well as the pre-edge position at 7114.5 eV are relevant of Fe(III) in an octahedral environment (Wilke et al., 2001). No change in the XANES was observable for low Al/Fe ratio while for Al/Fe = 0.4, Al induced modification in the white line intensity suggesting that Al impacted the local symmetry around Fe, improving the ordering of the O atoms distribution around Fe.

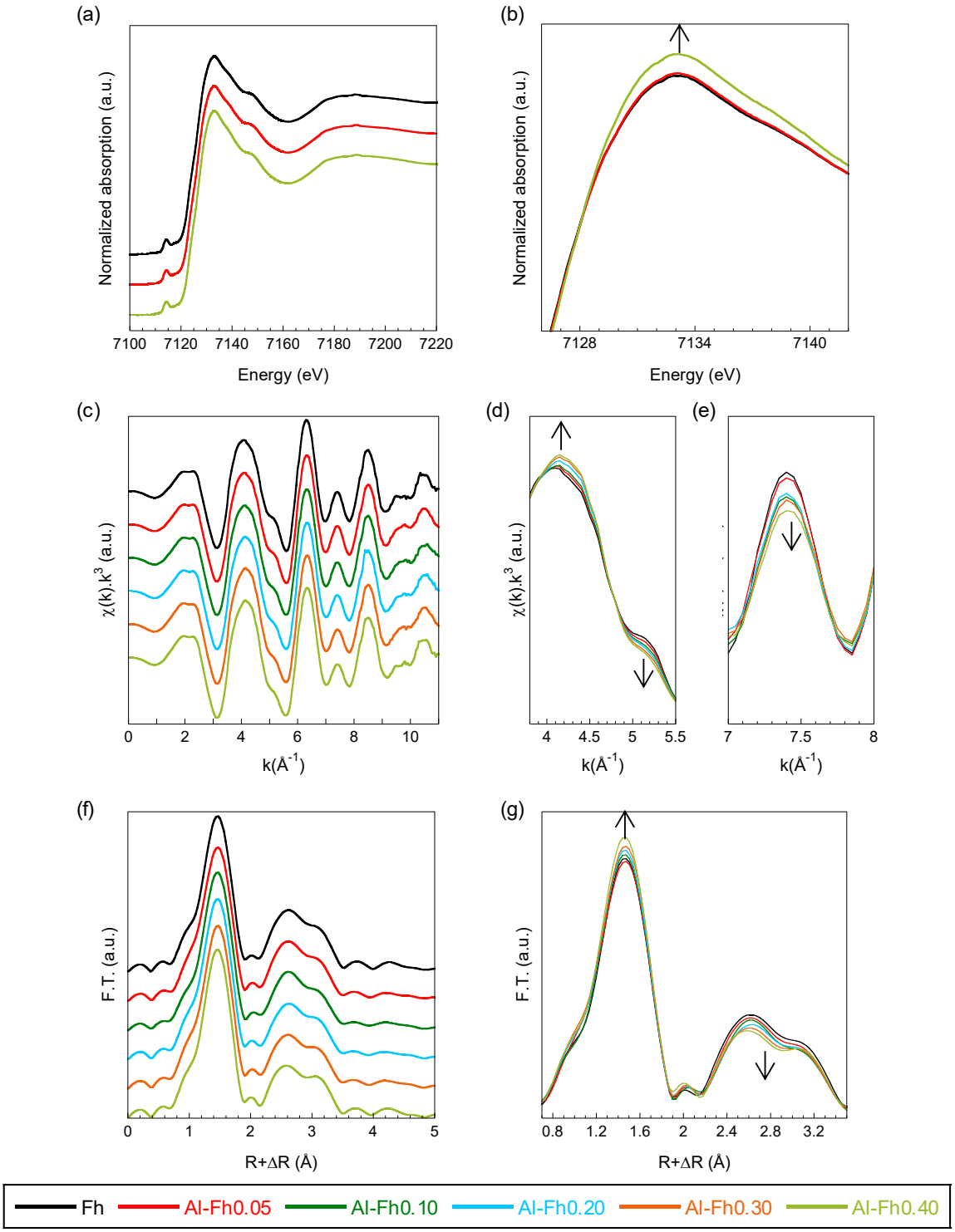

Figure II.2-4 – (a) Fe K-edge XANES spectra of Fh and Al-Fh samples, in (b) is represented a zoom of the superimposed Fe K-edge XANES white line centered ~ 7134 eV. (c) Fe K-edge EXAFS signal of Fh and Al-Fh samples, in (d) and (e) are represented a zoom of the superimposed Fe K-edge EXAFS signal in the range of 3.8-5.5 $Å^{-1}$ and 7-8 $Å^{-1}$ respectively. (f) Magnitude of the Fourier transform of Fh and Al-Fh, in (g) is represented a zoom of the superimposed Fourier transform in the range 0.7-3.5 Å. The black arrows highlight the behavior of the spectra and pseudo-radial distributions with the increasing Al/Fe ratio.

The EXAFS spectra at the Fe K-edge exhibited similar oscillations than those reported for Fh and Al-substituted Fh (Adra et al., 2013; Hofmann et al., 2013) (Figure II.2-4c). Some variations can be observed relative to the Al content, indicating slight differences in the local environment of Fe. In particular, the amplitude of the oscillation at 4.2 $Å^{-1}$ increased with the increasing Al/Fe ratio (Figure II.2-4d). The shoulder at 5 $Å^{-1}$, which is well defined for pure Fh, was smoothed with the increasing Al/Fe ratio (Figure II.2-4d). The same feature was obtained at 7.5 $Å^{-1}$ which amplitude decreased with the increasing Al/Fe ratio (Figure II.2-4e). The corresponding pseudo radial distribution function from Fourier transform reported a peak at ~ 1.5 Å which can be assigned to the first coordination sphere, i.e. O atoms (Figure II.2-4f). This peak appeared to be sharpened with the increasing Al/Fe ratio suggesting an improved ordering of the O atoms around Fe. This is consistent with the XANES observations (Figure II.2-4a). The second peak, standing between 2.2 and 3.4 Å, was assigned to the second neighbor shells i.e. Fe, Al and O atoms. Its intensity decreased with the increasing Al/Fe ratio (Figure II.2-4g). Two explanations can be proposed: (i) Al exhibits a lower electronic density than Fe, thus it is a weaker backscatterer element than Fe, (ii) backscattering signals provided by Al and Fe located at the same distance are in phase opposition and results in a cancel of each contribution (Figure II.2-5). The decrease of the intensity of the pseudo-radial distribution second peak is therefore related to the incorporation of Al in the Fh structure.

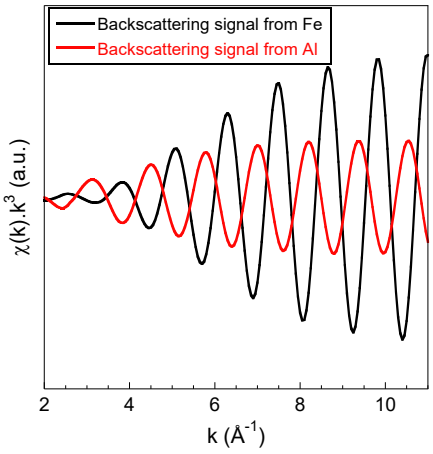

Figure II.2-5 – Backscattering Fe K-edge EXAFS signal provided by a Fe atom (black) and an Al atom (red) at the same distance (3.02 Å) from the absorbing Fe.

II.2.3.4. Aluminum speciation within Al substituted ferrihydrites

The Al K-edge XANES spectra were representative of Al in an octahedral symmetry (Ildefonse et al., 1998; Cismasu et al., 2012; Hofmann et al., 2013) (Figure II.2-6a). The Al-Fh samples exhibited a pre-edge at 1562 eV and a shoulder in the edge by contrast with the samples without Fe. For all the samples, the white line arose at ~ 1571 eV (peak A) with a shoulder occurring at ~ 1568 eV (peak B). According to Ducher et al. (2016), the pre-edge can be assigned to Fe as second neighbors around the absorbing Al atoms. The pre-edge decrease with the increasing Al/Fe ratio (Figure II.2-6b) provided evidence of the formation of Al clusters incorporated in the Fh structure, as the more Al is substituted, the less it has Fe neighbors. These results are in agreement with Cismasu et al. (2012) NMR based observations. In the meantime, the intensity of the shoulder in the edge increased with the increasing Al content. This can be due to the substitution of the tetrahedrally coordinated Fe occurring in the Fh structure as proposed by Michel et al. (2007). Finally, the white line intensity (peak A) tended to decrease as compared to the shoulder intensity (peak B) with the increasing Al/Fe ratio (Figure II.2-6c). This decrease can be related to either the average decrease of the distance between the absorbing Al atom and the first Al or Fe neighbors or the distortion of Al octahedral, or both (Ducher et al., 2016).

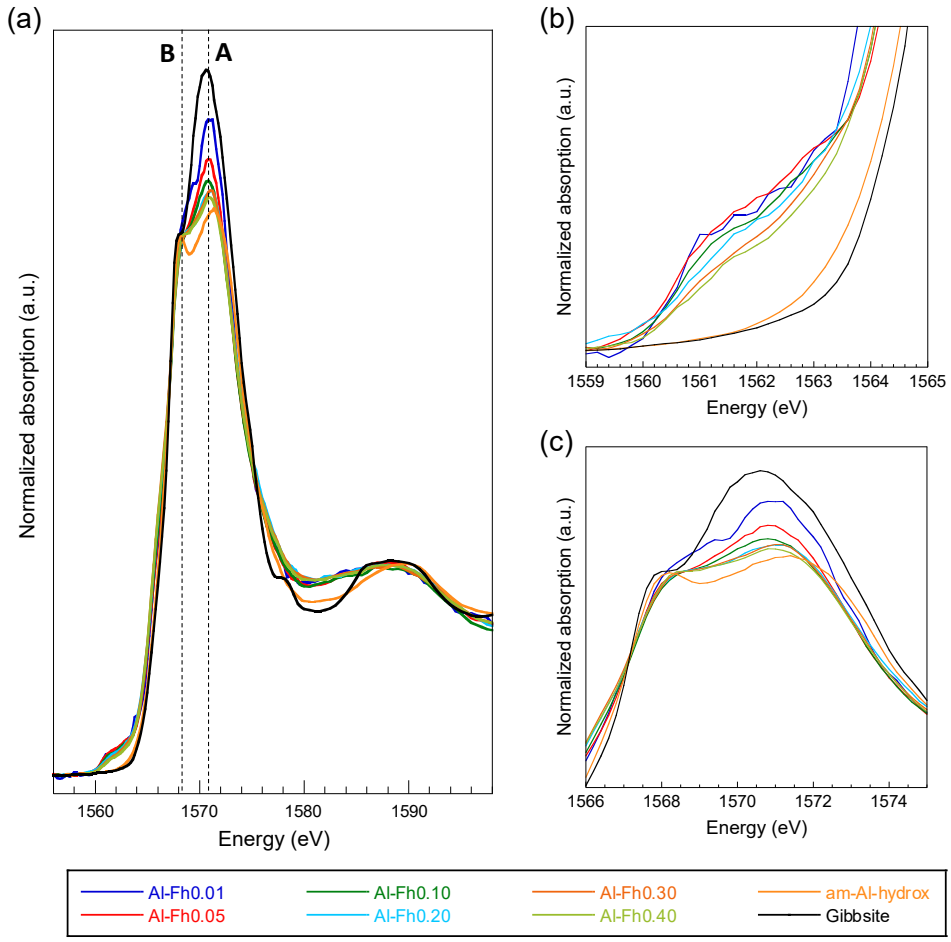

Figure II.2-6 – (a) Al K-edge XANES spectra of Al-Fh samples, am-Al-hydrox and gibbsite; in (b) and (c) is representing a zoom of the pre-edge in the range of 1559-1565 eV and the edge in the range of 1566-1574 eV, respectively.

II.2.3.5. Aluminum speciation within Al-OM aggregates

The Al K-edge XANES spectra of Al-OM aggregates exhibited a white line occurring at ~ 1570 eV which is representative of Al in octahedral symmetry (Ildefonse et al., 1998; Cismasu et al., 2012; Hofmann et al., 2013) (Figure II.2-7a). The Al-OM complex with Al/OC = 0.0003 and 0.002 displayed a white line centered at 1572 eV and at 1571.8 eV, respectively. For Al/OC = 0.086, the white line exhibited a main peak at 1569.9 eV and a shoulder at ~ 1572 eV. The XANES spectra of Al-OM aggregates were poorly structured as compared to the gibbsite and am-Al-hydrox suggesting no Al hydroxide precipitation and a low Al polymerization. However, the shoulder occurrence at 1572 eV at the higher Al/OC ratio provided evidence that the atomic environment around Al was more structured for Al/OC = 0.086 than for Al/OC = 0.0003 and 0.002, probably in response to the Al

polymerization. This was confirmed by the first XANES spectra derivative (Figure II.2-7b) for which the maximum was at 1568 eV for gibbsite and am-Al-hydrox, 1569.8 eV for Al-OM0.0003, 1568.8 eV for Al-OM0.002 and 1568.1 eV for Al-OM0.086. A shift of ~ 2 eV to the high energies occurred therefore from gibbsite and am-Al-hydrox to Al-OM0.0003. Hagvall et al. (2015) also reported an energy shift between gibbsite and Al-OM aggregates and free Al(III), the latter was measured at pH = 1.9 which ensured dispersed Al^{3+} monomers surrounded by 6 O. Considering these results, the affinity of Al for binging OM (Lippold et al., 2005; Tipping, 2005; Marsac et al., 2012) and given that the Al concentration in Al-OM0.0003 was selected to avoid Al precipitation, Al within Al-OM0.0003 can be considered as monomers bound to OM. With the increasing [Al] at pH = 6.5, the polymerization-condensation of Al was expected (Bi, 2004). This polymerization resulted in the shift of the edge to the lower energy as observed in Figure II.2-7b. The Al XANES edge energy therefore indicated the Al polymerization stage.

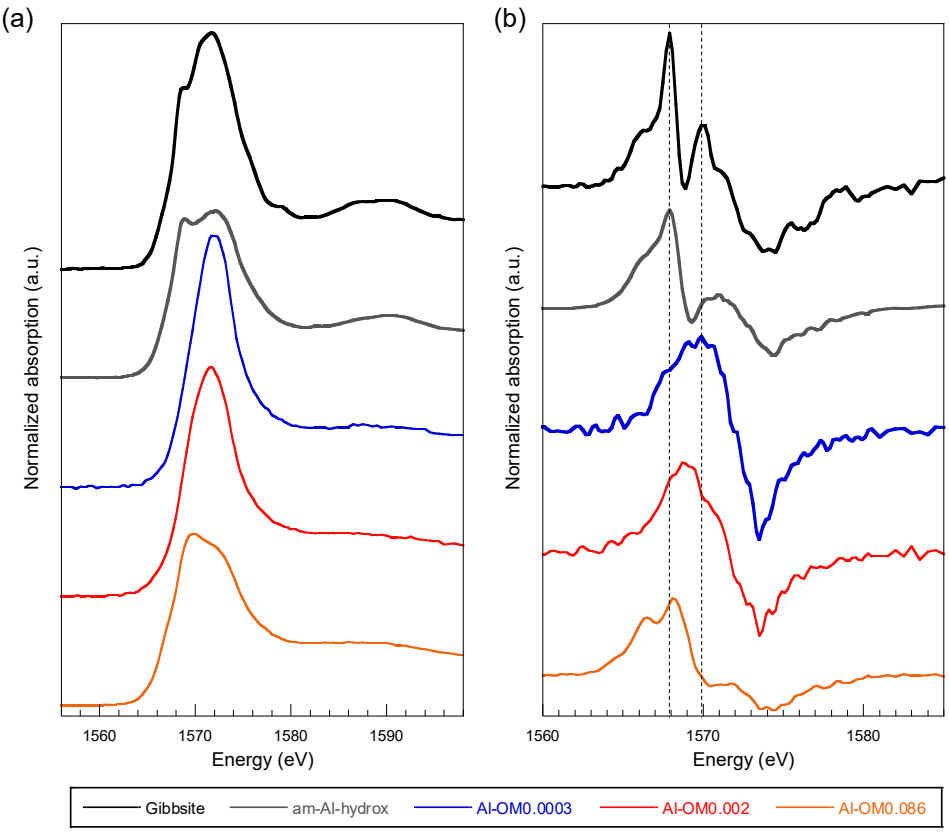

Figure II.2-7 – (a) Al K-edge XANES spectra and (b) corresponding first derivatives of gibbsite (black), am-Al-hydrox (grey) and Al-OM aggregates with Al/OC = 0.0003(bleu), 0.002 (red) and 0.086 (orange).

II.2.3.6. Aluminum interaction with Fe-OM aggregates

The white line of Fe-OM-Al aggregates Al K-edge XANES spectra was centered at ~ 1570 eV which is relevant of Al mainly in an octahedral geometry (Ildefonse et al., 1998; Cismasu et al., 2012; Hofmann et al., 2013) (Figure II.2-8a). Except for Fe0.02-Al0.1, all the Fe-Al-OM XANES spectra exhibited a pre-edge at ~ 1562 eV as observed for Al-Fh samples (Figure II.2-8b). The pre-edge occurrence is mainly due to the formation of Al-O-Fe bond (Ducher et al., 2016). However, the intensity of the pre-edge was weaker than those observe for Al-Fh, suggesting that less Al interacted with Fe. For each Fe/OC, the white line of samples with Al/Fe = 0.1 was sharpened as compared to higher Al/Fe ratio for which the white line was more spread out. With the increasing Al/OC ratio, the edge position as expressed by the maximum of the first XANES derivative (Figure II.2-8c, d and Table II.2-3) continuously shifted from 1568.8 eV for Fe0.02-Al0.1 until 1568.1 eV for Fe0.08-Al1.0. This result, in light of the results provided by Al-OM aggregates, demonstrated that Al within Fe-OM-Al aggregates is organized as monomers bound to OM which ones polymerized with the increasing [Al] to form amorphous hydroxides, partially interacting with Fe phases.

Table II.2-3 – Position of the maximum of the Al K-edge XANES first derivative.

Position of the edge		**Al/Fe**		
		0.1	**0.5**	**1**
Fe/OC	**0.02**	1568.8	1568.5	1568.3
	0.05	1568.3	1568.4	1568.2
	0.08	1568.2	1568.1	1568.1

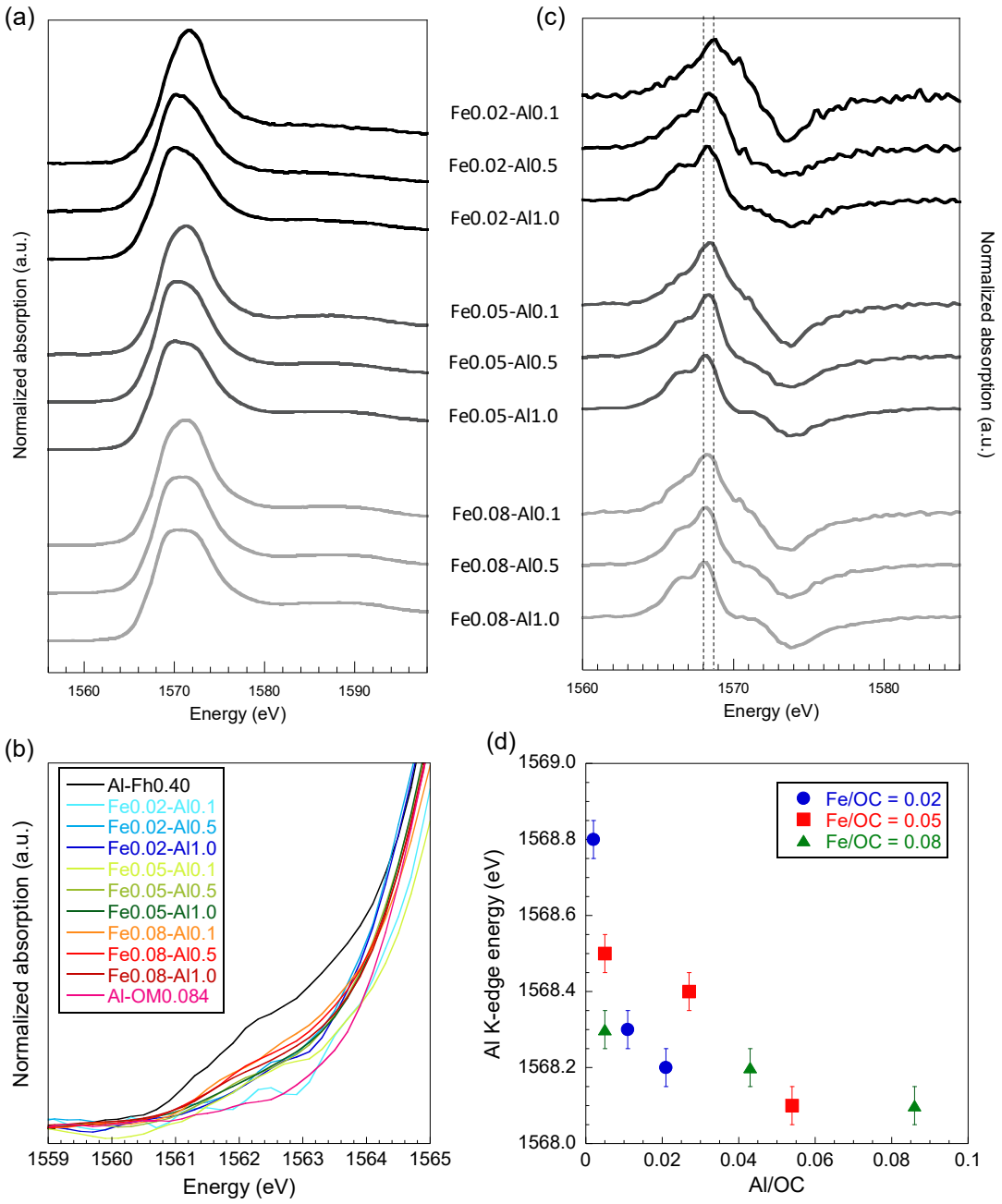

Figure II.2-8 – (a) Al K-edge XANES spectra, (b) zoom of the spectra in the pre-edge region between 1559 and 1565 eV, (c) first derivatives of the Fe-Al-OM aggregates spectra and (d) evolution of the edge position relative to Al/OC ratio for Fe/OC = 0.02 (blue circles), 0.05 (red squares) and 0.08 (green traingles).

II.2.3.7. Fe particles organization within Fe-OM-Al aggregates

The X-ray contrast only depends on the electronic density of the element which is substantially higher for Fe than for OM. Therefore, only the Fe part of Fe-OM-Al aggregates was characterized with the SAXS measurements (Figure II.2-9). In the high q domain, the scattered intensity corresponded to the Fe primary beads (Fe- PB) and can be modelled using a spherical form factor with a radius of 0.8 nm. All the SAXS curves exhibited a shoulder between 2×10^{-1} and 9×10^{-3} $Å^{-1}$ highlighting a typical sized Fe organization that corresponded to the Fe primary aggregates (PA) composed of Fe-PB. The shoulder moved to the low q values with the increasing Al/Fe ratio indicating an increase of the Fe-PA size. For Fe/OC = 0.02, the inflexion of the curve was stronger with Al than without Al while for Fe/OC ≥ 0.05, it was weaker for high Al than low Al contents. In low q domain, the increase of the scattered intensity was relevant of the Fe-PA aggregation as Fe secondary aggregates (Fe-SA) which size cannot be determined due to the limited q range covered by the analytical conditions. In the intermediate q domain, the SAXS curves were modelled with a spherical form factor describing the Fe-PA (Table II.2-4 and Figure II.2-10).

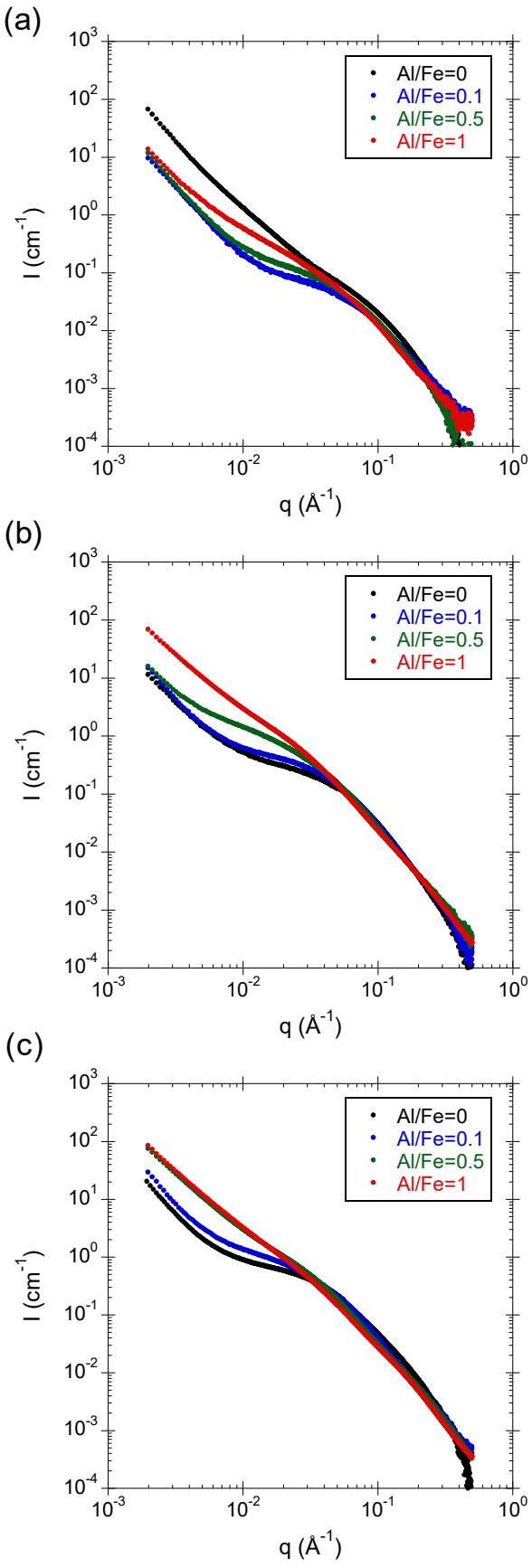

Figure II.2-9 – SAXS curves for samples with (a) Fe/OC = 0.02, (b) Fe/OC = 0.05 and (c) Fe/OC = 0.08.

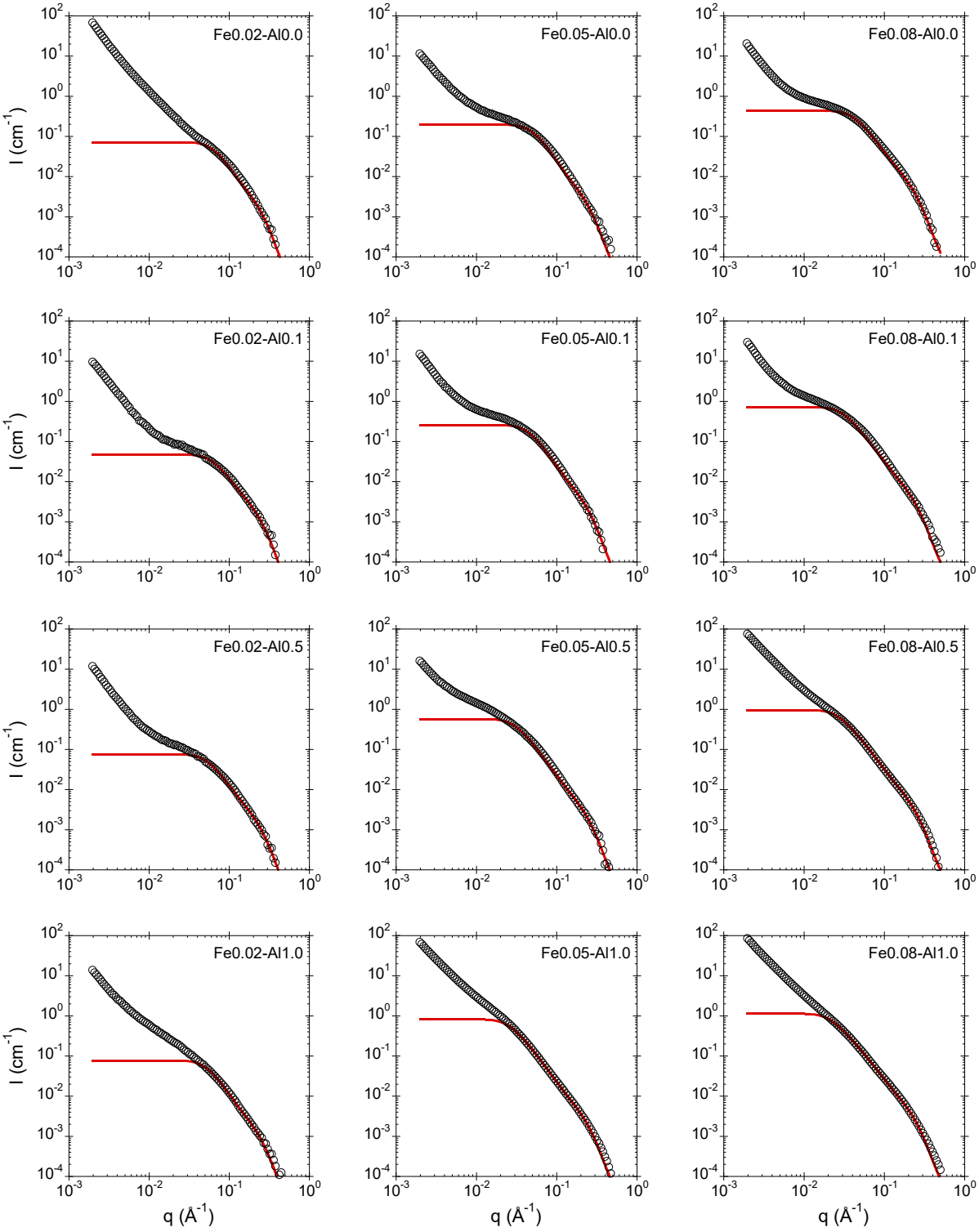

Figure II.2-10 – SAXS curves (black empty circles) and the modelled Fe-PA form factor (red line) for Fe-Al-OM aggregates.

Table II.2-4 – Fitting parameters used to simulate the form factor of the intermediate aggregates. Fixed parameters were the radius of the primary bead R_0=0.8 nm, the log normal distribution σ = 0.3 and the contrast $\Delta\rho^2 = 2.37\times10^{21}$ cm^{-4}. The errors on the parameters were 15%. (*) represent the parameters adjusted for fitting the curves and (**) represent the parameter calculated from parameter denoted (*).

Sample	φ_0 ($\times10^{-4}$)*	N_{PA}*	R_{PA} (nm)**	D_{fPA}*
Fe0.02-Al0.0	7.00	6.0	1.6	2.5
Fe0.02-Al0.1	5.50	5.0	1.7	2.2
Fe0.02-Al0.5	5.50	8.0	2.0	2.3
Fe0.02-Al1.0	4.50	10	2.0	2.5
Fe0.05-Al0.0	9.50	12	2.1	2.6
Fe0.05-Al0.1	10.0	15	2.4	2.5
Fe0.05-Al0.5	9.50	35	3.5	2.4
Fe0.05-Al1.0	9.50	50	4.1	2.4
Fe0.08-Al0.0	20.0	12	2.5	2.2
Fe0.08-Al0.1	14.0	30	3.5	2.3
Fe0.08-Al0.5	14.0	40	4.0	2.3
Fe0.08-Al1.0	12.0	55	4.7	2.2

The radius of the Fe-PA was calculated from the form factor (Figure II.2-11). The results demonstrated the increase of the Fe-PA size with the increasing Fe/OC ratio, as previously observed (Guénet et al., 2017; Beauvois et al., 2020b). Moreover, $R_{Fe\text{-}PA}$ increased with the increasing Al/Fe ratio. The Fe-PA fractal dimension remained, however, constant at 2.4 ± 0.2 irrespective of the Fe/OC neither the Al/Fe ratio highlighting the stable morphology of the Fe-PA.

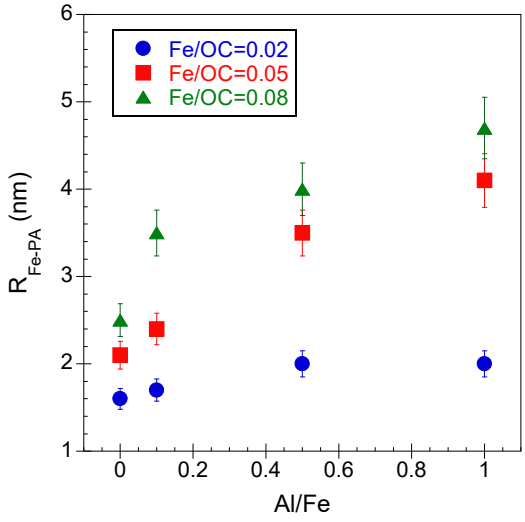

Figure II.2-11 – Evolution of the Fe-PA radius relative to the Al/Fe ratio for Fe/OC = 0.02 (blue circles), Fe/OC = 0.08 (red squares) and Fe/OC = 0.08 (green triangles).

Dividing the total scattered intensity by the form factor, the apparent total structure factor ($S_T(q)$) could be extracted (Figure II.2-12).

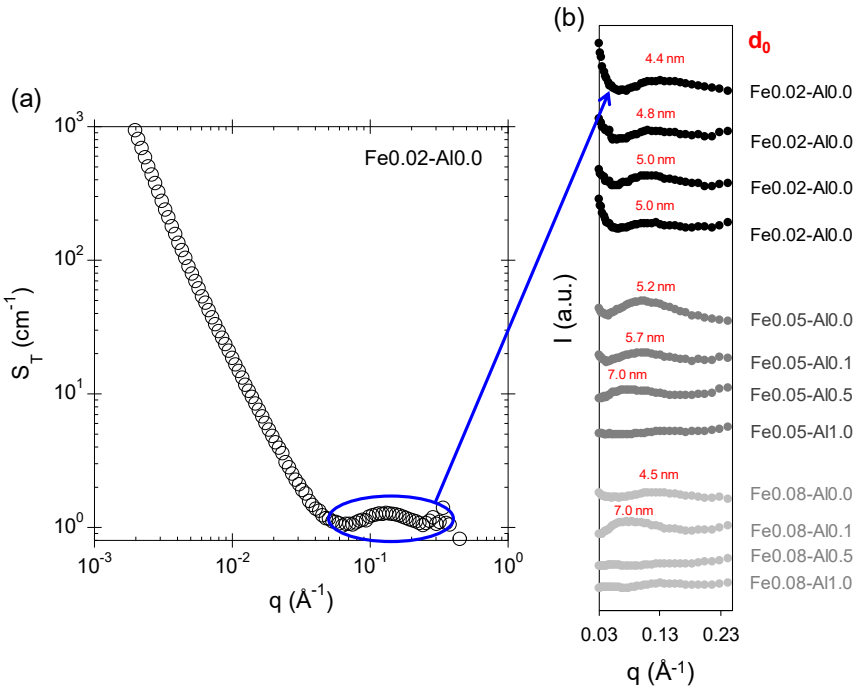

Figure II.2-12 – (a) Apparent total structure factor $S_T(q)$ for Fe0.02-Al0.0 and (b) evolution of the peak representing the interaction between Fe-PA.

The shoulder occurring at ~ 10^{-1} Å^{-1} was relevant of the interaction between the Fe-PA and its position allowed estimating the center-to-center distance d_0 between two Fe-PA (Table II.2-5). The distance d_0 increased with the increasing Fe/OC and Al/Fe ratios. For the 3 samples that settled (Figure II.2-1), corresponding to the higher Al contents, no shoulder was observable suggesting an increase in the value and/or in the polydispersity of the d_0 distance. Therefore, the increasing Al/Fe ratio led to the increase of the long range correlation between Fe-PA.

Table II.2-5 – Center-to-center distance d_0 between two Fe-PA. The symbol >> is reported when no shoulder was observable in $S_T(q)$ indicating high d_0 values.

d0 (nm)		**Al/Fe**			
		0.0	**0.1**	**0.5**	**1.0**
Fe/OC	**0.02**	4.4	4.8	5.0	5.0
	0.05	5.2	5.7	7.0	>>
	0.08	4.5	7.0	>>	>>

II.2.3.8. Fe speciation within Fe-OM-Al aggregates

The speciation of Fe within Fe-OM-Al aggregates was investigated by XAS at Fe K-edge. All the XANES spectra exhibited a white line at ~ 7128 eV and a shape that was representative of Fe(III) in an octahedral symmetry (Wilke et al., 2001) (Figure II.2-13).

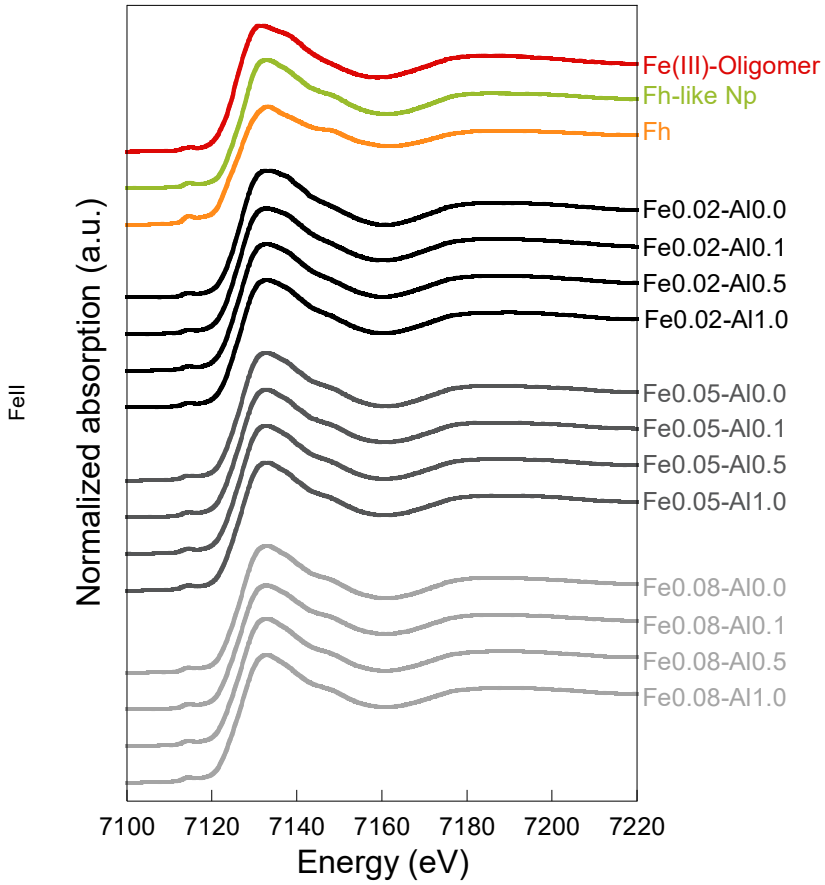

Figure II.2-13 – Fe K-edge XANES spectra for the references used for LCF and the samples.

All the EXAFS spectra exhibited a maximum of amplitude at the photoelectron wavevector, k, of ~ 6.3 $Å^{-1}$ (Figure II.2-14). The Fe(III)-oligomer damping shape was close to monotonous. The Fe(III)-Np, Fh and samples with Fe/OC ≥ 0.05 exhibited a shoulder at ~ 5.1 $Å^{-1}$ and a small oscillation at ~ 7.5 $Å^{-1}$. The samples with Fe/OC = 0.02 were less structured since only a small shoulder occurs at ~ 5.1 $Å^{-1}$.

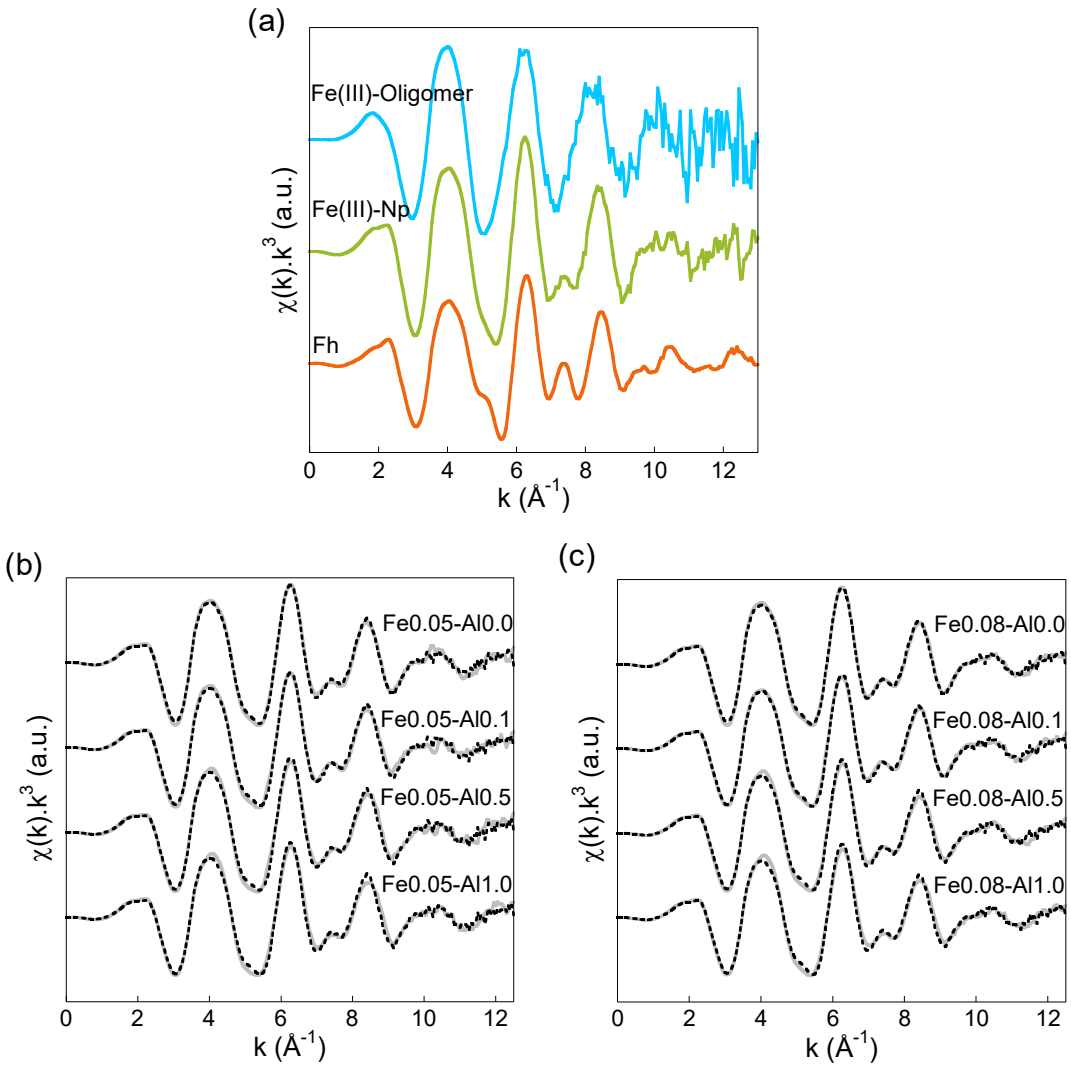

Figure II.2-14 – EXAFS spectra at the Fe K-edge for (a) the references used for performing LCF, (b) samples with Fe/OC = 0.05 and (c) Fe/OC = 0.08. In (b) and (c), the grey solid lines represent the experimental data and the black dotted lines represent the LCF results.

The EXAFS spectra of the samples were analyzed by LCF over the range of 3-12.5 $Å^{-1}$. In a recent study, Beauvois et al. (2020b) demonstrated that only Fe(III)-oligomers, Fe(III)-Np and Fh were necessary to well-reproduced the EXAFS signal of similar samples that contained Ca instead of Al. Therefore, the LCF were performed using the same 3 references (Figure II.2-14, Table II.2-6). The results demonstrated that the Fe(III)-oligomers amount decreased with the increasing Fe/OC ratio while it remained constant irrespective of the Al/Fe ratio. However, the Fh % increased with both the Fe/OC and Al/OC ratios.

Table II.2-6 – Fitting parameters obtained for the best LCF for samples with Fe/OC = 0.02, 0.05 and 0.08. The error on each components weight is estimated at ±10%.

Sample	Oligomer	Fh-like Np	Fh	R-factor (×10^{-3})
Fe0.02-Al0.0	0.30	0.70	0.00	26.1
Fe0.02-Al0.1	0.41	0.56	0.03	21.6
Fe0.02-Al0.5	0.37	0.52	0.11	17.9
Fe0.02-Al1.0	0.34	0.54	0.12	21.1
Fe0.05-Al0.0	0.19	0.58	0.24	11.9
Fe0.05-Al0.1	0.21	0.45	0.34	14.6
Fe0.05-Al0.5	0.24	0.44	0.32	19.5
Fe0.05-Al1.0	0.22	0.42	0.35	19.6
Fe0.08-Al0.0	0.15	0.55	0.30	7.1
Fe0.08-Al0.1	0.18	0.43	0.40	7.9
Fe0.08-Al0.5	0.18	0.39	0.43	13.0
Fe0.08-Al1.0	0.17	0.40	0.43	16.2

For the lowest Fe/OC ratio, the LCF results exhibited more structured EXAFS signals as compared to the experimental data. This was mainly visible at 7.5 Å^{-1}, where the shoulder of the LCF spectra was stronger than in the experimental EXAFS signal (Figure II.2-15), as previously observed.

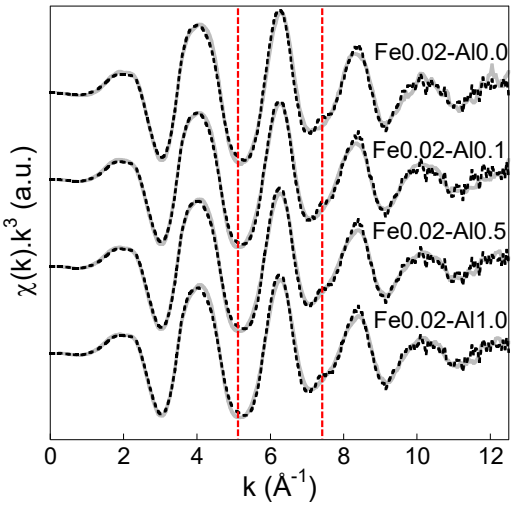

Figure II.2-15 – EXAFS spectra at the Fe K-edge for Fe/OC = 0.02. The grey solid lines represent the experimental data and the black dotted lines represent the LCF results

Beauvois et al. (2020a) demonstrated that the shoulder occurrence at 7.5 $Å^{-1}$ in the LCF EXAFS signal was a consequence of the use of an EXAFS signal provided by Fh-like Np larger than in the experimental sample. Here, the same method as Beauvois et al. (2020a) was therefore implemented to determine the percentage of Fe(III) phases within Fe-Al-OM aggregates. As a first step, for each Al/Fe ratio of the Fe/OC = 0.02 ratio, the EXAFS signal corresponding to the Fe(III)-oligomers % provided by LCF was subtracted to the raw data. The obtained EXAFS signals were then fitted (Figure II.2-16). The fit results returned a maximum of 1 Fe at ~ 3.03 Å against 1.3 for the Fh-like Np (Table II.2-7). This low number of neighbors suggested that Fe(III)-oligomers remained in the signal since this amount of neighbors was too low to be provided by particulate Fe. The operation was therefore repeated by increasing the percentage of subtracted Fe(III)-oligomers until the simulation of the residual EXAFS signal corresponded to that of a Fh-like Np.

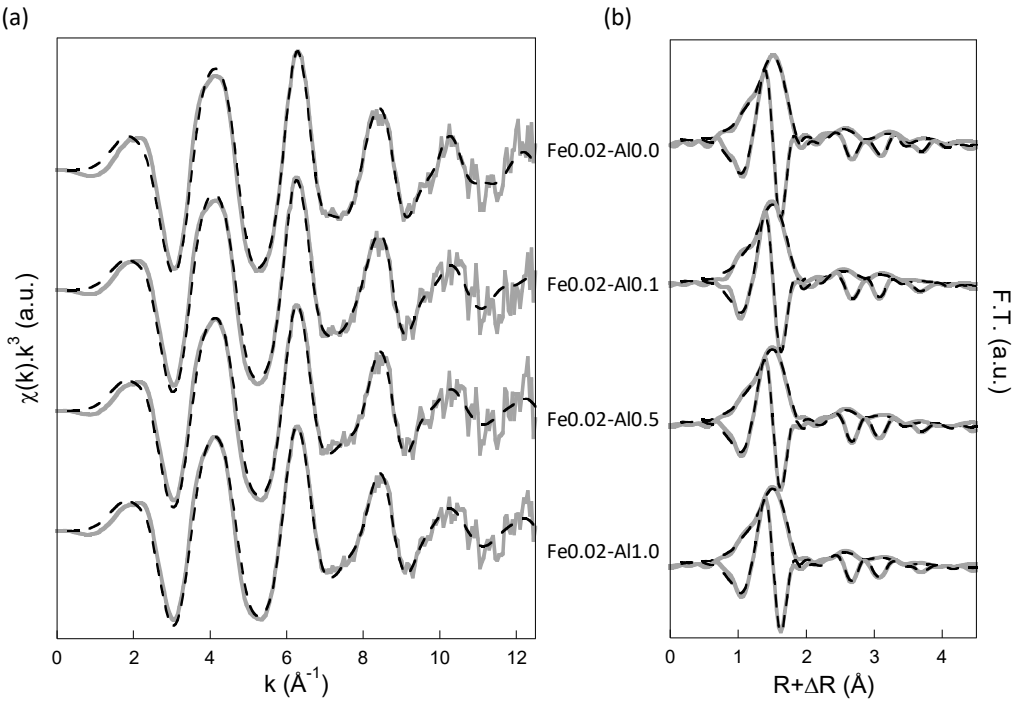

Figure II.2-16 – (a) EXAFS signal at the Fe K-edge and (b) corresponding Fourier transform obtained by the subtraction of the signal provided by the Fe(III)-oligomers percentage reported by LCF. Solid lines are experimental data and dotted lines are the fit results.

Table II.2-7 – Parameters used for fitting the Fe K-edge residual EXAFS signal obtained by the subtraction of the signal provided by the Fe(III)-oligomers percentage reported by LCF to the experimental data.

Sample		30% oligomers subtracted to Fe0.02-Al0.0	40% oligomers subtracted to Fe0.02-Al0.1	40% oligomers subtracted to Fe0.02-Al0.5	30% oligomers subtracted to Fe0.02-Al1.0
Fe-O1	***N***	6.4	6.3	6.1	6.0
	***R* (Å)**	1.98	1.98	1.98	1.98
	σ^2	0.009	0.010	0.010	0.009
Fe-Fe1	***N***	0.8	0.8	1.0	0.9
	***R* (Å)**	3.03	3.03	3.04	3.03
	σ^2	0.009‡	0.011‡	0.010‡	0.009‡
Fe-Fe2	***N***	1.5	2.4	1.5	1.3
	***R* (Å)**	3.50	3.48	3.47	3.46
	σ^2	0.009‡	0.011‡	0.010‡	0.009‡
Fe-O2	***N***	2.3‡‡	3.2‡‡	2.5‡‡	2.2‡‡
	***R* (Å)**	3.69	3.66	3.66	3.65
	σ^2	0.007	0.006	0.010	0.010
Fe-O3	***N***	4.0*	4.0*	4.0*	4.0*
	***R* (Å)**	4.38	4.41	4.42	4.42
	σ^2	0.008	0.009	0.011	0.011
R-factor ($\times 10^{-3}$)		6.0	10.2	7.9	7.4

The amplitude reduction factor S_0^2 and the energy shift ΔE were set to 0.75 and -3.3 eV, respectively. *N* is the coordination number, *R* is the interatomic distance (Å) and σ^2 is the Debye-Weller factor. The error on *N*, *R* and σ^2 are usually estimated to be ± 10%, ± 1% and ± 20%, respectively. '*' denotes fixed parameters. ‡The σ² were forced to be equal to each other. ‡‡The coordination number for the Fe-O2 path was constrained as followed: $N_{Fe\text{-}O2} = N_{Fe\text{-}Fe1} + N_{Fe\text{-}Fe2}$.

To obtain a signal representative of a Fh-like Np, it was necessary to subtract the signal corresponding to 60% (Al/Fe = 0.0, 0.1 and 1.0) and 50% (Al/Fe = 0.5) of Fe(III)-oligomer to the raw data. For each sample, the fit of the obtained EXAFS signal reported 1.2 Fe at ~ 3.03 Å against 1.3 and 1.2 Fe at 3.03 Å for the Fh-like Np and Fh reference (Figure II.2-17 and Table II.2-8). The number of Fe second neighbors at ~ 3.48 Å was below the one reported for the Fh confirming that the obtained signal was relevant of a nano-sized Fh, i.e. a Fh-like Np.

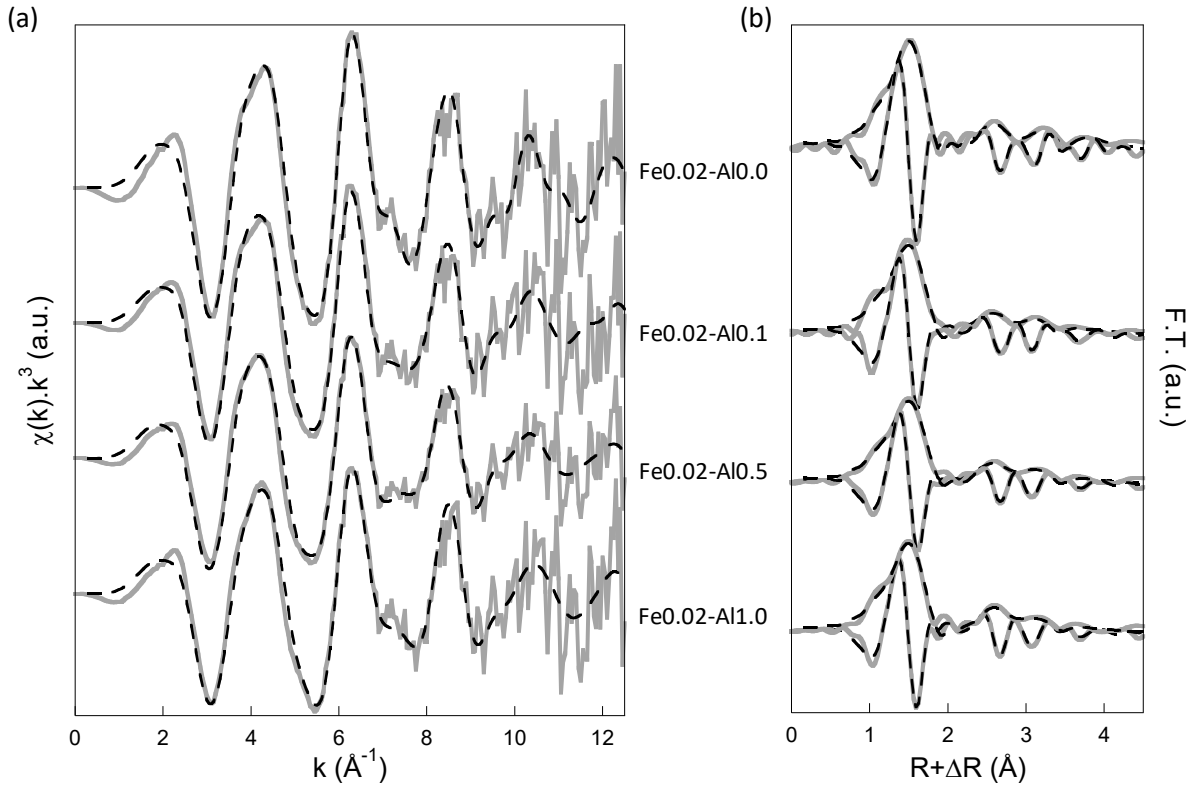

Figure II.2-17 – (a) Fe K-edge EXAFS spectra and (b) corresponding Fourier transform of Fh-like Np obtained by subtracting 60% of the EXAFS signal for the Fe(III)-oligomers from the raw signal of Fe0.02-Al0.0, Fe0.02-Al0.1 and Fe0.02-Al1.0 and 50% from the raw signal of Fe0.02-Al0.5. The gray solid lines are the EXAFS signals after subtraction and the black dotted lines are the fit results

Table II.2-8 – Parameters used to fit the EXAFS signals at the Fe K-edge.

Sample		Fh-like Np	Fh	Np from Fe0.02-Al0.0	Np from Fe0.02-Al0.1	Np from Fe0.02-Al0.5	Np from Fe0.02-Al1.0
Fe-O1	***N***	6.3	4.4	6.5	6.2	6.0	5.5
	R (Å)	1.99	1.97	1.96	1.97	1.97	1.96
	σ²	0.009	0.010	0.008	0.009	0.010	0.008
Fe-Fe1	***N***	1.3	1.2	1.2	1.2	1.2	1.2
	R (Å)	3.04	3.02	3.04	3.04	3.04	3.03
	σ²	0.009‡	0.009‡	0.008‡	0.010‡	0.009‡	0.008‡
Fe-Fe2	***N***	2.4	3.5	1.9	2.7	1.6	1.4
	R (Å)	3.47	3.47	3.51	3.48	3.47	3.46
	σ²	0.009‡	0.009‡	0.008‡	0.010‡	0.009‡	0.008‡
Fe-O2	***N***	3.7‡‡	4.7‡‡	3.1‡‡	3.9‡‡	2.8‡‡	2.4‡‡
	R (Å)	3.63	3.61	3.70	3.66	3.66	3.65
	σ²	0.005	0.007	0.006	0.006	0.010	0.011
Fe-O3	***N***	4.0*	4.0*	4.0*	4.0*	4.0*	4.0*
	R (Å)	4.41	4.45	4.38	4.41	4.42	4.42
	σ²	0.015	0.015	0.004	0.008	0.010	0.010
R-factor ($\times 10^{-3}$)		3.5	5.6	10.7	18.4	10.8	15.6

The amplitude reduction factor S_0^2 and the energy shift ΔE were set to 0.75 and -3.3 eV, respectively. *N* is the coordination number, *R* is the interatomic distance (Å) and *σ²* is the Debye-Weller factor. The error on *N*, *R* and *σ²* are usually estimated to be ± 10%, ± 1% and ± 20%, respectively. '*' denotes fixed parameters. ‡The σ² were forced to be equal to each other. ‡‡The coordination number for the Fe-O2 path was constrained as followed: $N_{Fe\text{-}O2} = N_{Fe\text{-}Fe1} + N_{Fe\text{-}Fe2}$.

The final proportion of Fe(III)-oligomers, Fh-like Np and Fh within Fe-Al-OM aggregates were reported in Figure II.2-18. The results demonstrated a decrease of the Fe(III)-oligomers % with the increasing Fe/OC ratios while it remained constant irrespective of the Al/Fe ratio. However, for Fe/OC ≥ 0.05, the Fh % increased with both the increasing Fe/OC and Al/Fe ratios. Note that here, Fh also corresponded to nano-sized Fh, but larger than Fh-like Nps. Therefore, the Fh % indicated an increase of the Fh-like Nps size with the increasing Fe/OC and Al/Fe ratios rather than Fh presence as observed with SAXS measurements (Figure II.2-11).

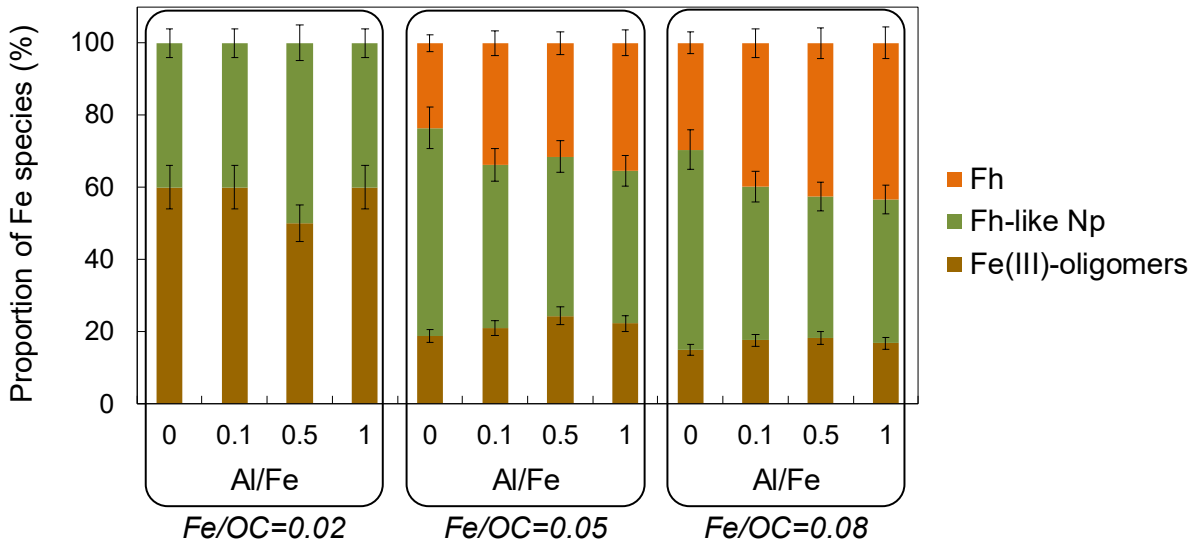

Figure II.2-18 – Proportion of Fe(III)-oligomers (brown), Fh-like Np (green) and Fh (orange).

II.2.4. Discussion

Aluminum significantly impacted the macroscopic behavior of Fe-OM aggregates. While for the lowest [Al], the aggregates was as colloidal suspension, highest [Al] induced a settlement of the samples (Figure II.2-1). Interestingly, Al interacted with the OM part as well as the Fe part of the Fe-OM aggregates. Concerning the interaction with OM, several authors already demonstrated the ability of Al to be bound by OM colloids via their carboxylic sites (Lippold et al., 2005; Tipping, 2005; Marsac et al., 2012; Adusei-Gyamfi et al., 2019). This binding limited the Al polymerization as previously observed for Fe oxyhydroxides (Karlsson et Persson, 2010; Pédrot et al., 2011; Guénet et al., 2017; Vantelon et al., 2019). As a

consequence, at low [Al], Al was mainly organized as monomers and/or oligomers bound to OM. The slight structuration of the XANES spectra and the energy shift of the edge demonstrated that the Al polymerization increased with the increasing [Al] until form amorphous Al hydroxides (Figure II.2-8), as also observed for Fe. Therefore, Fe was organized as Fe(III)-oligomers and Fh-like Nps with and without Al. The Al binding by OM partially limits the Fe interactions with OM and allows the Fh-like Nps size to increase.

Aluminum also interacted with the Fe phases, as highlighted by the pre-edge observed on the Al k-edge XANES spectra which indicated the formation of Al-O-Fe bonds (Figure II.2-8c). Aluminum is known to incorporate Fe oxyhydroxides without modifying the Fe phases crystallographic structure (Hazemann et al., 1991; Hansel et al., 2011; Cismasu et al., 2012; Adra et al., 2013). The quite constant edge intensity and the edge shifting suggested that the same Al fraction is involved in Al-O-Fe bounds despite the variation of the polymerization rate.

All these results allowed proposing a schematic evolution of the structure of the Fe-OM aggregates with the Al concentration. For low [Al], Fe-OM-Al associations were organized as colloidal aggregates. The Fe phases were distributed as Fe(III)-oligomers with various size, bound to OM and Fh-like Nps exhibiting the same fractal organization of 3 levels of aggregation as previously described (Guénet et al., 2017; Beauvois et al., 2020b) (Figure II.2-19, left). In this system, Al is distributed following the same scheme, in which monomers and oligomers dominate. For high [Al], Fe-OM-Al associations form a non-colloidal system (Figure II.2-1) in which amorphous Al hydroxides are the predominant Al species while the Al monomers and oligomers proportion is low. In such conditions, Fe is distributed as Fe(III)-oligomers and Fh-like Nps bound to OM, which content and size is higher than for low [Al]. In Fe-OM-Al aggregates, Al and Fe exhibit therefore a quite similar organization. At high (Fe+Al) concentrations, Fe-OM aggregates form an OM micrometric network branched by Al species (Figure II.2-19, right). The high amounts of Al control a structural transition of the global size of the Fe-OM aggregates and affect their colloidal stability.

This dynamic structural organization of Fe-OM aggregate is probably not without consequences for the surface and global reactivity of the aggregates. Aluminum oxyhydroxides were reported to adsorb many pollutants (Islam et al., 2018) such as arsenic (Mertens et al., 2016). Moreover, mixed Al(III)-Fe(III) oxyhydroxides exhibit higher sorption capacity with regards to phosphate (Harvey et Rhue, 2008), chromate (Ni et al., 2016) or sulfate (Namayandeh et Kabengi, 2019) than Fe(III) oxyhydroxides. An increase of the overall aggregates sorption capacity with the increasing [Al] is expected. Moreover, the settlement of the Fe-OM aggregates with the increasing [Al], will immobilize the pollutants potentially adsorbed at their surface through their trapping in the soil porous media (Kretzschmar et Schäfer, 2005). Concerning their reactivity regarding bioreduction, Lovley et al. (1996) reported that OM acts as an electron shuttle in the bioreduction of Fe(III)-OM colloids resulting in a faster transformation than particulate Fe oxyhydroxides. Ekstrom et al. (2010) demonstrated that the Fe(III) bioreduction rate of Al substituted ferrihydrite was lower than for Fh and Masue-Slowey et al. (2011) explained that the presence of Al^{3+} in the Fh structure inhibits the electron transfer. Organic matter and Al have thus an opposite impact on Fe(III) reduction. The question is thus raised on which Al or OM could control the reduction rate of Fe within these organo-mineral aggregates.

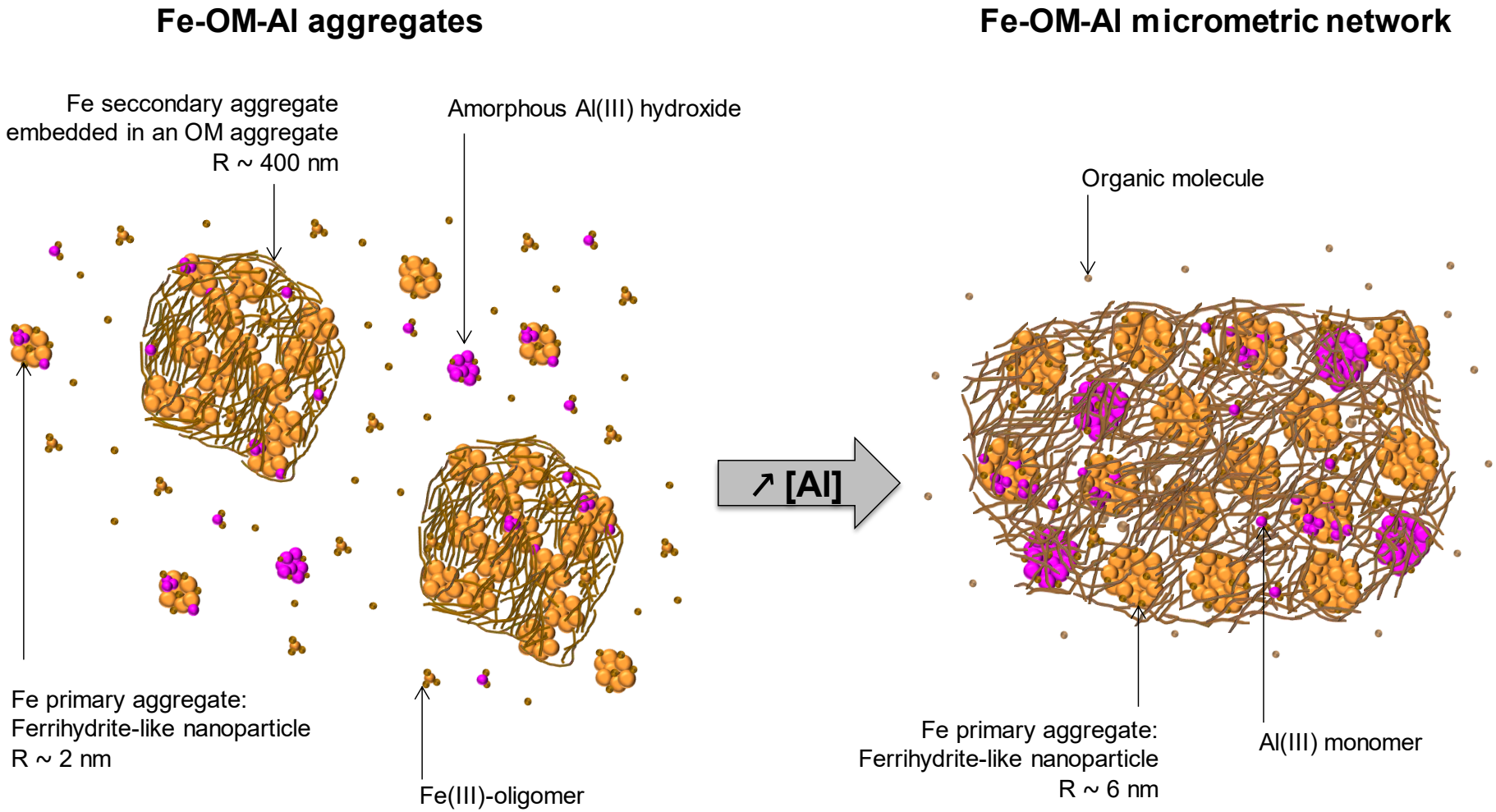

Figure II.2-19 – Schematic representation of the structural organization of the Fe-OM-Al modification with the increasing Al concentration.

Although the global impact on the Fe-OM aggregates colloidal stability is the same for Ca than for Al, the involved mechanisms are different. The affinity of Ca to bind OM is significantly lower than that of Fe(III) (Milne et al., 2003; Cabaniss, 2009). Nonetheless, when Ca occurred at high concentration, Ca dimers are bound to OM even with Fe (Davis et Edwards, 2017; Adhikari et al., 2019; Beauvois et al., 2020b). Aluminum, exhibits a quite lower binding for OM than Fe (Nierop et al., 2002; Milne et al., 2003; Cabaniss, 2009). However, during the coprecipitation of Fe, Al and OM, Al interacts with OM and Fe (present study, Nierop et al., 2002; Pokrovsky et al., 2005). Under environmental conditions, cations generally occur together, which raises questions on their concomitant impact on the Fe-OM aggregates structure. The binding strength with OM is higher for Al than for Ca (Milne et al., 2003; Cabaniss, 2009). Therefore, when Fe, Al, Ca and OM occurred together, OM is expected to bind preferentially Fe and Al than Ca. Studying a Peat soil solutions, where Fe-Al-organic colloids were formed, Pokrovsky et al. (2005) observed that Ca^{2+} was mainly distributed in dissolved fractions for low [OM]. But, for higher organic-rich waters in the boreal area, Pokrovsky et Schott (2002) provided evidence that Ca was associated to organic colloids. Moreover, the variation in [Ca] within natural systems leads to a variation in the ionic strength, a parameter that must be taken into account for the fate of Fe-OM aggregates organization. The structural arrangement between Fe and OM when Al and Ca occurred simultaneously should thus be investigated in further studies.

II.2.5. Conclusion

In this study, the impact of Al on the structural organization of Fe-OM aggregates was investigated. These results shed new light for the understanding on the impact major ion such as Al on Fe-OM aggregates which are recognized as a key parameter of chemical element environmental cycling. Aluminum interacted with both Fe and OM and was distributed as Al monomers and polymerized to form oligomers and then Al amorphous hydroxides, all bound to OM. The polymerization rate of Al increased with the increasing Al concentration. At high Al and Fe concentration, Fe-OM-Al aggregates moved from a colloidal

to a settling system. Aluminum hydroxides offered new reactive sites for binding pollutants. Moreover, the Fe nanoparticles sorption capacity would increase in response to the decrease of the OM binding and subsequent increase of the Fe nanoparticles functional group availability. The transfer/transport of adsorbed pollutants is therefore controlled by the presence of major ions such as Ca and Al that control the transition between colloidal and particulate regime. In view of these results, it is now appropriate to investigate the simultaneous impact of Ca and Al on the structural organization of Fe-OM aggregates to determine whether their independent effect would add or compete to each other. In case of competition, the hypothesis that Al would present the major influence seems to be more reasonable. In such conditions, what would be the impact of the variation in ionic strength, consequent to changes in the Ca concentration, on the structural organization of the Fe-OM aggregates?

Chapitre III. Impact des cations majeurs sur la réactivité des agrégats fer-matière organique

Le chapitre 2 a montré que les cations majeurs, Ca et Al, ont un impact significatif sur l'organisation structurale des agrégats Fe-MO. Cette structure varie à différentes échelles. D'un point de vue macroscopique, des fortes teneurs en cations entraînent une déstabilisation colloïdale des agrégats. Si le Ca n'interagit qu'avec la MO, l'Al, quant à lui, interagit à la fois avec le Fe et la MO. Pour autant, leur impact sur l'organisation structurelle des Fe-OM reste quasiment le même. A fortes concentrations, ils induisent la formation d'un réseau interconnecté, soit par des dimères de Ca, soit par des polymères d'Al. D'un point de vue plus global, ils contrôlent non seulement la répartition oligomères/nanoparticules de Fe et la taille des nanoparticules, mais aussi le taux de recouvrement de ces nanoparticules par la MO et donc très probablement la disponibilité de leurs groupements de surface. Face à ce constat, je me suis intéresse à l'impact de ces modifications structurales sur la réactivité de surface des agrégats Fe/MO vis-à-vis des éléments chimiques, et notamment de l'As. Mon choix s'est porté sur l'As pour trois raisons principales : 1) sa grande affinité pour les phases de Fe et sa faible affinité pour la MO, 2) la bonne connaissance des mécanismes de sorption de l'As par les oxyhydroydes de Fe et 3) ce comportement très diffèrent entre le Fe et la MO qui permettra, dans cette première approche, de mieux discriminer les mécanismes mis en jeux.

Ce chapitre correspond à un article publié dans la revue Journal of Hazardous Materials *: How crucial is the impact of calcium on the reactivity of iron-organic matter aggregates? Insights from arsenic, Anthony Beauvois, Delphine Vantelon, Jacques Jestin, Martine Bouhnik-Le Coz, Charlotte Catrouillet, Valérie Briois, Thomas Bizien, Mélanie Davranche, DOI : 10.1016/j.jhazmat.2020.124127*

Résumé

Les agrégats environnementaux fer-matière organique (Fe-MO) sont un facteur clé dans la compréhension de la dynamique des polluants. Aujourd'hui, l'impact de leur organisation structurale, qui est fortement influencée par les ions majeurs tels que le calcium, sur leur réactivité vis-à-vis des métaux et métalloïdes reste mal connue. Nous avons étudié la capacité d'adsorption d'agrégats modèles Fe-MO-Ca avec différents rapports Fe/carbone organique (CO) et Ca/Fe en utilisant l'As comme sonde. Nous avons ainsi démontré que la spéciation du Fe est le facteur clé qui contrôle la réactivité des agrégats Fe-MO-Ca. Si les oligomères de Fe(III) présentent une plus grande affinité pour l'As que les nanoparticules de type ferrihydrite (Np-Fh), ces dernières offrent une plus grande capacité d'adsorption. De plus, lorsqu'il est présent à des concentrations élevées, le Ca agit comme un compétiteur du fer dans son interaction avec la MO. Ainsi, l'augmentation de la concentration en Ca entraîne une augmentation de la quantité de Np-Fh et de la disponibilité des sites d'adsorption. Par conséquent, le Ca n'est pas qu'un ajusteur de la force ionique, puisqu'il a également un impact considérable sur l'organisation structurale des agrégats Fe-MO à plusieurs échelles, ce qui se traduit par une augmentation des capacités d'adsorption. En présence de quantités élevées de Ca, les agrégats Fe-MO-Ca pourraient immobiliser les polluants car ils forment un réseau micrométrique pouvant être piégé dans la porosité du sol et présentant une forte capacité d'adsorption.

Abstract

Environmental iron-organic matter (Fe-OM) aggregates play a major role in the dynamic of pollutants. Nowadays, there is a lack of information about the control exerted by their structural organization; in particular, the impact of major ions, such as calcium, on their reactivity towards metal(loid)s. The sorption capacity of mimetic environmental Fe-OM-Ca aggregates was investigated relative to the Fe/organic carbon (OC) and Ca/Fe ratios by using As as a probe. It was thus shown that Fe speciation is the key factor controlling the reactivity of Fe-OM-Ca. Fe(III)-oligomers exhibit a higher affinity for As while ferrihydrite-like nanoparticles exhibit a higher sorption capacity. Moreover, when it occurs at a high concentration, Ca competes with Fe for OM binding. Thus, the increase in the Ca concentration leads to an increase in the amount of ferrihydrite-like nanoparticles and binding site availability. As a consequence, Ca not only impacts the ionic strength but it also has a dramatic impact on the structural organization of Fe-OM at several scales of organization, resulting in an increased sorption capacity. In the presence of high amounts of Ca, Fe-OM-Ca aggregates could immobilize pollutants in the soil porous media as they form a micrometric network exhibiting a strong sorption capacity.

III.1. Introduction

Environmental colloids are of major importance given their high reactivity towards metal and metalloid pollutants (Kretzschmar et Schäfer, 2005). They are nanometric particles, either aggregated or not, with a high specific surface area (SSA), mainly composed of minerals and/or organic matter (OM). Among them, those composed of iron (Fe) and OM, usually called “iron-organic matter (Fe-OM) aggregates”, are widely encountered in natural systems such as wetlands where they are mainly produced by drying/wetting cycles in the uppermost soils (Wigginton et al., 2007; Pédrot et al., 2008; Al-Sid-Cheikh et al., 2015; Guénet et al., 2017; Ratié et al., 2019).

For many years, the structure and organization of Fe-OM aggregates was only simply described as poorly crystallized iron oxyhydroxides embedded in an OM matrix (Poggenburg et al., 2016). The overall multiscale complexity of the organization between Fe and OM was poorly investigated. Only recently, several studies have demonstrated that within Fe-OM aggregates, OM as molecules and colloidal aggregates (Guénet et al., 2017; Gentile et al., 2018; Beauvois et al., 2020b) constrains the growth and crystallinity of the Fe phases (Pédrot et al., 2011; Vantelon et al., 2019). The result is that Fe forms Fe(III) monomers, small oligomers and ferrihydrite-like nanoparticles (Fh-like Nps) bound to the OM involving its carboxylic (COOH) and phenolic (PhOH) sites (Karlsson et al., 2008; Karlsson et Persson, 2010; Karlsson et Persson, 2012; Chen et al., 2014; Kleber et al., 2015; Vantelon et al., 2019; Beauvois et al., 2020b). Fh-like Nps exhibit a fractal organization, composed of primary beads (radius ~0.8 nm) forming primary aggregates (radius ~4 nm) that can aggregate to form secondary aggregates (radius > 100 nm) bound to large OM aggregates (Guénet et al., 2017; Beauvois et al., 2020b). As a consequence, despite the fact that they are known to react strongly with pollutants, many questions still remain with regards to the binding capacities of such heterogeneous and polymorph aggregates. For many years, it was accepted that the sorption capacities of such entities follow an additive rule, i.e. for a given chemical element, the total sorption capacity was the sum of the ability of the components of

each aggregate to sorb this element. However, although some experimental data was successfully modelled and reproduced following this additive model (Zachara et al., 1994; Bruggeman et al., 2010), many other data were not (Vermeer et al., 1999; Saito et al., 2005; Lippold et Lippmann-Pipke, 2009; Janot et al., 2013). As an example, Weng et al. (2009) observed an additivity behavior for fulvic acid and goethite while Christl and Kretzschmar (2001) observed a non-additive behavior for fulvic acid and hematite. The most probable explanation is that the structural organization between components strongly influences the global surface reactivity of the aggregate (e.g. in response to the surface covering). More recently, Guénet et al. (2017) demonstrated that the sorption capacity of Fe-OM aggregates increased with the increasing Fe/organic carbon (OC) ratio while the SSA of the Fe-NPs remained constant, providing evidence that SSA was not the only parameter that controls the reactivity of Fe-OM aggregates towards chemical elements. These authors considered that with the increasing Fe/OC ratio, the distance between Fe primary aggregates within Fe secondary aggregates increases, involving a decrease in the Fe coating rate and an increase in the availability of the binding sites. In light of the recent evidence of the Fe-OM structural and organizational complexity, these results bring the simplistic additive model into question and highlight the importance of the structural organization of Fe-OM aggregates in their sorption reactivity towards chemical elements.

Furthermore, in natural systems, major ions such as Ca coexist with Fe and OM (Iglesias et al., 2003). In a recent study, we demonstrated that Ca can strongly influence the structural organization of Fe-OM aggregates, depending on the Ca concentration (Beauvois et al., 2020b). When low amounts of Ca are present, the overall structural organization of Fe-OM aggregates is not modified. By contrast, for high Ca concentrations (i.e. Ca/OC ≥ 0.026), Ca drives the structural transition of the Fe-OM aggregates from a colloidal state to a non-colloidal micrometric Ca-branched OM network in which Fh-like Nps remained embedded. This dramatic change is mainly involved through the binding of Ca to the OM COOH sites. For high amounts of Ca, the divalent cation could thus compete against metals and metalloids for OM binding. In these conditions, the interactions between Fe and OM are

partially screened and two antagonist results are expected: an increase in the availability of Fe binding sites, free from OM, or an increase in the size of the Fh-like Nps (Davis et Edwards, 2017; Beauvois et al., 2020b) involving a decrease in their SSA and subsequently, their decreased sorption capacity.

To understand the overall adsorption capacity of the Fe-OM aggregates, it is necessary to investigate the reactivity of the Fe and OM phases independently. In the present study, we investigate the reactivity of the Fe phases within Fe-OM aggregates at several Fe/organic carbon (OC) and Ca/Fe ratios. Thus, our goal is to provide a clear description of the parameters that control their sorption capacity. For this purpose, arsenic (As) was used as a probe of the Fe surface reactivity as it is known to have stronger affinity for Fe than for OM. Iron-OM-Ca aggregates were synthesized at various Fe/OC and Ca/Fe ratios. The speciation of Fe was studied by X-ray absorption spectroscopy (XAS) at the Fe K-edge and the size and specific surface of the particulate Fe in the Fe-OM-Ca aggregates was investigated using small-angle X-ray scattering (SAXS). To evaluate the binding capacity of the Fe-OM aggregates and the parameters controlling this process, Arsenic sorption experiments were carried out and coupled with (ultra)filtrations to investigate the distribution of As relative to the size evolution of the Fe-OM aggregates.

III.2. Experimental method

III.2.1. Sample syntheses and chemical analyses

III.2.1.1. Synthesis of the Fe-OM-Ca aggregates

All of the aqueous solutions were prepared with Milli-Q water (Millipore). Samples were synthesized at three Fe/OC ratios (0.02, 0.05 and 0.08 mol./mol.) and four Ca/Fe ratios (0, 0.1, 0.5 and 1 mol./mol.) following the procedure described by Guénet et al. (2017). The samples are labelled Fe*xx*-Ca*yy*, where *xx* and *yy* represent the Fe/OC and Ca/Fe ratios, respectively. The OM used was Leonardite Humic Acid (LHA) purchased from the international humic substance society (IHSS) with the elemental composition C = 63.81%, O

= 31.27%, H = 3.70% and N = 1.23% (as a mass fraction). An iron(II) stock solution of 1.79×10^{-2} mol L^{-1} was prepared with $FeCl_2.4H_2O$ (Sigma Aldrich). From this solution, three Fe(II)-Ca(II) solutions were prepared at [Ca] = 2.50×10^{-3} mol L^{-1}, 1.25×10^{-2} mol L^{-1} and 2.50×10^{-2} mol L^{-1} with $CaCl_2.2H_2O$ (Sigma Aldrich). The Fe-OM-Ca aggregates were synthesized through a titration of the LHA suspension at [OC] = 1.00×10^{-1} mol L^{-1} with the Fe(II)-Ca(II) solution at 0.05 mL min^{-1} in 5×10^{-3} mol L^{-1} of NaCl using an automated titrator (Titrino 794, Metrohm). The pH was monitored at 6.5 ± 0.04 with a 0.1 M NaOH solution using a second titrator (Titrino 794, Metrohm) at a set pH mode. A solution of pure LHA was prepared by dissolving 25 mg of the LHA in a 1×10^{-3} mol L^{-1} NaCl solution at pH = 6.0 as a reference for the chemical analyses.

III.2.1.2. Arsenic sorption experiments

Arsenic sorption isotherms were performed in triplicate for all of the samples at five As/Fe ratios (i.e. 0.0007, 0.004, 0.04, 0.15 and 0.4 mol/mol). For this purpose, various As(III) solutions were prepared from $NaAsO_2$ (Sigma Aldrich) at 5.00×10^{-2} mol L^{-1}, 5.00×10^{-3} mol L^{-1} and 5.00×10^{-4} mol L^{-1}. An aliquot of each As(III) solution was added to the suspension of Fe-OM-Ca aggregates to reach the fixed As/Fe ratio. The pH of the suspensions was adjusted to 6.5 ± 0.04 using 1 mol L^{-1} HCl or NaOH. The equilibrium time for goethite in the presence of HA and hematite nanoparticles was demonstrated to be 4 h and 24 h, respectively (Grafe et al., 2001; Dickson et al., 2017). Similarly, Raven et al. (1998) observed an equilibrium time for As adsorption by Fh of 24 h, irrespective of the pH or the initial As concentration. The suspensions were therefore stirred for 24 h to ensure that the equilibrium is reached. A fraction of each solution was ultrafiltrated at 30 kDa (Vivaspin VS2022, Sartorius). The ultrafiltrate corresponds to the dissolved species. The arsenic concentration was measured in the bulk fraction and in the <30 kDa fraction in order to determine the quantity of adsorbed As on Fe phases.

For As/Fe = 0.004 and 0.15, additional (ultra)filtrations were performed at 0.2 µm (cellulose acetate membrane filter, Sartorius), 1000 kDa (Vivaspin VS2062, Sartorius) and

100 kDa (Vivaspin VS2042, Sartorius). Each 0.2 µm filter was rinsed with 200 mL of Milli-Q water (Millipore) before use. Each ultrafiltration cell was washed several times with 15 mL of a 0.1 mol L^{-1} NaOH solution and Milli-Q water until the DOC concentration in the ultrafiltrate was below 0.2 mg L^{-1}. An As/Fe ratio = 0.004 was chosen since it is close to the ratio observed in riparian wetland soil solutions (Dia et al., 2000; Olivie-Lauquet, 2001) and As/Fe = 0.15 was chosen because it ensured a high As adsorption rate (Dixit et Hering, 2003; Guénet et al., 2017).

III.2.13. Chemical analyses

Chemical analyses were performed on the bulk fraction and all of the (ultra)filtrates. The OC concentrations were determined using an OC analyzer (Shimadzu TOC-V CSH). The uncertainty of the C measurement was determined to be ± 5% using a standard solution of potassium hydrogen phthalate (Sigma Aldrich). The Fe, Ca and As concentrations were measured by inductively coupled plasma mass spectrometry (ICP-MS) using an Agilent Technologies 7700x instrument at the University of Rennes 1. To solubilize Fe, Ca and As and to eliminate OM, the samples were predigested with 14.6 mol L^{-1} distilled HNO_3 at 90°C and evaporated. A second oxidative predigestion with a mixture of 14.6 mol L^{-1} distilled HNO_3 and Suprapur 30% H_2O_2 (a HNO_3/H_2O_2 volume ratio of ~75/25) at 90°C was necessary to completely dissolve the samples. Finally, the samples were evaporated to complete dryness and solubilized with HNO_3 at 0.37 mol L^{-1} prior to the ICP-MS measurements. The detection limits of the ICP-MS measurements were 1×10^{-2}, 2×10^{-3} and 5×10^{-5} mol L^{-1} for Ca, Fe and As, respectively.

III.2.2. Adsorption isotherm modelling

As adsorption isotherms were fitted with the Langmuir equation (eq. III-1):

$$q = \frac{q_{max}.K_{ads}.C}{1 + K_{ads}.C} \qquad \text{(eq. III-1)}$$

where q is the quantity of adsorbed As per unit mass of adsorbent (µmol g^{-1}), q_{max} is the maximal quantity of adsorbed As per unit mass of adsorbent (µmol g^{-1}), Langmuir K_{ads} is a

constant related to the binding strength of adsorbent (L μmol^{-1}) and C is the final concentration of As in solution ($\mu mol\ L^{-1}$), i.e. in the <30 kDa fraction as described above (Sparks, 2003). Isotherms were fitted using KaleidaGraph software with the Levenberg-Marquardt algorithm to calculate the best curve fit using an iterative procedure.

III.2.3. Fe K-edge XAS data acquisition and analyses

Before the adsorption experiments were performed, a fraction of each sample was freeze dried (Freeze dryer Alpha 1-2 LD plus, Christ). The powder was then mixed with cellulose (Merck) and pressed into a 6 mm pellet. The Fe K-edge spectra were recorded on the ROCK (Briois et al., 2016) beamline at the SOLEIL synchrotron (Saint-Aubin, France). The monochromator used was a Si(111) channel-cut. The spectra were recorded in transmission mode using three ionization chambers (Ohyo Koken) filled with N_2. The energy was calibrated using a Fe foil located between the 2nd and 3rd ionization chambers and measured simultaneously with the samples. The calibration was done by setting the maximum of the first derivate of the Fe foil to 7112 eV. The reference used for further data analysis was a Fh synthesized following the procedure described in Schwertmann and Cornell (2000). All of the XAS data were processed using the Athena software (Ravel et Newville, 2005) including the Autbk algorithm (Rbkb = 1, k-weight = 3). The Fe spectra were normalized by fitting the pre-edge region with a linear function and the post-edge region with a quadratic polynomial function. The Fourier transforms of the k^3-weighted EXAFS spectra were calculated over a range of 2-12.5 $Å^{-1}$ using a Hanning apodization window (window parameter = 1). Back Fourier filters were extracted over the R-range of 1.15-4.1 Å, using the same apodization window shape. The EXAFS data were analyzed by linear combination fitting (LCF) available in the Athena software over the range 3-12.5 $Å^{-1}$; all of the component weights were forced to be positive. Beauvois et al. (2020b) demonstrated that the EXAFS data at the Fe K-edge could be reproduced by performing LCF using Fe(III)-oligomers and Fe(III)-Np isolated by Vantelon et al. (2019) as well as Fh. The total LCF weight for each sample varied between 0.95 and 1.05 without any constraint. To facilitate the comparison

between each sample, the total LCF weight was arbitrary fixed to 1. EXAFS data were also fitted in the range 1.15-4.1 Å with the Artemis (Ravel et Newville, 2005) interface to IFEFFIT using least-squares refinements. Theoretical backscattering paths used were calculated from a goethite structure (Hazemann et al., 1991) using the FEFF6 algorithm (Rehr et al., 1992; Newville, 2001) included in the Artemis interface.

III.2.4. SAXS measurements

Small-angle X-ray scattering (SAXS) measurements were performed on the SWING beamline at the SOLEIL synchrotron. Using two sample-to-detector distances (1 and 6 m) at a wavelength of 1.03 Å, a momentum transfer q range of 2.0×10^{-3}-0.7 $Å^{-1}$ was reached using a EIGERX 4M detector. Measurements were also carried out on the XEUSS 2.0 spectrometer from Xenocs (CEA-LIONS/LLB, Saclay, France). With two sample-to-detector distances (0.33 and 2.49 m) and a wavelength of 1.54 Å (Cu X-ray source), a momentum transfer range of 4.5×10^{-3}-0.5 $Å^{-1}$ was reached. In the high q domain of the SAXS curves, the so-called Porod region, the scattered intensity is proportional to the surface scattering per unit volume S/V and can be modelled according to the following equation (eq. III-2):

$$\lim\big(I(q)\big) = \frac{2\pi\varphi_0\Delta\rho^2}{q^4}\frac{S}{V}$$

where φ_0 is the volume fraction of the primary beads, $\Delta\rho^2$ is the contrast term (cm^{-4}), both estimated by Beauvois et al. (2020b). Dividing S/V by the mean density of the Fe aggregates (i.e. 3.96 g cm^{-3} (Hofmann et al., 2004)), we were able to calculate the SSA of the Fh-like Nps.

III.3. Results

III.3.1. OC, Fe, Ca and As distribution in the size fractions

The OC, Ca, Fe and As concentrations in each fraction are reported in Table A-1 to A-7, respectively. For samples at Ca/Fe = 0, 0.11 mmol L^{-1} of Ca was detected which

corresponded to the Ca naturally present in the LHA (Table A-8). The ICP-MS measurements of the LHA alone also displayed [Fe] = 0.04 mmol L^{-1}, which is low as compared to the lowest Fe/OC with [Fe] = 1.23 mmol L^{-1} and [As] was below the detection limit.

The % distribution of OC, Ca, Fe and As in each size fraction is reported in Figure III-3 (for As/Fe = 0.004) and Figure III-2 (for As/Fe = 0.15). In the <30 kDa fraction, ~5% of OC and less than 1% of Fe were present. The dissolved As% decreased with the increasing Fe/OC ratio for all Ca/OC. By contrast, irrespective of the Fe/OC ratio, the Ca% in the <30 kDa fraction remained < 10% for Ca/Fe ≤ 0.1. Then, it increased with the increasing Ca/Fe ratio. This increase was less pronounced for Fe/OC = 0.02 compared to Fe/OC ≥ 0.05. The results provided evidence of a perfect co-distribution of OC, Ca, Fe and As in the >30 kDa fractions. For Fe/OC = 0.02, ~80% of the OC, Ca, Fe and As in the >30 kDa fraction were distributed in the 1000-100 kDa fraction, ~15% were in the >0.2 µm fraction and the remaining 5% were distributed in the other fractions for both Ca/Fe = 0 and 0.1. With the increasing Ca/Fe ratio, the amount of OC, Ca, Fe and As in the 1000-100 kDa fraction decreased until ~60% for Ca/Fe = 1, and simultaneously increased in the >0.2 µm fraction (~30%) and to a lower extent in the 0.2 µm-1000 kDa fraction (~10%). The same behavior was observed for the higher Fe/OC values. For Fe/OC = 0.05, with the increasing Ca/OC from 0 to 0.1, the proportion of OC, Ca, Fe and As decreased from ~75% to ~65% from the 1000-100 kDa fraction to the >0.2 µm fraction for which the % increased from ~20% to ~30%. For Ca/Fe = 0.5, the concentration was below the ICP-MS detection limit in the 1000-100 kDa fraction while ~30% and ~65% were observed in the 0.2 µm-1000 kDa and >0.2 µm fractions, respectively. This distribution was higher for Ca/Fe = 1, as almost all of the OC, Fe, Ca and As were distributed in the >0.2 µm fraction. For the highest Fe/OC = 0.08, OC, Fe, Ca and As in the 1000-100 kDa fraction decreased from ~60% for Ca/Fe = 0 to ~0% for Ca/Fe ≥ 0.5 and increased in the >0.2 µm fraction, which reached 100% for Ca/Fe ≥ 0.5.

In summary, for Ca/Fe = 0, OC, Fe, Ca and As occurred mainly in the 1000-100 kDa fraction. When Fe/OC and Ca/Fe increased, they were transferred to the >0.2 µm fraction. The Ca/Fe ratio had a greater influence than that of Fe/OC. Therefore, the size of the Fe-OM-Ca association increased with the increasing Ca concentration.

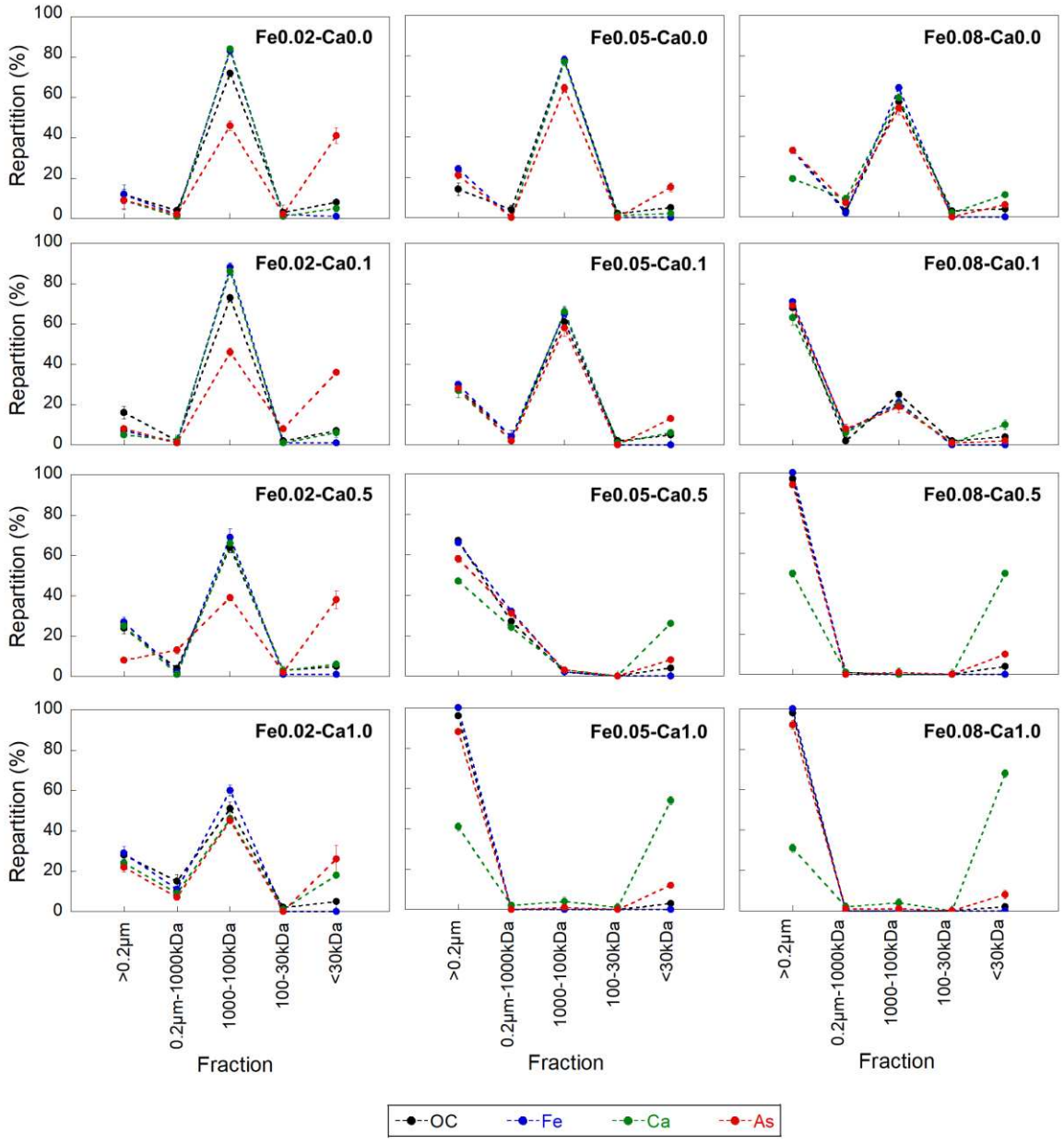

Figure III-1 – Percentage of the distribution of OC (black), Fe (blue), Ca (green) and As (red) relative to the size fraction for each Fe/OC and Ca/OC ratio at As/Fe = 0.004.

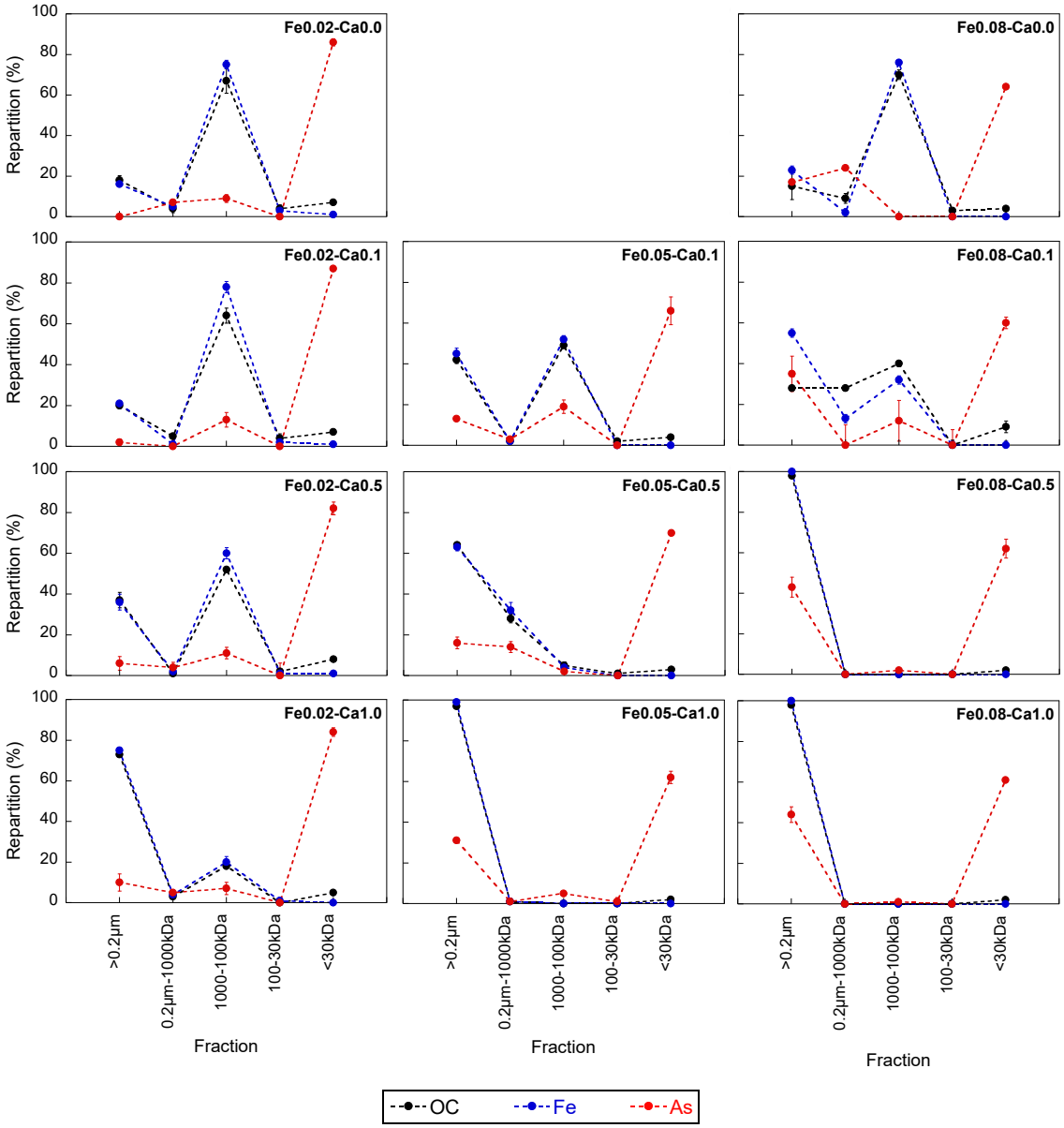

Figure III-2 – Percentage of the distribution of OC (black), Fe (blue), Ca (green) and As (red) relative to the size fraction for each Fe/OC and Ca/OC ratio at As/Fe = 0.15.

III.3.2. Arsenic adsorption isotherms

Arsenic adsorption isotherms exhibited an L-type curve shape for which the slope decreased with the increasing As concentration. The isotherms were fitted with the Langmuir equation (eq. IV-1) (Figure III-3, Table III-1). The good quality of the fit (R^2 > 0.975) demonstrated that the Langmuir isotherm is suitable for As sorption by Fe-OM-Ca aggregates.

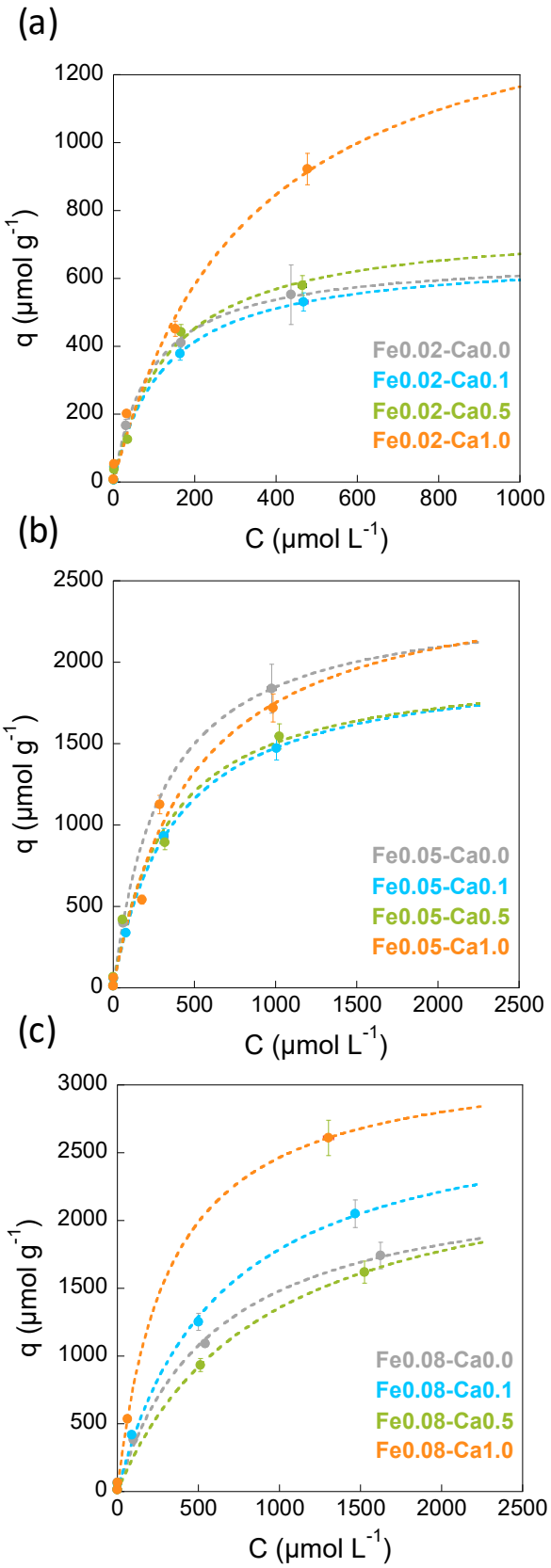

Figure III-3 – Arsenic adsorption isotherms for (a) Fe/OC = 0.02, (b) Fe/OC = 0.05 and (c) Fe/OC = 0.08. The circles represent the experimental points and the dotted lines represent the Langmuir isotherm.

Table III-1 – Parameters used to fit the adsorption isotherms with the Langmuir model.

Sample	q_{max} (µmol g^{-1})	Langmuir K_{ads} (L μmol^{-1})	R^2
Fe0.02-Ca0.0	6.7×10^{2}	10×10^{-3}	0.995
Fe0.02-Ca0.1	6.7×10^{2}	8×10^{-3}	0.993
Fe0.02-Ca0.5	7.6×10^{2}	7×10^{-3}	0.991
Fe0.02-Ca1.0	1.5×10^{3}	3×10^{-3}	0.986
Fe0.05-Ca0.0	2.4×10^{3}	3×10^{-3}	0.999
Fe0.05-Ca0.1	2.0×10^{3}	3×10^{-3}	0.998
Fe0.05-Ca0.5	2.0×10^{3}	3×10^{-3}	0.983
Fe0.05-Ca1.0	2.6×10^{3}	2×10^{-3}	0.975
Fe0.08-Ca0.0	2.4×10^{3}	2×10^{-3}	0.997
Fe0.08-Ca0.1	2.9×10^{3}	2×10^{-3}	0.998
Fe0.08-Ca0.5	2.6×10^{3}	1×10^{-3}	0.998
Fe0.08-Ca1.0	3.2×10^{3}	3×10^{-3}	0.999

Iron-OM-Ca aggregates exhibited a sorption capacity, q_{max}, varying from ~665 µmol g^{-1} for Fe0.02-Ca0.0 to 3240 µmol g^{-1} for Fe0.08-Ca1.0. The q_{max} value increased with the increasing Fe/OC ratio. These q_{max} were in the range of those calculated for Fh under similar pH conditions (Table III-2). However, they are around one order of magnitude higher than crystallized Fe-oxides such as magnetite or goethite (Table III-2). By contrast, the Fe-OM-Ca aggregates Langmuir K_{ads} decreased with the increasing Fe/OC ratio. For the Fe/OC = 0.02, Langmuir K_{ads} decreased with the increasing Ca/Fe ratio while remaining constant irrespective of the Ca/Fe ratio for Fe/OC ≥ 0.05. The calculated Langmuir K_{ads} values are 10 times lower than those reported for Fh. For the lowest Fe/OC and Ca/Fe ratio, the Langmuir K_{ads} values are similar to the Langmuir K_{ads} values for Fh bound with OM, but decrease by one order of magnitude with the decreasing Fe/OC and Ca/Fe ratio. Xue et al. (2019) demonstrated that the increase in the amount of OM leads to a decrease in the Fh Langmuir K_{ads} value. Thus, the presence of OM and Ca may be responsible for the decrease in the Langmuir K_{ads} of As by Fe Ca-OM aggregates.

Table III-2 – q_{max} and Langmuir K_{ads} of various Fe-oxyhydroxides.

Fe oxyhydroxides	q_{max} (µmol g^{-1})	Langmuir K_{ads}	Experimental conditions	Reference
Fh	1.1×10^{3}	7.0×10^{-2}	pH = 6.0 IS* = 0.02	Zhu et al. (2011)
Fh	5.0×10^{3}	1.5×10^{-2}	pH = 7.0 IS* = 0.01	Xue et al. (2019)
Fh-HA (5 wt%)	3.6×10^{3}	1.1×10^{-2}	pH = 7.0 IS* = 0.01	Xue et al. (2019)
Fh-HA (15 wt%)	2.7×10^{3}	8.8×10^{-3}	pH = 7.0 IS* = 0.01	Xue et al. (2019)
Magnetite	1.4×10^{1}	1.0×10^{-1}	pH = 6.1 IS* = 0.01	Yean et al. (2005)
Nano-magnetite	1.4×10^{2}	5.4×10^{-1}	pH = 6.1 IS* = 0.01	Yean et al. (2005)
Goethite	1.7×10^{2}	4.0×10^{-2}	pH = 4 IS* = 0.01	Dixit and Hering (2003)
HFO	2.7×10^{2}	9.0×10^{-2}	pH = 4 IS* = 0.01	Dixit and Hering (2003)

*IS: ionic strength in mol L^{-1}

III.3.3. Speciation of Fe within Fe-OM-Ca aggregates

The maximum amplitude of the EXAFS spectra was reached at 6.3 $Å^{-1}$ (Figure III-4). The Fe(III)-oligomer reference displayed a close monotonous damping shape. The Fh-like Np and Fh spectra showed a shoulder at 5.1 $Å^{-1}$ and an oscillation at 7.5 $Å^{-1}$ that was more pronounced for Fh compared to Fh-like Np. For Fe/OC = 0.02, the shape of the spectra were monotonous but a shoulder occurred at 7.5 $Å^{-1}$. For Fe/OC ≥ 0.05, the EXAFS spectra were more structured with an additional shoulder and a more pronounced shoulder occurring at 5.1 $Å^{-1}$ and 7.4 $Å^{-1}$, respectively.

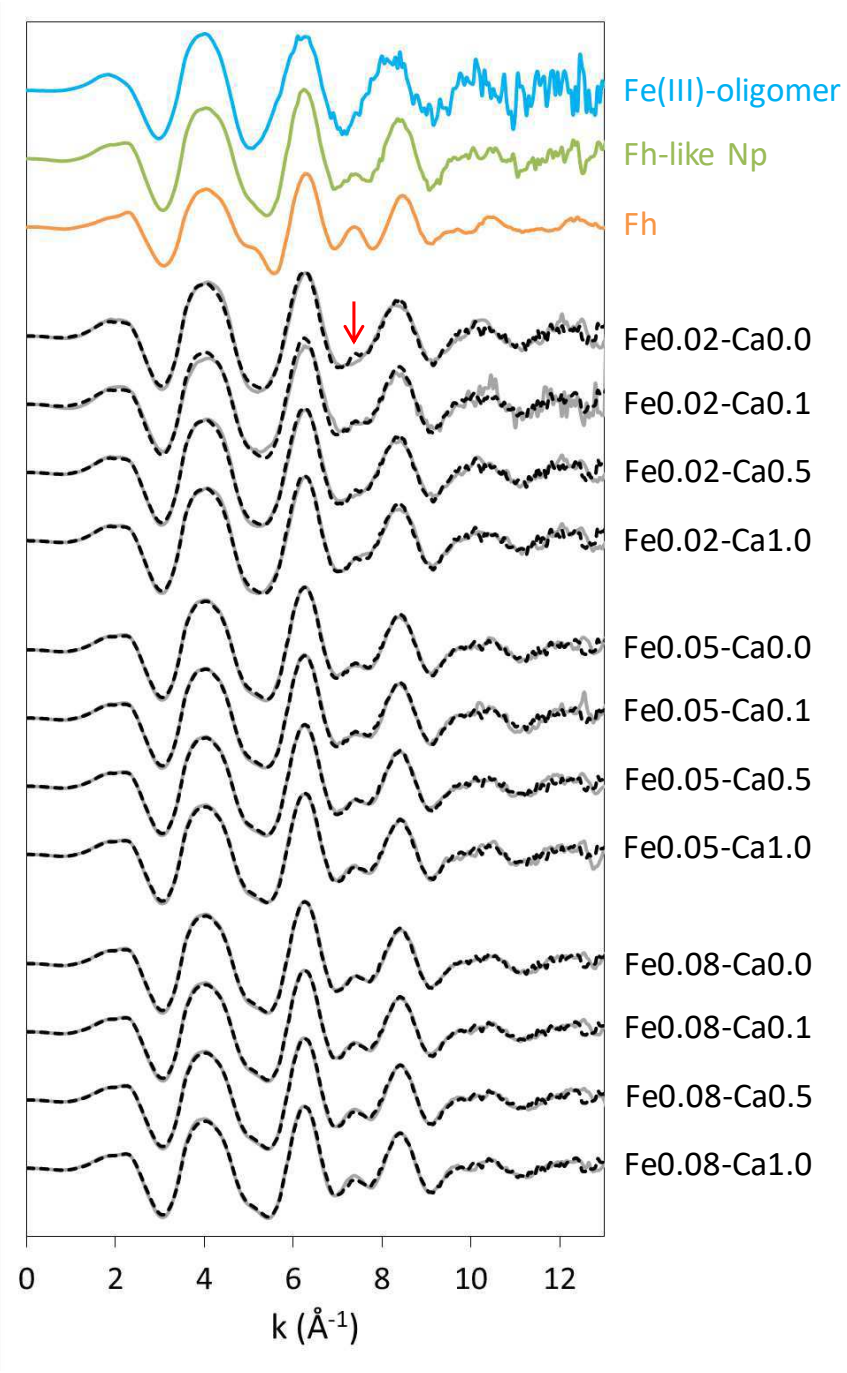

Figure III-4 – Fe K-edge EXAFS spectra of the references used to perform the LCF and for each sample. The solid lines are experimental data and the dotted lines are the LCF results. The red arrow highlights the main discrepancy between the LCF result and the experimental data.

For Fe/OC ≥ 0.05, the LCF reproduced well the EXAFS signal. The percentage of nanoparticulate Fe, i.e. the percentage of Fe organized as Fh-like Np and Fh was calculated from LCF (Table III-5). It was ≥ 80% and increased with the increasing Ca/Fe ratio, as already reported (Beauvois et al., 2020b). For Fe/OC = 0.02, the LCF results reported ~70%

of nanoparticulate Fe. However, the LCF exhibited a shoulder at 7.5 $Å^{-1}$ that was much more pronounced than in the experimental data (highlighted by the red arrow in Figure III-4). This shoulder was mostly due to the neighbors siting at a distance larger than 3 Å (Figure III-5). Therefore, when the size of the Fe particle was smaller, it was expected that the shoulder at 7.5 $Å^{-1}$ would be less pronounced. This effect was observed for the Fh-like Np; the EXAFS spectrum exhibited a shoulder at 7.5 $Å^{-1}$ lower than Fh (Figure III-4). The strongly pronounced shoulder at 7.5 $Å^{-1}$ provided evidence that the size of the Fe nanoparticle used for LCF is too large. This assumption was also supported by the size of the particulate Fe reported from the SAXS experiments showing that they were smaller for Fe/OC = 0.02 than for Fe/OC ≥ 0.05 (Beauvois et al., 2020b).

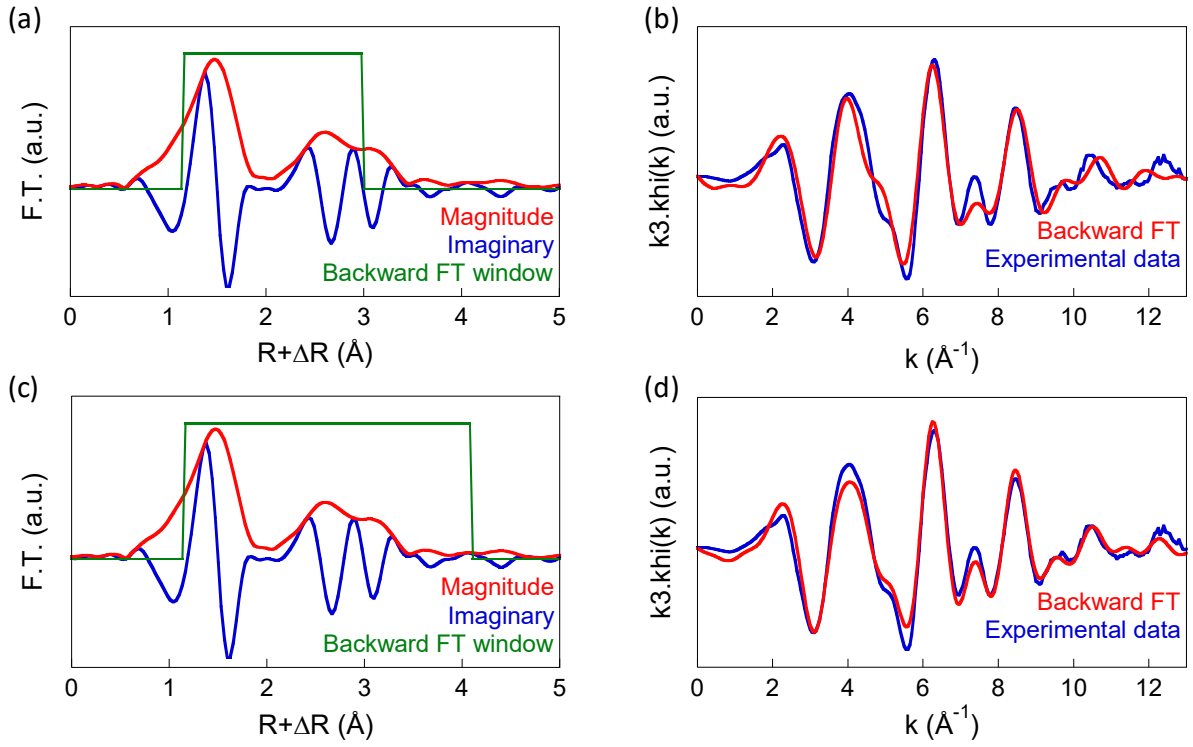

Figure III-5 – (a) and (c) Magnitude and imaginary part of the Fourier Transform of Fe K-edge EXAFS spectra of Fh with the window used for backward FT calculation; and EXAFS spectra compared to the backward FT calculated on the range of (b) 1.15-3 Å and (d) 1.15-4.1 Å.

For Fe0.02-Ca1.0, the EXAFS signal was subtracted from the experimental data corresponding to 30% of the oligomers, as given by the LCF results. The signal is reported in Figure III-6a along with the shell-by-shell fit result. The corresponding Fourier transform is

reported in Figure III-6b. The results of the fit (Table III-4) showed 6.5 O at 1.98 Å and 1.6 Fe at 3.04 Å, in accordance with an Fh-like Np structure. However, 1.5 Fe at 3.47 Å were needed to fit the Np of Fe0.02-Ca1.0 versus 2.4 Fe for the Fh-like Np. This decrease in the number of second neighbors illustrates that the Fe0.02-Ca1.0 nanoparticles were smaller than the Fh-like Np nanoparticles. For Fe0.02-Ca0.05, the fit of the EXAFS signal, after 30% of the EXAFS signal for the Fe(III)-oligomers was subtracted from the experimental data returned 1 Fe at 3.04 Å (Figure III-7 and Table III-3). This low number of neighbors suggests that Fe(III)-oligomers remain in the signal as this amount of neighbors is too low to be provided by particulate Fe. The same is observed for Fe0.02-Ca0.0; the signal for these nanoparticles, after subtracting 30% of the Fe(III)-oligomers, exhibited less than 1 Fe (0.8) at 3.03 Å (Figure III-8 and Table III-3).

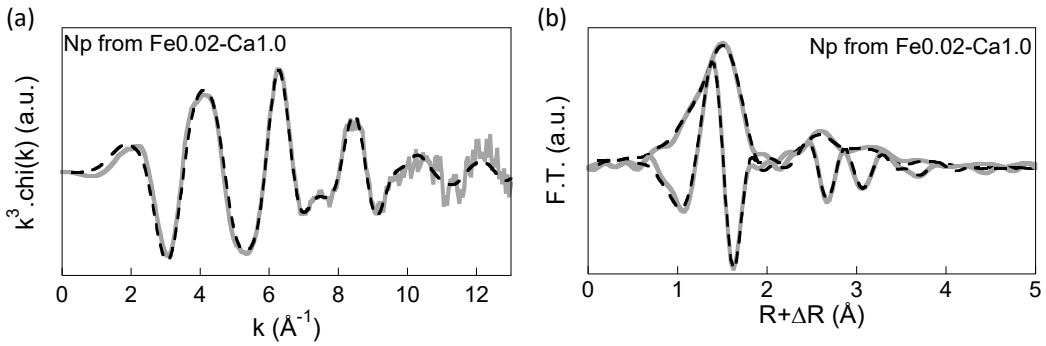

Figure III-6 – (a) Fe K-edge EXAFS spectra of nanoparticulate Fe obtained by subtracting 30% of the EXAFS signal for the Fe(III)-oligomers from the raw signal of Fe0.02-Ca1.0 and (b) corresponding Fourier transform. The gray solid lines are the EXAFS signals after subtraction and the black dotted lines are the fit results.

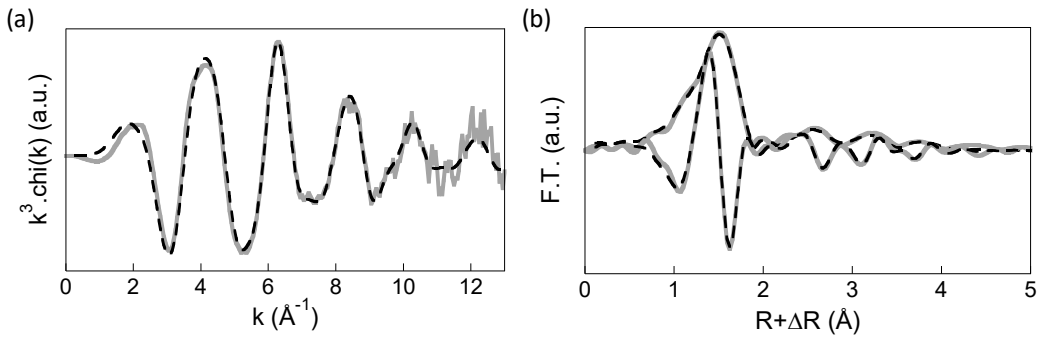

Figure III-7 – (a) EXAFS spectra at Fe K-edge and (b) Fourier Transform of the signal obtained by subtraction of the EXAFS signal of the 30 % of oligomers given by the LCF results to the experimental data of Fe0.02-Ca0.5. Solid lines are experimental data and dotted lines are the fit results.

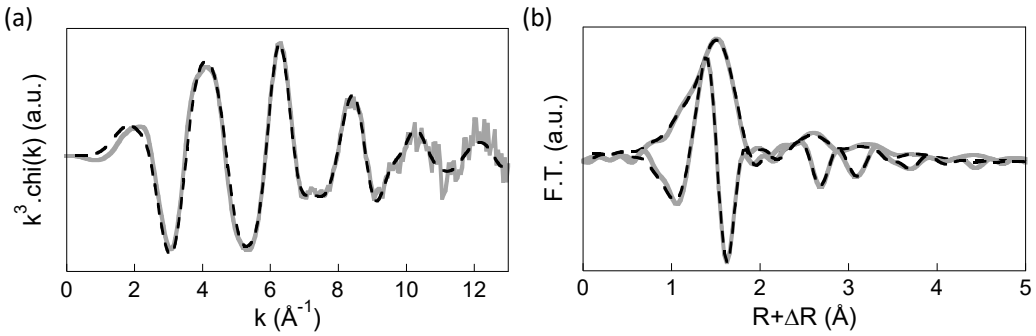

Figure III-8 – (a) EXAFS spectra at Fe K-edge and (b) Fourier Transform of the signal obtained by subtraction of the EXAFS signal of the 30 % of oligomers given by the LCF results to the experimental data of Fe0.02-Ca0.0. Solid lines are experimental data and dotted lines are the fit results.

Table III-3 – Parameters used for fitting EXAFS at Fe K-edge.

Sample		30% oligomers subtracted to Fe0.02-Ca0.0	30% oligomers subtracted to Fe0.02-Ca0.5
Fe-O	***N***	6.4	6.3
	R (Å)	1.98	1.98
	σ²	n.d.9	n.d.9
Fe-Fe	***N***	0.8	1.0
	R (Å)	3.03	3.04
	σ²	n.d.9**	n.d.9**
Fe-Fe	***N***	1.5	1.6
	R (Å)	3.50	3.48
	σ²	n.d.9**	n.d.9**
Fe-O	***N***	2.3**	2.6**
	R (Å)	3.69	3.65
	σ²	n.d.7	0.010
Fe-O	***N***	4.0*	4.0*
	R (Å)	4.38	4.40
	σ²	n.d.8	n.d.9
R-factor (×10^{-3})		6.0	6.5

The amplitude reduction factor S_0^2 and the energy shift ΔE were set to 0.75 and -3.3 eV, respectively. *N* is the coordination number, *R* is the interatomic distance (Å) and σ^2 is the Debye-Weller factors. The error on *N*, *R* and σ^2 are usually estimated to be ± 10%, ± 1% and ± 20%, respectively. '*' denotes fixed parameters and '**' denotes constraint parameters.

These results demonstrate that the amount of Fe(III)-oligomers was underestimated by LCF in both samples. In order to isolate the EXAFS signal of the particulate Fe (i.e. a signal containing a comparable number of Fe first neighbors as in Fh and Fh-like Np), it is necessary to subtract 60% of the Fe(III)-oligomers (Figure III-9a and b) from Fe0.02-Ca0.5 and 70% of the Fe(III)-oligomers (Figure III-9c and d) from Fe0.02-Ca0.0. In both cases, the number of Fe at 3.47 Å (Table III-4) was lower than for the Fh-like Nps, demonstrating that the Nps from Fe0.02-Ca0.0 and Fe0.02-Ca0.5 were smaller than the Fh-like Nps initially used for the LCF calculations.

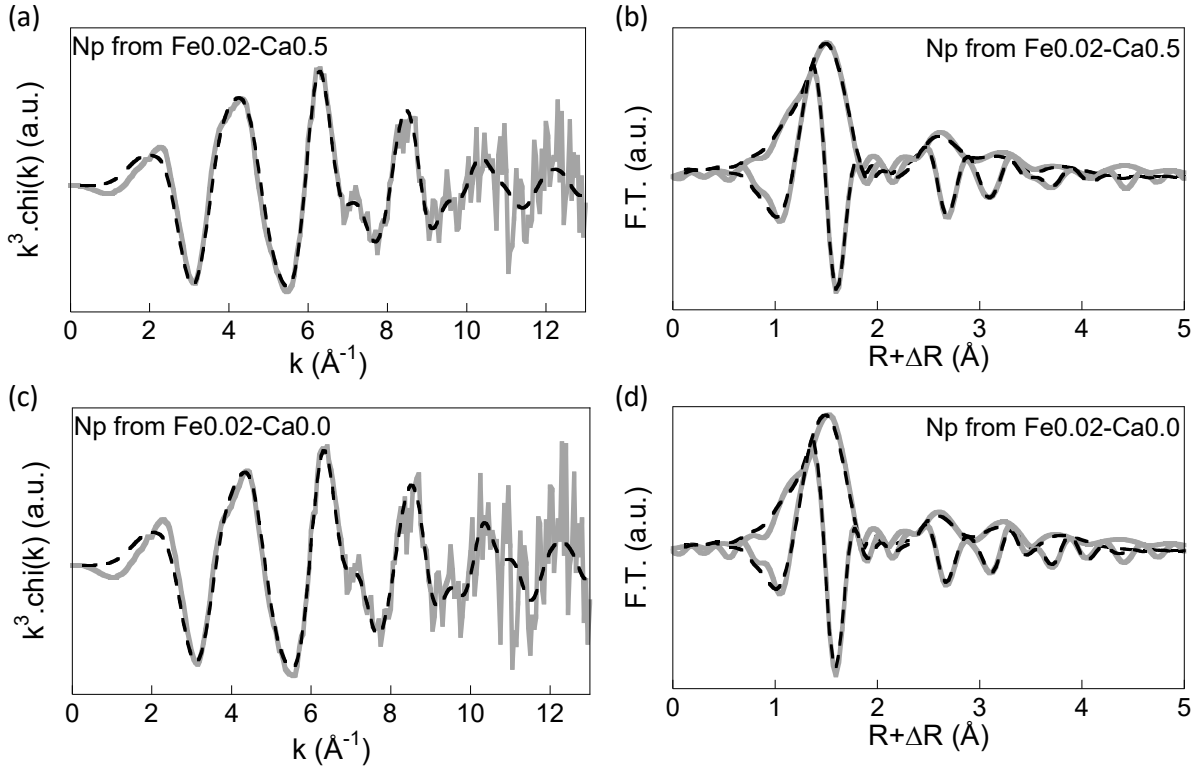

Figure III-9 – (a) Fe K-edge EXAFS spectra of nanoparticulate Fe obtained by subtracting 60% of the EXAFS signal for the Fe(III)-oligomers from the raw signal of Fe0.02-Ca0.5 and (b) corresponding Fourier transform. (c) Fe K-edge EXAFS spectra of nanoparticulate Fe obtained by subtracting 70% of the EXAFS signal for the Fe(III)-oligomers from the raw signal of Fe0.02-Ca0.0 and (d) corresponding Fourier transform. The gray solid lines are the EXAFS signals after subtraction and the black dotted lines are the fit results.

Table III-4 – Parameters used to fit the EXAFS signals at the Fe K-edge.

Sample		Fh-like Np	Fh	Np from Fe0.02-Ca0.0	Np from Fe0.02-Ca0.5	Np from Fe0.02-Ca1.0
Fe-O1	***N***	6.3	4.4	6.8	6.4	6.5
	***R* (Å)**	1.99	1.97	1.94	1.96	1.98
	σ²	0.009	0.010	0.007	0.008	0.010
Fe-Fe1	***N***	1.3	1.2	1.4	1.7	1.6
	***R* (Å)**	3.04	3.02	3.04	3.05	3.04
	σ²	0.009‡	0.009‡	0.007‡	0.009‡	0.010‡
Fe-Fe2	***N***	2.4	3.5	2.1	2.0	1.5
	***R* (Å)**	3.47	3.47	3.50	3.48	3.47
	σ²	0.009‡	0.009‡	0.007‡	0.009‡	0.010‡
Fe-O2	***N***	3.7‡‡	4.7‡‡	3.5‡‡	3.7‡‡	3.1‡‡
	***R* (Å)**	3.63	3.61	3.70	3.66	3.69
	σ²	0.005	0.007	0.006	0.012	0.015
Fe-O3	***N***	4.0*	4.0*	4.0*	4.0*	4.0*
	***R* (Å)**	4.41	4.45	4.37	4.39	4.39
	σ²	0.015	0.015	0.002	0.006	0.010
R-factor ($\times 10^{-3}$)		3.5	5.6	16.8	11.6	9.7

The amplitude reduction factor S_0^2 and the energy shift ΔE were set to 0.75 and -3.3 eV, respectively. *N* is the coordination number, *R* is the interatomic distance (Å) and *σ²* is the Debye-Weller factor. The error on *N*, *R* and *σ²* are usually estimated to be ± 10%, ± 1% and ± 20%, respectively. '*' denotes fixed parameters. ‡The σ² were forced to be equal to each other. ‡‡The coordination number for the Fe-O2 path was constrained as followed: $N_{Fe\text{-}O2} = N_{Fe\text{-}Fe1} + N_{Fe\text{-}Fe2}$.

As a consequence, the proportion of nanoparticulate Fe increased with both the Fe/OC and Ca/Fe ratios (Table III-5). This increased ratio is much more pronounced with the increasing Ca/Fe ratio for Fe/OC = 0.02 than for Fe/OC ≥ 0.05.

Table III-5 – Percentage of Fh-like Nps. For Fe/OC ≥ 0.05, the % was calculated by LCF. For Fe/OC = 0.02, the % was deduced from the isolation of the Fh-like Nps EXAFS signal. The error is estimated to be ± 10%. n.d.: not determined

Fh-like Nps %		**Ca/Fe ratio**			
		0.0	**0.1**	**0.5**	**1.0**
Fe/OC	**0.02**	30	n.d.	40	70
	0.05	82	80	80	83
	0.08	85	86	87	88

III.3.4. Specific surface area

The SAXS curves displayed a shoulder between 10^{-2} and 10^{-1} $Å^{-1}$ providing evidence of the existence of Fe nanoparticles (Figure III-10). The size of these Fe nanoparticles corresponded to Fe primary aggregates (radius between 2 and 5 nm) comprised of an assemblage of Fe primary beads (radius = 0.8 nm) (Guénet et al., 2017; Beauvois et al., 2020b). However, the increase in the scattered intensity at low q indicates that the Fe nanoparticles are aggregated as larger objects (Guénet et al., 2017; Beauvois et al., 2020b). For Fe/OC ≥ 0.05 and Ca/Fe ≥ 0.5, the shoulder is less pronounced indicating a dispersity in the Fe nanoparticle size and a high contribution of the larger objects to the total scattered intensity.

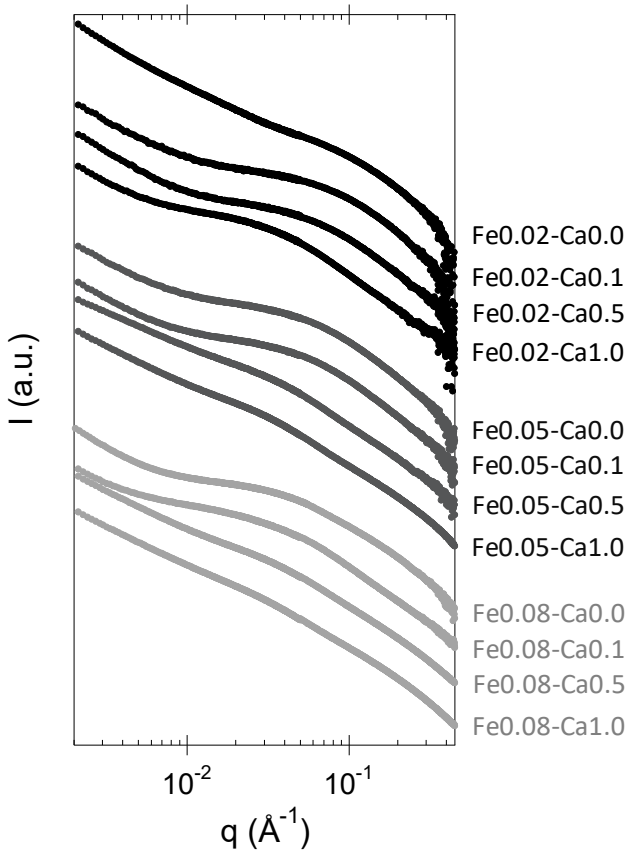

Figure III-10 – SAXS curves obtained for all samples.

Without Ca, the SSA remains constant ~1300 m² g^{-1} irrespective of the Fe/OC ratio, as demonstrated by Guénet et al. (2017). For Fe/OC = 0.02, the SSA remains constant while it increased with the increasing Ca/Fe ratio for Fe/OC ≥ 0.05 (Table III-6).

Table III-6 – Specific surface area (SSA, in m^2 g^{-1}) calculated for each sample. The errors on the parameters were 15%.

SSA (m^2 g^{-1})		Ca/Fe			
		0.0	**0.1**	**0.5**	**1.0**
Fe/OC	**0.02**	1300	1100	1300	1300
	0.05	1250	1250	1650	1600
	0.08	1400	1800	2000	1700

III.4. Discussion

The huge structural transition from aggregates to a micrometric network observed for the Fe-OM aggregates in the presence of Ca is not accompanied by a dramatic evolution of their sorption capacity as we expected (Beauvois et al., 2020b). However, the impact of Ca is far more complex. Calcium interacts with OM COOH sites that partially screen the interactions between Fe and OM (Beauvois et al., 2020b). As a consequence, the size of the Fh-like Nps increases, which should involve a decrease in their SSA and q_{max} (Hofmann et al., 2004; Wang et Shadman, 2013; Wang et al., 2013; Hiemstra et al., 2019). Surprisingly, our results did not confirm these expectations: q_{max} and the SSA increased concomitantly with the increasing size of Fh-like Nps (Figure III-11). Guénet et al. (2017) assumed that these unexpected data result from the decrease in the OM coating of the Fe aggregates.

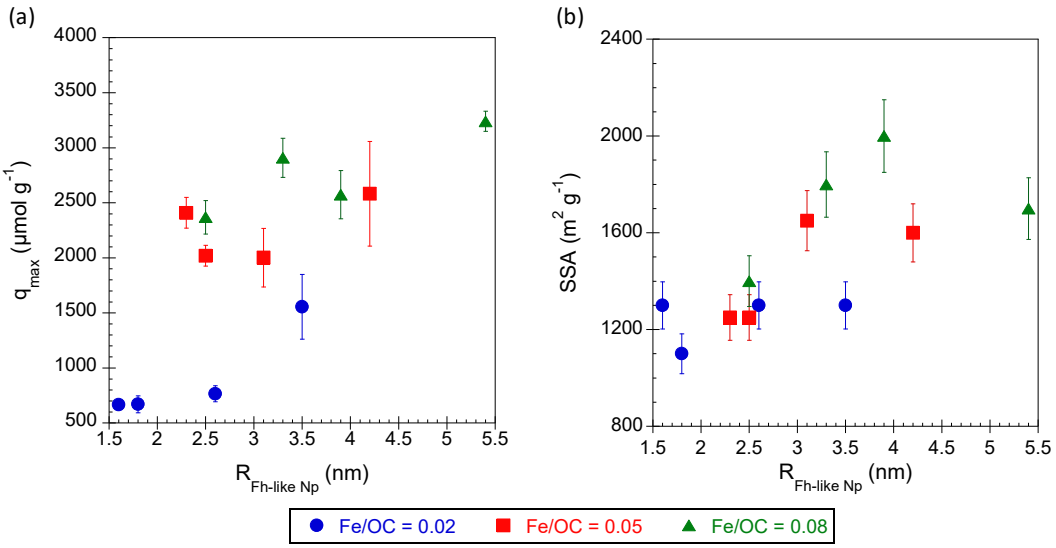

Figure III-11 – Variations in (a) the As q_{max} calculated from the Langmuir isotherm and (b) the SSA relative to the radius of Fh-like Nps for Fe/OC = 0.02 (blue circles), 0.05 (red squares) and 0.08 (green triangles).

In Fe-OM-Ca associations, Ca interacts mainly with OM COOH sites. Since LHA is composed of 7.5×10^{-3} mol of COOH per gram of C (Ritchie et Perdue, 2003), an apparent COOH concentration can be calculated for the >30kDa fraction for each sample. The subsequent molar ratio $(COOH/Ca)_{>30kDa}$ decreased with the increasing Ca content (Figure III-12). From a total [Ca] = 1.4 mmol L^{-1}, $(COOH/Ca)_{>30kDa}$ remains constant at 3 which is consistent with EXAFS data at Ca K-edge that revealed the presence of 3 C as second

neighbour for 1 Ca (Beauvois et al., 2020b). This result suggested a saturation of OM COOH sites by the Ca can partially screened the interactions between Fe and OM.

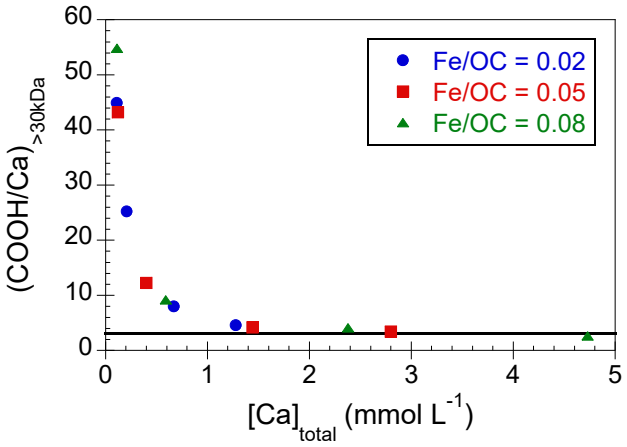

Figure III-12 – Ca concentration (mmol L^{-1}) in the >30kDa fraction relative to the total Ca concentration.

Knowing the OM COOH density, Fe and Ca concentrations in the >30 kDa fraction and given that Ca is bound to OM with a molar ratios $(COOH/Ca)_{>30\ kDa}$ = 3, the quantity of available OM COOH that are able to bind the Fe phases can be calculated. For Fe/OC = 0.02, the SSA remained constant whereas for Fe/OC ≥ 0.05, the SSA tended to decrease with the increasing availability of the OM COOH sites (Figure III-13). Therefore, at a high [Ca], the coating of the Fe phases by OM decreased and the site availability of the Fe phases increased.

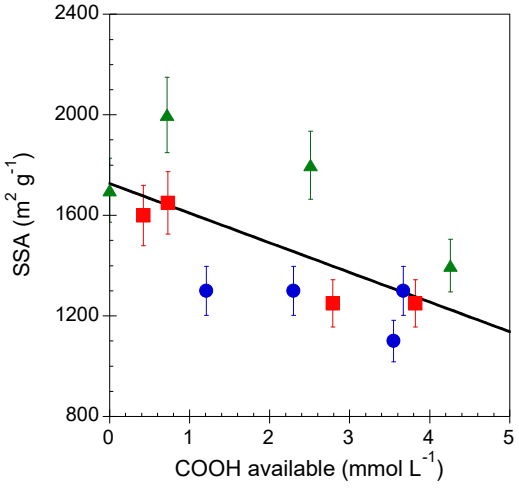

Figure III-13 – Evolution of the SSA (m^2 g^{-1}) relative to the quantity of available COOH (mmol L^{-1}).

Another major parameter that controls the adsorption capacity of Fe-OM aggregates is the Fe speciation (Figure III-14). An exponential fit of the dataset demonstrated that when Fh-like Nps were not formed, As adsorption could occur through the Fe(III)-oligomers. This assumption was in agreement with previous results demonstrating that As binding by Fe(III) monomers or tetramers may have occurred, leading to the formation of As-Fe-OM ternary complexes (Mikutta et Kretzschmar, 2011; Hoffmann et al., 2013; Catrouillet et al., 2016). The adsorption capacity of Fe(III)-oligomers can thus be estimated as q_{max} ~250 µmol g^{-1} with a Langmuir K_{ads} value of ~20×10^{-3} L μmol^{-1}. The q_{max} value increases with the increasing Fh-like Np% which suggests that Fh-like Nps exhibit higher adsorption capacities than Fe(III)-oligomers. For As-Fe-OM ternary complexes, in which Fe speciation was dominated by Fe(III)-oligomers, As is only bound to Fe as a bidentate mononuclear edge-sharing complex (^{2}E) due to geometric constraints (Guénet et al., 2016). For Fh-like Nps, As is bound as ^{2}E complexes and as bidentate binuclear corner-sharing (^{2}C) complexes (Ona-Nguema et al., 2005). Therefore, As can bind to Fh-like Nps in two ways as compared to Fe(III) oligomers. Moreover, the Fe vacancies in the Fh structure provide a higher density of adsorption sites for Fh-like Nps than for Fe(III)-oligomers (Jambor et Dutrizac, 1998; Ona-Nguema et al., 2005). However, Langmuir K_{ads} decreased with the increasing Fh-like Nps % suggesting that As has higher affinity for Fe(III)-oligomers than for Fh-like Nps.

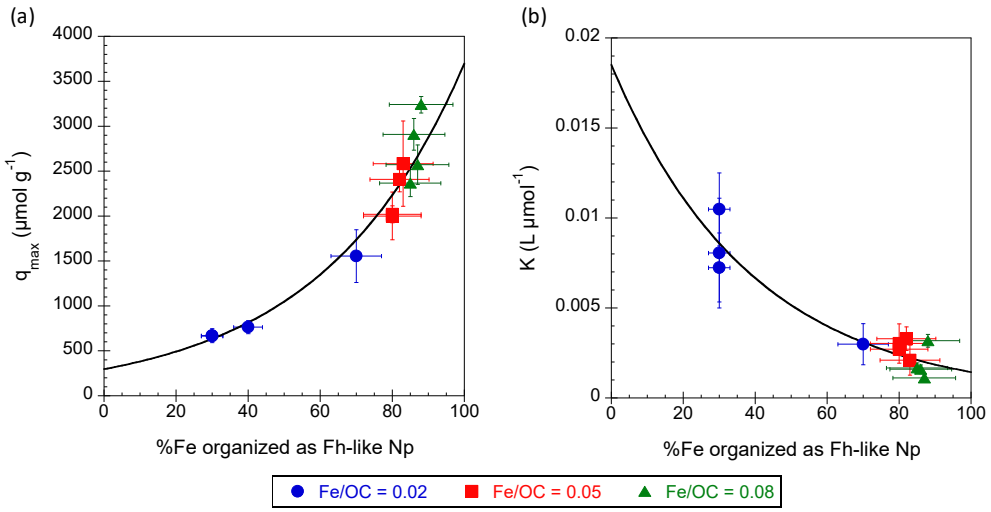

Figure III-14 – Variations of (a) q_{max} and (b) Langmuir K_{ads} relative to the percentage of Fe organized as Fh-like Np for Fe/OC = 0.02 (blue circles), 0.05 (red squares) and 0.08 (green triangles).

As a consequence, the speciation of Fe impacts the oxidation-reduction behavior of the adsorbed As given that the formation of ^{2}E stabilizes As(III) while ^{2}C complexes lead to the oxidation of As(III) as As(V) (Guénet et al., 2016). Moreover, these results demonstrate that the speciation of Fe within Fe-OM aggregates should thus be taken into account to evaluate and predict their ability to control metal(loid) mobility under environmental conditions. Since this distribution is dependent on the amounts of Ca and OM, their concentrations must be systematically determined. To reach this objective, the distribution of Fe between Fe(III)-oligomers and Fh-like Nps could, for example, be used to improve existing geochemical models via the implementation of new parameters.

III.5. Conclusions

The overall reactivity of Fe-OM aggregates strongly depends on their complex structural organization that varies in the presence of Ca. In this study, we developed a complete description of the parameters that control the surface reactivity of Fe within synthesized Fe-OM-Ca aggregates using As as a probe. Our study provided evidence that:

- Calcium not only controls the ionic strength but also plays a significant role in the reactivity of Fe-OM aggregates by increasing their sorption capacity acting as a competitor of Fe for binding OM;
- Fe(III)-oligomers and Fh-like Nps exhibit a high affinity for As and a high sorption capacity, respectively. The percentage of Fe distributed as Fe(III)-oligomers and Fh-like Nps is therefore a major parameter controlling As binding by Fe-OM aggregates;
- The partial screening of the interaction between Fe and OM by Ca leads to an increase in the percentage of Fh-like Nps for low Fe/OC and to the decrease in the Fh-like Nps coating rate by OM for high Fe/OC values. The consequence of these interactions is the subsequent increase in the availability of the Fe binding sites;
- The concentration of Fe(III)-oligomers is a major parameter controlling the As binding as they exhibit a high affinity for As;
- For low Fe/OC, the increase in the amount of Ca leads to an increase in Fh-like Nps and increases the reactivity of the Fe-OM aggregates.

Chapitre IV. Conclusions et perspectives

IV.1. Conclusions

L'objectif de ce travail de thèse était d'appréhender les modifications structurales des agrégats fer-matière organique (Fe-MO) induites par la présence de cations majeurs, eux-mêmes omniprésents dans le milieu naturel, et cela afin de mieux comprendre leur réactivité vis-à-vis, notamment, des polluants métalliques. Comprendre ces mécanismes est absolument nécessaire puisque les agrégats Fe-MO sont ubiquistes et peuvent être des facteurs majeurs dans le contrôle des cycles biogéochimiques de nombreux éléments traces.

Dans ce contexte, ce travail de recherche a permis de :

- décrire indépendamment l'influence du calcium (Ca) et de l'aluminium (Al) sur l'organisation structurale multi-échelle des agrégats Fe-MO ainsi que les mécanismes mis en jeux.
- Montrer que la transition structurale des agrégats Fe-MO induite par le Ca modifie leur réactivité vis-à-vis de l'arsenic.

IV.1.1. Impact du Ca et de l'Al sur l'organisation structurale des agrégats Fe-MO.

Dans la première partie de cette thèse, j'ai caractérisé l'organisation multi-échelle d'hétéro-agrégats biphasiques Fe-MO à différents rapports Fe/carbone organique (CO) et cations (Ca ou Al)/Fe. En combinant des techniques expérimentales de caractérisation structurale de l'échelle atomique à l'échelle macroscopique, la structure des agrégats a pu être finement décrite. J'ai pu mettre en évidence que le Ca et l'Al modifient significativement l'organisation structurelle des agrégats.

Avec l'augmentation des teneurs en Ca et Al, les agrégats Fe-MO évoluent d'un état colloïdal stable vers un réseau micrométrique dont les connexions sont assurées par Ca et Al. Si d'un point de vue macroscopique, le Ca et l'Al induisent la formation d'un réseau, les mécanismes mis en jeu sont pourtant différents.

Les plus fortes concentrations en Ca agissent uniquement sur la MO. Pour les plus fortes teneurs en Ca, l'ensemble des agrégats Fe-MO est retenu dans la fraction >0.2 µm. Le Ca induit donc la décantation des agrégats Fe-MO. L'observation par cryo-microscopie (électronique et des rayons X) des agrégats a distinctement mis en évidence la formation d'un réseau. Ces résultats ont été confirmés par des mesures SANS. Les mesures XAS au seuil K du Ca, et en particulier la simulation des signaux EXAFS, ont mis en évidence la présence d'un voisin Ca à 3.85 Å, démontrant la formation de dimères de Ca. En outre, pour reproduire au mieux le signal EXAFS, il est nécessaire d'ajouter 3 atomes de C dans la deuxième sphère de coordination du Ca, indiquant la formation de complexes de sphère interne entre le Ca et la MO. Ces dimères sont principalement liés aux groupements carboxyliques de la MO. **A forte concentration en Ca, la formation de dimères de Ca permet de créer des ponts Ca entre les colloïdes/macromolécules de MO qui induisent la formation d'un réseau micrométrique qui décante pour un rapport, Ca/CO ≥ 0.023.**

L'Al agit sur la MO et les phases ferriques. Les spectres XANES au seuil K de l'Al ont démontré que pour les plus faibles concentrations en Al, ce dernier est principalement sous forme de monomères et d'oligomères liés à la MO. Avec l'augmentation de la teneur en Al, le décalage du seuil d'absorption vers les basses énergies révèle un processus de polymérisation des monomères/oligomères. La structuration des spectres XANES, bien que faible, suggère la formation d'hydroxydes d'Al amorphes. La présence d'un pré-seuil indique la présence de liaisons Al-O-Fe suggérant soit la formation de complexes de surface soit l'incorporation d'Al dans les nanoparticules de Fe. Les différentes espèces d'Al, monomères, oligomères et hydroxydes, sont liées aux molécules de MO *via* les groupements carboxyliques. Ceci mène à la **formation de MO micrométrique qui décante pour un rapport Al/OC ≥ 0.043**.

La présence de Ca et Al entraine une augmentation du nombre et de la taille des nanoparticules de Fe. La phase ferrique des agrégats Fe-MO est constituée d'oligomères de Fe(III) et de nanoparticules de type ferrihydrite (Np-Fh), tous deux liés à la MO (Guénet et al., 2017). Avec l'augmentation de la teneur en Ca ou Al, la taille des nanoparticules

augmente comme le montre les combinaisons linéaires des signaux EXAFS au seuil K du Fe et les mesures SAXS. Ces dernières ont montré que leur rayon augmente de ~ 2 nm à 5 nm Pour les fortes concentrations en Ca et Al, la création du réseau micrométrique via les liaisons Ca-MO et polymères d'Al-MO induit une diminution du taux de recouvrement des nanoparticules de Fe par la MO. La conséquence directe est un accroissement de la taille de ces nanoparticules.

L'ensemble de ces résultats est schématisé sur la Figure IV-1.

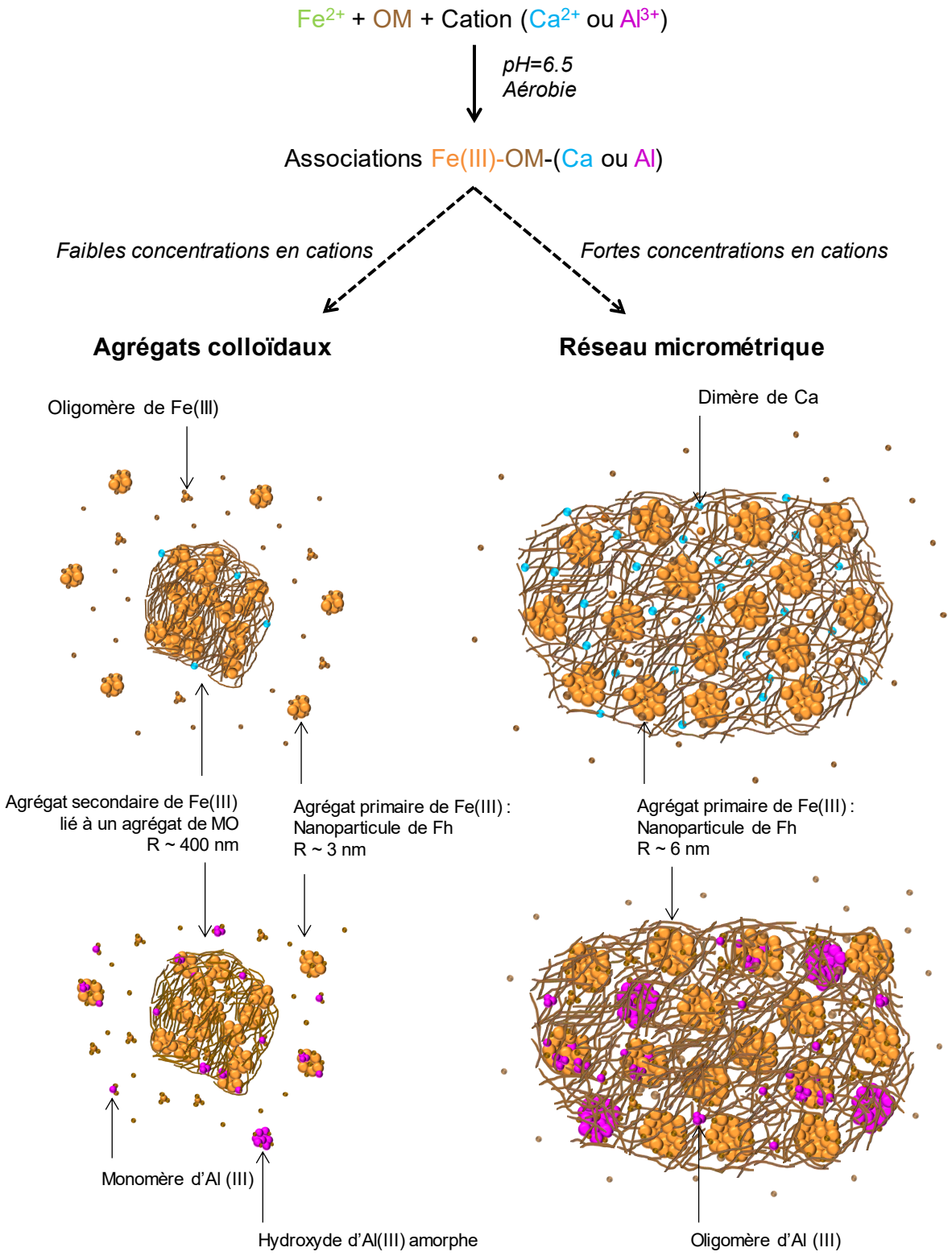

Figure IV-1 – Schéma récapitulatif de l'organisation structurale des agrégats Fe-MO en fonction de la concentration en Ca ou Al.

IV.1.2. Impact sur la réactivité des agrégats Fe-MO vis à vis de l'As

Dans la deuxième partie de mon travail, je me suis intéressé à l'impact des modifications structurales en présence de Ca sur la réactivité des agrégats Fe-MO vis-à-vis des éléments chimiques. Dans une première approche, je me suis plus particulièrement intéressé à la réactivité de surface des phases de Fe. Pour cela, j'ai utilisé l'As comme sonde étant donné sa forte affinité pour le Fe comparé à la MO.

La transition structurale a peu d'impact sur la réactivité des phases ferriques vis à vis de l'As. Cependant la présence de Ca induit une augmentation de la capacité d'adsorption des agrégats Fe-MO. Les mécanismes impliqués dans cette augmentation sont plus complexes que la seule transition structurale.

En fait, c'est la proportion oligomères/nanoparticules de Fe qui contrôle la capacité de sorption des agrégats Fe-MO. Les isothermes de Langmuir ont montré qu'avec l'augmentation du pourcentage de nanoparticules :

- la constante de complexation, K_{ads}, décroit
- la capacité d'adsorption maximale, q_{max}, croît

Les oligomères de Fe(III) ont donc une forte affinité pour l'As alors que les nanoparticules ont une grande capacité d'adsorption. A faible rapport Fe/CO, le Ca forme des complexes Ca-MO qui limitent partiellement les interactions Fe-MO, permettant la croissance des oligomères en nanoparticules. Indirectement, le Ca augmente donc les capacités d'adsorption des agrégats Fe-MO.

La présence de Ca diminue le recouvrement des nanoparticules de Fe par la MO. Les fonctions de surface de la MO majoritairement impliquées dans les liaisons Fe-MO et Ca-MO sont les groupements carboxyliques. En combinant le nombre de sites C lié au Ca aux résultats de modélisation des courbes de SAXS, j'ai mis en évidence que la surface spécifique des nanoparticules de Fe diminue avec l'augmentation de la disponibilité des sites carboxyliques. Ainsi, plus il y a de Ca, moins la MO se complexe au Fe, et plus les sites de surface des nanoparticules de Fe sont disponibles pour adsorber l'As.

L'ensemble de ces résultats est résumé dans le schéma de la Figure IV-2.

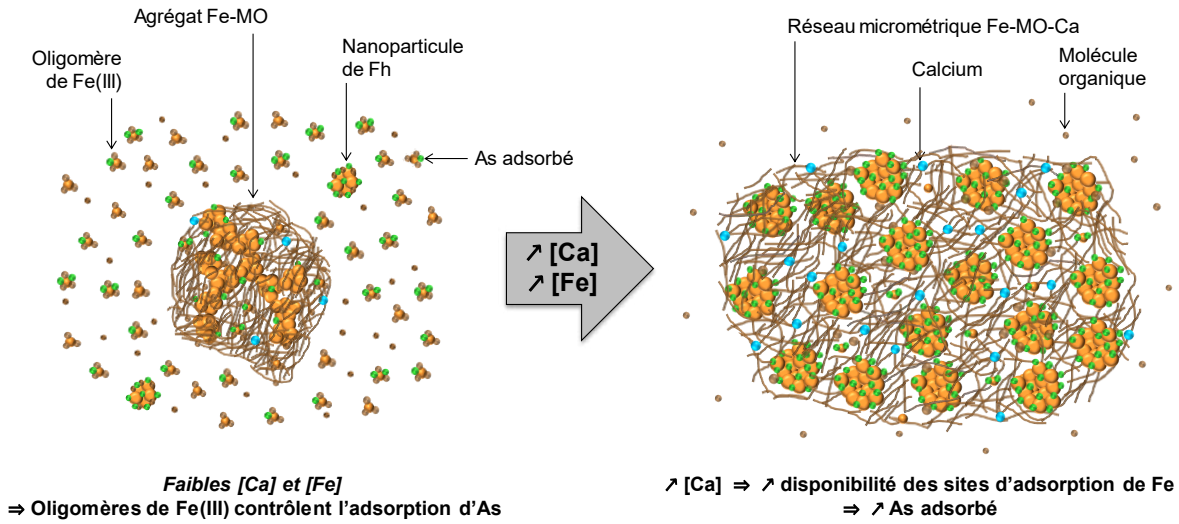

Figure IV-2 – Schéma récapitulatif de la réactivité des phases de Fe vis-à-vis de l'As dans les agrégats Fe-MO en présence de Ca.

IV.1.3. Impact environnemental : cas des zones humides

Les zones humides (ZH) sont des réacteurs biogéochimiques capables de former de grandes quantités d'agrégats Fe-MO. La dynamique du Fe et de la MO dans les ZH, y est majoritairement contrôlée par les alternances de saturation/désaturation en eau des sols qui induisent des variations de conditions d'oxydoréduction. Ces variations agissent en premier lieu sur la solubilité du Fe qui, à son tour, contrôle celle des éléments associés au Fe tels que la MO mais aussi les éléments traces (Ponnamperuma, 1972; Grybos et al., 2009). En période de hautes eaux, les sols sont saturés, des conditions réductrices se mettent en place, le Fe(III) est libéré sous forme de Fe(II) ainsi que tous les élèments associés. Lorsque le niveau de l'eau baisse, les conditions oxydantes sont rétablies et le Fe(II) s'oxyde et s'hydrolyse en présence de grandes quantités de MO soluble ou colloidale, mais aussi de métaux traces et de cations majeurs pour former des hétéro-agrégats Fe-cation-MO. La MO inhibe la croissance des phases de Fe qui sont ainsi distribuées en oligomères et nanoparticules, liés à la MO. Les études structurales et de réactivité menées au cours de

mes travaux ont montré que la présence de Ca ne modifiait pas drastiquement la réactivité des associations Fe-MO. En revanche, pour dans des conditions telles que Ca/CO $\geq$ 0.026 mon étude a montré la formation d'un réseau micrométrique. Des mesures de concentrations des éléments majeurs et traces sur une solution de sol de la zone humide riparienne de Mercy filtrée à 0.2 µm ont mis en évidence une valeur moyenne de 0.11 pour les rapports Ca/CO. Les conditions dans ce système d'étude sont donc favorables à la formation du réseau, les hétéro-agrégats Fe-MO sont peu mobiles et restent probablement piégés dans la porosité du sol et/ou sédimentent à la surface des composants du sol. La mobilité du Fe et de la MO mais aussi de tous les éléments qui y sont associés, pourrait donc être plus limitée que ce qui est communément admis dans les études de transfert colloïdal des éléments chimiques. Cette remarque doit cependant être nuancée, puisque la mobilité des agrégats Fe-MO et des éléments associés dépendra de la solidité du réseau notamment face aux flux d'eau qui sont une des plus fortes contraintes physiques dans un sol de ZH. Or, s'il est possible de penser que dans la porosité d'un sol de ZH, où les flux sont relativement faibles, cette contrainte n'est pas suffisante pour entrainer une dislocation du réseau, cela est moins probable, lors du dégel des pergélisols dont on sait qu'ils sont une source importante d'agrégat Fe-MO dans l'environnement. Ce sont autant de points qu'il reste à éclaircir.

IV.2. Perspectives

IV.2.1. Approfondissement de l'étude des processus de nucléation-croissance des agrégats Fe-MO

Une étude connexe à mon travail de thèse s'est intéressée aux processus de nucléation-croissance des phases de Fe en présence de MO, à un rapport Fe/CO = 0.08, *via* le suivi de synthèses *in situ* par 'quick-EXAFS' (Annexe 2). L'analyse chimiométrique par MCR-ALS des données a permis d'extraire deux espèces de Fe(III) finales, des oligomères et des nanoparticules de type ferrihydrite. Nous les avons utilisées pour étudier les signaux EXAFS des agrégats synthétisés au laboratoire en présence de cations. Si l'analyse s'est

avérée concluante pour les hauts rapports Fe/CO, la spéciation du Fe pour les faibles Fe/CO est différente. Une piste pour l'étude des processus de nucléation-croissance du Fe est la réalisation de synthèses dans un circuit micro-fluidique. En effet, la technologie micro-fluidique a ceci d'intéressant qu'elle permet de transposer l'échelle temporelle en échelle spatiale, le long du canal (Chan et al., 2007). Dans de telles conditions, il est possible de discriminer les différentes étapes de nucléation-croissance des oxyhydroxydes de Fe, le long du canal en suivant l'évolution de la spéciation du Fe par XAS. Dans ce contexte, nous avons développé un circuit de micro-fluidique pour étudier l'oxydation-hydrolyse du Fe(II) en présence de MO par augmentation de pH (Figure IV-3).

Figure IV-3 – Circuit micro-fluidique utilisé pour la synthèse d'agrégats Fe-MO en laboratoire.

Des tests préliminaires ont permis de déterminer les conditions opératoires optimales : taille des canaux, vitesses d'injection et concentrations des réactifs. Nous avons ensuite réalisé les synthèses *in situ* sur la ligne de lumière LUCIA avec un suivi par XAS. Le faisceau émis par cette ligne peut être focalisé ce qui permet d'obtenir une bonne résolution spatiale et donc temporelle. L'enceinte expérience étant sous vide primaire, il a été nécessaire de développer un outil permettant la circulation de liquide dans de telles conditions (Figure IV-4 et Annexe 3).

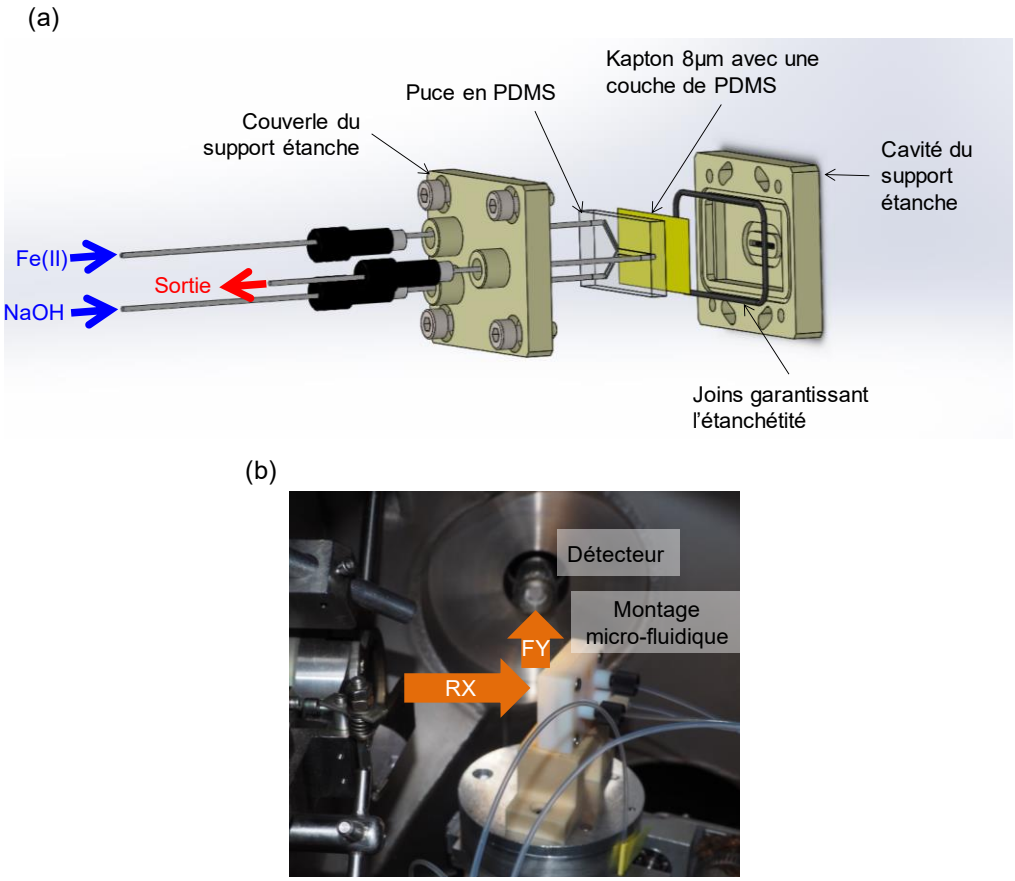

Figure IV-4 – (a) Schéma du support étanche et de la puce micro-fluidique utilisée pour les mesures sur la ligne LUCIA et (b) montage expérimental installé sur la ligne LUCIA.

Les résultats obtenus sont assez encourageants puisqu'il a été possible d'enregistrer des spectres Fe(II) stables au cours du temps (Figure IV-5a). Ce qui démontre l'efficacité de cette technique pour s'affranchir des effets de photo-altération des espèces mesurées en circulation Dans les mêmes conditions (concentration de Fe et pH), des mesures statiques ont démontré que le Fe(II) s'oxyde sous le faisceau. La circulation dans le canal permet de renouveler la solution et de s'affranchir de cet artéfact. La transposition de l'échelle temporelle en échelle spatiale le long du flux a été cependant limitée par la précipitation très rapide du Fe(II) en oxyhydroxyde de Fe dès le contact entre Fe(II) et NaOH, comme en témoigne la ligne marron foncée sur la Figure IV-3. Etant donnée la différence d'acidité entre les deux solutions, un gradient de pH se créé perpendiculairement au flux, ce qui permettrait de pouvoir observer la transition du Fe(II) au Fe(III). Cependant, les oxyhydroxydes de Fe s'accumulent sous l'effet du faisceau et il est donc difficile de suivre leur évolution en un

point donné du canal. En déplaçant le canal régulièrement, nous avons pu nous affranchir partiellement de cet artéfact. Nous avons réussi à obtenir un jeu de spectres XANES montrant un décalage vers les hautes énergies du seuil d'absorption, révélateur de l'oxydation du Fe(II) en Fe(III) (Figure IV-5b). Mon objectif est de réaliser une analyse chimiométrique par MCR-ALS mais pour cela plus de données doivent être acquises.

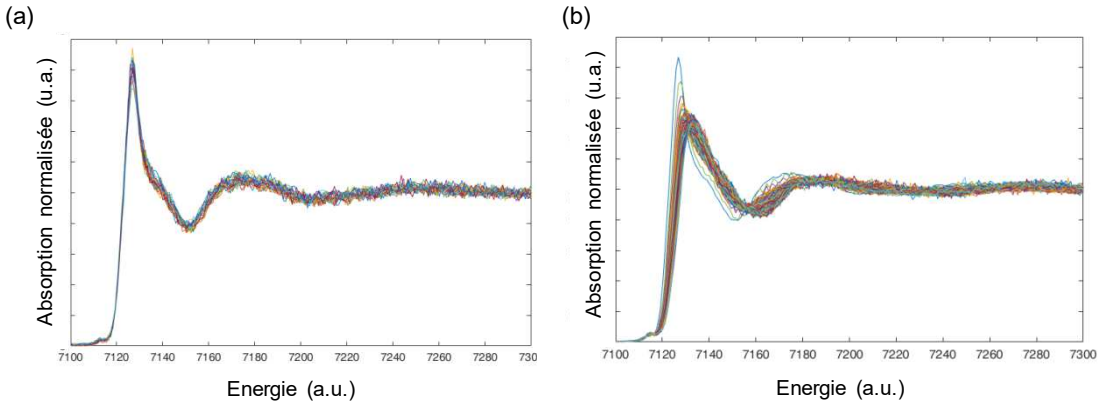

Figure IV-5 – Spectres XANES (a) de Fe(II) enregistrés sous circulation et (b) d'une expérience ayant fonctionnée correctement.

Cette démarche pourrait également permettre d'étudier la polymérisation des hydroxydes d'Al amorphes dans les agrégats Fe-MO-Al afin de déterminer plus finement les phases d'Al formées

IV.2.2. Impact des flux d'eau

Pour de fortes concentrations en Ca ou Al, les agrégats Fe-MO forment des réseaux micrométriques qui sédimentent. Ces structures micrométriques sont très probablement piégées dans la porosité du sol ce qui limite leur mobilité. Cependant, dans les systèmes naturels, la porosité de sol peut être traversée de façon plus ou moins temporaire par des flux d'eau, notamment lors de la reprise des écoulements. Le réseau micrométrique va-t-il résister ou bien va-t-il se segmenter en petites structures plus mobiles ? Pour répondre à ces questions, la flow field fractionnation (A4F) pourrait être une technique adaptée. Les nanoparticules sont éluées dans un canal, les plus petites en premier suivies des plus

grosses. Elles passent successivement dans un détecteur UV-visible et de diffusion de lumière (DLS). Le temps d'élution est proportionnel à leur taille.

Nous avons réalisé des premiers tests sur les associations Fe-MO-Ca. Les résultats obtenus pour Fe/OC = 0.08 et Ca/Fe = 0.5 sont présentés Figure IV-6. Un pic est visible entre 0 et 5 min, indiquant la présence de petites molécules dont le poids moléculaire est de l'ordre de 10 kDa. Cette population contient de la MO et du Ca dont la présence a été montré dans la fraction <30 kDa (Table II.1-9). Le dernier pic à 13 min indique la présence de nanoparticules de taille > 200 nm. Le pic entre 5 et 10 m indique, quant à lui, la présence d'agrégats de taille ≈ 100nm. Cette population n'a cependant jamais été observée ni par SANS/SAXS ni par ultrafiltration. La fraction 0.2 µm-30 kDa est en effet exempte de Fe, MO et Ca (Table II.1-9). Ces observations suggèrent donc que le réseau micrométrique formé pour Ca/CO $\geq$ 0.023 se morcèle sous l'effet d'un flux et d'une pression. L'étude des autres agrégats doit être poursuivie afin de confirmer ou d'affirmer ces premières observations. Il est également crucial pour valider l'utilisation de cette technique de comparer les forces appliquées dans le canal de micro-fluidiques avec les forces en action dans la porosité des sols de zones humide en période d'écoulements.

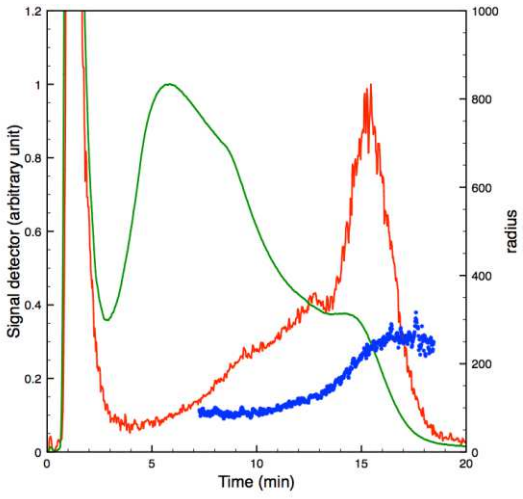

Figure IV-6 – Résultats d'A4F pour l'association Fe-MO-Ca avec Fe/CO = 0.08 et Ca/Fe = 0.5. Sur cette figure sont représentés le signal de d'absorption UV (vert) et de diffusion de lumière (rouge) en fonction du temps. Le rayon de gyration des agrégats est représenté en bleu.

IV.2.3. Influence de l'aluminium sur la réactivité des agrégats Fe-MO

A fortes concentrations, les monomères et oligomères d'Al polymérisent pour former des hydroxydes amorphes. Il a été démontré que les phases alumineuses interagissaient avec les phases de Fe via la formation de liaisons Al-O-Fe. Ceci pourrait diminuer la disponibilité des sites d'adsorption du Fe. Mais, ces hydroxydes d'Al possèdent la capacité d'adsorber les métaux et métalloïdes (Manning, 2005; Mertens et al., 2016), ce qui pourrait aussi augmenter la réactivité globale des associations Fe-MO. Deux effets antagonistes sont donc possibles et des expériences d'adsorption d'As sur les associations Fe-MO-Al permettraient d'apporter quelques réponses à cette interrogation.

IV.2.4. Impact du silicium sur la structure et la réactivité des agrégats Fe-MO

Au cours de ce travail, je me suis intéressé à l'impact de deux cations majeurs sur la structure globale des associations Fe-MO, chacun ayant un comportement particulier vis-à-vis des composantes de ces hétéroagrégats :

- le Ca a plus d'affinité pour la MO que le Fe
- l'Al interagit, quand à lui, à la fois avec le Fe et la MO

Si les mécanismes d'interaction sont différents, le résultat macroscopique est le même. Dans ce contexte, il semble intéressant d'étudier l'impact d'un troisième ion majeur. Le choix pourrait se porter sur le silicium (Si) car il est connu pour inhiber la croissance et la cristallinité des oxyhyrdoxydes de Fe en venant se placer à leur surface (Doelsch et al., 2000; Doelsch et al., 2001; Pokrovski et al., 2003). De plus, le Si a une très faible affinité pour la MO (Pokrovski et Schott, 1998). Les mécanismes d'interaction du Si avec les agrégats Fe-MO et les conséquences sur leur organisation structurale globale et leur réactivité doivent être très différentes du Ca ou de l'Al.

IV.2.5. Complexification des systèmes Fe-MO modèles

Pour la compréhension globale du devenir des associations Fe-MO dans l'environnement, il convient d'étudier des systèmes modèles simplifiés. Ainsi des agrégats contenant du Fe et une MO particulière (la léonardite, un acide humique) a permis de donner une description fine de l'organisation structurale des agrégats (Guénet et al., 2017). Au cours de mes travaux, je me suis impliqué à complexifier ce système modèle pour se rapprocher un peu plus des conditions environnementales. Ainsi, j'ai ajouté soit du Ca soit de l'Al pour déterminer les mécanismes d'interaction de ces deux cations avec les différentes phases de Fe et/ou de MO. Cependant, les cations, et plus généralement les ions, sont la plupart du temps présents en même temps dans les systèmes naturels. Il semble donc judicieux de complexifier d'avantage le système modèle en y intégrant plusieurs ions concomitamment. En particulier, l'impact simultané du Ca et de l'Al doit être envisagé pour déterminer si leur effet sur les structures Fe-MO s'additionneront, s'ils entreront en compétition l'un avec l'autre ou s'ils interagiront de manière indépendante.

IV.2.6. Interaction des agrégats Fe-MO avec les nano-plastiques

L'utilisation du plastique s'est considérablement accrue ces dernières années. Sa présence sous forme de nano-plastiques dans de nombreux systèmes environnementaux a été récemment mise en avant. L'un des grands enjeux environnementaux actuels est donc la compréhension du comportement, du devenir et de la dynamique des nano-plastiques dans les systèmes naturels. Les plastiques peuvent interagir avec les colloïdes organiques ou inorganiques avec des conséquences différentes sur leur mobilité (Cai et al., 2018; Oriekhova et Stoll, 2018; Song et al., 2019). De plus, il a été démontré que les nano-plastiques sont de très bons adsorbants des métaux (Davranche et al., 2019). Au-delà de ces considérations, leur présence dans des sols riches en Fe et MO rend crucial l'étude de l'interaction entre les plastiques, les phases organiques et/ou inorganiques et les métaux polluants. Pour ce faire, la démarche scientifique employée dans ma thèse à l'étude des

associations plastiques-Fe, plastique-MO et plastiques-Fe-MO s'appliquerait parfaitement. Il s'agirait dans un premier temps de caractériser l'organisation multi-échelle des associations *via* l'approche multi-technique développée pour les agrégats Fe-MO et, ensuite, d'étudier la réactivité des associations plastiques-(Fe)-(MO) à la lumière de leur organisation structurale.

Références

Adhikari D., Sowers T., Stuckey J. W., Wang X., Sparks D. L. et Yang Y. (2019) Formation and redox reactivity of ferrihydrite-organic carbon-calcium co-precipitates. *Geochim. Cosmochim. Acta* **244**, 86-98. DOI: 10.1016/j.gca.2018.09.026.

Adra A., Morin G., Ona-Nguema G., Menguy N., Maillot F., Casiot C., Bruneel O., Lebrun S., Juillot F. et Brest J. (2013) Arsenic Scavenging by Aluminum-Substituted Ferrihydrites in a Circumneutral pH River Impacted by Acid Mine Drainage. *Environ. Sci. Technol.* **47**, 12784-12792. DOI: 10.1021/es4020234.

Adusei-Gyamfi J., Ouddane B., Rietveld L., Cornard J.-P. et Criquet J. (2019) Natural organic matter-cations complexation and its impact on water treatment: A critical review. *Water Res.* **160**, 130-147. DOI: 10.1016/j.watres.2019.05.064.

Ali M. A. et Dzombak D. A. (1996) Effects of simple organic acids on sorption of Cu2+ and Ca2+ on goethite. *Geochim. Cosmochim. Acta* **60**, 291-304. DOI: 10.1016/0016-7037(95)00385-1.

Al-Sid-Cheikh M., Pédrot M., Dia A., Guenet H., Vantelon D., Davranche M., Gruau G. et Delhaye T. (2015) Interactions between natural organic matter, sulfur, arsenic and iron oxides in re-oxidation compounds within riparian wetlands: NanoSIMS and X-ray adsorption spectroscopy evidences. *Sci. Total Environ.* **515-516**, 118-128. DOI: 10.1016/j.scitotenv.2015.02.047.

Auffan M., Rose J., Proux O., Borschneck D., Masion A., Chaurand P., Hazemann J.-L., Chaneac C., Jolivet J.-P., Wiesner M. R., Van Geen A. et Bottero J.-Y. (2008) Enhanced Adsorption of Arsenic onto Maghemites Nanoparticles: As(III) as a Probe of the Surface Structure and Heterogeneity. *Langmuir* **24**, 3215-3222. DOI: 10.1021/la702998x.

Baalousha M., Manciulea A., Cumberland S., Kendall K. et Lead J. R. (2008) Aggregation and surface properties or iron oxide nanoparticles: influence of pH and natural organic matter. *Environ. Toxicol. Chem.* **27**, 1875. DOI: 10.1897/07-559.1.

Baalousha M., Motelica-Heino M. et Coustumer P. L. (2006) Conformation and size of humic substances: Effects of major cation concentration and type, pH, salinity, and residence time. *Colloids Surf. Physicochem. Eng. Asp.* **272**, 48-55. DOI: 10.1016/j.colsurfa.2005.07.010.

Beauvois A., Vantelon D., Jestin J., Bouhnik-Le Coz M., Catrouillet C., Briois V., Bizien T. et Davranche M. (2020a) How crucial is the impact of calcium on the reactivity of iron-organic matter aggregates? Insights from arsenic. *J. Hazard. Mater.*, 124127. DOI: 10.1016/j.jhazmat.2020.124127.

Beauvois A., Vantelon D., Jestin J., Rivard C., Bouhnik-Le Coz M., Dupont A., Briois V., Bizien T., Sorrentino A., Wu B., Appavou M.-S., Lotfi-Kalahroodi E., Pierson-Wickmann A.-C. et Davranche M. (2020b) How does calcium drive the structural organization of iron–organic matter aggregates? A multiscale investigation. *Environ. Sci. Nano* **7**, 2833-2849. DOI: 10.1039/D0EN00412J.

Bi S. (2004) Studies on the mechanism of hydrolysis and polymerization of aluminum salts in aqueous solution: correlations between the “Core-links” model and “Cage-like” Keggin-Al13 model. *Coord. Chem. Rev.* **248**, 441-455. DOI: 10.1016/j.ccr.2003.11.001.

Briois V., La Fontaine C., Belin S., Barthe L., Moreno T., Pinty V., Carcy A., Girardot R. et Fonda E. (2016) ROCK: the new Quick-EXAFS beamline at SOLEIL. *J. Phys. Conf. Ser.* **712**, 012149. DOI: 10.1088/1742-6596/712/1/012149.

Bruggeman C., Liu D. J. et Maes N. (2010) Influence of Boom Clay organic matter on the adsorption of Eu^{3+} by illite – geochemical modelling using the component additivity approach. *Radiochim. Acta* **98**, 597-605. DOI: 10.1524/ract.2010.1759.

Cabaniss S. E. (2009) Forward Modeling of Metal Complexation by NOM: I. *A priori* Prediction of Conditional Constants and Speciation. *Environ. Sci. Technol.* **43**, 2838-2844. DOI: 10.1021/es8015793.

Cabaniss S. E. (2011) Forward Modeling of Metal Complexation by NOM: II. Prediction of Binding Site Properties. *Environ. Sci. Technol.* **45**, 3202-3209. DOI: 10.1021/es102408w.

Cai L., Hu L., Shi H., Ye J., Zhang Y. et Kim H. (2018) Effects of inorganic ions and natural organic matter on the aggregation of nanoplastics. *Chemosphere* **197**, 142-151. DOI: 10.1016/j.chemosphere.2018.01.052.

Cao J., Xue H. et Sigg L. (2006) Effects of pH and Ca competition on complexation of cadmium by fulvic acids and by natural organic ligands from a river and a lake. *Aquat. Geochem.* **12**, 375-387. DOI: 10.1007/s10498-006-9004-6.

Catrouillet C., Davranche M., Dia A., Bouhnik-Le Coz M., Demangeat E. et Gruau G. (2016) Does As(III) interact with Fe(II), Fe(III) and organic matter through ternary complexes? *J. Colloid Interface Sci.* **470**, 153-161. DOI: 10.1016/j.jcis.2016.02.047.

Chan E. M., Marcus M. A., Fakra S., ElNaggar M., Mathies R. A. et Alivisatos A. P. (2007) Millisecond Kinetics of Nanocrystal Cation Exchange Using Microfluidic X-ray Absorption Spectroscopy †. *J. Phys. Chem. A* **111**, 12210-12215. DOI: 10.1021/jp073474u.

Chen C., Dynes J. J., Wang J. et Sparks D. L. (2014) Properties of Fe-Organic Matter Associations via Coprecipitation versus Adsorption. *Environ. Sci. Technol.* **48**, 13751-13759. DOI: 10.1021/es503669u.

Chen C. et Thompson A. (2018) Ferrous Iron Oxidation under Varying pO_2 Levels: The Effect of Fe(III)/Al(III) Oxide Minerals and Organic Matter. *Environ. Sci. Technol.* **52**, 597-606. DOI: 10.1021/acs.est.7b05102.

Christl I. (2012) Ionic strength- and pH-dependence of calcium binding by terrestrial humic acids. *Environ. Chem.* **9**, 89. DOI: 10.1071/EN11112.

Christl I. et Kretzschmar R. (2001) Interaction of copper and fulvic acid at the hematite-water interface. *Geochim. Cosmochim. Acta* **65**, 3435-3442. DOI: 10.1016/S0016-7037(01)00695-0.

Cismasu A. C., Michel F. M., Stebbins J. F., Levard C. et Brown G. E. (2012) Properties of impurity-bearing ferrihydrite I. Effects of Al content and precipitation rate on the

structure of 2-line ferrihydrite. *Geochim. Cosmochim. Acta* **92**, 275-291. DOI: 10.1016/j.gca.2012.06.010.

Davis C. C. et Edwards M. (2017) Role of Calcium in the Coagulation of NOM with Ferric Chloride. *Environ. Sci. Technol.* **51**, 11652-11659. DOI: 10.1021/acs.est.7b02038.

Davranche M., Gélabert A. et Benedetti M. F. (2020) Electron Transfer Drives Metal Cycling in the Critical Zone. *Elements* **16**, 185-190. DOI: 10.2138/gselements.16.3.185.

Davranche M., Veclin C., Pierson-Wickmann A.-C., El Hadri H., Grassl B., Rowenczyk L., Dia A., Ter Halle A., Blancho F., Reynaud S. et Gigault J. (2019) Are nanoplastics able to bind significant amount of metals? The lead example. *Environ. Pollut.* **249**, 940-948. DOI: 10.1016/j.envpol.2019.03.087.

Dentel S. K. (1988) Application of the precipitation-charge neutralization model of coagulation. *Environ. Sci. Technol.* **22**, 825-832. DOI: 10.1021/es00172a013.

Dia A., Gruau G., Olivié-Lauquet G., Riou C., Molénat J. et Curmi P. (2000) The distribution of rare earth elements in groundwaters: assessing the role of source-rock composition, redox changes and colloidal particles. *Geochim. Cosmochim. Acta* **64**, 4131-4151. DOI: 10.1016/S0016-7037(00)00494-4.

Diallo M. S., Glinka C. J., Goddard W. A. et Johnson J. H. (2005) Characterization of nanoparticles and colloids in aquatic systems 1. Small angle neutron scattering investigations of Suwannee River fulvic acid aggregates in aqueous solutions. *J. Nanoparticle Res.* **7**, 435-448. DOI: 10.1007/s11051-005-7524-4.

Dickson D., Liu G. et Cai Y. (2017) Adsorption kinetics and isotherms of arsenite and arsenate on hematite nanoparticles and aggregates. *J. Environ. Manage.* **186**, 261-267. DOI: 10.1016/j.jenvman.2016.07.068.

Dixit S. et Hering J. G. (2003) Comparison of Arsenic(V) and Arsenic(III) Sorption onto Iron Oxide Minerals: Implications for Arsenic Mobility. *Environ. Sci. Technol.* **37**, 4182-4189. DOI: 10.1021/es030309t.

Doelsch E., Rose J., Masion A., Bottero J. Y., Nahon D. et Bertsch P. M. (2000) Speciation and Crystal Chemistry of Iron(III) Chloride Hydrolyzed in the Presence of SiO_4 Ligands. 1. An Fe K-Edge EXAFS Study. *Langmuir* **16**, 4726-4731. DOI: 10.1021/la991378h.

Doelsch E., Stone W. E. E., Petit S., Masion A., Rose J., Bottero J.-Y. et Nahon D. (2001) Speciation and Crystal Chemistry of Fe(III) Chloride Hydrolyzed in the Presence of SiO_4 Ligands. 2. Characterization of Si−Fe Aggregates by FTIR and ^{29} Si Solid-State NMR. *Langmuir* **17**, 1399-1405. DOI: 10.1021/la0013188.

Duan J. et Gregory J. (2003) Coagulation by hydrolysing metal salts. *Adv. Colloid Interface Sci.* **100-102**, 475-502. DOI: 10.1016/S0001-8686(02)00067-2.

Dubochet J. et McDowall A. W. (1981) Vitrification of pure water for electron microscopy. *J. Microsc.* **124**, 3-4. DOI: 10.1111/j.1365-2818.1981.tb02483.x.

Ducher M., Blanchard M., Vantelon D., Nemausat R. et Cabaret D. (2016) Probing the local environment of substitutional Al^{3+} in goethite using X-ray absorption spectroscopy and first-principles calculations. *Phys. Chem. Miner.* **43**, 217-227. DOI: 10.1007/s00269-015-0788-z.

Ekstrom E. B., Learman D. R., Madden A. S. et Hansel C. M. (2010) Contrasting effects of Al substitution on microbial reduction of Fe(III) (hydr)oxides. *Geochim. Cosmochim. Acta* **74**, 7086-7099. DOI: 10.1016/j.gca.2010.09.008.

Evans C. D., Monteith D. T. et Cooper D. M. (2005) Long-term increases in surface water dissolved organic carbon: Observations, possible causes and environmental impacts. *Environ. Pollut.* **137**, 55-71. DOI: 10.1016/j.envpol.2004.12.031.

Ferro-Vázquez C., Nóvoa-Muñoz J. C., Costa-Casais M., Klaminder J. et Martínez-Cortizas A. (2014) Metal and organic matter immobilization in temperate podzols: A high resolution study. *Geoderma* **217-218**, 225-234. DOI: 10.1016/j.geoderma.2013.10.006.

Flank A.-M., Cauchon G., Lagarde P., Bac S., Janousch M., Wetter R., Dubuisson J.-M., Idir M., Langlois F., Moreno T. et Vantelon D. (2006) LUCIA, a microfocus soft XAS beamline. *Nucl. Instrum. Methods Phys. Res. Sect. B Beam Interact. Mater. At.* **246**, 269-274. DOI: 10.1016/j.nimb.2005.12.007.

Fulton J. L., Heald S. M., Badyal Y. S. et Simonson J. M. (2003) Understanding the Effects of Concentration on the Solvation Structure of Ca^{2+} in Aqueous Solution. I: The Perspective on Local Structure from EXAFS and XANES. *J. Phys. Chem. A* **107**, 4688-4696. DOI: 10.1021/jp0272264.

Gentile L., Wang T., Tunlid A., Olsson U. et Persson P. (2018) Ferrihydrite Nanoparticle Aggregation Induced by Dissolved Organic Matter. *J. Phys. Chem. A* **122**, 7730-7738. DOI: 10.1021/acs.jpca.8b05622.

Goldberg S. (1987) Effect of Saturating Cation, pH, and Aluminum and Iron Oxide on the Flocculation of Kaolinite and Montmorillonite. *Clays Clay Miner.* **35**, 220-227. DOI: 10.1346/CCMN.1987.0350308.

Graf D. (1961) Crystallographic Tables for the Rhombohedral Carbonates. *Am. Mineral.* **46**, 1283-1316.

Grafe M., Eick M. J. et Grossl P. R. (2001) Adsorption of Arsenate (V) and Arsenite (III) on Goethite in the Presence and Absence of Dissolved Organic Carbon. *Soil Sci. Soc. Am. J.* **65**, 1680-1687. DOI: 10.2136/sssaj2001.1680.

Grybos M., Davranche M., Gruau G., Petitjean P. et Pédrot M. (2009) Increasing pH drives organic matter solubilization from wetland soils under reducing conditions. *Geoderma* **154**, 13-19. DOI: 10.1016/j.geoderma.2009.09.001.

Guénet H., Davranche M., Vantelon D., Gigault J., Prévost S., Taché O., Jaksch S., Pédrot M., Dorcet V., Boutier A. et Jestin J. (2017) Characterization of iron–organic matter nano-aggregate networks through a combination of SAXS/SANS and XAS analyses: impact on As binding. *Environ. Sci. Nano* **4**, 938-954. DOI: 10.1039/C6EN00589F.

Guénet H., Davranche M., Vantelon D., Pédrot M., Al-Sid-Cheikh M., Dia A. et Jestin J. (2016) Evidence of organic matter control on As oxidation by iron oxides in riparian wetlands. *Chem. Geol.* **439**, 161-172. DOI: 10.1016/j.chemgeo.2016.06.023.

Guo H. et Barnard A. S. (2013) Naturally occurring iron oxide nanoparticles: morphology, surface chemistry and environmental stability. *J Mater Chem A* **1**, 27-42. DOI: 10.1039/C2TA00523A.

Hagvall K., Persson P. et Karlsson T. (2015) Speciation of aluminum in soils and stream waters: The importance of organic matter. *Chem. Geol.* **417**, 32-43. DOI: 10.1016/j.chemgeo.2015.09.012.

Hammouda B. (2010) A new Guinier–Porod model. *J. Appl. Crystallogr.* **43**, 716-719. DOI: 10.1107/S0021889810015773.

Hansel C. M., Learman D. R., Lentini C. J. et Ekstrom E. B. (2011) Effect of adsorbed and substituted Al on Fe(II)-induced mineralization pathways of ferrihydrite. *Geochim. Cosmochim. Acta* **75**, 4653-4666. DOI: 10.1016/j.gca.2011.05.033.

Harvey O. R. et Rhue R. D. (2008) Kinetics and energetics of phosphate sorption in a multi-component Al(III)–Fe(III) hydr(oxide) sorbent system. *J. Colloid Interface Sci.* **322**, 384-393. DOI: 10.1016/j.jcis.2008.03.019.

Hay M. B. et Myneni S. C. B. (2008) Geometric and Electronic Structure of the Aqueous $Al(H_2O)_6^{3+}$ Complex. *J. Phys. Chem. A* **112**, 10595-10603. DOI: 10.1021/jp802675v.

Hay M. B. et Myneni S. C. B. (2010) X-ray Absorption Spectroscopy of Aqueous Aluminum-Organic Complexes. *J. Phys. Chem. A* **114**, 6138-6148. DOI: 10.1021/jp909656q.

Hazemann J.-L., Bérar J. F. et Manceau A. (1991) Rietveld Studies of the Aluminium-Iron Substitution in Synthetic Goethite. *Mater. Sci. Forum* **79-82**, 821-826. DOI: 10.4028/www.scientific.net/MSF.79-82.821.

Heidmann I., Christl I. et Kretzschmar R. (2005) Sorption of Cu and Pb to kaolinite-fulvic acid colloids: Assessment of sorbent interactions. *Geochim. Cosmochim. Acta* **69**, 1675-1686. DOI: 10.1016/j.gca.2004.10.002.

Herzog S. D., Gentile L., Olsson U., Persson P. et Kritzberg E. S. (2020) Characterization of Iron and Organic Carbon Colloids in Boreal Rivers and Their Fate at High Salinity. *J. Geophys. Res. Biogeosciences* **125**, 1-14. DOI: 10.1029/2019JG005517.

Hiemstra T., Mendez J. C. et Li J. (2019) Evolution of the reactive surface area of ferrihydrite: time, pH, and temperature dependency of growth by Ostwald ripening. *Environ. Sci. Nano* **6**, 820-833. DOI: 10.1039/C8EN01198B.

Hirst C., Andersson P. S., Shaw S., Burke I. T., Kutscher L., Murphy M. J., Maximov T., Pokrovsky O. S., Mörth C.-M. et Porcelli D. (2017) Characterisation of Fe-bearing particles and colloids in the Lena River basin, NE Russia. *Geochim. Cosmochim. Acta* **213**, 553-573. DOI: 10.1016/j.gca.2017.07.012.

Hoffmann M., Mikutta C. et Kretzschmar R. (2013) Arsenite Binding to Natural Organic Matter: Spectroscopic Evidence for Ligand Exchange and Ternary Complex Formation. *Environ. Sci. Technol.* **47**, 12165-12173. DOI: 10.1021/es4023317.

Hofmann A., Pelletier M., Michot L., Stradner A., Schurtenberger P. et Kretzschmar R. (2004) Characterization of the pores in hydrous ferric oxide aggregates formed by freezing and thawing. *J. Colloid Interface Sci.* **271**, 163-173. DOI: 10.1016/j.jcis.2003.11.053.

Hofmann A., Vantelon D., Montargès-Pelletier E., Villain F., Gardoll O., Razafitianamaharavo A. et Ghanbaja J. (2013) Interaction of Fe(III) and Al(III) during hydroxylation by forced hydrolysis: The nature of Al–Fe oxyhydroxy co-precipitates. *J. Colloid Interface Sci.* **407**, 76-88. DOI: 10.1016/j.jcis.2013.06.020.

Hu Y. F., Xu R. K., Dynes J. J., Blyth R. I. R., Yu G., Kozak L. M. et Huang P. M. (2008) Coordination nature of aluminum (oxy)hydroxides formed under the influence of tannic acid studied by X-ray absorption spectroscopy. *Geochim. Cosmochim. Acta* **72**, 1959-1969. DOI: 10.1016/j.gca.2008.02.002.

Hua M., Zhang S., Pan B., Zhang W., Lv L. et Zhang Q. (2012) Heavy metal removal from water/wastewater by nanosized metal oxides: A review. *J. Hazard. Mater.* **211-212**, 317-331. DOI: 10.1016/j.jhazmat.2011.10.016.

Iglesias A., López R., Fiol S., Antelo J. M. et Arce F. (2003) Analysis of copper and calcium–fulvic acid complexation and competition effects. *Water Res.* **37**, 3749-3755. DOI: 10.1016/S0043-1354(03)00236-7.

Ildefonse P., Cabaret D., Sainctavit P., Calas G., Flank A.-M. et Lagarde P. (1998) Aluminium X-ray absorption Near Edge Structure in model compounds and Earth's surface minerals. *Phys. Chem. Miner.* **25**, 112-121. DOI: 10.1007/s002690050093.

Iskrenova-Tchoukova E., Kalinichev A. G. et Kirkpatrick R. J. (2010) Metal Cation Complexation with Natural Organic Matter in Aqueous Solutions: Molecular Dynamics Simulations and Potentials of Mean Force. *Langmuir* **26**, 15909-15919. DOI: 10.1021/la102535n.

Islam Md. A., Morton D. W., Johnson B. B., Pramanik B. K., Mainali B. et Angove M. J. (2018) Metal ion and contaminant sorption onto aluminium oxide-based materials: A review and future research. *J. Environ. Chem. Eng.* **6**, 6853-6869. DOI: 10.1016/j.jece.2018.10.045.

Jambor J. L. et Dutrizac J. E. (1998) Occurrence and Constitution of Natural and Synthetic Ferrihydrite, a Widespread Iron Oxyhydroxide. *Chem. Rev.* **98**, 2549-2586. DOI: 10.1021/cr970105t.

Janot N., Reiller P. E. et Benedetti M. F. (2013) Modelling Eu(III) speciation in a Eu(III)/PAHA/α-Al2O3 ternary system. *Colloids Surf. Physicochem. Eng. Asp.* **435**, 9-15. DOI: 10.1016/j.colsurfa.2013.02.052.

Jarvie H. P. et King S. M. (2007) Small-Angle Neutron Scattering Study of Natural Aquatic Nanocolloids. *Environ. Sci. Technol.* **41**, 2868-2873. DOI: 10.1021/es061912p.

Jin P., Song J., Yang L., Jin X. et Wang X. C. (2018) Selective binding behavior of humic acid removal by aluminum coagulation. *Environ. Pollut.* **233**, 290-298. DOI: 10.1016/j.envpol.2017.10.058.

Kalinichev A. G. et Kirkpatrick R. J. (2007) Molecular dynamics simulation of cationic complexation with natural organic matter. *Eur. J. Soil Sci.* **58**, 909-917. DOI: 10.1111/j.1365-2389.2007.00929.x.

Karlsson T. et Persson P. (2010) Coordination chemistry and hydrolysis of Fe(III) in a peat humic acid studied by X-ray absorption spectroscopy. *Geochim. Cosmochim. Acta* **74**, 30-40. DOI: 10.1016/j.gca.2009.09.023.

Karlsson T. et Persson P. (2012) Complexes with aquatic organic matter suppress hydrolysis and precipitation of Fe(III). *Chem. Geol.* **322-323**, 19-27. DOI: 10.1016/j.chemgeo.2012.06.003.

Karlsson T., Persson P., Skyllberg U., Mörth C.-M. et Giesler R. (2008) Characterization of Iron(III) in Organic Soils Using Extended X-ray Absorption Fine Structure Spectroscopy. *Environ. Sci. Technol.* **42**, 5449-5454. DOI: 10.1021/es800322j.

Kim J., Ilott A. J., Middlemiss D. S., Chernova N. A., Pinney N., Morgan D. et Grey C. P. (2015) ^{2} H and ^{27} Al Solid-State NMR Study of the Local Environments in Al-Doped 2-Line Ferrihydrite, Goethite, and Lepidocrocite. *Chem. Mater.* **27**, 3966-3978. DOI: 10.1021/acs.chemmater.5b00856.

King S. M. et Jarvie H. P. (2012) Exploring How Organic Matter Controls Structural Transformations in Natural Aquatic Nanocolloidal Dispersions. *Environ. Sci. Technol.* **46**, 6959-6967. DOI: 10.1021/es2034087.

Kleber M., Eusterhues K., Keiluweit M., Mikutta C., Mikutta R. et Nico P. S. (2015) Mineral–Organic Associations: Formation, Properties, and Relevance in Soil Environments. In *Advances in Agronomy* Elsevier. p. 1-140. DOI: 10.1016/bs.agron.2014.10.005.

Klop E. A., Schouten A., van der Sluis P. et Spek A. L. (1984) Structure of calcium acetate monohydrate, Ca(C2H3O2)2.H2O. *Acta Crystallogr. C* **40**, 51-53. DOI: 10.1107/S0108270184002985.

Klöppel H., Fliedner A. et Kördel W. (1997) Behaviour and ecotoxicology of aluminium in soil and water - Review of the scientific literature. *Chemosphere* **35**, 353-363. DOI: 10.1016/S0045-6535(97)00161-6.

Kloster N. et Avena M. (2015) Interaction of humic acids with soil minerals: adsorption and surface aggregation induced by Ca2+. *Environ. Chem.* **12**, 731. DOI: 10.1071/EN14157.

Kretzschmar R. et Schäfer T. (2005) Metal Retention and Transport on Colloidal Particles in the Environment. *Elements* **1**, 205-210. DOI: 10.2113/gselements.1.4.205.

Leenheer J. A. et Croué J.-P. (2003) Peer Reviewed: Characterizing Aquatic Dissolved Organic Matter. *Environ. Sci. Technol.* **37**, 18A-26A. DOI: 10.1021/es032333c.

Letterman R. D., Vanderbrook S. G. et Sricharoenchaikit P. (1982) Electrophoretic mobility measurements in coagulation with aluminum salts. *J. - Am. Water Works Assoc.* **74**, 44-51. DOI: 10.1002/j.1551-8833.1982.tb04843.x.

Lippold H. et Lippmann-Pipke J. (2009) Effect of humic matter on metal adsorption onto clay materials: Testing the linear additive model. *J. Contam. Hydrol.* **109**, 40-48. DOI: 10.1016/j.jconhyd.2009.07.009.

Lippold H., Mansel A. et Kupsch H. (2005) Influence of trivalent electrolytes on the humic colloid-borne transport of contaminant metals: competition and flocculation effects. *J. Contam. Hydrol.* **76**, 337-352. DOI: 10.1016/j.jconhyd.2004.11.005.

Lotfi-Kalahroodi E., Pierson-Wickman A.-C., Guenet H., Rouxel O., Ponzevera E., Bouhnik-Le Coz M., Vantelon D., Dia A. et Davranche M. (2019) Iron isotope fractionation in iron-organic matter associations: Experimental evidence using filtration and ultrafiltration. *Geochim. Cosmochim. Acta* **250**, 98-116. DOI: 10.1016/j.gca.2019.01.036.

Lovley D. R., Coates J. D., Blunt-Harris E. L., Phillips E. J. P. et Woodward J. C. (1996) Humic substances as electron acceptors for microbial respiration. *Nature* **382**, 445-448. DOI: 10.1038/382445a0.

Lu X., Chen Z. et Yang X. (1999) Spectroscopic study of aluminium speciation in removing humic substances by Al coagulation. *Water Res.* **33**, 3271-3280. DOI: 10.1016/S0043-1354(99)00047-0.

Manning B. (2005) Arsenic Speciation in As(III)- and As(V)-Treated Soil Using XANES Spectroscopy. *Microchim. Acta* **151**, 181-188. DOI: 10.1007/s00604-005-0398-4.

Marsac R., Davranche M., Gruau G., Dia A. et Bouhnik-Le Coz M. (2012) Aluminium competitive effect on rare earth elements binding to humic acid. *Geochim. Cosmochim. Acta* **89**, 1-9. DOI: 10.1016/j.gca.2012.04.028.

Martin-Diaconescu V., Gennari M., Gerey B., Tsui E., Kanady J., Tran R., Pécaut J., Maganas D., Krewald V., Gouré E., Duboc C., Yano J., Agapie T., Collomb M.-N. et DeBeer S. (2015) Ca K-Edge XAS as a Probe of Calcium Centers in Complex Systems. *Inorg. Chem.* **54**, 1283-1292. DOI: 10.1021/ic501991e.

Masion A., Vilgé-Ritter A., Rose J., Stone W. E. E., Teppen B. J., Rybacki D. et Bottero J.-Y. (2000) Coagulation-Flocculation of Natural Organic Matter with Al Salts: Speciation and Structure of the Aggregates. *Environ. Sci. Technol.* **34**, 3242-3246. DOI: 10.1021/es9911418.

Masue-Slowey Y., Loeppert R. H. et Fendorf S. (2011) Alteration of ferrihydrite reductive dissolution and transformation by adsorbed As and structural Al: Implications for As retention. *Geochim. Cosmochim. Acta* **75**, 870-886. DOI: 10.1016/j.gca.2010.11.016.

Mertens J., Rose J., Wehrli B. et Furrer G. (2016) Arsenate uptake by Al nanoclusters and other Al-based sorbents during water treatment. *Water Res.* **88**, 844-851. DOI: 10.1016/j.watres.2015.11.018.

Michel F. M., Ehm L., Antao S. M., Lee P. L., Chupas P. J., Liu G., Strongin D. R., Schoonen M. A. A., Phillips B. L. et Parise J. B. (2007a) The Structure of Ferrihydrite, a Nanocrystalline Material. *Science* **316**, 1726-1729. DOI: 10.1126/science.1142525.

Michel F. M., Ehm L., Liu G., Han W. Q., Antao S. M., Chupas P. J., Lee P. L., Knorr K., Eulert H., Kim J., Grey C. P., Celestian A. J., Gillow J., Schoonen M. A. A., Strongin D. R. et Parise J. B. (2007b) Similarities in 2- and 6-Line Ferrihydrite Based on Pair Distribution Function Analysis of X-ray Total Scattering. *Chem. Mater.* **19**, 1489-1496. DOI: 10.1021/cm062585n.

Mikutta C. (2011) X-ray absorption spectroscopy study on the effect of hydroxybenzoic acids on the formation and structure of ferrihydrite. *Geochim. Cosmochim. Acta* **75**, 5122-5139. DOI: 10.1016/j.gca.2011.06.002.

Mikutta C. et Kretzschmar R. (2011) Spectroscopic Evidence for Ternary Complex Formation between Arsenate and Ferric Iron Complexes of Humic Substances. *Environ. Sci. Technol.* **45**, 9550-9557. DOI: 10.1021/es202300w.

Mikutta C., Mikutta R., Bonneville S., Wagner F., Voegelin A., Christl I. et Kretzschmar R. (2008) Synthetic coprecipitates of exopolysaccharides and ferrihydrite. Part I: Characterization. *Geochim. Cosmochim. Acta* **72**, 1111-1127. DOI: 10.1016/j.gca.2007.11.035.

Milne C. J., Kinniburgh D. G., van Riemsdijk W. H. et Tipping E. (2003) Generic NICA−Donnan Model Parameters for Metal-Ion Binding by Humic Substances. *Environ. Sci. Technol.* **37**, 958-971. DOI: 10.1021/es0258879.

Namayandeh A. et Kabengi N. (2019) Calorimetric study of the influence of aluminum substitution in ferrihydrite on sulfate adsorption and reversibility. *J. Colloid Interface Sci.* **540**, 20-29. DOI: 10.1016/j.jcis.2019.01.001.

Neubauer E., Schenkeveld W. D. C., Plathe K. L., Rentenberger C., von der Kammer F., Kraemer S. M. et Hofmann T. (2013) The influence of pH on iron speciation in podzol extracts: Iron complexes with natural organic matter, and iron mineral nanoparticles. *Sci. Total Environ.* **461-462**, 108-116. DOI: 10.1016/j.scitotenv.2013.04.076.

Newville M. (2001) EXAFS analysis using *FEFF* and *FEFFIT*. *J. Synchrotron Radiat.* **8**, 96-100. DOI: 10.1107/S0909049500016290.

Ni C., Liu S., Cui L., Han Z., Wang L., Chen R. et Liu H. (2016) Adsorption performance of Cr(VI) onto Al-free and Al-substituted ferrihydrites. *RSC Adv.* **6**, 66412-66419. DOI: 10.1039/C6RA09465A.

Nierop K. G. J. J., Jansen B. et Verstraten J. M. (2002) Dissolved organic matter, aluminium and iron interactions: precipitation induced by metal/carbon ratio, pH and competition. *Sci. Total Environ.* **300**, 201-211. DOI: 10.1016/S0048-9697(02)00254-1.

Olivie-Lauquet G. (2001) Release of Trace Elements in Wetlands: Role of Seasonal Variability. *Water Res.* **35**, 943-952. DOI: 10.1016/S0043-1354(00)00328-6.

Ona-Nguema G., Morin G., Juillot F., Calas G. et Brown G. E. (2005) EXAFS Analysis of Arsenite Adsorption onto Two-Line Ferrihydrite, Hematite, Goethite, and Lepidocrocite. *Environ. Sci. Technol.* **39**, 9147-9155. DOI: 10.1021/es050889p.

Oriekhova O. et Stoll S. (2018) Heteroaggregation of nanoplastic particles in the presence of inorganic colloids and natural organic matter. *Environ. Sci. Nano* **5**, 792-799. DOI: 10.1039/C7EN01119A.

Osterberg R. et Mortensen K. (1992) Fractal dimension of humic acids: A small angle neutron scattering study. *Eur. Biophys. J.* **21**, 163-167. DOI: 10.1007/BF00196759.

Osterberg R. et Mortensen K. (1994) The growth of fractal humic acids: Cluster correlation and gel formation. *Radiat. Environ. Biophys.* **33**, 269-276. DOI: 10.1007/BF01212682.

Otón J., Sorzano C. O. S., Marabini R., Pereiro E. et Carazo J. M. (2015) Measurement of the modulation transfer function of an X-ray microscope based on multiple Fourier orders analysis of a Siemens star. *Opt. Express* **23**, 9567. DOI: 10.1364/OE.23.009567.

Ouatmane A., Hafidi M., EL Gharous M. et Revel J. C. (1999) Complexation of calcium ions by humic and fulvic acids. *Analusis* **27**, 428-431. DOI: 10.1051/analusis:1999270428.

Packham R. F. (1965) Some studies of the coagulation of dispersed clays with hydrolyzing salts. *J. Colloid Sci.* **20**, 81-92. DOI: 10.1016/0095-8522(65)90094-2.

Paluchowska B., Maurin J. K. et Leciejewicz J. (1996) Carboxylate and Furan-Ring Oxygen Bonded to Calcium in Polymeric Calcium Furoate. *Acta Crystallogr. C* **52**, 347-351. DOI: 10.1107/S0108270195009553.

Pédrot M., Boudec A. L., Davranche M., Dia A. et Henin O. (2011) How does organic matter constrain the nature, size and availability of Fe nanoparticles for biological reduction? *J. Colloid Interface Sci.* **359**, 75-85. DOI: 10.1016/j.jcis.2011.03.067.

Pédrot M., Dia A., Davranche M., Bouhnik-Le Coz M., Henin O. et Gruau G. (2008) Insights into colloid-mediated trace element release at the soil/water interface. *J. Colloid Interface Sci.* **325**, 187-197. DOI: 10.1016/j.jcis.2008.05.019.

Pinheiro J. P., Mota A. M. et Benedetti M. F. (2000) Effect of Aluminum Competition on Lead and Cadmium Binding to Humic Acids at Variable Ionic Strength. *Environ. Sci. Technol.* **34**, 5137-5143. DOI: 10.1021/es0000899.

Pipich V. et Fu Z. (2015) KWS-3: Very small angle scattering diffractometer with focusing mirror. *J. Large-Scale Res. Facil. JLSRF* **1**, A31. DOI: 10.17815/jlsrf-1-28.

Poggenburg C., Mikutta R., Sander M., Schippers A., Marchanka A., Dohrmann R. et Guggenberger G. (2016) Microbial reduction of ferrihydrite-organic matter coprecipitates by Shewanella putrefaciens and Geobacter metallireducens in comparison to mediated electrochemical reduction. *Chem. Geol.* **447**, 133-147. DOI: 10.1016/j.chemgeo.2016.09.031.

Pokrovski G. S. et Schott J. (1998) Experimental study of the complexation of silicon and germanium with aqueous organic species: implications for germanium and silicon transport and Ge/Si ratio in natural waters. *Geochim. Cosmochim. Acta* **62**, 3413-3428. DOI: 10.1016/S0016-7037(98)00249-X.

Pokrovski G. S., Schott J., Farges F. et Hazemann J.-L. (2003) Iron (III)-silica interactions in aqueous solution: insights from X-ray absorption fine structure spectroscopy. *Geochim. Cosmochim. Acta* **67**, 3559-3573. DOI: 10.1016/S0016-7037(03)00160-1.

Pokrovsky O. S., Dupré B. et Schott J. (2005) Fe–Al–organic Colloids Control of Trace Elements in Peat Soil Solutions: Results of Ultrafiltration and Dialysis. *Aquat. Geochem.* **11**, 241-278. DOI: 10.1007/s10498-004-4765-2.

Pokrovsky O. S. et Schott J. (2002) Iron colloids/organic matter associated transport of major and trace elements in small boreal rivers and their estuaries (NW Russia). *Chem. Geol.* **190**, 141-179. DOI: 10.1016/S0009-2541(02)00115-8.

Pokrovsky O. S., Shirokova L. S., Kirpotin S. N., Audry S., Viers J. et Dupré B. (2011) Effect of permafrost thawing on organic carbon and trace element colloidal speciation in the thermokarst lakes of western Siberia. *Biogeosciences* **8**, 565-583. DOI: 10.5194/bg-8-565-2011.

Ponnamperuma F. N. (1972) The Chemistry of Submerged Soils. In *Advances in Agronomy* Elsevier. p. 29-96. DOI: 10.1016/S0065-2113(08)60633-1.

Pullin M. J. et Cabaniss S. E. (2003) The effects of pH, ionic strength, and iron–fulvic acid interactions on the kinetics of non-photochemical iron transformations. I. Iron(II) oxidation and iron(III) colloid formation. *Geochim. Cosmochim. Acta* **67**, 4067-4077. DOI: 10.1016/S0016-7037(03)00366-1.

Rabajczyk A. et Namieśnik J. (2014) Speciation of Iron in the Aquatic Environment. *Water Environ. Res.* **86**, 741-758. DOI: 10.2175/106143014X13975035525906.

Radulescu A., Szekely N. K. et Appavou M.-S. (2015) KWS-2: Small angle scattering diffractometer. *J. Large-Scale Res. Facil. JLSRF* **1**, A29. DOI: 10.17815/jlsrf-1-27.

Ratié G., Vantelon D., Lotfi Kalahroodi E., Bihannic I., Pierson-Wickmann A. C. et Davranche M. (2019) Iron speciation at the riverbank surface in wetland and potential impact on the mobility of trace metals. *Sci. Total Environ.* **651**, 443-455. DOI: 10.1016/j.scitotenv.2018.09.143.

Ravel B. et Newville M. (2005) *ATHENA* , *ARTEMIS* , *HEPHAESTUS* : data analysis for X-ray absorption spectroscopy using *IFEFFIT*. *J. Synchrotron Radiat.* **12**, 537-541. DOI: 10.1107/S0909049505012719.

Raven K. P., Jain A. et Loeppert R. H. (1998) Arsenite and Arsenate Adsorption on Ferrihydrite: Kinetics, Equilibrium, and Adsorption Envelopes. *Environ. Sci. Technol.* **32**, 344-349. DOI: 10.1021/es970421p.

Rehr J. J., Albers R. C. et Zabinsky S. I. (1992) High-order multiple-scattering calculations of x-ray-absorption fine structure. *Phys. Rev. Lett.* **69**, 3397-3400. DOI: 10.1103/PhysRevLett.69.3397.

Ritchie J. D. et Perdue E. M. (2003) Proton-binding study of standard and reference fulvic acids, humic acids, and natural organic matter. *Geochim. Cosmochim. Acta* **67**, 85-96. DOI: 10.1016/S0016-7037(02)01044-X.

Ritter K., Aiken G. R., Ranville J. F., Bauer M. et Macalady D. L. (2006) Evidence for the Aquatic Binding of Arsenate by Natural Organic Matter−Suspended Fe(III). *Environ. Sci. Technol.* **40**, 5380-5387. DOI: 10.1021/es0519334.

Robertus C., Philipse W. H., Joosten J. G. H. et Levine Y. K. (1989) Solution of the Percus–Yevick approximation of the multicomponent adhesive spheres system applied to the small angle x-ray scattering from microemulsions. *J. Chem. Phys.* **90**, 4482-4490. DOI: 10.1063/1.456635.

Saito T., Koopal L. K., Nagasaki S. et Tanaka S. (2005) Analysis of Copper Binding in the Ternary System Cu^{2+}/Humic Acid/Goethite at Neutral to Acidic pH. *Environ. Sci. Technol.* **39**, 4886-4893. DOI: 10.1021/es0500308.

Ščančar J. et Milačič R. (2006) Aluminium speciation in environmental samples: a review. *Anal. Bioanal. Chem.* **386**, 999-1012. DOI: 10.1007/s00216-006-0422-5.

Schwertmann U. et Cornell R. M. éd. (2000) *Iron Oxides in the Laboratary*., Wiley-VCH Verlag GmbH, Weinheim, Germany. DOI: 10.1002/9783527613229.

Senn A.-C., Kaegi R., Hug S. J., Hering J. G., Mangold S. et Voegelin A. (2015) Composition and structure of Fe(III)-precipitates formed by Fe(II) oxidation in water at near-neutral pH: Interdependent effects of phosphate, silicate and Ca. *Geochim. Cosmochim. Acta* **162**, 220-246. DOI: 10.1016/j.gca.2015.04.032.

Siéliéchi J.-M., Lartiges B. S., Kayem G. J., Hupont S., Frochot C., Thieme J., Ghanbaja J., d'Espinose de la Caillerie J. B., Barrès O., Kamga R., Levitz P. et Michot L. J. (2008) Changes in humic acid conformation during coagulation with ferric chloride: Implications for drinking water treatment. *Water Res.* **42**, 2111-2123. DOI: 10.1016/j.watres.2007.11.017.

Song Z., Yang X., Chen F., Zhao F., Zhao Y., Ruan L., Wang Y. et Yang Y. (2019) Fate and transport of nanoplastics in complex natural aquifer media: Effect of particle size and surface functionalization. *Sci. Total Environ.* **669**, 120-128. DOI: 10.1016/j.scitotenv.2019.03.102.

Sorrentino A., Nicolás J., Valcárcel R., Chichón F. J., Rosanes M., Avila J., Tkachuk A., Irwin J., Ferrer S. et Pereiro E. (2015) MISTRAL: a transmission soft X-ray microscopy beamline for cryo nano-tomography of biological samples and magnetic domains imaging. *J. Synchrotron Radiat.* **22**, 1112-1117. DOI: 10.1107/S1600577515008632.

Sowers T. D., Adhikari D., Wang J., Yang Y. et Sparks D. L. (2018a) Spatial Associations and Chemical Composition of Organic Carbon Sequestered in Fe, Ca, and Organic Carbon Ternary Systems. *Environ. Sci. Technol.* **52**, 6936-6944. DOI: 10.1021/acs.est.8b01158.

Sowers T. D., Stuckey J. W. et Sparks D. L. (2018b) The synergistic effect of calcium on organic carbon sequestration to ferrihydrite. *Geochem. Trans.* **19**, 4. DOI: 10.1186/s12932-018-0049-4.

Sparks D. L. (2003) *Environmental soil chemistry*. 2nd ed., Academic Press, Amsterdam ; Boston.

Stolpe B., Guo L., Shiller A. M. et Aiken G. R. (2013) Abundance, size distributions and trace-element binding of organic and iron-rich nanocolloids in Alaskan rivers, as revealed by field-flow fractionation and ICP-MS. *Geochim. Cosmochim. Acta* **105**, 221-239. DOI: 10.1016/j.gca.2012.11.018.

ThomasArrigo L. K., Byrne J. M., Kappler A. et Kretzschmar R. (2018) Impact of Organic Matter on Iron(II)-Catalyzed Mineral Transformations in Ferrihydrite–Organic Matter Coprecipitates. *Environ. Sci. Technol.* **52**, 12316-12326. DOI: 10.1021/acs.est.8b03206.

ThomasArrigo L. K., Mikutta C., Byrne J., Barmettler K., Kappler A. et Kretzschmar R. (2014) Iron and Arsenic Speciation and Distribution in Organic Flocs from Streambeds of an Arsenic-Enriched Peatland. *Environ. Sci. Technol.* **48**, 13218-13228. DOI: 10.1021/es503550g.

Thurman E. M. (1985) *Organic Geochemistry of Natural Waters*., Springer Netherlands, Dordrecht.

Tipping E. (2005) Modelling Al competition for heavy metal binding by dissolved organic matter in soil and surface waters of acid and neutral pH. *Geoderma* **127**, 293-304. DOI: 10.1016/j.geoderma.2004.12.003.

Tipping E., Berggren D., Mulder J. et Woof C. (1995) Modelling the solid–solution distributions of protons, aluminium, base cations and humic substances in acid soils. *Eur. J. Soil Sci.* **46**, 77-94. DOI: 10.1111/j.1365-2389.1995.tb01814.x.

Van Benschoten J. E. et Edzwald J. K. (1990) Chemical aspects of coagulation using aluminum salts—I. Hydrolytic reactions of alum and polyaluminum chloride. *Water Res.* **24**, 1519-1526. DOI: 10.1016/0043-1354(90)90086-L.

van Schaik J. W. J., Persson I., Kleja D. B. et Gustafsson J. P. (2008) EXAFS Study on the Reactions between Iron and Fulvic Acid in Acid Aqueous Solutions. *Environ. Sci. Technol.* **42**, 2367-2373. DOI: 10.1021/es072092z.

Vantelon D., Davranche M., Marsac R., La Fontaine C., Guénet H., Jestin J., Campaore G., Beauvois A. et Briois V. (2019) Iron speciation in iron-organic matter nanoaggregates: A kinetic approach coupling Quick-EXAFS and MCR-ALS chemometry. *Environ. Sci. Nano* **6**, 2641-2651. DOI: 10.1039/C9EN00210C.

Vantelon D., Trcera N., Roy D., Moreno T., Mailly D., Guilet S., Metchalkov E., Delmotte F., Lassalle B., Lagarde P. et Flank A.-M. (2016) The LUCIA beamline at SOLEIL. *J. Synchrotron Radiat.* **23**, 635-640. DOI: 10.1107/S1600577516000746.

Vermeer A. W. P., McCulloch J. K., van Riemsdijk W. H. et Koopal L. K. (1999) Metal Ion Adsorption to Complexes of Humic Acid and Metal Oxides: Deviations from the Additivity Rule. *Environ. Sci. Technol.* **33**, 3892-3897. DOI: 10.1021/es990260k.

Vilgé-Ritter A., Rose J., Masion A., Bottero J.-Y. et Lainé J.-M. (1999) Chemistry and structure of aggregates formed with Fe-salts and natural organic matter. *Colloids Surf. Physicochem. Eng. Asp.* **147**, 297-308. DOI: 10.1016/S0927-7757(98)00325-2.

Voegelin A., Kaegi R., Frommer J., Vantelon D. et Hug S. J. (2010) Effect of phosphate, silicate, and Ca on Fe(III)-precipitates formed in aerated Fe(II)- and As(III)-containing water studied by X-ray absorption spectroscopy. *Geochim. Cosmochim. Acta* **74**, 164-186. DOI: 10.1016/j.gca.2009.09.020.

Wang H. et Shadman F. (2013) Effect of particle size on the adsorption and desorption properties of oxide nanoparticles. *AIChE J.* **59**, 1502-1510. DOI: 10.1002/aic.13936.

Wang X. C., Jin P. K. et Gregory J. (2002) Structure of Al-humic flocs and their removal at slightly acidic and neutral pH. *Water Supply* **2**, 99-106. DOI: 10.2166/ws.2002.0051.

Wang X., Li W., Harrington R., Liu F., Parise J. B., Feng X. et Sparks D. L. (2013) Effect of Ferrihydrite Crystallite Size on Phosphate Adsorption Reactivity. *Environ. Sci. Technol.* **47**, 10322-10331. DOI: 10.1021/es401301z.

Weng L. P., Koopal L. K., Hiemstra T., Meeussen J. C. L. et Van Riemsdijk W. H. (2005) Interactions of calcium and fulvic acid at the goethite-water interface. *Geochim. Cosmochim. Acta* **69**, 325-339. DOI: 10.1016/j.gca.2004.07.002.

Weng L., Van Riemsdijk W. H. et Hiemstra T. (2009) Effects of Fulvic and Humic Acids on Arsenate Adsorption to Goethite: Experiments and Modeling. *Environ. Sci. Technol.* **43**, 7198-7204. DOI: 10.1021/es9000196.

Wigginton N. S., Haus K. L. et Hochella Jr M. F. (2007) Aquatic environmental nanoparticles. *J. Environ. Monit.* **9**, 1306. DOI: 10.1039/b712709j.

Wilke M., Farges F., Petit P.-E., Brown G. E. et Martin F. (2001) Oxidation state and coordination of Fe in minerals: An Fe *K*- XANES spectroscopic study. *Am. Mineral.* **86**, 714-730. DOI: 10.2138/am-2001-5-612.

Xu R. K., Hu Y. F., Dynes J. J., Zhao A. Z., Blyth R. I. R., Kozak L. M. et Huang P. M. (2010) Coordination nature of aluminum (oxy)hydroxides formed under the influence of low molecular weight organic acids and a soil humic acid studied by X-ray absorption spectroscopy. *Geochim. Cosmochim. Acta* **74**, 6422-6435. DOI: 10.1016/j.gca.2010.07.029.

Xue Q., Ran Y., Tan Y., Peacock C. L. et Du H. (2019) Arsenite and arsenate binding to ferrihydrite organo-mineral coprecipitate: Implications for arsenic mobility and fate in

natural environments. *Chemosphere* **224**, 103-110. DOI: 10.1016/j.chemosphere.2019.02.118.

Yean S., Cong L., Yavuz C. T., Mayo J. T., Yu W. W., Kan A. T., Colvin V. L. et Tomson M. B. (2005) Effect of magnetite particle size on adsorption and desorption of arsenite and arsenate. *J. Mater. Res.* **20**, 3255-3264. DOI: 10.1557/jmr.2005.0403.

Yu W.-Z., Gregory J. et Campos L. (2010) Breakage and Regrowth of Al-Humic Flocs - Effect of Additional Coagulant Dosage. *Environ. Sci. Technol.* **44**, 6371-6376. DOI: 10.1021/es1007627.

Zachara J. M., Resch C. T. et Smith S. C. (1994) Influence of humic substances on Co2+ sorption by a subsurface mineral separate and its mineralogic components. *Geochim. Cosmochim. Acta* **58**, 553-566. DOI: 10.1016/0016-7037(94)90488-X.

Zhu J., Pigna M., Cozzolino V., Caporale A. G. et Violante A. (2011) Sorption of arsenite and arsenate on ferrihydrite: Effect of organic and inorganic ligands. *J. Hazard. Mater.* **189**, 564-571. DOI: 10.1016/j.jhazmat.2011.02.071.

Liste des figures

Chapitre I

Chapitre II

Chapitre III

Chapitre IV

Liste des tables

Chapitre I

Chapitre II

Chapitre III

Annexes

Annexe 1

Table A-1– OC concentration (mmol L^{-1}) in each fraction for As/Fe = 0.004. The uncertainties were calculated from the triplicate. <LOD: below the detection limit.

As/Fe = 0.004	Fractions					
OC (mmol L^{-1})	**Total**	**> 0.2 µm**	**0.2 µm – 1000 kD**	**1000 – 100 kD**	**100 – 30 kD**	**< 30 kD**
Fe0.02-Ca0.0	58.8 ± 0.9	7.3 ± 1.6	2.5 ± 0.9	42.4 ± 0.5	2.0 ± 0.8	4.6 ± 0.7
Fe0.02-Ca0.1	59.1 ± 1.0	9.4 ± 2.0	1.2 ± 1.6	42.8 ± 0.7	1.4 ± 0.4	4.2 ± 0.4
Fe0.02-Ca0.5	59.8 ± 1.7	14.2 ± 2.1	2.6 ± 0.5	38.0 ± 0.6	1.7 ± 0.7	3.2 ± 0.4
Fe0.02-Ca1.0	55.2 ± 0.2	15.5 ± 0.5	8.1 ± 1.8	28.0 ± 1.9	1.1 ± 0.2	2.5 ± 0.2
Fe0.05-Ca0.0	55.8 ± 0.8	7.7 ± 1.6	2.1 ± 0.1	44.4 ± 0.1	1.2 ± 0.2	3.1 ± 0.1
Fe0.05-Ca0.1	53.7 ± 0.1	15.0 ± 0.2	2.3 ± 0.3	32.7 ± 0.5	0.9 ± 0.2	2.7 ± 0.2
Fe0.05-Ca0.5	51.9 ± 0.9	34.6 ± 0.5	13.9 ± 1.0	1.2 ± 0.1	0.2 ± 0.1	1.9 ± 0.2
Fe0.05-Ca1.0	52.2 ± 2.8	50.4 ± 2.6	0.2 ± 0.3	0.2 ± 0.1	<LOD	1.6 ± 0.1
Fe0.08-Ca0.0	61.2 ± 1.1	20.1 ± 0.8	1.7 ± 0.9	35.0 ± 1.0	2.0 ± 0.4	2.4 ± 0.2
Fe0.08-Ca0.1	55.6 ± 0.2	37.7 ± 0.6	0.9 ± 0.1	14.2 ± 0.2	1.3 ± 0.2	2.1 ± 0.1
Fe0.08-Ca0.5	56.8 ± 1.9	54.9 ± 2.1	0.4 ± 0.5	<LOD	<LOD	2.2 ± 0.4
Fe0.08-Ca1.0	52.3 ± 1.1	51.2 ± 1.0	0.2 ± 0.2	0.1 ± 0.1	<LOD	0.9 ± 0.1

Table A-2 – Fe concentration (mmol L^{-1}) in each fraction for As/Fe = 0.004. The uncertainties were calculated from the triplicate. <LOD: below the detection limit.

As/Fe = 0.004	Fractions					
Fe (mmol L^{-1})	**Total**	**> 0.2 µm**	**0.2 µm – 1000 kD**	**1000 – 100 kD**	**100 – 30 kD**	**< 30 kD**
Fe0.02-Ca0.0	1.23 ± 0.04	0.15 ± 0.06	0.03 ± 0.03	1.02 ± 0.01	0.02 ± 0.01	0.01 ± 0.01
Fe0.02-Ca0.1	1.12 ± 0.01	0.08 ± 0.02	0.01 ± 0.01	0.99 ± 0.01	0.01 ± 0.01	0.01 ± 0.01
Fe0.02-Ca0.5	1.23 ± 0.04	0.33 ± 0.04	0.03 ± 0.03	0.86 ± 0.02	0.01 ± 0.01	0.01 ± 0.01
Fe0.02-Ca1.0	1.29 ± 0.04	0.37 ± 0.06	0.14 ± 0.01	0.77 ± 0.01	<LOD	<LOD
Fe0.05-Ca0.0	3.12 ± 0.01	0.73 ± 0.01	<LOD	2.43 ± 0.01	0.01 ± 0.01	0.01 ± 0.01
Fe0.05-Ca0.1	3.27 ± 0.07	0.98 ± 0.03	0.14 ± 0.11	2.14 ± 0.07	<LOD	0.01 ± 0.01
Fe0.05-Ca0.5	2.81 ± 0.13	1.85 ± 0.11	0.89 ± 0.03	0.06 ± 0.01	<LOD	<LOD
Fe0.05-Ca1.0	2.70 ± 0.12	2.70 ± 0.12	<LOD	<LOD	<LOD	<LOD
Fe0.08-Ca0.0	4.76 ± 0.12	1.59 ± 0.11	0.10 ± 0.07	3.05 ± 0.07	0.01 ± 0.01	<LOD
Fe0.08-Ca0.1	5.01 ± 0.10	3.57 ± 0.08	0.36 ± 0.10	1.07 ± 0.12	0.01 ± 0.01	<LOD
Fe0.08-Ca0.5	4.78 ± 0.10	4.78 ± 0.10	<LOD	<LOD	<LOD	<LOD
Fe0.08-Ca1.0	4.94 ± 0.06	4.94 ± 0.06	<LOD	<LOD	<LOD	<LOD

Table A-3 – Ca concentration (mmol L^{-1}) in each fraction for As/Fe = 0.004. The uncertainties were calculated from the triplicate. <LOD: below the detection limit.

As/Fe = 0.004	Fractions					
Ca (mmol L^{-1})	Total	> 0.2 µm	0.2 µm – 1000 kD	1000 – 100 kD	100 – 30 kD	< 30 kD
Fe0.02-Ca0.0	0.11 ± 0.01	0.01 ± 0.01	<LOD	0.10 ± 0.01	<LOD	0.01 ± 0.01
Fe0.02-Ca0.1	0.21 ± 0.01	0.01 ± 0.01	0.01 ± 0.01	0.18 ± 0.01	<LOD	0.01 ± 0.01
Fe0.02-Ca0.5	0.67 ± 0.02	0.17 ± 0.02	0.01 ± 0.01	0.44 ± 0.01	0.02 ± 0.01	0.04 ± 0.01
Fe0.02-Ca1.0	1.28 ± 0.05	0.31 ± 0.03	0.12 ± 0.02	0.59 ± 0.01	0.02 ± 0.01	0.23 ± 0.01
Fe0.05-Ca0.0	0.12 ± 0.01	0.02 ± 0.01	<LOD	0.09 ± 0.01	<LOD	<LOD
Fe0.05-Ca0.1	0.40 ± 0.02	0.11 ± 0.02	0.01 ± 0.01	0.26 ± 0.01	<LOD	0.03 ± 0.01
Fe0.05-Ca0.5	1.44 ± 0.06	0.68 ± 0.04	0.34 ± 0.02	0.04 ± 0.01	<LOD	0.38 ± 0.01
Fe0.05-Ca1.0	2.80 ± 0.09	1.14 ± 0.09	0.06 ± 0.02	0.10 ± 0.01	0.03 ± 0.01	1.58 ± 0.01
Fe0.08-Ca0.0	0.11 ± 0.01	0.02 ± 0.01	0.01 ± 0.01	0.06 ± 0.01	<LOD	0.01 ± 0.01
Fe0.08-Ca0.1	0.59 ± 0.01	0.37 ± 0.01	0.04 ± 0.01	0.12 ± 0.01	<LOD	0.06 ± 0.01
Fe0.08-Ca0.5	2.38 ± 0.07	1.18 ± 0.12	0.03 ± 0.02	<LOD	<LOD	1.19 ± 0.02
Fe0.08-Ca1.0	4.73 ± 0.01	1.45 ± 0.08	0.10 ± 0.05	0.18 ± 0.12	<LOD	3.22 ± 0.06

Table A-4 – As concentration (µmol L^{-1}) in each fraction for As/Fe = 0.004. The uncertainties were calculated from the triplicate. <LOD: below the detection limit.

As/Fe = 0.004	Fractions					
As (µmol L^{-1})	Total	> 0.2 µm	0.2 µm – 1000 kD	1000 – 100 kD	100 – 30 kD	< 30 kD
Fe0.02-Ca0.0	4.67 ± 0.13	0.40 ± 0.27	0.13 ± 0.20	2.13 ± 0.20	0.13 ± 0.27	2.00 ± 0.13
Fe0.02-Ca0.1	4.53 ± 0.20	0.40 ± 0.20	<LOD	2.13 ± 0.20	0.40 ± 0.20	1.60 ± 0.20
Fe0.02-Ca0.5	4.27 ± 0.13	0.40 ± 0.20	0.53 ± 0.13	1.60 ± 0.20	0.13 ± 0.13	1.60 ± 0.13
Fe0.02-Ca1.0	5.20 ± 0.13	1.20 ± 0.13	0.40 ± 0.20	2.40 ± 0.13	<LOD	1.33 ± 0.27
Fe0.05-Ca0.0	11.87 ± 0.20	2.53 ± 0.20	<LOD	7.73 ± 0.20	<LOD	1.73 ± 0.27
Fe0.05-Ca0.1	12.53 ± 0.13	3.60 ± 0.20	0.13 ± 0.53	7.20 ± 0.40	<LOD	1.60 ± 0.20
Fe0.05-Ca0.5	11.47 ± 0.53	6.67 ± 0.53	3.60 ± 0.13	0.27 ± 0.20	<LOD	0.93 ± 0.20
Fe0.05-Ca1.0	10.80 ± 0.67	9.47 ± 0.67	<LOD	0.13 ± 0.13	<LOD	1.33 ± 0.13
Fe0.08-Ca0.0	18.40 ± 0.53	6.13 ± 0.27	1.33 ± 0.53	9.87 ± 0.40	<LOD	1.20 ± 0.20
Fe0.08-Ca0.1	18.40 ± 0.67	12.67 ± 0.40	1.60 ± 0.40	3.47 ± 0.67	0.27 ± 0.40	0.40 ± 0.27
Fe0.08-Ca0.5	18.00 ± 0.67	16.93 ± 0.80	<LOD	0.13 ± 0.20	<LOD	1.73 ± 0.13
Fe0.08-Ca1.0	19.87 ± 0.93	18.27 ± 0.80	0.13 ± 0.13	0.13 ± 0.20	<LOD	1.47 ± 0.13

Table A-5 – OC concentration (mmol L^{-1}) in each fraction for As/Fe = 0.15. The uncertainties were calculated from the triplicate. n.d.: not determined. <LOD: below the detection limit.

As/Fe = 0.15	Fractions					
OC (mmol L^{-1})	Total	> 0.2 µm	0.2 µm – 1000 kD	1000 – 100 kD	100 – 30 kD	< 30 kD
Fe0.02-Ca0.0	54.5 ± 0.7	9.6 ± 1.3	2.3 ± 1.1	36.3 ± 2.9	2.4 ± 1.1	3.9 ± 0.1
Fe0.02-Ca0.1	54.8 ± 0.2	10.7 ± 0.8	2.7 ± 0.3	34.9 ± 1.9	1.9 ± 1.2	4.1 ± 0.1
Fe0.02-Ca0.5	63.3 ± 0.9	23.6 ± 2.7	0.7 ± 1.1	32.9 ± 0.1	1.3 ± 0.4	4.7 ± 0.3
Fe0.02-Ca1.0	52.2 ± 0.5	38.2 ± 0.2	1.3 ± 0.2	9.7 ± 0.5	0.2 ± 0.1	2.8 ± 0.1
Fe0.05-Ca0.0	n.d.	n.d.	n.d.	n.d.	n.d.	n.d.
Fe0.05-Ca0.1	55.5 ± 0.2	23.5 ± 0.9	1.2 ± 0.3	27.0 ± 0.5	1.4 ± 0.2	2.4 ± 0.1
Fe0.05-Ca0.5	54.5 ± 1.1	34.9 ± 0.9	15.2 ± 0.9	2.7 ± 1.0	0.4 ± 0.1	1.4 ± 0.1
Fe0.05-Ca1.0	47.2 ± 0.5	45.7 ± 0.6	0.4 ± 0.1	0.2 ± 0.1	<LOD0.1	1.1 ± 0.1
Fe0.08-Ca0.0	53.5 ± 0.1	7.9 ± 3.5	5.0 ± 1.3	37.5 ± 1.2	1.4 ± 0.7	2.0 ± 0.2
Fe0.08-Ca0.1	56.7 ± 0.1	15.7 ± 0.1	16.0 ± 0.5	22.7 ± 0.8	<LOD	5.2 ± 1.6
Fe0.08-Ca0.5	61.8 ± 0.9	60.4 ± 1.0	0.2 ± 0.2	<LOD	<LOD	1.2 ± 0.1
Fe0.08-Ca1.0	56.4 ± 0.6	55.5 ± 0.7	0.1 ± 0.1	<LOD	<LOD	1.1 ± 0.1

Table A-6 – Fe concentration (mmol L^{-1}) in each fraction for As/Fe = 0.15. The uncertainties were calculated from the triplicate. n.d.: not determined. <LOD: below the detection limit.

As/Fe = 0.15	Fractions					
Fe (mmol L^{-1})	Total	> 0.2 µm	0.2 µm – 1000 kD	1000 – 100 kD	100 – 30 kD	< 30 kD
Fe0.02-Ca0.0	1.23 ± 0.04	0.20 ± 0.06	0.07 ± 0.03	0.92 ± 0.01	0.03 ± 0.01	0.01 ± 0.01
Fe0.02-Ca0.1	1.22 ± 0.01	0.26 ± 0.02	0.01 ± 0.01	0.94 ± 0.01	0.02 ± 0.01	0.01 ± 0.01
Fe0.02-Ca0.5	1.20 ± 0.04	0.43 ± 0.04	0.02 ± 0.03	0.72 ± 0.02	0.01 ± 0.01	0.01 ± 0.01
Fe0.02-Ca1.0	1.25 ± 0.04	0.94 ± 0.06	0.05 ± 0.01	0.25 ± 0.01	0.02 ± 0.01	<LOD
Fe0.05-Ca0.0	n.d.	n.d.	n.d.	n.d.	n.d.	n.d.
Fe0.05-Ca0.1	3.02 ± 0.07	1.37 ± 0.03	0.07 ± 0.11	1.57 ± 0.07	<LOD	0.01 ± 0.01
Fe0.05-Ca0.5	2.72 ± 0.13	1.71 ± 0.11	0.88 ± 0.03	0.12 ± 0.01	<LOD	<LOD
Fe0.05-Ca1.0	2.81 ± 0.12	2.79 ± 0.12	0.02 ± 0.01	<LOD	<LOD	<LOD
Fe0.08-Ca0.0	5.05 ± 0.12	1.14 ± 0.11	0.08 ± 0.07	3.84 ± 0.07	0.01 ± 0.01	0.01 ± 0.01
Fe0.08-Ca0.1	5.05 ± 0.10	2.78 ± 0.08	0.65 ± 0.10	1.61 ± 0.12	<LOD	<LOD
Fe0.08-Ca0.5	5.08 ± 0.10	5.07 ± 0.10	<LOD	<LOD	<LOD	<LOD
Fe0.08-Ca1.0	4.80 ± 0.06	4.80 ± 0.06	<LOD	<LOD	<LOD	<LOD

Table A-7 – As concentration (µmol L^{-1}) in each fraction for As/Fe = 0.15. The uncertainties were calculated from the triplicate. n.d.: not determined. <LOD: below the detection limit.

As/Fe = 0.15	Fractions					
As (µmol L^{-1})	Total	> 0.2 µm	0.2 µm – 1000 kD	1000 – 100 kD	100 – 30 kD	< 30 kD
Fe0.02-Ca0.0	193.6 ± 4.4	0.93 ± 1.9	13.1 ± 0.3	17.2 ± 3.5	<LOD	165.6 ± 3.3
Fe0.02-Ca0.1	189.6 ± 3.7	4.53 ± 3.3	<LOD	23.6 ± 7.1	<LOD	164.1 ± 4.9
Fe0.02-Ca0.5	191.9 ± 3.9	11.2 ± 6.4	6.9 ± 4.9	21.2 ± 5.7	<LOD	157.9 ± 8.8
Fe0.02-Ca1.0	184.4 ± 2.8	18.0 ± 7.6	9.3 ± 1.1	13.9 ± 5.7	<LOD	154.8 ± 6.1
Fe0.05-Ca0.0	n.d.	n.d.	n.d.	n.d.	n.d.	n.d.
Fe0.05-Ca0.1	467.7 ± 20.3	61.1 ± 2.3	14.0 ± 0.9	90.53 ± 10.4	<LOD	310.5 ± 31.6
Fe0.05-Ca0.5	453.5 ± 9.2	73.7 ± 14.4	62.1 ± 11.2	9.47 ± 2.8	<LOD	317.5 ± 4.5
Fe0.05-Ca1.0	463.2 ± 10.9	145.2 ± 7.7	3.2 ± 4.4	25.20 ± 1.9	3.5 ± 9.3	286.0 ± 4.9
Fe0.08-Ca0.0	848.5 ± 3.2	145.9 ± 13.2	201.6 ± 10.0	<LOD	<LOD	539.7 ± 8.0
Fe0.08-Ca0.1	834.8 ± 2.7	291.7 ± 72.4	<LOD	101.6 ± 10	<LOD	500.4 ± 22.5
Fe0.08-Ca0.5	797.9 ± 36.1	346.7 ± 10	<LOD	18.0 ± 10	<LOD	494.5 ± 15.3
Fe0.08-Ca1.0	738.7 ± 16.7	326.8 ± 33.5	<LOD	8.8 ± 5.1	<LOD	454.0 ± 4.9

Table A-8 – Chemical analyses for a solution of pure Leonardite HA. The experimental data are measured for the solution prepared with 25 mg of LHA in 500 mL Milli-Q water. The calculated data were determined for the same OC concentration than the Fe-OM-Ca aggregates.

Concentration (mmol L^{-1})	Experimental	Calculated
OC	2.43	60
Ca	4.35×10^{-3}	0.11
Fe	1.64×10^{-3}	0.04
As	n.d.	n.d.

Annexe 2

Environmental Science Nano

PAPER

Cite this: *Environ. Sci.: Nano*, 2019, **6**, 2641

Iron speciation in iron–organic matter nanoaggregates: a kinetic approach coupling Quick-EXAFS and MCR-ALS chemometrics†

Delphine Vantelon, *[a] Mélanie Davranche,[b] Rémi Marsac, [b] Camille La Fontaine,[a] Hélène Guénet,[abc] Jacques Jestin,[c] Grace Campaore,[b] Anthony Beauvois[abc] and Valérie Briois[a]

Received 21st February 2019,
Accepted 30th June 2019

DOI: 10.1039/c9en00210c

rsc.li/es-nano

Iron–organic matter (Fe–OM) nanoaggregates are highly abundant in wetlands. Iron oxyhydroxides and natural OM are strong sorbents for metals and metalloids due to their high density of binding sites. They are thus considered as a major vector for the transport of metallic pollutants in this type of aquatic system. However, their structural organization is complex and varies under physico-chemical environmental conditions. The goal of this present study is to characterize these various iron phases and their growth processes. The formation of Fe-species was followed by Quick-EXAFS during oxidation/hydrolysis kinetics of pre-formed Fe(II)–humic acid complexes. Data were then processed using the MCR-ALS chemometric method. It demonstrated that, in the presence of OM, Fe(II) oxidation/hydrolysis leads to the synthesis of Fe-oligomers and ferrihydrite-like nanoparticles, both being bound to OM. The formation of the oligomers is the result of the inhibition of ferrihydrite polymerization by OM. Ferrihydrite and oligomers grow concomitantly during Fe(II) oxidation. When Fe(II) is completely oxidized, ferrihydrite forms at the expense of oligomers. For a given Fe/OM ratio, the ferrihydrite/oligomer ratio depends on the oxidation/hydrolysis kinetics which is strongly influenced by O_2 and OH^- availability. The organization of these structures constrains their binding site density and availability, which induces dramatic environmental implications regarding their capacity to trap metallic pollutants.

Environmental significance

In natural water, iron (Fe)–organic matter (OM) nanoaggregates are major vectors controlling the fate of inorganic pollutants such as metals and metalloids. However, their structural organization, complex and variable as a function of physico-chemical environmental conditions, remains poorly understood. Herein, we evidenced, singled out and characterized the Fe-phases coexisting in Fe–OM nanoaggregates, as well as their dynamics of formation during the oxidation/hydrolysis of Fe(II)–humic acid complexes. These phases are Fe-oligomers and ferrihydrite-like nanoparticles bound to OM, whose proportion varies with the degree and rate of oxidation of Fe(II). This work provides new insights into understanding of variations of natural Fe–OM nanoaggregates capable of uptaking metals and metalloids observed in aquatic systems.

Introduction

Among natural nanoaggregates, those composed of iron (Fe) and organic matter (OM) are of particular importance. They are produced from organic soils and organic soil horizons in contrasted areas such as wetlands, peatlands and permafrosts.[1–4] They are released in response to soil leaching, alternating redox condition, storm events and, in boreal zones, subsequently to permafrost thawing. They are considered as a vector for the transport of numerous contaminants. Iron oxyhydroxides and natural OM are indeed known to be strong sorbents of metals and metalloids due to their high density of binding sites.[5] As an example, Pédrot *et al.*[2] demonstrated that in a soil solution, when Fe and OM are associated as nanoparticles (*i.e.* present in the 0.2 μm–30 KDa size fraction), they are the main bearing-phases of trace metal elements. Plach *et al.*[6] recorded significant concentration increases of Ag, Cu and Fe–OM nanoparticles following storm events. Thomas Arrigo *et al.*[7] demonstrated that Fe-rich organic flocs observed in the surface waters of wetlands have a high affinity for trace metals and metalloids.

[a] *Synchrotron SOLEIL, L'ormes des Merisiers, Saint Aubin BP48, 91192 Gif sur Yvette cedex, France. E-mail: delphine.vantelon@synchrotron-soleil.fr*
[b] *Géosciences Rennes, UMR 6118, Univ. Rennes 1, Campus de Beaulieu, 35042, Rennes Cedex, France*
[c] *Laboratoire Léon Brillouin, CEA Saclay, 91191 Gif/Yvette Cedex, France*

† Electronic supplementary information (ESI) available. See DOI: 10.1039/c9en00210c

Several studies have examined the Fe speciation of Fe–OM nanometric associations with regard to their importance in metal and metalloid binding. Based on Fe(II) oxidation/hydrolysis experiments in the presence of humic or fulvic acids at very low Fe/OM ratios, Mikutta and Kretzschmar[8] demonstrated the formation of Fe trimers bound to OM, according to X-ray absorption spectroscopy (XAS) measurements. Similar observations were performed by Vilgé-Ritter *et al.*,[9] after Fe(III) hydrolysis experiments in the presence of river natural organic matter (NOM). Combining small-angle X-ray scattering (SAXS) with XAS measurements, they demonstrated that OM is strongly complexed with Fe, limiting Fe hydrolysis by occupying the growth sites thereby resulting in the formation of small oligomeric species (typically trimers) within the Fe–OM aggregates. The speciation of Fe and the level of complexation do not depend on the coagulation pH or on the nature of the OM. In contrast, using similar experiments (hydrolysis of Fe(III) in the presence of peat and Suwannee River NOM), Karlsson and Persson[10] concluded that only a low pH value and a low Fe concentration led to the formation of Fe monomers bound to OM. An increase of pH and Fe concentration led to the coexistence of ferrihydrite nanoparticles and Fe bound to OM as mononuclear complexes. Similar results were also observed by Chen *et al.*[11] for Fe(III) hydrolysis in the presence of soil NOM. The coexistence of several phases is also reported in natural systems. Guénet *et al.*[4] demonstrated that, in a riparian wetland, the Fe phases are composed of nano-lepidocrocite embedded in the OM matrix and Fe monomers and oligomers bound to OM. In contrast, in nano-associations collected in low-flow streams (pH 5.3–6.3) draining a peatland, Thomas Arrigo *et al.*[7] combined Mössbauer with XAS measurements and showed the predominance of ferrihydrite as well as the presence of nanocrystalline lepidocrocite. In contrast, working on Fe rich flocs from a peatland, Thomas Arrigo *et al.*[12] used Mössbauer and isotopic exchanges to demonstrate that, in environmental systems where solid-solution equilibria are rapidly reached, OM stabilizes poorly crystalline Fe-oxyhydroxides such as ferrihydrite thereby impairing their transformation into more crystalline phases such as goethite or lepidocrocite. SAXS studies of Fe nano-oxyhydroxides in the presence of humic or fulvic acids showed that they are organized according to a fractal network.[13–15] Interestingly, Karlsson and Persson[10] and Chen *et al.*[11] suggested that the formation of Fe nano-oxides involved structural changes of OM that could impact their reactivity. All these studies suggested that the organization of Fe–OM nanometric associations, although heterogeneous, displays a coherent distribution of the Fe species ranging from adsorbed monomers to nano-oxyhydroxides. They also pointed out some variability in the Fe nano-oxyhydroxides and oligomers formed under natural or experimental conditions. Here, we aim to gain a greater understanding of the processes and influencing parameters responsible for such differences.

Under environmental conditions, Fe–OM nanometric associations form in response to the redox alteration prevailing in areas subjected to water level variations such as wetlands and peatlands or soil thawing like in permafrosts. They are formed by the oxidation/hydrolysis of complexes between Fe(II) and NOM (nanoparticulate or dissolved).[16] No information is currently available on the species that precipitate at the early stage of the reaction or about their subsequent evolution (if it exists) with running reaction time. However, the early-formed Fe species and the impact of OM on their evolution are critical for the structural diversity of the Fe–OM associations observed in the environment and produced in the laboratory. The aim of the present study is therefore to monitor the nucleation–growth process of Fe-species in such Fe–OM nanometric associations in order to determine if their structural arrangement is acquired at an early stage of the reaction or is a consequence of ageing. For this purpose, Fe speciation was dynamically followed by Fe K-edge Quick-XAS during oxidation/hydrolysis kinetics experiments on preformed Fe(II)–OM complexes. Data were then processed using the chemometric multivariate curve resolution with alternating least square analysis (MCR-ALS) method[17,18] which enabled the isolation of signals from individual species and thus the determination of their structural organization and abundance. It corresponds to the bilinear decomposition of the data set into a matrix of concentrations of species and a matrix of related pure spectra according to the Beer–Lambert law which XAS obeys.

Materials and methods

The experiment consisted of the kinetic study of the oxidation/hydrolysis of a pre-equilibrated Fe(II)–OM complex. All aqueous solutions were prepared with analytical grade Milli-Q water (Millipore). Fe(II) stock solutions were prepared with iron chloride tetrahydrate ($FeCl_2{\cdot}4H_2O$) from Acros Organics. NaOH, HCl and HNO_3, all of ultrapure, were provided by Fisher Chemical, Merck and VWR, respectively. Ammonium acetate, hydroxyammonium chloride and dimethyl-2,9 phenanthroline-1,10 chlorhydrate were obtained from Fisher Scientific, Merck and VWR Prolabo, respectively. The humic acid (HA) used here was the standard Leonardite HA provided by the International Humic Substance Society (IHSS). All materials were soaked in 10% HNO_3 and then rinsed with deionized water twice for 24 h.

Fe(II)–OM complexes

Prior to production of the complexes, 2 g L^{-1} and 4 g L^{-1} HA were solubilized in a 10^{-3} M NaCl solution at pH 11 using 0.1 M NaOH, respectively. After 24 h of stirring, the pH was fixed at 6.5 using 0.25 M HCl. In an anaerobic chamber (Jacomex), volumes of 500 mg L^{-1} and 1 g L^{-1} Fe(II) stock solutions were added to 100 mL of the HA solutions in order to obtain solutions with an iron/organic carbon (Fe/OC) ratio of 0.4 (wt/wt): [Fe] = 280 mg L^{-1} and [HA] = 1 g L^{-1} and [Fe] = 500 mg L^{-1} and [HA] = 2 g L^{-1}, respectively. The pH was maintained at 6.5. The solution was continuously stirred for at least 48 h to reach equilibrium. These high concentrations of OC and Fe

were chosen as a good compromise for the acquisition of Quick-XAS spectra with good signal/noise ratios and a convenient time frame to monitor the dynamics of transformation. However, the Fe/OC ratio corresponds to ratios that may be encountered in soil solutions from riparian wetlands.[16]

Fe speciation modelling

Geochemical speciation code PHREEQC (version 2 (ref. 19)) was used to model Fe(II/III)–HA binding with Model VI.[20] PHREEQC-Model VI coupling was done by Marsac *et al.*[21] Corresponding Fe(III)–HA and Fe(II)–HA binding parameters were determined by Marsac *et al.*[22] and Catrouillet *et al.*,[23] respectively. The "minteq.v4" database, provided with PHREEQC, was implemented with the specific binding parameters of Model VI. Briefly, Model VI assumes that the complexation of ions by humic substances occurs through various discrete groups (carboxylic and phenolic groups), which can form either mono-, bi- or tri-dentate binding sites. As HAs are large and negatively charged polyelectrolytes, electrostatic effects are also encountered.[20] Speciation was calculated under conditions where ferrihydrite is allowed to precipitate and where Fe(III) oligomers are allowed to form.[22] A high solubility product value ($Ks = a_{Fe^{3+}}/(a_{H^+})^3 = 10^{5.4}$, where a_X is the activity of the X species) was determined for ferrihydrite formed in the presence of HA under circumneutral pH conditions.[22,24] This value is in agreement with the thermodynamic approach of Hiemstra,[25] who expressed the solubility of ferrihydrite as a function of particle size. Thus our Ks value corresponds to particle diameters of ~1.6 nm which is the size of the ferrihydrite primary beads we have calculated from SAXS measurements.[13] Fe speciation was studied relative to the Fe(II)/Fe_{tot} ratio (where Fe_{tot} is the initial Fe concentration). To do so, equilibrium calculations were performed at various redox potential values at fixed values of pH (6.5), [Fe] (282 mg L^{-1}), [HA] (1 g L^{-1}) and ionic strength (fixed with 10 mM NaCl as the background electrolyte). The Fe(II)/Fe_{tot} ratio was recalculated afterward using PHREEQC-Model VI, by accounting for the Nernst equation and the various chemical equilibria affecting the Fe(II)–Fe(III) redox transition.

Oxidation kinetic experiments

Fe(II)–OM complexes were oxidized under ambient air at pH 6.5. For this purpose, 100 mL of the Fe(II)–OM complexes at pH 6.5 ([Fe] = 282 mg L^{-1}, [HA] = 1 g L^{-1}) were taken out of the anaerobic chamber using anaerobic containers. Solutions were rapidly transferred to the titration cell of an automatic titrator (719S Trinito Metrohm) in SET mode in order to maintain the pH at 6.5 throughout the oxidation/hydrolysis reaction. The pH was monitored with a 0.1 M NaOH standard solution. The total Fe(II) concentration was measured relative to the running experiment time using the 1,10-phenanthroline colorimetric method (AFNOR, 1982) at 510 nm with an UV-visible spectrophotometer ("Lambda 25" UV/Vis Spectrometer from Perkin Elmer). The Fe(II) calibration curve was carried out with HA, at the same concentration used for the kinetics experiments, to account for the OM UV-vis absorption.

Quick-EXAFS monitoring of Fe(II) oxidation/hydrolysis

The Fe(II) oxidation/hydrolysis kinetics were monitored by Quick-EXAFS at the ROCK beamline at SOLEIL.[26] Quick-XAS spectra were acquired at the Fe K-edge with a 0.5 Hz oscillation frequency for the Si(111) channel-cut. This resulted in the recording of one XAS spectrum between 6910 and 8180 eV for 1 s every 2 s. The energy calibration was performed by setting the first inflection point of the XANES spectrum of Fe metallic foil at 7112 eV. Oxidation/hydrolysis experiments were performed in a dedicated liquid cell, designed by the beamline team, placed at 45° with respect to the incident X-rays. The geometry and thickness of the cell (9 mm) were optimized in order to allow for vigorous stirring of the solution during the measurements. Beams passing in and out entered through a 24 μm thick Kapton window. Detection was performed in fluorescence mode using an X-PIPS detector placed at 45° to the liquid cell window surface.

Aliquots of 100 mL of Fe(II)–OM complex solutions ([Fe] = 500 mg L^{-1} and [HA] = 2 g L^{-1}, pH = 6.5) prepared in an anaerobic chamber at Geosciences Rennes were put into sealed bottles and brought to SOLEIL. Solutions were then transferred into the ROCK reaction cell under a N_2 flux. They were then left to oxidize in ambient air. The pH was monitored at 6.5 with 0.1 M NaOH using an automatic titrator (719S Trinito Metrohm). A first experiment was performed under vigorous stirring with a blade agitator (Metrodis) and suspension circulation using a peristaltic pump (Heidolph) to prevent aggregate sedimentation (Exp-Air). In order to slow down the kinetics reaction, a second experiment was performed with suspension circulation and nitrogen bubbling, without additional stirring (Exp-N_2).

EXAFS data processing

Data were extracted by averaging successive spectra that were first interpolated in a common energy grid in order to obtain a good signal/noise ratio with the constraint of extracting at least two superimposable spectra at the beginning of the reaction to ensure the start of the analysis with the initial speciation. One spectrum is then the merge of 15 spectra, corresponding to the cumulative information of 30 s of the transformation dynamics. Due to the fact that no photon could exit the cell in transmission mode, it was not possible to simultaneously record the spectrum of Fe metallic foil as a reference associated with each spectrum for the energy calibration. The energy alignment of the spectra was thus based on the presence of glitches on the I_0 channel (incoming beam) of each spectrum, the energy position of which was related to the absolute energy calibration previously performed with the Fe metallic foil. This option is available in the Python GUI developed at the ROCK beamline for the normalization procedure for raw XAS data and dedicated to the handling of

hundreds of spectra within a few seconds.[27] The time-resolved normalized XAS dataset was analysed by principal component analysis (PCA) and multivariate curve resolution with alternating least squares (MCR-ALS) fitting analysis using the MCR-ALS GUI 2.0 free toolbox developed by Tauler and collaborators on the Matlab® platform.[28] A detailed description of the MCR-ALS method applied to the XAS data can be found in the studies of Rochet *et al.*[18] and Lesage *et al.*[27]

EXAFS extraction and Fourier transformation were performed using the Athena software package.[29] A linear background was fitted to the pre-edge region and subtracted from the spectra which were normalized using a quadratic polynomial function defined between 50 and 900 eV above the edge (E_0) that was set to 7128 and 7125 eV for the Fe(III) and Fe(II) species, respectively. EXAFS oscillations were extracted using the Autobk algorithm with a cut-off Rbkg = 1 and *k*-weight = 3. The Fourier transform of the k^3-weighted EXAFS spectra was calculated, using a Hanning apodization window (dk = 1), over the ranges 2–12.5 and 2–10 $Å^{-1}$ for the Fe(III) and Fe(II) species, respectively. EXAFS fitting was performed in the 1.15–4.1 Å distance range with the Artemis interface to IFEFFIT using least-squares refinements.[30] Theoretical backscattering paths were calculated from goethite,[31] lepidocrocite[32] and Fe-carboxylate[33] structures using FEFF6.

Ferrihydrite and lepidocrocite, synthetized following the protocols described in the work of Schwertmann and Cornell,[34] were used as references. For both references, powders were mixed with cellulose and pressed into pellets to obtain an edge jump of 1 for EXAFS measurement in transmission mode.

Results and discussion

Fe speciation modelling

The modelled evolution of the Fe species distribution relative to the Fe(II)/Fe_{tot} ratio for Fe/OC = 0.4 is reported in Fig. 1. The modelling results at various Fe(II)/Fe_{tot} ratios refer to ferrihydrite particles with a single solubility product and therefore a single constant particle size, whereas the rate of Fe(II) oxidation may influence the size of the particles formed and consequently, its solubility. Nevertheless, our modelling results provide important insights into understanding of the Fe speciation change in the presence of HA. When Fe is totally reduced (Fe(II)/Fe_{tot} = 1), the model predicts that 44% of Fe(II) is bound to HA (Fe(II)–HA) and 56% occurs as Fe(II) dissolved species (Fe(II) aq). With the oxidation progress, dissolved Fe(II) decreases more strongly than Fe(II) bound to HA to form ferrihydrite precipitates. The content of the Fe(II)–HA complexes remains relatively stable up to the almost complete disappearance of dissolved Fe(II) (Fe(II)/Fe_{tot} ≈ 0.4). Then, Fe(II)–HA complexes disappear for the benefit of Fe(III) monomers and oligomers bound to HA (Fe(III) monomer–HA and Fe(III) oligomer–HA, respectively). When Fe is totally oxidized (Fe(II)/Fe_{tot} = 0), the model predicts that Fe occurs at 9% as Fe(III) monomers bound to HA, 8% as Fe(III) oligomers bound to HA and 83% as ferrihydrite.

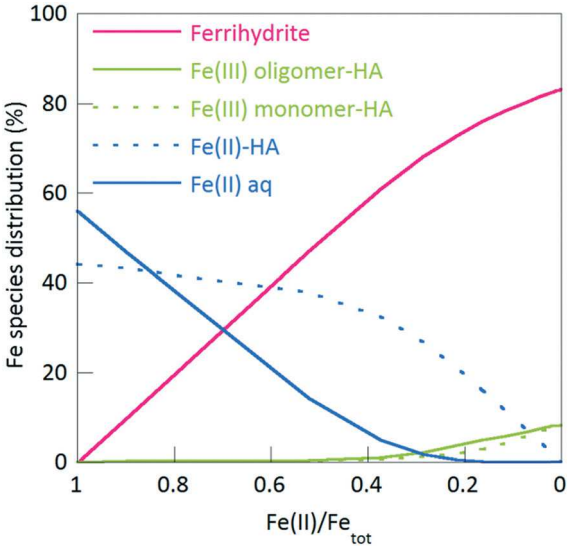

Fig. 1 Calculated Fe speciation evolution relative to the Fe(II)/Fe_{tot} ratio for Fe/OC = 0.4 (pH = 6.5, [Fe] = 282 mg L^{-1}, [HA] = 1 g L^{-1}, 10 mM NaCl). Solubility product of ferrihydrite (K_s) was set to $10^{5.4}$.[22]

Fe oxidation/hydrolysis kinetics

Fig. 2a plots the evolution of the Fe(II)/Fe_{tot} ratio measured using the 1,10-phenantroline colorimetric method for the laboratory kinetics experiments performed with and without HA. The results show that, under our experimental conditions, more than 90% of Fe(II) is oxidized after 1 h regardless of the amount of HA. The kinetics rates are compared by applying a pseudo first-order kinetics to the experimental datasets. The $\log k$ (s^{-1}) values are equal to −4.4 and −3.2 without and with HA, respectively, showing that the kinetics have been slightly slowed down by the presence of HA. The slowdown is even higher when OM was reduced by hydrogenation prior to the oxidation/hydrolysis experiment.[35] The binding of Fe(II) to HA therefore slightly decreases the Fe(II) oxidation kinetics under our experimental conditions.

The XANES spectra collected *in situ* during the oxidation/hydrolysis of Fe(II) for Fe/OC = 0.4 (Exp-Air) exhibit regular evolution from the initial to the final spectrum (Fig. 2b). The iron oxidation state evolves from Fe(II) to Fe(III) according to the edge position that shifts from 7125 eV to 7128 eV. The pre-edge intensity of both the initial and final spectra suggests that the Fe coordination is octahedral for all species.[36] The spectrum obtained after 1 h of reaction can almost be superimposed on the final one in agreement with the laboratory oxidation experiments showing that after 1 h of oxidation, more than 90% of Fe is oxidized into Fe(III) (Fig. 2a). The profile of the initial and final spectra proportion derived from MCR-ALS analysis is reported in Fig. 2c. These spectra respectively represent the whole Fe(II) and Fe(III) phases present in the system. The concentration of the final Fe(III) phases increases linearly at the expense of the initial Fe(II) phases. As for the laboratory oxidation/hydrolysis kinetics measurements (Fig. 2a), half of the Fe(II) is oxidized after 25 min and complete oxidation is achieved after 2 h.

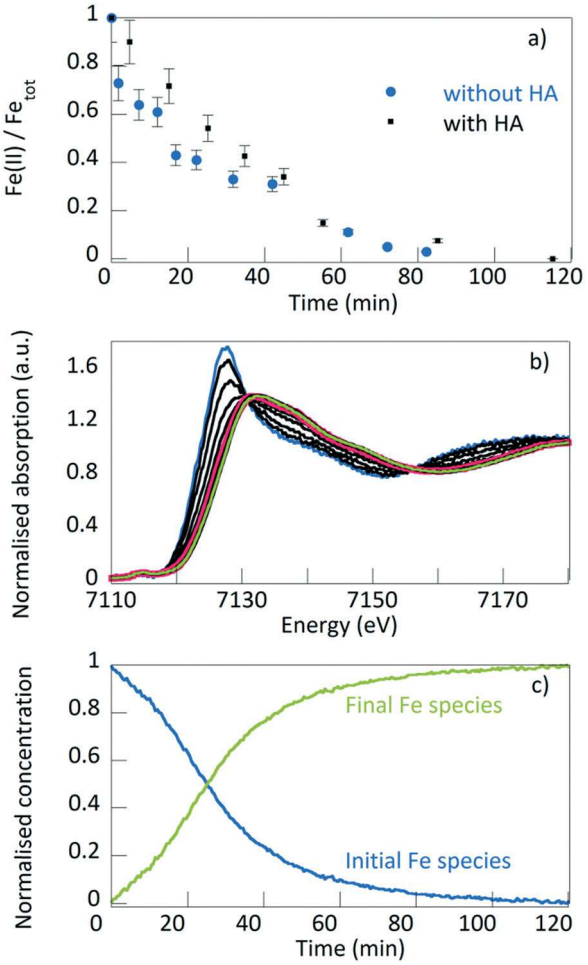

Fig. 2 Fe(II) oxidation/hydrolysis at pH 6.5, under ambient air at Fe/OC = 0.4. a) Fe(II)/Fe$_{tot}$ ratio evolution as a function of time with (black squares) and without (blue dots) HA during laboratory measurements; error bars correspond to standard deviation of 10%; b) XANES spectra evolution as a function of time during the oxidation kinetics in Exp-Air. Fifteen averaged spectra are reported every 10 min. The initial and final spectra are reported in blue and green, respectively. The spectrum obtained after 1 h of reaction is reported in red. The in-between spectra are reported in black; c) corresponding evolution of the Exp-Air initial and final spectra proportion as a function of time derived from the MCR-ALS analysis.

Determination and structural characterization of the produced Fe phases

According to the Fe(II) oxidation experiments (Fig. 2b), the decrease in the initial Fe(II) phase concentration is very fast and, according to modelling calculations, two minor Fe(III) phases are expected to increase concomitantly (Fig. 1). They represent 20% of the total Fe(III) final phases, the major phase (80% of the total Fe(III)) being ferrihydrite (Fig. 1). Only two components, an initial and a final one, can be extracted when the MCR-ALS chemometric analysis is applied to a single experiment data set. Indeed, this analysis cannot be used to resolve all the species because the technique has an intrinsic limitation, called "rank deficiency", that arises when two species evolve with a similar transformation rate in a mixture.[37] To overcome this issue and break the rank deficiency, the MCR-ALS analysis must be performed on a set of two or more experiments in which the initial and formed phases are identical. However, these experiments must display a slightly different dynamic of occurrence, such as in Exp-Air and Exp-N_2, in which the oxidation/hydrolysis kinetics were modified by changing the experimental conditions. By using the so-called column-wise augmented method, it was possible to extract three components: an Fe(II) initial phase and two Fe(III) phases, reported as Cpt-1, Cpt-2 and Cpt-3 in Fig. 3. The results of the MCR-ALS analysis are detailed in SI-1 ESI.† The profile of the concentration of the three extracted components for both Exp-Air and Exp-N_2 are reported in Fig. 3a. As the MCR-ALS analysis was carried out on the normalized XAS spectra over an extended energy range (between 6910 and 8038 eV), the spectra of pure species can be analyzed by the common EXAFS analysis including EXAFS extraction, Fourier transform and EXAFS fitting. The XANES and EXAFS spectra and corresponding Fourier transforms for the three species are reported in Fig. 3b–d, together with their best fits that allow their identification. The EXAFS fit parameters are reported in Table 1.

The Exp-Air kinetics is in line with the laboratory oxidation/hydrolysis experiments (Fig. 2a), for which half of Fe(II) is oxidized after 20 min and a complete oxidation is observable within 90 min. By contrast, the Exp-N_2 kinetics is slower. Half of Fe(II) is oxidized after 40 min and the oxidation is completed after 7 h. The kinetics is slowed down by the nitrogen bubbling coupled with the reduced stirring which drives the reduction of the oxygen diffusion rate as also observed by Chen and Thompson.[38]

The Cpt-1, Cpt-2 and Cpt-3 MCR-ALS components can be considered as Exp-Air and Exp-N_2 common species since the experimental spectra, for both experiments, are perfectly reproduced when weighing their spectra by their concentration profiles. The fit residue is then only composed of white noise. In both experiments, the most abundant final phase is Cpt-3 and the least abundant is Cpt-2. Their concentrations increase with the decrease of the Cpt-1 concentration until it reaches 0. Then the Cpt-3 concentration increases at the expense of the Cpt-2 one. Their final abundance varies with a ratio evolving from 60/40 for Exp-Air to 95/5 for Exp-N_2 (Fig. 3a).

The XANES spectra (Fig. 3b) of the formed phases are very similar. The Cpt-2 spectrum exhibits a less intense pre-edge at 7115 eV, a shoulder in the edge and a more intense shoulder at 7138 eV. The Cpt-3 spectrum exhibits a shoulder at 7148.5 eV. The decrease of the resonance at 7138 eV associated with the increase of the resonance at 7148.5 eV can be assigned to the increase in Fe(III) polymerisation.[39] This assignment can be qualitatively correlated to the structural interpretation of the corresponding EXAFS spectra (Fig. 3c). The Cpt-2 EXAFS spectrum shape is close to monotonous. As a result, its Fourier transform exhibits an intense peak located between 1 and 2 Å and two broad peaks between 2 and 3 Å and 3 and 4 Å (where R^* is the distance not corrected

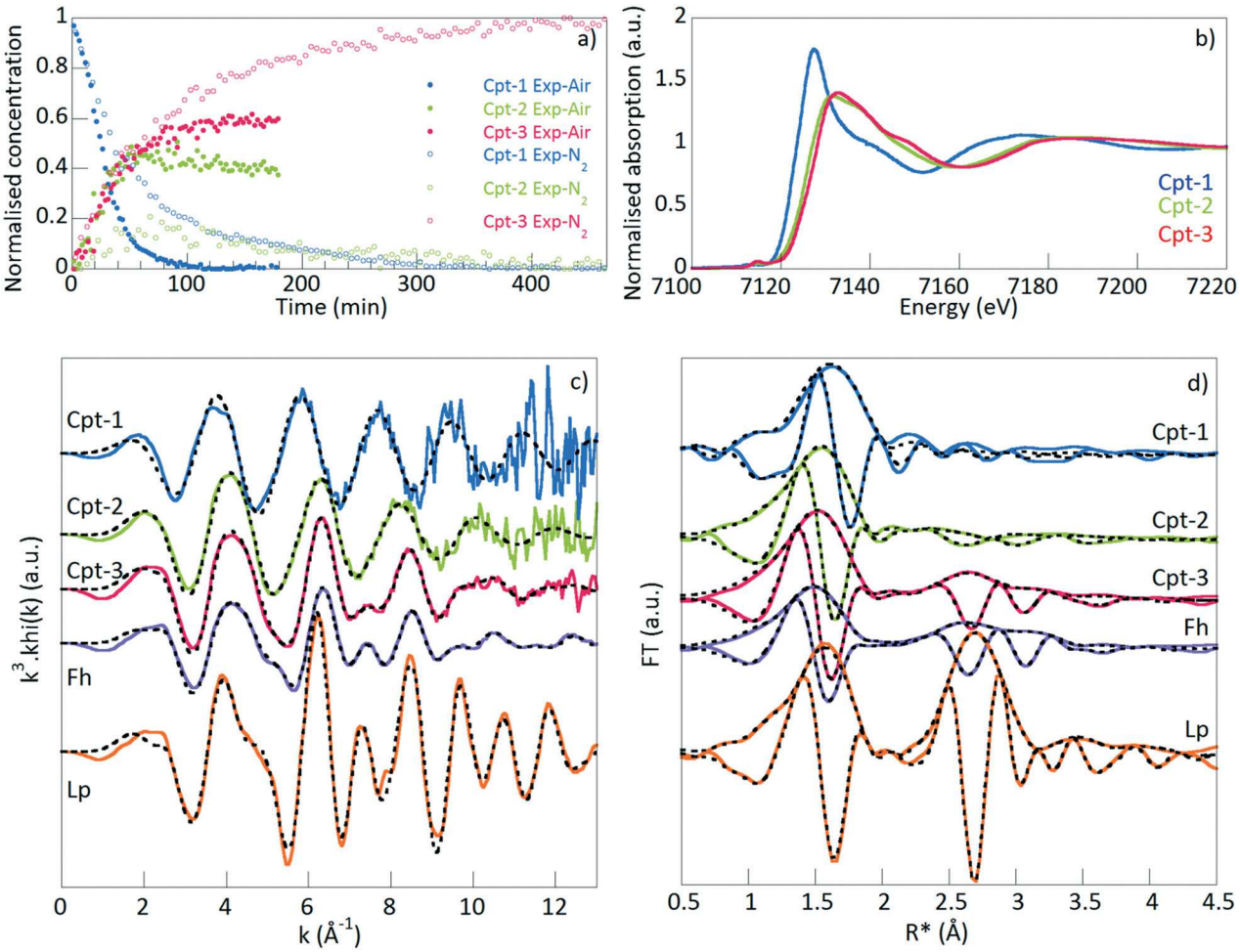

Fig. 3 a) Profiles of concentration as a function of time of the pure Fe phases extracted by MCR-ALS analysis for the Exp-Air and Exp-N_2 experiments. Only one out of five points is reported so as to make the figure easy to read. Convergence occurred after 11 iterations. The returned parameters were: standard deviation of residual *versus* experimental data = 5.68×10^{-3}, lack of fit (PCA) = 0.087185%, lack of fit (exp) = 0.61086%, variance explained at the optimum = 99.9963%. b) XANES spectra of the obtained pure compounds. c) and d) Corresponding EXAFS spectra and Fourier transforms, respectively, plotted with the fit results reported as dotted lines. Ferrihydrite (Fh) and lepidocrocite (Lp) spectra are reported as references.

from the phase shift), corresponding to the first, second and third coordination shells, respectively. The Cpt-3 EXAFS spectrum exhibits shoulders at 5.0 and 7.5 $Å^{-1}$. Two peaks dominate its Fourier transform: the first peak, due to the scattering of the first neighbours, located at approximately 1.5 Å, and a second broad peak located between 2.2 and 3.8 Å that arises from the scattering of the second coordination shell neighbours. These features, although less intense, are similar to those observed for the ferrihydrite spectrum. The EXAFS oscillations provided by the Cpt-1 Fe(II) phase are monotonous and shifted to the lowest *k*-values, compared with the Cpt-2 and Cpt-3 Fe(III) phases, leading to a single Fourier transform peak, corresponding to the signal for the first shell neighbours that are slightly shifted to higher distances.

The MCR-ALS EXAFS spectrum of the Fe(II) initial phase (Cpt-1) contributes to the full data set in a lower number of spectra with rapidly dropping percentages, and then its rebuilt MCR-ALS spectrum displays a weaker signal/noise ratio than the spectra rebuilt for the Fe(III) species. As a consequence, only the first neighbour shell of the Fe(II) EXAFS spectrum was fitted, with 6 oxygen (O) at 2.11 Å in agreement with octahedral Fe as shown in the XANES spectrum (Fig. 3b) and with the Fe–O distances of the Fe(II) species such as aqueous Fe(II).[40] According to the modelling calculations (Fig. 1), at the beginning of the oxidation/hydrolysis, Fe(II) should occur in similar proportions as dissolved and bound to HA. An Fe–C distance can be added to the fit at a reasonable distance (0.7 C at 3.16 Å). However, the fit quality is not drastically improved with this additional path as expressed in Fig. SI-2-a in the ESI.†

Without any OM, the oxidation/hydrolysis protocol used results in the formation of lepidocrocite.[34,41] The EXAFS signal provided by lepidocrocite is reported in Fig. 3c. The clearly different shape of this spectrum as compared with the spectra of the experimental phases suggests that HA prevents lepidocrocite formation for the benefit of new Fe phases.

Table 1 EXAFS fit results for the MCR-ALS components, Cpt-1, Cpt-2 and Cpt-3, and ferrihydrite and lepidocrocite references

	Cpt-1 (Fe(II))			Cpt-2 (Fe(III))			Cpt-3 (Fe(III))			Ferrihydrite			Lepidocrocite		
Path	CN	*R*	σ^2	CN	*R*	σ^2	CN	*R*	σ^2	CN	*R*	σ^2	CN	*R*	σ^2
Fe–O	6.0*	2.11	0.005	1.0**	1.92	0.003	2.9	1.93	0.004**	2.7	1.93	0.006**	3.0*	1.94	0.003
				5.0**	2.03	0.007	2.8	2.05	0.004**	1.5	2.06	0.006**	3.0*	2.05	0.002
Fe–C				1.1	2.83	0.008									
Fe–Fe				1.1	3.02	0.015**	1.6	3.05	0.011**	1.4	3.02	0.011**	6.0*	3.07	0.006
Fe–Fe							2.8	3.46	0.010**	3.6	3.46	0.010**			
Fe–O							4.4**	3.61	0.007	4.9**	3.61	0.008	6.0*	3.47	0.008
Fe–Fe				0.9	3.93	0.015**							2.0*	3.68	0.004
Fe–O							4.0	4.41	0.014	3.6	4.45	0.015	4.0*	4.38	0.002
R_{factor}	$56.1.10^{-5}$			$3.8.10^{-5}$			$1.9.10^{-5}$			$2.1.10^{-5}$			$2.6.10^{-5}$		

The amplitude reduction factor, S_0^2, was set to 0.75. The energy shift parameter, ΔE, was set to −0.36 eV for the Fe(III) species and −1.7 eV for the Fe(II) species. CN: coordination number; *R*: interatomic distance (Å); σ^2: Debye–Waller factor (Å^2). Uncertainties in CN, *R* and σ^2 are usually estimated to be ±10%, 1% and 20%, respectively. *R*-factor = $\Sigma i(data_i\text{-}fit_i)^2/\Sigma idata$. Multiple scattering paths were added for the fits of the lepidocrocite and Cpt-2 signals: a triangular Fe–Fe–O path (degeneracy = 4) at 3.80 Å, σ^2 = 0.012 Å^2 for lepidocrocite and a collinear Fe–O–Fe–O path (degeneracy = 6) at 3.85 Å, σ^2 = 0.008 Å^2 for Cpt-2. Fixed parameters are denoted by "*". Constraint parameters are denoted by "**".

Similar observations were reported with either humic or fulvic acids by Pédrot *et al.*[2] and Chen and Thompson,[38] respectively. Furthermore, using the parameters derived by Marsac *et al.*,[22] modelling predicts the presence of ferrihydrite and Fe(III) bound to HA as monomers and oligomers (Fig. 1). Since monomer and oligomer concentrations are expected to grow concomitantly, MCR-ALS analysis could not differentiate their signal but only single out two different spectra, one provided by ferrihydrite and one corresponding to the average spectrum of oligomers bound to HA. The spectrum of the lowest abundant phase, Cpt-2, could be fitted with 1 O at 1.92 Å and 5 O at 2.03 Å as first neighbours. Second neighbours are 1 Fe at 3.02 Å and 1 Fe at 3.93 Å. One C neighbour could be added at 2.83 Å to improve the fit quality. The improvement of the fit quality with the addition of paths for the different neighbours is reported in Fig. SI-2-b in the ESI.† The Cpt-2 signal can thus be assigned to an overall signal for oligomers of Fe octahedra bound to HA *via* carboxylic groups as predicted by Catrouillet *et al.*[23] The Fe–C distance corresponds to the distances reported in the literature for both natural and synthetic systems.[4,8–10,13,42,43] Short and long Fe–Fe distances correspond to edge and single corner sharing Fe octahedra, respectively.[44] Thus, according to the number and distance of the neighbours, the overall average signal could be described as a tetramer formed by two edge sharing dimers in which each octahedron is bound by its upper corner to an octahedron of the second dimer. Each octahedron is bound to HA.

The spectrum of the most abundant phase, Cpt-3, is fitted with 2.9 O at 1.93 Å and 2.8 O at 2.05 Å as first neighbours. Second neighbours are 1.6 Fe at 3.05 Å and 2.8 Fe at 3.46 Å. The representative shell by shell fit results are reported in Fig. SI-2-c in the ESI.† The obtained neighbours, distances and Debye–Waller (σ^2) factors are similar to the fitting parameters reported for ferrihydrite, although the number of O neighbours is higher (5.7 compared to 4.2 for ferrihydrite) and the number of Fe neighbours for the longest distance is lower (2.8 atoms compared to 3.6 for ferrihydrite). These differences can be attributed to a smaller size of the ferrihydrite particles. First of all, according to Voegelin *et al.*,[39] the number of O neighbours lower than 6–10% reported for ferrihydrite can be explained by partially destructive interferences for the individual scattering waves produced by the multiple Fe–O distances within the octahedron. In our samples, this multiplicity in terms of distances may be also related to the Debye–Waller value that is higher for ferrihydrite (σ^2 = 0.006) than that for Cpt-3 (σ^2 = 0.004). The apparent increase of O neighbours in Cpt-3 could then be a consequence of the smaller size of the Fe clusters, which results in fewer constraints on the geometry of the Fe octahedra and therefore smaller Fe–O distances and a lower Debye–Waller factor value as compared to ferrihydrite. Secondly, the particle size affects the coordination number in nanoparticles for long distance coordination shells.[45,46] Ferrihydrite is described as aggregates of primary particles measuring 1.6 to 3 nm in diameter.[13,47] Applying SAXS measurements on Fe–OM nanoaggregates synthesized from anoxic solutions of Fe(II) with HA, Guénet *et al.*[13] demonstrated that the presence of HA decreases the size of the ferrihydrite aggregates formed by these primary particles, from 150 to 5–10 nm. Furthermore, OM may affect both ferrihydrite size and crystallinity as demonstrated by Eusterhues *et al.*[48] based on TEM observations of ferrihydrites synthesized from Fe(III) with soil OM and Cismasu *et al.*,[49] using X-ray diffraction (XRD) and scattering combined with pair distribution function (PDF) analysis of ferrihydrites sampled in an acid mine drainage site.

The oxidation/hydrolysis of Fe(II) with HA at neutral pH and for Fe/OC = 0.4 leads to heterogeneous Fe–OM nanoaggregates composed of ferrihydrite-like nanoparticles (Fh-NPs) and oligomers of various sizes, the average structure of which can be described as a tetramer bound to HA. Oligomers bound to OM are reported in the literature for very low Fe/OC ratios. Their structure is variable although they are all described as bound to OM *via* carboxylic groups.[10,11,22] For Fe/OC ≤ 0.02, Daugherty *et al.*[35] and Karlsson and Persson[10] reported the formation of monomers from Fe(II) oxidation/

hydrolysis and Fe(III) hydrolysis, respectively. By contrast, for the same ratio, trimers can be observed as well. Mikutta and Kretzschmar[8] concluded that trimers are formed by three corner sharing octahedra from the Fe(III) hydrolysis with fulvic and humic acids. Based on the hydrolysis of Fe(III) in natural water, Vilgé-Ritter *et al.*[9] observed the formation of trimers formed by edge sharing dimers with one of the octahedra bound to another octahedron *via* an apical corner. Based on XAS measurements combined with thermodynamic equilibrium and density functional theory calculations, Zhu *et al.*[50] and Collins *et al.*[51] demonstrated that the hydrolysis of Fe(III) with increasing pH leads to the formation of hydrated monomers that are rapidly condensed into corner sharing dimers (so called μ-oxo dimers) that slowly rearrange into edge sharing dimers (so called dihydroxo dimers). Their assembly leads finally to the nucleation of ferrihydrite *via* the formation of trimers, tetramers and other oligomers. These results are also in agreement with molecular dynamic simulations performed by Zhang *et al.*[52] and the aqueous iron chemistry described in the study of Jolivet *et al.*[53] These results are therefore in agreement with the present study although Mikutta and Kretzschmar[8] did not detect the short Fe–Fe distance at 3.02 Å.

For very low Fe content, OM complexes Fe and prevents polymerization at its starting stage, and only monomer binding to OM can occur.[9] The Fe content increase results in the occurrence of free surface sites which allows the formation of corner sharing dimers as well as their slower condensation into edge sharing dimers.[50,51] Fh-NPs appear when the Fe/OC ratio sufficiently increases (typically above 0.02)[10] and the Fh/oligomer ratio increases with Fe/OC.[10,11,13,42] However, Chen *et al.*[11] did no longer observe oligomers for Fe/OC ≥ 0.3, while Guénet *et al.*[13,42] reported the coexistence of oligomers and ferrihydrite for Fe/OC ≥ 0.4. This discrepancy may be explained by the references used by Chen *et al.*[11] to perform EXAFS linear combination fits which include a ferrihydrite-free Fe(III)-organo-complex reference. However, according to Karlsson and Persson,[10] the Fe/OC ratio (0.04) used to synthesize this reference was certainly not low enough to prevent the formation of ferrihydrite in the complex. In the present work, for Fe/OC = 0.4, the presence of 5 or 40% of oligomers was evidenced depending on the experiment.

This difference in the content can be explained by the control of the ferrihydrite polymerization kinetics by the O_2 and OH^- input at constant pH. As compared to Exp-Air, in Exp-N_2, nitrogen bubbling slowed down the solution oxygenation and the Fe(II) oxidation. This drives the diminution of the base addition used to maintain a constant pH after OH^- consumption by ferrihydrite polymerization. Chen *et al.*[11] synthetized Fe–OM complexes by a slow pH increase in an Fe(III)–OM solution, and thus a slow base addition, the slowness of which allowed the modification over time of the intermediate equilibrium states as observed by Zhu *et al.*,[50] which subsequently led to a higher Fh/oligomer ratio as some of the oligomers slowly polymerized to form Fh-NPs due to their dynamics of ageing. Furthermore, it has been demonstrated that the ferrihydrite particle size grows with ageing and the pH increase, which leads to a decrease of the ferrihydrite solubility.[25,54] This phenomenon also contributes to the increase of the Fh/oligomer ratio over time. Fig. 3a shows that, at the beginning of the reaction, Fh-NP and oligomer concentrations increase concomitantly during Fe(II) oxidation, regardless of the rate of Fe(II) oxidation. After a reaction time of 70 min, 70–75 and 90–95% of Fe(II) are oxidized, and the oligomer content reaches a maximum, 15–20 and 45–50%, in Exp-N2 and Exp-Air, respectively. At a low rate of production by Fe(II) oxidation, the ferrihydrite particles have more time to grow and, consequently, they can be slightly larger in size and thus less soluble, lowering the fraction of oligomers. At a high rate of Fe(II) oxidation, there may be more nucleation and then more formation of ferrihydrite particles of smaller size. Consequently, these particles are more soluble, which leads to a higher fraction of Fe(III) oligomers. The difference in the amount of Fe(III) oligomers as observed can be explained by a very small difference in the solubility product of the Fh-NPs. As an example, a small difference in the Fh-NP size such as 1.68 *vs.* 1.65 nm would not lead to any significant modification of the Fh-NP EXAFS spectrum but can lead to a difference in the solubility product from Ks ~5.4 to Ks ~5.6 which leads to different Fh/oligomer ratios.[25,54] Accordingly, the observed slow decrease of the oligomer/Fh ratio after Fe(II) oxidation (Fig. 3a) can be explained by the ferrihydrite solubility decrease with its size growth over time.

Conclusions

Quick-EXAFS measurements combined with a MCR-ALS chemometric approach demonstrated that Fe(II) oxidation/hydrolysis in the presence of OM leads to the synthesis of Fe–OM complexes formed by oligomers and Fh-NPs bound to OM. The structure of the oligomers is the result of ferrihydrite polymerization inhibition by OM. Fh-NPs are formed at the expense of oligomers. The Fh/oligomer ratio depends on the Fe/OC ratio and on the oxidation/hydrolysis kinetics which is strongly influenced by OH^- availability in the solution. These structures and the Fe/OC ratios have dramatic environmental implications regarding their capacity to trap metal and metalloid pollutants. Guénet *et al.*[42] and Mikutta and Kretzschmar[8] demonstrated that, as ferrihydrite, Fe(III)-oligomers bound to OM are able to sorb arsenic (As). OM-embedded Fh-NPs are complexed to OM *via* surface reaction sites.[10,11] The sorption capacity of these ferrihydrites should therefore decrease with increasing nanoparticle size, and subsequently with increasing Fe content. By contrast, Guénet *et al.*[13] demonstrated that the As sorption capacity increases with increasing Fe content. Sorption sites occupied by OM therefore become released when the Fe content increases or the size of the nanoparticles increases.

The experimental conditions used in this study were close to the environmental conditions found in riparian wetlands (ionic strength and Fe/OC ratio) although they were optimized to allow the identification of Fe–OM complex

components by Quick-EXAFS combined with MCR-ALS chemometric analysis. They complete experiments that have already been published on systems with lower Fe/OC ratios.[8,10,11,35] It has been demonstrated that, even at a high Fe/OC ratio, Fe-oligomers and Fh-NPs bound to OM still coexist in Fe–OM complexes. However, these experiments do not represent the full range of possible environmental conditions. If a simple system (Fe(II) + OM) leads to the formation of a bi-phase system, published studies on natural soils subjected to redox cycles revealed the additional occurrence of lepidocrocite.[4,7] Chen and Thompson[38] provided evidence that the oxidation of Fe(II) in an OM matrix containing goethite or alumina results in the formation of ferrihydrite and goethite or lepidocrocite, respectively. In addition, the anoxic transformation of ferrihydrite bound to OM in the presence of Fe(II) leads to the formation of goethite, and, to a lower extent, lepidocrocite.[12,55] Since the Quick-EXAFS experiments combined with the MCR-ALS chemometric analysis performed in the present work provided unprecedented information regarding the formation of phases, we demonstrated that this combined technique is a very promising tool to study more complex systems, by adding competitor ions or other minerals that are expected to modify Fe–OM interactions.

Conflicts of interest

There are no conflicts to declare.

Acknowledgements

The authors acknowledge SOLEIL for beamtime allocation at the ROCK beamline (proposal 20160470) and the beamline staff, especially Laurent Barthe, for their kind support. The work at ROCK was supported by a public grant overseen by the French National Research Agency (ANR) as a part of the "Investissements d'Avenir" program ref: ANR-10-EQPX-45. D. Vantelon thanks the CNRS GdR "*Catalyse, Réactivité de Surface et Rayonnement Synchrotron*" for the provided MCR-ALS formation. Dr Sara Mullin is acknowledged for post-editing the English style.

Notes and references

1 O. S. Pokrovsky and J. Schott, Iron colloids/organic matter associated transport of major and trace elements in small boreal rivers and their estuaries (NW Russia), *Chem. Geol.*, 2002, **190**, 141–179.

2 M. Pédrot, A. Dia, M. Davranche, M. Bouhnik-Le Coz, O. Henin and G. Gruau, Insights into colloid-mediated trace element release at the soil/water interface, *J. Colloid Interface Sci.*, 2008, **325**, 187–197.

3 E. Neubauer, S. J. Köhler, F. von der Kammer, H. Laudon and T. Hofmann, Effect of pH and Stream Order on Iron and Arsenic Speciation in Boreal Catchments, *Environ. Sci. Technol.*, 2013, **47**, 7120–7128.

4 H. Guénet, M. Davranche, D. Vantelon, M. Pédrot, M. Al-Sid-Cheikh and J. Jestin, Implication of Organic Matter and iron oxides in the As immobilization in riparian wetlands, *Chem. Geol.*, 2016, **439**, 161–172.

5 W. Stumm and J. J. Morgan *Aquatic chemistry: chemical equilibria and rates in natural waters*, John Wiley & Sons, Inc., New York, 3rd edition, 1996.

6 J. Plach, A. Elliott, I. Droppo and L. Warren, Physical and Ecological Controls on Freshwater Floc Trace Metal Dynamics, *Environ. Sci. Technol.*, 2011, **45**(6), 2157–2164.

7 L. K. Thomas Arrigo, C. Mikutta, J. Byrne, K. Barmettler, A. Kappler and R. Kretzschmar, Iron and Arsenic Speciation and Distribution in Organic Flocs from Streambeds of an Arsenic-Enriched Peatland, *Environ. Sci. Technol.*, 2014, **48**, 13218–13228.

8 C. Mikutta and R. Kretzschmar, Spectroscopic Evidence for Ternary Complex Formation between Arsenate and Ferric Iron Complexes of Humic Substances, *Environ. Sci. Technol.*, 2011, **45**, 9550–9557.

9 A. Vilgé-Ritter, J. Rose, A. Masion, J.-Y. Bottero and J.-M. Lainé, Chemistry and structure of aggregates formed with Fe-salts and natural organic matter, *Colloids Surf., A*, 1999, **147**, 297–308.

10 T. Karlsson and P. Persson, Complexes with aquatic organic matter suppress hydrolysis and precipitation of Fe(III), *Chem. Geol.*, 2012, **322–323**, 19–27.

11 C. Chen, J. J. Dynes, J. Wang and D. L. Sparks, Properties of Fe-Organic Matter Associations via Coprecipitation versus Adsorption, *Environ. Sci. Technol.*, 2014, **48**, 13751–13759.

12 L. K. Thomas Arrigo, C. Mikutta, J. Byrne, A. Kappler and R. Kretzschmar, Iron(II)-Catalyzed Iron Atom Exchange and Mineralogical Changes inIron-rich Organic Freshwater Flocs: An Iron Isotope Tracer Study, *Environ. Sci. Technol.*, 2017, **51**(12), 6897–6907.

13 H. Guénet, M. Davranche, D. Vantelon, J. Gigault, S. Prévost, O. Taché, S. Jaksch, M. Pédrot, V. Dorcet, A. Boutier and J. Jestin, Characterization of iron-organic matter aggregate networks through a combination of SAXS/SANS and XAS analyses: impact on As binding, *Environ. Sci.: Nano*, 2017, **4**, 938–954.

14 H. P. Jarvie and S. M. King, Small-Angle Neutron Scattering Study of Natural Aquatic Nanocolloids, *Environ. Sci. Technol.*, 2007, **41**, 2868–2873.

15 C. W. Neil, J. R. Ray, B. Leeb and Y.-S. Jun, Fractal aggregation and disaggregation of newly formed iron(III) (hydr)oxide nanoparticles in the presence of natural organic matter and arsenic, *Environ. Sci.: Nano*, 2016, **3**, 647–656.

16 M. Davranche, A. Dia, M. Fakih, B. Nowack, G. Gruau, G. Ona-Nguema, P. Petitjean, S. Martin and R. Hochreutener, Organic matter control on the reactivity of Fe(III)-oxyhydroxides and associated As in wetland soils: a kinetic modeling study, *Chem. Geol.*, 2013, **335**, 24–35.

17 A. De Juan, J. Jaumot and R. Tauler, Mutlivariate Curve Resolution (MCR). Solving the mixture analysis problem, *Anal. Methods*, 2014, **6**, 4964–4976.

18 A. Rochet, B. Baubet, V. Moizan, E. Devers, A. Hugon, C. Pichon, E. Payen and V. Briois, Intermediate Species Revealed during Sulfidation of Bimetallic Hydrotreating

Catalyst: A Multivariate Analysis of Combined Time-Resolved Spectroscopies, *J. Phys. Chem. C*, 2017, **121**, 18544–18556.

19 D. L. Parkhurst and C. A. J. Appelo, *User's guide to PHREEQC (Version 2) — a computer program for speciation, batch reaction, one-dimensional transport and inverse geochemical calculation. Water-resources Investigation Report 99–4259*, USGS, Denver, Colorado, 1999.

20 E. Tipping, Humic ion-binding model VI: an improved description of the interactions of protons and metal ions with humic substances, *Aquat. Geochem.*, 1998, **4**, 3–48.

21 R. Marsac, M. Davranche, G. Gruau, M. Bouhnik-Le Coz and A. Dia, An improved description of the interactions between rare earth elements and humic acids by modeling: PHREEQC-Model VI coupling, *Geochim. Cosmochim. Acta*, 2011, **75**, 5625–5637.

22 R. Marsac, M. Davranche, G. Gruau, A. Dia, M. Pédrot, M. Le Coz-Bouhnik and N. Briant, Effects of Fe competition on REE binding to humic acid: Origin of REE pattern variability in organic waters, *Chem. Geol.*, 2013, **342**, 119–127.

23 C. Catrouillet, M. Davranche, A. Dia, M. Bouhnik-Le Coz, R. Marsac, O. Pourret and G. Gruau, Geochemical modeling of Fe(II) binding to humic and fulvic acids, *Chem. Geol.*, 2014, **372**, 109–118.

24 T. Weber, T. Allard, E. Tipping and M. Benedetti, Modelling iron binding to organic matter, *Environ. Sci. Technol.*, 2006, **40**, 7488–7493.

25 T. Hiemstra, Formation, stability, and solubility of metal oxide nanoparticles: Surface entropy, enthalpy, and free energy of ferrihydrite, *Geochim. Cosmochim. Acta*, 2015, **158**, 179–198.

26 V. Briois, C. La Fontaine, S. Belin, L. Barthe, T. Moreno, V. Pinty, A. Carcy, R. Girardot and E. Fonda, ROCK: the new Quick-EXAFS beamline at SOLEIL, *J. Phys.: Conf. Ser.*, 2016, **712**, 012149.

27 C. Lesage, C. Legens, E. Devers, G. Fernandes, O. Roudenko and V. Briois, High Pressure Cell for Edge Jumping X-ray Absorption Spectroscopy: Applications to industrial liquid sulfidation of hydrotreatment catalysts, *Catal. Today*, 2019, DOI: 10.1016/j.cattod.2019.01.081, in press.

28 J. Jaumot, R. Gargallo, A. De Juan and R. Tauler, A graphical user-friendly interface for MCR-ALS: a new tool for multivariate curve resolution in MATLAB, *Chemom. Intell. Lab. Syst.*, 2005, **76**, 101–110.

29 B. Ravel and M. Newville, ATHENA, ARTEMIS, HEPHAESTUS. Data analysis for X-ray absorption spectroscopy using IFEFFIT, *J. Synchrotron Radiat.*, 2005, **12**, 537–541.

30 M. Newville, IFEFFIT: interactive XAFS analysis and FEFF fitting, *J. Synchrotron Radiat.*, 2001, **8**, 322–324.

31 J.-L. Hazemann, J. Bérar and A. Manceau, Rietveld Studies of the Aluminium-Iron Substitution in Synthetic Goethite, *Mater. Sci. Forum*, 1991, **79–82**, 821–826.

32 A. P. Zhukhlistov, Crystal structure of lepidocrocite FeO(OH) from the electron-diffractometry data, *Crystallogr. Rep.*, 2001, **46**, 730–733.

33 P. Horcajada, S. Surble, C. Serre, D.-Y. Hong, Y. K. Seo, J. S. Chang, J. M. Greneche, I. Margiolaki and G. Ferey, Synthesis and catalytic properties of MIL-100(Fe), an iron(III) carboxylate with large pores, *Chem. Commun.*, 2007(27), 2820–2822.

34 U. Schwertmann and R. M. Cornell, *Iron Oxides in the Laboratory: Preparation and Characterization. 2nd Completely Revised and Extended Edition*, Wiley-VCH, Weinheim, Germany, 2000.

35 E. E. Daugherty, B. Gilbert, P. S. Nico and T. Borch, Complexation and Redox Buffering of Iron(II) by Dissolved Organic Matter, *Environ. Sci. Technol.*, 2017, **51**, 11096–11104.

36 M. Wilke, F. Farges, P.-E. Petit, G. E. Brown Jr. and F. Martin, Oxidation state and coordination of Fe in minerals: An Fe K-XANES spectroscopic study, *Am. Mineral.*, 2001, **86**, 714–730.

37 A. De Juan and R. Tauler, Chemometrics applied to unravel multicomponent processes and mixture. Revisiting latest trends in multivariate resolution, *Anal. Chim. Acta*, 2003, **500**, 195–210.

38 C. Chen and A. Thompson, Ferrous Iron Oxidation under Varying pO2 Levels: The Effect of Fe(III)/Al(III) Oxide Minerals and Organic Matter, *Environ. Sci. Technol.*, 2018, **52**, 597–606.

39 A. Voegelin, R. Kaegi, J. Frommer, D. Vantelon and S. J. Hug, Effect of phosphate, silicate, and Ca on Fe(III)-precipitates formed in aerated Fe(II)- and As(III)-containing water studied by X-ray absorption spectroscopy, *Geochim. Cosmochim. Acta*, 2010, **74**, 164–186.

40 E. Elzinga, Formation of Layered Fe(II)–Al(III)-Hydroxides during Reaction of Fe(II) with Aluminum Oxide, *Environ. Sci. Technol.*, 2012, **46**, 4894–4901.

41 M. Fakih, M. Davranche, A. Dia, B. Nowack, P. Petitjean, X. Chatellier and G. Gruau, A new tool for in situ monitoring of Fe-mobilization in soils, *Appl. Geochem.*, 2008, **23**, 3372–3383.

42 H. Guénet, M. Davranche, D. Vantelon, M. Bouhnik-Le Coz, E. Jarde, A.-C. Pierson-Wickmann, V. Dorcet and J. Jestin, Highlighting the wide variability in arsenic speciation in wetlands: a new insight into the control of the behaviour of arsenic, *Geochim. Cosmochim. Acta*, 2017, **203**, 284–302.

43 T. Karlsson, P. Persson, U. Skyllberg, C.-M. Morth and R. Giesler, Characterization of Iron(III) in Organic Soils Using Extended X-ray Absorption Fine Structure Spectroscopy, *Environ. Sci. Technol.*, 2008, **42**, 5449–5454.

44 A. Manceau and V. A. Drits, Local structure of ferrihydrite and feroxyhite by EXAFS spectroscopy, *Clay Miner.*, 1993, **28**, 165–184.

45 A. I. Frenkel, Solving the structure of nanoparticles by multiple-scattering EXAFS analysis, *J. Synchrotron Radiat.*, 1999, **6**, 293–295.

46 T. Hiemstra, Surface structure controlling nanoparticle behaviour: magnetism of ferrihydrite, magnetite, and maghemite, *Environ. Sci.: Nano*, 2018, **5**, 752–764.

47 F. M. Michel, L. Ehm, G. Liu, Q. Han, X. S. M. Antao, P. J. Chupas, P. L. Lee, K. Knorr, H. Eulert, J. Kim, C. P. Grey, A. J. Celestian, O. J. Gillow, M. A. A. Schoonen, D. R.

Strongin and J. B. Parise, Similarities in 2- and 6-Line Ferrihydrite Based on Pair Distribution Function Analysis of X-ray Total Scattering, *Chem. Mater.*, 2007, **19**, 1489–1496.

48 K. Eusterhues, F. E. Wagner, W. Hausler, M. Hanzlik, H. Knicker, K. U. Totsche, I. Kogel-Knabner and U. Schwertmann, Characterization of Ferrihydrite-Soil Organic Matter Coprecipitates by X-ray Diffraction and Mossbauer, *Environ. Sci. Technol.*, 2008, **42**, 7891–7897.

49 A. C. Cismasu, F. M. Michel, A. P. Tcaciuc, T. Tyliszczak and G. E. Jr. Brown, Composition and structural aspects of naturally occurring ferrihydrite, *C. R. Geosci.*, 2011, **343**, 210–218.

50 M. Zhu, C. Frandsen, A. F. Wallace, B. Legg, S. Khalid, H. Zhang, S. Mørup, J. F. Banfield and G. A. Waychunas, Precipitation pathways for ferrihydrite formation in acidic solutions, *Geochim. Cosmochim. Acta*, 2016, **172**, 247–264.

51 R. N. Collins, K. M. Rosso, A. L. Rose, C. J. Glover and T. D. Waite, An in situ XAS study of ferric iron hydrolysis and precipitation in the presence of perchlorate, nitrate, chloride and sulfate, *Geochim. Cosmochim. Acta*, 2016, **177**, 150–169.

52 H. Zhang, G. A. Waychunas and J. F. Banfeld, Molecular dynamics simulation study of the early stages of nucleation of iron oxyhydroxide nanoparticles in aqueous solution, *J. Phys. Chem. B*, 2015, **119**, 10630–10642.

53 J. P. Jolivet, E. Tronc and C. Chanéac, Iron oxides: from molecular clusters to solid. A nice example of chemical versatility, *C. R. Geosci.*, 2006, **338**, 488–497.

54 T. Hiemstra, J. C. Mendez and J. Li, Evolution of the reactive surface area of ferrihydrite: time, pH, and temperature dependency of growth by Ostwald ripening, *Environ. Sci.: Nano*, 2019, **6**, 820–833.

55 C. Chen, R. Kukkadapu and D. L. Sparks, Influence of Coprecipitated Organic Matter on Fe^{2+} (aq)-Catalyzed Transformation of Ferrihydrite: Implications for Carbon Dynamics, *Environ. Sci. Technol.*, 2015, **49**, 10927–10936.

Annexe 3

JOURNAL OF SYNCHROTRON RADIATION

ISSN 1600-5775

Received 22 July 2019
Accepted 7 November 2019

Edited by I. Schlichting, Max Planck Institute for Medical Research, Germany

Keywords: SOLEIL; microfluidics; X-ray microfluorescence; X-ray absorption; small-angle X-ray scattering; macromolecular crystallography.

Supporting information: this article has supporting information at journals.iucr.org/s

The microfluidic laboratory at Synchrotron SOLEIL

Igor Chaussavoine,[a] Anthony Beauvois,[a,b,c] Tiphaine Mateo,[a] Ramakrishna Vasireddi,[a] Nadine Douri,[a] Jordan Priam,[a] Youssef Liatimi,[a] Stéphane Lefrançois,[a] Hervé Tabuteau,[d] Mélanie Davranche,[b] Delphine Vantelon,[a]* Thomas Bizien,[a]* Leonard, M. G. Chavas[a]* and Benedikt Lassalle-Kaiser[a]*

[a]Synchrotron SOLEIL, Saint-Aubin, 91192 Gif-sur-Yvette, France, [b]Univ. Rennes, CNRS, Géosciences Rennes – UMR 6118, F-35000 Rennes, France, [c]Laboratoire Léon Brillouin, Commissariat à l'Energie Atomique Saclay, 91191 Gif-sur-Yvette, France, and [d]Univ. Rennes, CNRS, IPR (Institut de Physique de Rennes) – UMR 6251, F-35000 Rennes, France. *Correspondence e-mail: delphine.vantelon@synchrotron-soleil.fr, thomas.bizien@synchrotron-soleil.fr, leonard.chavas@synchrotron-soleil.fr, benedikt.lassalle@synchrotron-soleil.fr

A microfluidic laboratory recently opened at Synchrotron SOLEIL, dedicated to in-house research and external users. Its purpose is to provide the equipment and expertise that allow the development of microfluidic systems adapted to the beamlines of SOLEIL as well as other light sources. Such systems can be used to continuously deliver a liquid sample under a photon beam, keep a solid sample in a liquid environment or provide a means to track a chemical reaction in a time-resolved manner. The laboratory provides all the amenities required for the design and preparation of soft-lithography microfluidic chips compatible with synchrotron-based experiments. Three examples of microfluidic systems that were used on SOLEIL beamlines are presented, which allow the use of X-ray techniques to study physical, chemical or biological phenomena.

1. Introduction

Microfluidics is a rapidly evolving field that covers a wide range of scientific domains for both applied and fundamental research (Whitesides, 2006). Commercial applications using microfluidics range from biomedical analyses to drug discovery and printing systems, with a particularly high impact on health technologies. Fundamental research also takes advantage of microfluidic systems to explore physical phenomena that can only be accessed under specific physical conditions: interfacial physics (Hemmerle *et al.*, 2016), emulsions (Zarzar *et al.*, 2015) and droplets (Joanicot & Ajdari, 2005) formation or (bio)chemical kinetics (Song & Ismagilov, 2003). Microfluidic systems also offer exciting opportunities for spectroscopic, structural and imaging techniques. On the one hand, the possibility to study samples in liquid environments; on the other hand, an access to novel physical properties that are specific to the micrometre scale (Tabeling, 2005). The advances in polymer-based soft-lithography techniques (Qin *et al.*, 2010) now allow designing, producing and analyzing microfluidic systems within less than a day. This short-time production is ideal to meet the time constraints of typical beam time allocation schemes at synchrotrons or free-electron lasers. These manufacturing procedures offer the possibility to produce disposable chips that meet the requirements of both the system to be studied and the photon-based tool to be used. Such experiments have already been conducted at synchrotrons, where a wide range of photon energies are available with a high brilliance and thus allow

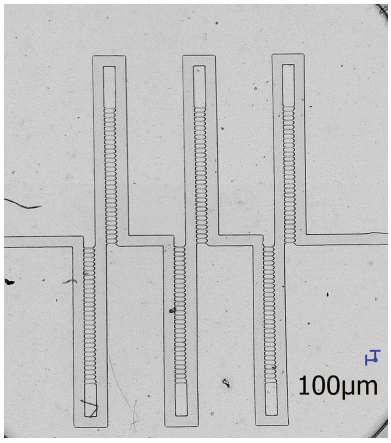

unique experiments (Zheng *et al.*, 2004; Polte *et al.*, 2010; Reich *et al.*, 2005). However, coupling microfluidic devices with synchrotron techniques is a significant challenge since each photon-based technique has specific requirements such as photon penetration depth, low pressures, sample dimensions or physical constraints. In order to satisfy this increasing need at synchrotron facilities, a microfluidic laboratory was recently opened at SOLEIL. Its aim is to sustainably provide the environment and know-how for the implementation of microfluidic systems in photon-based experiments. It is worth mentioning that the current or upcoming upgrade of several synchrotrons into diffraction-limited storage rings will increase the photon density at the sample, which will require fast sample replacement to either avoid radiation damage or provide a new sample to optimize data-collection strategies.

The present article describes the environment and tools that are available to produce and analyze microfluidic systems in this laboratory. Examples of the first projects carried out using this facility highlight specific research applications where microfluidic devices can be adapted to synchrotron-based techniques to generate new and original approaches. As a prospectus, this article outlines the research areas where we expect microfluidic and synchrotron research to cooperate in the near future.

2. Facilities and instruments

The microfluidics laboratory at SOLEIL has a 25 m^2 clean room with a controlled environment located in the experimental hall within the synchrotron building (Fig. 1). Separated from the synchrotron hall by a double-door entry, with the air temperature and quality controlled, the laboratory's ceiling illuminations and windows are filtered to absorb more than 90% of the natural UV light. The room is equipped with all the required instrumentation for basic chemical or biochemical work (fume hood, laminar flow cabinet, water purifying system, solvent cabinet, waste containers, refrigerator, oven and hot plates). The clean room was classified as class 10.000/ISO 7 (US FED/ISO system).

The purpose of the microfluidic laboratory is to host and maintain instruments for the fabrication and analysis of microfluidic systems applied to synchrotron-based experiments. In this prospect, micro-fabrication processes can be performed using the following apparatus.

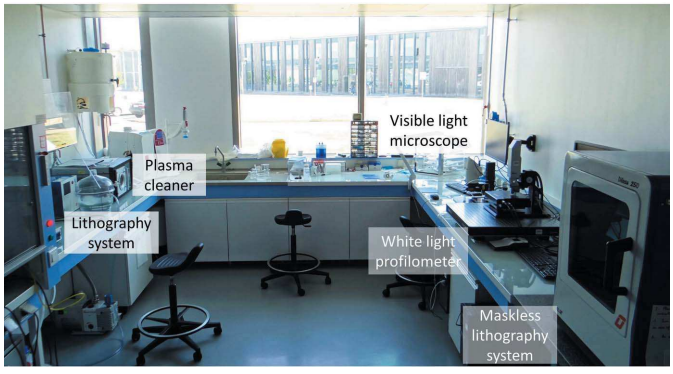

Figure 1
Overview of the clean room of the microfluidic laboratory.

(i) A spin coater (Laurell Technologies) with a maximum rotation speed of 12 000 r.p.m., which allows producing thin films (down to tens of nanometres) on substrates (*e.g.* silicon wafers or glass plates).

(ii) A direct maskless lithography system (Dilase-250, KLOE), which allows the patterning of photosensitive resins. The laser wavelength is 375 nm for a maximum power of 18 mJ. The laser spot size can be tuned from 4 to 50 µm. The time required for the patterning of a complete microfluidic system using this device is much higher than using a traditional light-exposure device using masks (*vide infra*) since the laser system literally has to draw the whole pattern including filling large areas. The choice of this instrument was motivated by its flexibility in fabricating patterns in a minimal amount of time directly from the design step to the printed pattern, as opposed to delays in purchasing a mask from an external company.

(iii) A hydraulic high-temperature press (Vogt GmbH), which allows producing microfluidic chips based on COC (cyclic olefins copolymers). Using COC is particularly interesting for chips that are destined for synchrotron experiments since the thickness of the chip window can be as thin as 10 µm, thus minimizing the background.

(iv) A UV-light-exposure system (UV-KUB 2, KLOE) is available for photolithography processes using dedicated masks.

(v) A plasma-generating device (Henniker Ltd) that allows O_2, N_2, Ar or air plasma-induced bonding processes. A portable corona-effect device (Blackhole Laboratory) is also available for small scale or rapid bonding.

(vi) A 3D printer based on the polyjet technology (Objet 30 Pro, Stratasys Ltd). Two proprietary printing materials are currently available: VeroWhite and VeroClear. The VeroWhite material can be deposited with 32 µm-thick layers, while the VeroClear material is translucent and can be deposited with 16 µm-thick layers for twice the printing time. The smallest features performed by the machine in the *xy* coplanar directions are $\sim$60 $\pm$ 10 µm. When working on microfluidic applications, one of the main disadvantages of such a device is the use of a support material that is printed within the channels and therefore needs to be removed by mechanical and/or chemical means after the printing process. Despite this drawback, the smallest channels produced for our applications had an inner diameter of 300–500 µm (depending on the channel length), while self-supported membranes $\sim$100 µm thick were successfully fabricated.

To inspect the various features of the produced devices, quality-control equipment is available for analyses during and after the microfabrication processes. These include the following.

(i) A contact-free profilometer (WLI GmbH) based on white-light interferometry is typically used to map the 3D topology of micrometre-sized objects in less than a minute with a vertical resolution of $\sim$20 nm. In practice, this equip-

ment helps in observing the pattern's quality in the resin after the lithography process.

(ii) A custom-made microscope with infinity-corrected optics and a working distance of 34 mm adapting 5×, 10× and 50× objectives (Mitutoyo). It is equipped with a Basler camera and allows observing microfluidic systems under circulation with a high resolution.

(iii) A Leica DMS 1000 macroscope with front and back illumination directly casts images on a computer screen for easy manipulation of microfluidic chips.

(iv) Pressure controllers (Elveflow, Fluigent), peristaltic pumps (Ismatec) and syringe pumps (New Era Pump Systems Inc.).

3. First results

3.1. A vacuum-compatible microfluidic chip for the *in situ* study of iron oxide nanoparticles formation using μ-XRF and μ-XAS

In natural water, iron oxyhydroxides are major vectors controlling the behavior of inorganic pollutants such as metals and metalloids. They are indeed known to be strong sorbents of metals and metalloids regarding their high density of binding sites. Under environmental conditions, their structure and their subsequent reactivity is strongly influenced by the physico-chemical conditions that occur during their formation (such as pH, ionic strength, concentration, or the presence of competing cations or anions). As of now, little is known on the species that are formed at the early stage of the reaction and about their evolution with the running time reaction, as a function of physico-chemical conditions. However, the early formed Fe species are critical regarding the structural diversity of the Fe phases observable in natural systems. To better understand these structures, we followed the nucleation process of Fe oxides using *in situ* microfluidic synthesis, which allows the transposing of the time scale into a spatial one (Chan *et al.*, 2007). The evolution of the Fe speciation was followed by Fe *K*-edge X-ray absorption spectroscopy (XAS) during *in situ* synthesis of Fe(III) oxides by the oxidation hydrolysis of a Fe(II) solution, increasing its pH, on the LUCIA beamline (Vantelon *et al.*, 2016).

We have designed a microfluidic device (see Figs. 2 and 3) that is compatible with the primary vacuum (10^{-2} mbar)

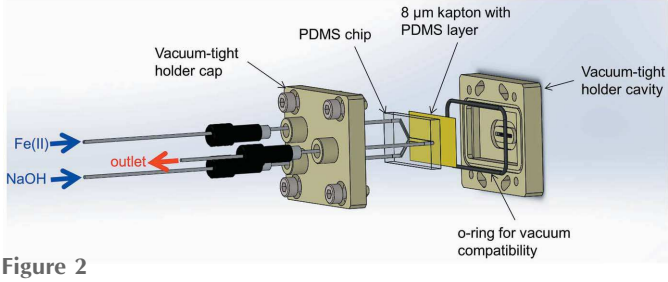

Figure 2
Schematic representation of the vacuum-compatible microfluidic device used on the LUCIA beamline.

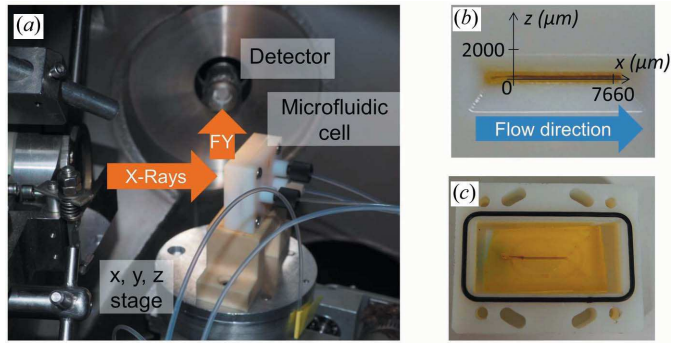

Figure 3
(*a*) Picture of the experimental setup inside the LUCIA beamline experimental chamber. FY stands for fluorescence yield. (*b*) Back view of the chip holder during a microfluidic synthesis experiment. The brown color observed inside the channel shows the formation of Fe(III) oxides. (*c*) Inside view of the vacuum-compatible cell with the PDMS chip at the end of the experiment.

environment of the LUCIA beamline and allows the collection of μ-XAS spectra under microfluidic circulation.

The device consists of a polydimethylsiloxane (PDMS) chip inserted into a vacuum-tight holder. The chip circuit is a Y shape, with two inlets to introduce the reactants and an observation channel connected to the outlet (see Fig. S1 in the supporting information). The channel was 300 μm wide, 500 μm deep and 1 mm long. The chip was microfabricated using an SU-8 mold, which was replicated into a 1 cm-thick PDMS block. The chip was sealed with a 8 μm-thick Kapton foil on which a 30 μm layer of PDMS was spin-coated and activated by plasma treatment. The chip was then inserted into the vacuum-tight holder. The holder consists of a 3D-printed block with a cavity to insert the chip and a cap to close the cavity. The cavity has a 1 mm-wide opening at its back, located in front of the observation channel. The cap has three threaded inlets that allow the connection of tubings to and from the measurement chamber and the chip. The inlet and outlet tubings were connected to the outside of the chamber using feed-through flanges. The holder is made vacuum compatible with an O-ring between the cap and the holder, and by gluing the Kapton foil at the bottom of the holder.

The device was installed on the LUCIA beamline (Vantelon *et al.*, 2016) to follow the evolution of Fe phases during Fe(III) oxides formation by Fe *K*-edge XAS. The monochromator used was Si(111) crystals. The energy was calibrated by setting the first inflection point of the *K*-edge of an Fe foil to 7112 eV. The beam size was set to 3.5 μm × 3.5 μm for the measurements. Data were collected in fluorescence mode with a monoelement silicon drift detector (SDD) (60 mm^2 Brucker). An iron(II) chloride ($FeCl_2 0.4H_2O$) solution of 1.1 × 10^{-3} mol l^{-1} and a sodium hydroxide solution of 1.0 × 10^{-3} mol l^{-1} (NaOH) were filled in the inlet channels using syringe pumps (NE-1002X from Pump System Inc.) with a rate of 100 μl min^{-1}. An X-ray fluorescence map of the channel was recorded around the opening with an excitation energy of 7300 eV, a step size of 5 μm and a counting time of 300 ms per point. The map is presented in Fig. 4(*a*) and one can clearly observe three regions: (i) a region without any iron (in green,

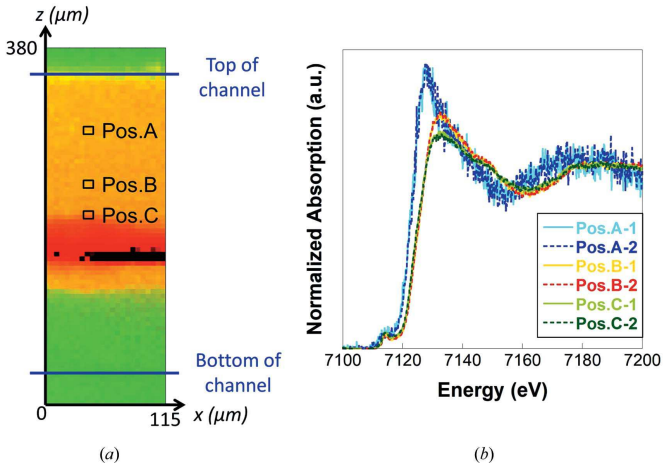

Figure 4
(*a*) μ-XRF map recorded on the observation channel. Green stands for the silicon of the chip, orange to red stands for the iron (low and high concentration, respectively) and black indicates a concentration of iron so high that the detector was saturated. (*b*) Normalized XANES spectra at the Fe *K*-edge recorded on the positions indicated on the μ-XRF map. The positions where the spectra were collected are reported in (*a*) as positions A, B and C. The collection of spectra was duplicated; the two successive XANES spectra being labeled 1 and 2, respectively.

at the bottom of the channel), which is the region where the NaOH solution flows; (ii) a region with low iron content (in orange, at the top of the channel), which is the region where the injected $FeCl_2$ flows; and (iii) an iron-enriched region (in red, in the center of the channel), where the interaction between the $FeCl_2$ and NaOH solutions occurs and Fe(III) oxide nanoparticles precipitate. X-ray absorption near-edge structure (XANES) spectra were collected at the Fe *K*-edge at different positions in the channel, going from the Fe(II) solution to the Fe(III) precipitates (from the top to the center of the channel). Data are reported in Fig. 4(*b*). The edge energy shift between the first spectrum and the others indicates that the starting Fe(II) ions have been oxidized at the contact with NaOH to form Fe(III) oxide nanoparticles. The different shapes observed from position B and position C spectra are caused by the increasing non-corrected dead-time subsequent to the accumulation of Fe(III) in the channel. The collection of two consecutive μ-XAS spectra on each spot [referred to as spectra 1 and 2 in Fig. 4(*b*)] shows that there are no beam-induced damages and deposition on the window. The further study of the iron oxides nucleation growth will be to create more complex systems using the addition of cations, ions and organic matter to make it closer to environmental conditions. However, these preliminary results demonstrate that the collection of μ-XRF (micro X-ray fluorescence) and μ-XANES spectra in microfluidic devices are possible under vacuum, which opens up a wide range of studies in the tender and soft X-ray energy ranges for the study of light elements.

3.2. Chemical kinetics of nanoparticle dilution using a 3D-printed and PDMS microfluidic mixer

The dynamics of protein (un)folding nanoparticles formation or fiber assembly can be studied efficiently using synchrotron-based X-ray scattering or spectroscopic techniques. *In situ* flow-cell devices are required in order to follow such fast kinetic phenomena. Although stop-flow systems have been traditionally used for these applications, the advent of 3D-printing systems at reasonable costs and with good resolution makes it a very attractive alternative (Au *et al.*, 2016). Although they require more advanced equipment and know-how, microfluidic chips can also be used as versatile and reactive mixing and/or flowing systems suitable for *in situ* X-ray diffusion techniques.

We describe here a PDMS-based microfluidic chip (see Figs. 5 and S2) for time-resolved *in situ* small-angle X-ray scattering/wide-angle X-ray scattering (SAXS/WAXS) data collection on liquid solutions. It is made of three parts: the upper layer containing channels of 180 μm × 180 μm (height × width), the lower part consisting of a spin-coated layer of PDMS (100 μm) on top of a Kapton foil (25 μm), and a 3D-printed backbone for stiffness and to prevent PDMS from leaking onto the area of measurement during the fabrication process. Thanks to this design, the X-ray beam only needs to go through two thin layers of PDMS (both 100 μm thick) and a

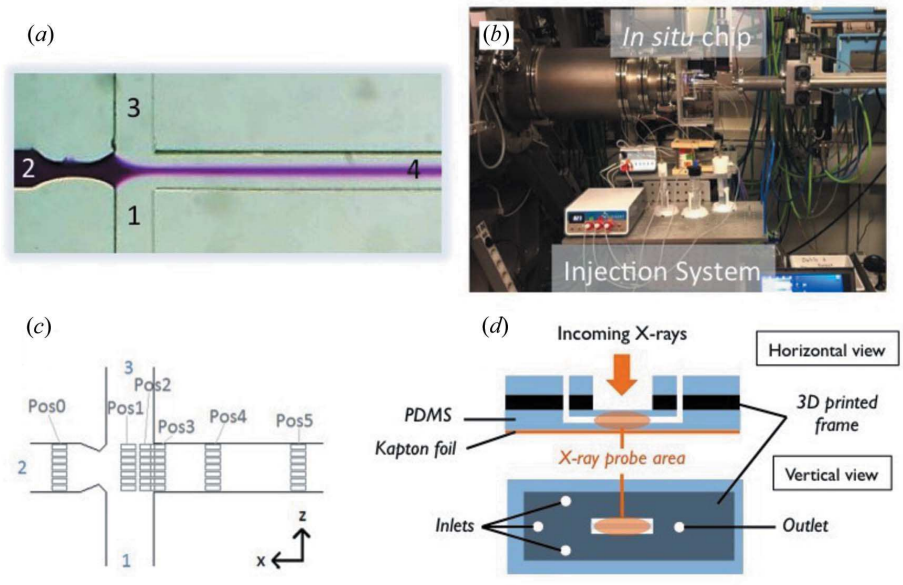

Figure 5
(*a*) Picture of the PDMS chip showing all the channels and the flow-focusing effect, (*b*) picture of the *in situ* cell and setup installed on the SWING beamline, (*c*) sketch of the positions where SAXS data were recorded into the PDMS chip and (*d*) scheme of the microfluidic chip design. Further information on the fabrication process can be found in Fig. S2.

Kapton foil (25 µm thick), thus resulting in minimal parasitic scattering.

The PDMS chip was designed as a four-channels cross with a restriction in the second channel [see Fig. 5(*a*)]. This geometry allows using the flow-focusing technique in order to investigate the first few milliseconds of assembly or reaction processes (Knight *et al.*, 1998; Otten *et al.*, 2005). The principle of flow focusing consists of squeezing a central stream of liquid (liquid in channel 2) arriving at the four channels intersection by the two side streams coming from channels 1 and 3 [see Fig. 5(*a*)]. As a result, a thin-sheathed stream is produced in the channel 4 outlet. This flowing configuration is a faster alternative to turbulent mixing since, at such small scales, solutes coming from channels 1 and 3 rapidly diffuse across the stream from channel 2 (Knight *et al.*, 1998).

We have used the PDMS chip to record SAXS data on Au nanoparticles (see Section S2 in the supporting information for Au nanoparticles preparation). SAXS data were recorded at 12 keV on the SWING (David & Pérez, 2009) beamline of SOLEIL and the q range was chosen in order to cover the full form-factor range of 5 and 10 nm-diameter Au nanoparticles spheres, corresponding to a distance of 1 m between the sample and the detector. The chip was placed into the beam path and connected to a piezo-controlled pressure system (Fluigent) for flow control and regulation [Fig. 5(*b*)]. SAXS images were recorded at the X-ray probe area of the PDMS chip [Fig. 5(*d*)].

First, SAXS images were recorded with citrate buffer flowing through the channels in order to subtract background from the sample measurements. Then, using the pressure-control system, two batches of 10 n*M* Au nanoparticles solutions (5 and 10 nm in diameter) were injected with a steady flow rate: 5 µl min^{-1} in channel 2 of the PDMS chip. The citrate buffer was injected at 11 µl min^{-1} in channels 1 and 3. SAXS images were recorded at the same position in the chip for the buffer and for the samples thanks to an accurate motorized table, 2D images were reduced to 1D curves and background was subtracted using the *Foxtrot* software (SOLEIL custom-made software). Despite the small volume probed by the X-ray beam (channel height is 180 µm) and the low-intensity signal obtained, curves were fitted using the *Irina* package (Ilavsky & Jemian, 2009), giving a radius for Au nanoparticles of 29.87 ± 0.06 Å (Fig. S4). The measured radius is therefore in good agreement with the one announced by the manufacturer (25 Å). As the signal was very low, we decided to use 10 nm-diameter Au nanoparticles in order to study their dilution in the chip.

We first recorded SAXS images at position 0 at different vertical spots. The five resulting curves show that there is no decrease in intensity at small q [Fig. 6(*a*) red circle] and that there is no modification of the nanoparticles form factor, while vertically scanning the channel. This is expected but confirms the reproducibility of the measurement on different vertical spots. Fitting those curves resulted in Au nanoparticles of 45.55 ± 0.07 Å in radius [Fig. 6(*c*)]. SAXS data were then collected at positions 1–5 at several vertical spots, corresponding to different positions in the buffer–nanoparticle solution gradient at different times of the diffusion process. While moving towards position 5, we observe as expected a dilution of the nanoparticles solution along channel 4. The dilution is visible on SAXS curves as the intensity at small q is increasing from the channel border towards the channel center [Fig. 6(*b*), red oval]. The signal being still strong, we were able to fit these curves. A radius of 46.71 ± 0.09 Å was found [Fig. 6(*d*)], in good agreement with the announced radius (50 Å). It should be noted that subtracting the chips/buffer background signal from the sample signal is mandatory, which requires foreseeing the position where the sample will be measured. Despite this procedure, small differences in the background can still be observed between the signal from the chip loaded with buffer and from the chip loaded with buffer and sample [Fig. 6(*a*), green curve]. This can be explained by slight changes in the optical path length because of the higher pressure required to flow the sample into the chip.

A fully 3D-printed *in situ* liquid flow cell was also fabricated and used to collect SAXS data. It is made of a single block VeroClear piece, as shown in Fig. S3. The only post-printing processing consisted of removing the printing support material from the outside of the block and the inside of the channel (using a thin needle), and machining the threads for the inlet and outlet liquid connectors. The channel inner diameter was 500 µm and the front and back membranes were ∼100 µm thick. PTFE (polytetrafluoroethylene) tubings were

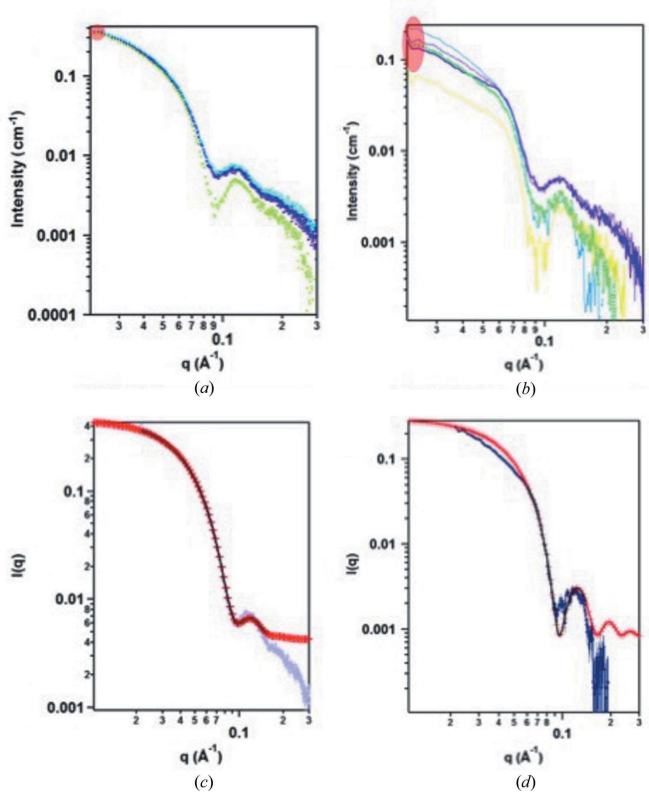

Figure 6
SAXS curves of 10 nm-diameter Au nanoparticles in the PDMS chips at different heights for position 0 (*a*) and position 5 (*b*). Fitted curves (black) of 10 nm-diameter Au nanoparticles recorded in the center of channel 4 at positions 0 (*c*) and 5 (*d*). Theoretical curves are shown in red.

connected to the cell's inlet and outlet, and a 10 n*M* solution of gold nanoparticle (5 nm in diameter) was flown through the cell. Although there was no mixing possible in this flow cell, the quality of the signal was much higher because of the larger volume probed by the X-rays (the channel is 500 µm thick *versus* 180 µm for the PDMS chip). The data collected with this cell and the associated curve fittings can be found in Fig. S4.

Thanks to 3D printing and to soft-lithography techniques, we have designed and manufactured chips in a very short time (1–2 d), in which we can record form factors of 5 and 10 nm-diameter Au nanoparticles at a concentration of 10 n*M* for two different optical paths (500 and 180 µm). Moreover, in the case of the PDMS chip, we have shown that the flow-focusing technique can be applied to record form factors of nanoparticles while they are being diluted and to follow this process *in situ*. These experimental setups could be easily used as disposable 3D-printed flow cells in order to replace quartz capillaries for inert samples and, for the flow-focusing device, as a convenient means of probing fast kinetic reactions or assembly processes.

3.3. Macromolecular serial crystallography using microfluidic-based trapping chips

The field of structural biology consists of a plethora of complementary methods aimed at obtaining functional information on complex macromolecular objects. Among the most popular techniques, macromolecular crystallography (MX) has been greatly recognized in obtaining near-atomic resolution details on such molecules. A typical MX experiment implies the use of cryo-protected protein crystals, the data measurements being performed at cryogenic temperatures in order to limit the propagation of radiation damage generated by the strong X-rays hitting the biological crystals. Although the use of cryogenic conditions and protocols appears as mandatory in accepted MX diffraction experiments, it shows some deleterious effects on the crystals' integrity and, for some specific systems, prevents dynamical studies. In such a context and without proper experimental methods available, molecular dynamics simulations appear to be an elegant approach in tackling these restricted applications (Vasil'ev & Bruce, 2006). The latest developments of X-ray free-electron laser (XFEL) sources moved the field to a new horizon where crystals not cryo-protected are measured once before being destroyed by the highly intense beam of the XFEL short pulses, yet open to diffraction measurements free of noticeable radiation damage deleterious to the understanding of biological processes (Chapman *et al.*, 2011). This new technique of serial femtosecond crystallography (SFX) has rapidly evolved and produced spectacular results linked to better understanding complicated enzymatic machineries (Martin-Garcia *et al.*, 2016; Kern *et al.*, 2018). Nevertheless, the SFX approach remains extremely challenging in terms of sample injection into the X-ray interaction point, which eventually reflects on the capacity to produce crystalline samples and produce with sufficiently good quality.

Alternative strategies to deliver crystals to an X-ray beam are being investigated and notably include microfluidic devices. Several such systems have recently been proposed for *in situ* protein crystallography, where crystals can be studied directly in their growing conditions without any further transfer or freezing process (Pinker *et al.*, 2013). Other systems immobilize the objects to be studied by circulating them within their growing media in a microfluidic environment with an array of traps along the path of the chip (Lyubimov *et al.*, 2015). However, most of these systems remain proof-of-principle demonstrations and were not fully applied to address specific biological questions.

Inspired by these previous studies, we developed and used several systems to quickly handle macromolecular crystals. Three-dimensional printed-capillary holders were designed for adapting diffraction experiments to *in situ* capillary-grown crystals (Fig. 7). Using the 3D printer of the MF-Lab, a rigid frame was fabricated on which a magnetic pin, an injection tube and the capillary to receive the crystals were assembled. Crystals grown in another microfluidic system (Gerard *et al.*, 2017) were injected from the storage capillary and into the X-ray diffraction capillary using a pressure controller and syringe pumps while connecting both capillaries with standard high-performance liquid chromatography tubing tools. After detaching the storage capillary, the frame was mounted on a goniometer of the PROXIMA-1 beamline (Coati *et al.*, 2017), as depicted in Fig. 7(*b*), and diffraction data were collected. Although in the current setup both storage and X-ray

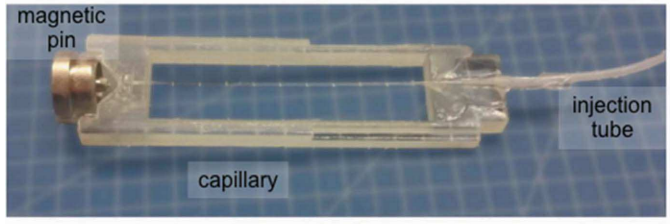

(*a*)

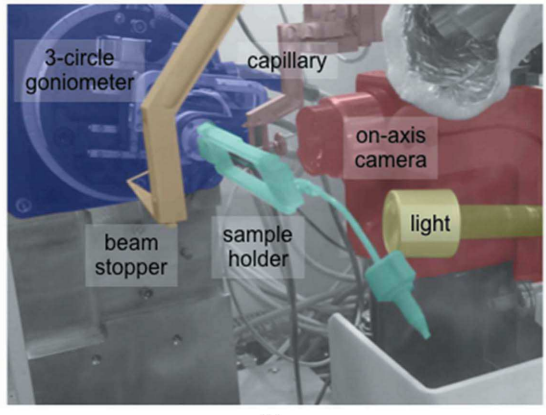

(*b*)

Figure 7
(*a*) Capillary and injection tube mounted on a magnetic pin for X-ray diffraction experiments. (*b*) 3D-printed adapting tool (cyan) mounted on a three-circle goniometer (purple) at the PROXIMA-1 beamline. The tubing used to load the samples remains visible.

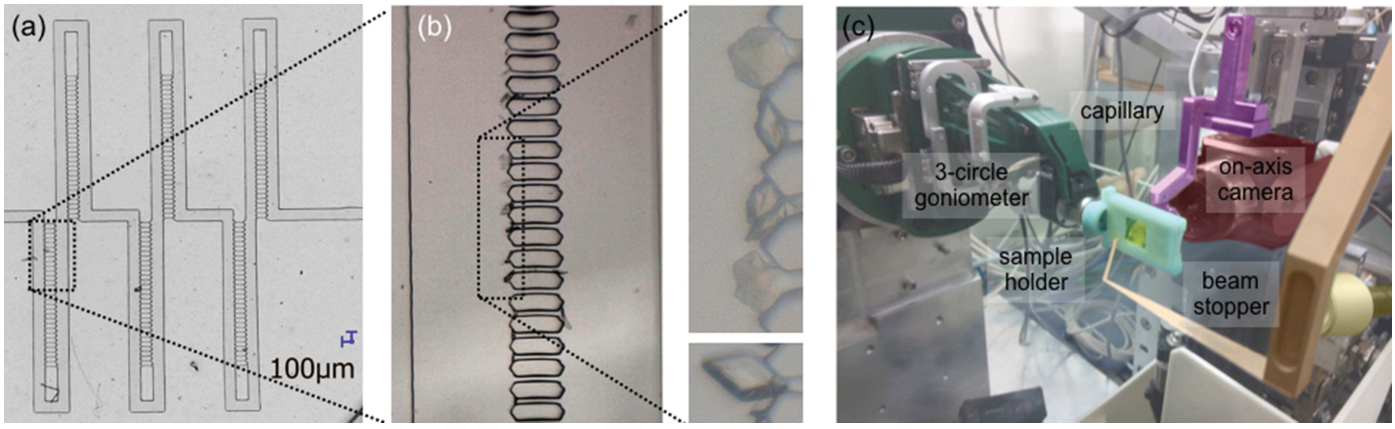

Figure 8
(*a*) Pattern overview inside the PDMS/Kapton chip used for trapping biological objects. A total of 180 traps arranged in three 'way and back' lines are shown in this view. (*b*) Enlarged view of trapped crystals within the chip. (*c*) 3D-printed chip holder (cyan) mounted on a three-circle goniometer (green).

diffraction capillaries were disconnected before the X-ray experiments, one could foresee some fields of interest in collecting X-ray diffraction data on solutions constantly flowing through the capillary, notably when screening for crystal conditions in an *in situ* crystal-growth approach.

A PDMS-based microfluidic chip was also designed and fabricated (see Fig. S5) in which crystals were loaded and trapped at known positions ready for X-ray diffraction experiments [Figs. 8(*a*) and 8(*b*)]. For X-ray diffraction data recording, this chip was inserted into a custom-designed 3D-printed chip holder, which includes a magnetic pin. The chip was loaded with protein crystals (40 µm in the longest dimension) by circulating a suspension of crystals in their mother liquor using a syringe pump. The chip holder was mounted on a three-circle goniometer at PROXIMA-1 and serial-crystallography experiments were recorded at an energy of 12.67 keV on a Pilatus 6M (Dectris Ltd) detector [Fig. 8(*c*)]. To obtain a complete data set, data collection from three isolated crystals exposed over an oscillation angle of 50° each were merged with good statistics up to a resolution of 1.6 Å (Table S1). The size of the X-ray beam at the sample position was restricted to 40 µm × 20 µm for a photon flux of 1×10^{10} photons s^{-1} mm^{-2}. Inspection of the diffraction images for each of the three selected data sets did not show noticeable radiation damage.

4. Conclusion

The availability of a dedicated microfluidic laboratory within a light-producing facility is ideal for on-demand and rapid fabrication of microfluidic systems that combine both the requirements of sample delivery and photon-based techniques. The variety of instruments available for both chip fabrication and analysis allows a fast response to the user's demands for off- and on-line requests. Maskless lithography and 3D-printing possibilities are instrumental in providing the emergency response that is required by typical synchrotron workflow. Beyond user-driven considerations, the presence of an in-house microfluidic laboratory at a synchrotron promotes the development of novel interaction points between spectroscopic and structural techniques and sample-delivery systems. We should stress once more that the high photon density of modern synchrotron sources can pose a serious threat to the sample's integrity, and microfluidic systems can provide solutions to this issue by rapidly regenerating the sample or removing the excess of heat or radicals generated by the beam.

In terms of scientific applications, microfluidic systems will be very helpful in providing liquid environments to solid samples such as crystals of biological objects, nanoparticles or micrometre-sized materials as they are analyzed by a photon beam. Drug discovery should be facilitated by the possibility to change the environment of a protein crystal at room temperature and *in situ*, the structure of reaction intermediates in the synthesis of nanoparticles can also be tracked *in situ* and the solid–liquid interface of catalytic films can be observed under operating conditions.

Although the microfluidic laboratory at SOLEIL is not opened yet to external users *via* the regular proposal review committees, it is available to all of the SOLEIL staff, associates and collaborators. Users interested in this facility should contact the laboratory manager or any beamline scientist from SOLEIL with whom a collaboration centered on microfluidics is to be developed.

Acknowledgements

Dr Paul Dumas, Dr Gabriel David and Ms. Valérie Rouam are greatly acknowledged for their help in setting up the microfluidic laboratory and its equipment. IC performed the experiments under a collaborative research program between SOLEIL and the SERVIER Research Institute. The LUCIA, SWING and PROXIMA-1 teams are greatly acknowledged for their assistance in data collection during commissioning beam time.

Funding information

LMGC acknowledges funding from the European Union's Horizon 2020 research and innovation programme under Grant Agreement No. 708130.

References

Au, A. K., Huynh, W., Horowitz, L. F. & Folch, A. (2016). *Angew. Chem. Int. Ed.* **55**, 3862–3881.
Chan, E. M., Marcus, M. A., Fakra, S., ElNaggar, M., Mathies, R. A. & Alivisatos, A. P. (2007). *J. Phys. Chem. A*, **111**, 12210–12215.
Chapman, H. N., Fromme, P., Barty, A., White, T. A., Kirian, R. A., Aquila, A., Hunter, M. S., Schulz, J., DePonte, D. P., Weierstall, U., Doak, R. B., Maia, F. R. N. C., Martin, A. V., Schlichting, I., Lomb, L., Coppola, N., Shoeman, R. L., Epp, S. W., Hartmann, R., Rolles, D., Rudenko, A., Foucar, L., Kimmel, N., Weidenspointner, G., Holl, P., Liang, M., Barthelmess, M., Caleman, C., Boutet, S., Bogan, M. J., Krzywinski, J., Bostedt, C., Bajt, S., Gumprecht, L., Rudek, B., Erk, B., Schmidt, C., Hömke, A., Reich, C., Pietschner, D., Strüder, L., Hauser, G., Gorke, H., Ullrich, J., Herrmann, S., Schaller, G., Schopper, F., Soltau, H., Kühnel, K., Messerschmidt, M., Bozek, J. D., Hau-Riege, S. P., Frank, M., Hampton, C. Y., Sierra, R. G., Starodub, D., Williams, G. J., Hajdu, J., Timneanu, N., Seibert, M. M., Andreasson, J., Rocker, A., Jönsson, O., Svenda, M., Stern, S., Nass, K., Andritschke, R., Schröter, C., Krasniqi, F., Bott, M., Schmidt, K. E., Wang, X., Grotjohann, I., Holton, J. M., Barends, T. R. M., Neutze, R., Marchesini, S., Fromme, R., Schorb, S., Rupp, D., Adolph, M., Gorkhover, T., Andersson, I., Hirsemann, H., Potdevin, G., Graafsma, H., Nilsson, B. & Spence, J. C. H. (2011). *Nature*, **470**, 73–77.
Coati, A., Chavas, L. M. G., Fontaine, P., Foos, N., Guimaraes, B., Gourhant, P., Legrand, P., Itie, J.-P., Fertey, P., Shepard, W., Isabet, T., Sirigu, S., Solari, P.-L., Thiaudiere, D. & Thompson, A. (2017). *Eur. Phys. J. Plus*, **132**, 174.
David, G. & Pérez, J. (2009). *J. Appl. Cryst.* **42**, 892–900.
Gerard, C. J. J., Ferry, G., Vuillard, L. M., Boutin, J. A., Chavas, L. M. G., Huet, T., Ferte, N., Grossier, R., Candoni, N. & Veesler, S. (2017). *Acta Cryst.* F**73**, 574–578.
Hemmerle, A., Fragneto, G., Daillant, J. & Charitat, T. (2016). *Phys. Rev. Lett.* **116**, 228101.
Ilavsky, J. & Jemian, P. R. (2009). *J. Appl. Cryst.* **42**, 347–353.
Joanicot, M. & Ajdari, A. (2005). *Science*, **309**, 887–888.
Kern, J., Chatterjee, R., Young, I. D., Fuller, F. D., Lassalle, L., Ibrahim, M., Gul, S., Fransson, T., Brewster, A. S., Alonso-Mori, R., Hussein, R., Zhang, M., Douthit, L., de Lichtenberg, C., Cheah, M. H., Shevela, D., Wersig, J., Seuffert, I., Sokaras, D., Pastor, E., Weninger, C., Kroll, T., Sierra, R. G., Aller, P., Butryn, A., Orville, A. M., Liang, M., Batyuk, A., Koglin, J. E., Carbajo, S., Boutet, S., Moriarty, N. W., Holton, J. M., Dobbek, H., Adams, P. D., Bergmann, U., Sauter, N. K., Zouni, A., Messinger, J., Yano, J. & Yachandra, V. K. (2018). *Nature*, **563**, 421–425.
Knight, J. B., Vishwanath, A., Brody, J. P. & Austin, R. H. (1998). *Phys. Rev. Lett.* **80**, 3863–3866.
Lyubimov, A. Y., Murray, T. D., Koehl, A., Araci, I. E., Uervirojnangkoorn, M., Zeldin, O. B., Cohen, A. E., Soltis, S. M., Baxter, E. L., Brewster, A. S., Sauter, N. K., Brunger, A. T. & Berger, J. M. (2015). *Acta Cryst.* D**71**, 928–940.
Martin-Garcia, J. M., Conrad, C. E., Coe, J., Roy-Chowdhury, S. & Fromme, P. (2016). *Arch. Biochem. Biophys.* **602**, 32–47.
Otten, A., Köster, S., Struth, B., Snigirev, A. & Pfohl, T. (2005). *J. Synchrotron Rad.* **12**, 745–750.
Pinker, F., Brun, M., Morin, P., Deman, A.-L., Chateaux, J.-F., OliéRic, V., Stirnimann, C., Lorber, B., Terrier, N., Ferrigno, R. & Sauter, C. (2013). *Cryst. Growth Des.* **13**, 3333–3340.
Polte, J., Erler, R., Thünemann, A. F., Sokolov, S., Ahner, T. T., Rademann, K., Emmerling, F. & Kraehnert, R. (2010). *ACS Nano*, **4**, 1076–1082.
Qin, D., Xia, Y. & Whitesides, G. M. (2010). *Nat. Protoc.* **5**, 491–502.
Reich, C., Hochrein, M. B., Krause, B. & Nickel, B. (2005). *Rev. Sci. Instrum.* **76**, 095103.
Song, H. & Ismagilov, R. F. (2003). *J. Am. Chem. Soc.* **125**, 14613–14619.
Tabeling, P. (2005). *Introduction to Microfluidics.* Oxford University Press.
Vantelon, D., Trcera, N., Roy, D., Moreno, T., Mailly, D., Guilet, S., Metchalkov, E., Delmotte, F., Lassalle, B., Lagarde, P. & Flank, A.-M. (2016). *J. Synchrotron Rad.* **23**, 635–640.
Vasil'ev, S. & Bruce, D. (2006). *Biophys. J.* **90**, 3062–3073.
Whitesides, G. M. (2006). *Nature*, **442**, 368–373.
Zarzar, L. D., Sresht, V., Sletten, E. M., Kalow, J. A., Blankschtein, D. & Swager, T. M. (2015). *Nature*, **518**, 520–524.
Zheng, B., Tice, J. D., Roach, L. S. & Ismagilov, R. F. (2004). *Angew. Chem. Int. Ed.* **43**, 2508–2511.

UNIVERSITÉ DE RENNES 1

Titre : Comment l'organisation physique des agrégats nano-particulaires fer-matière organique contrôle-t-elle leur réactivité ?

Mots clés : agrégats fer-matière organique, calcium, aluminium, arsenic, XAS, SANS-SAXS

Résumé : Dans les systèmes naturels, les hétéro-agrégats organo-minéraux fer-matière organique (Fe-MO) jouent un rôle clé dans la dynamique des polluants. Leur capacité à adsorber les métaux et métalloïdes dépend de leur organisation structurale, elle-même contrôlée par les conditions physico-chimiques dans l'environnement. Le calcium (Ca) et l'aluminium (Al) sont des cations majeurs qui peuvent interagir avec la MO et/ou le Fe. Leur impact sur la structure des agrégats Fe-MO et, par conséquent, sur leur réactivité peut donc s'avérer important.

En présence de Ca et d'Al, l'organisation structurale des associations Fe-MO évolue d'un état colloïdal vers un réseau micrométrique dont les connexions sont assurées soit par des dimères de Ca, soit par des monomères, oligomères ou hydroxydes amorphes d'Al. Le Fe(III) est organisé sous forme d'oligomères et de nanoparticules de type ferrihydrite (Nps-Fh). La taille et la proportion des Nps-Fh augmentent avec l'augmentation de la concentration en Ca ou Al en réponse à la diminution des liaisons Fe-MO ; cette diminution étant due, à la formation de liaisons Ca-MO ou Al-MO.

La présence du Ca contrôle la réactivité des phases de Fe vis-à-vis de l'arsenic. En limitant les interactions entre la MO et les Nps-Fh, le Ca augmente la disponibilité des sites d'adsorption pour l'arsenic.

Ces résultats apportent une nouvelle vision du rôle des hétéro-agrégats de Fe-MO dans la mobilité des éléments chimiques. Celle-ci apparait plus limitée qu'attendu, en raison de la formation d'un réseau Fe-MO micrométrique.

Title: How does the structural organization of iron-organic matter nano-aggregates control their reactivity?

Keywords: iron-organic matter aggregates, calcium, aluminum, arsenic, XAS, SANS-SAXS

Abstract: In natural systems, organo-mineral iron-organic matter (Fe-OM) heteroaggregates are a key factor in the dynamics of metallic pollutants. Their capacity to adsorb metals and metalloids depends on their structural organization, which is itself controlled by the physico-chemical conditions prevailing in the environment. Calcium (Ca) and aluminum (Al) are major cations commonly encountered in natural waters and can interact with OM and/or Fe. Their impact on the structure of Fe-OM aggregates and therefore on their reactivity could thus be major.

With Ca and Al, Fe-OM associations structural organization moves from a colloidal behavior to a micrometric network whose connections are ensured either by Ca dimers or by Al monomers, oligomers or amorphous hydroxides. Iron(III) is organized as oligomers and ferrihydrite-like nanoparticles (Fh-Nps). The size and proportion of Nps-Fh increase with the icnrease of Ca or Al concentration in response to the partial screening of Fe-OM interactions by the binding of Ca and Al with OM.

The presence of Ca which decreases the Fe and OM interactions, increases the availability of Fe binding sites, thus improving the adsorption capacities of Fe-MO aggregates with respect to As.

These results shed new light for the understanding of the dynamics of Fe, MO and associated elements which mobility could more limited as expected regarding the possible formation of an interconnected micrometric network.